

Copyright Warning & Restrictions

The copyright law of the United States (Title 17, United States Code) governs the making of photocopies or other reproductions of copyrighted material.

Under certain conditions specified in the law, libraries and archives are authorized to furnish a photocopy or other reproduction. One of these specified conditions is that the photocopy or reproduction is not to be “used for any purpose other than private study, scholarship, or research.” If a user makes a request for, or later uses, a photocopy or reproduction for purposes in excess of “fair use” that user may be liable for copyright infringement,

This institution reserves the right to refuse to accept a copying order if, in its judgment, fulfillment of the order would involve violation of copyright law.

Please Note: The author retains the copyright while the New Jersey Institute of Technology reserves the right to distribute this thesis or dissertation

Printing note: If you do not wish to print this page, then select “Pages from: first page # to: last page #” on the print dialog screen

The Van Houten library has removed some of the personal information and all signatures from the approval page and biographical sketches of theses and dissertations in order to protect the identity of NJIT graduates and faculty.

ABSTRACT

EFFECT OF PROCESS CONTROL AGENTS USED IN MECHANOCHEMICAL SYNTHESIS ON PROPERTIES OF THE PREPARED COMPOSITE REACTIVE MATERIALS

**by
Mehnaz Mursalat**

The study explores synthesis and reactivity of new reactive materials prepared by ball milling. High-energy ball milling became a ubiquitous mechano-chemical tool to manufacture diverse powders, from pharmaceuticals or foods to alloys to new solid rocket propellants. It enabled a dramatic expansion of the range of chemical compositions obtainable; however, it did not so far, allowed one to fine-tune morphology or interfaces in the generated powders. It is shown in this work how different process control agents (PCAs) can serve to tune the powder morphology and reactivity. Commonly used as lubricants and cooling agents during milling, liquid PCAs can be used as an effective tool in modifying both chemistry and morphology of mechanochemically prepared reactive materials. For example, a polar, non-oxidizing fluid, e.g., acetonitrile, can reduce the size of aluminum particles, but more interestingly, it can modify their surface to enable new redox reaction pathways leading to accelerated ignition and combustion. Using such modified aluminum in a composite prepared by milling makes it possible to design unusual reactive materials. Materials with the same chemical compositions, and thus the same overall energy densities can be made with controllable reaction dynamics and tunable heat release. Thus, it becomes possible to separate the effects of chemical composition and interface structure on the reaction mechanisms and rates.

An even more unusual capability of manipulating shapes and sizes of the synthesized powders is discovered in this study when liquid PCA comprises two immiscible fluids. A complex system including an emulsion combined with suspended particles is generated inside the milling vial. When such a system is milled, solid particles can be refined, mixed, and eventually accumulated inside the droplet phase. Thus, spherical solid aggregates are formed with narrow size distributions. Milling conditions can be found to tune size, density, and porosity of such spheres. Produced narrowly-sized spherical powders are attractive because of their dramatically improved flowability. The existing methods for synthesizing spherical powders (e.g., spray-drying, extrusion-spheronization, droplet-melting) are more expensive, time-consuming, and energy-intensive. Unlike milling, they cannot be employed to a diverse range of materials and the challenges associated with wide particle size distributions often are unsurmountable. Our approach has been validated experimentally for elemental (e.g., Al, B), alloyed (B·Ti, Al·Ti), ceramic (Fe_2O_3), organic (melamine), and composite (Al·CuO) spheres from materials with a broad range of initial particle sizes and mechanical properties. The average size of the particles could be selectable from 5 to 200 μm . Experiments also confirmed superior rheological properties of the prepared reactive powders and their enhanced reactivity. For future, this study can be expanded beyond reactive materials to discover a new generation of value-added materials for catalysts, adsorbents, and feedstock powders for additive manufacturing.

**EFFECT OF PROCESS CONTROL AGENTS USED IN MECHANOCHEMICAL
SYNTHESIS ON PROPERTIES OF THE PREPARED COMPOSITE REACTIVE
MATERIALS**

**by
Mehnaz Mursalat**

**A Dissertation
Submitted to the Faculty of
New Jersey Institute of Technology
In Partial Fulfillment of the Requirements for the Degree of
Doctor of Philosophy in Chemical Engineering**

**Otto H. York Department of
Chemical and Materials Engineering**

May 2022

Copyright © 2022 by Mehnaz Mursalat

ALL RIGHTS RESERVED

APPROVAL PAGE

EFFECT OF PROCESS CONTROL AGENTS USED IN MECHANOCHEMICAL SYNTHESIS ON PROPERTIES OF THE PREPARED COMPOSITE REACTIVE MATERIALS

Mehnaz Mursalat

Dr. Edward L. Dreizin, Dissertation Advisor Distinguished Professor of Chemical and Materials Engineering, NJIT	Date
--	------

Dr. Lisa B. Axe, Committee Member Professor and Head of Chemical and Materials Engineering, NJIT	Date
---	------

Dr. Mirko Schoenitz, Committee Member Associate Research Professor of Electrical and Computer Engineering, NJIT	Date
--	------

Dr. Murat Guvendiren, Committee Member Assistant Professor of Chemical and Materials Engineering, NJIT	Date
---	------

Dr. Stephen D. Tse, Committee Member Professor of Mechanical and Aerospace Engineering, Rutgers University	Date
---	------

BIOGRAPHICAL SKETCH

Author: Mehnaz Mursalat
Degree: Doctor of Philosophy
Date: May 2022

Undergraduate and Graduate Education:

- Doctor of Philosophy in Chemical Engineering,
New Jersey Institute of Technology, Newark, NJ, 2022
- Master of Science in Chemical Engineering,
New Jersey Institute of Technology, Newark, NJ, 2016
- Bachelor of Science in Electrical Engineering,
Bangladesh University of Engineering and Technology, Dhaka, Bangladesh, 2014

Major: Chemical Engineering

Presentations and Publications:

Publications:

- M. Mursalat**, M. Schoenitz, E. L. Dreizin, A. Neveu, and F. Francqui, Spherical Boron Powder Prepared by Mechanical Milling in Immiscible Liquids, Powder technology 388, p.41-50 (2021)
- M. Mursalat**, C. Huang, B. Julien, M. Schoenitz, A. Esteve, C. Rossi and E.L. Dreizin, Low Temperature Exothermic Reactions in Al/CuO Nanothermites Producing Copper Nanodots and Accelerating Combustion, ACS Applied Materials 4, p.3811-3820 (2021)
- S. Matveev, D. D. Dlott, S. Valluri, **M. Mursalat**, and E. L. Dreizin, Fast Energy Release from Reactive Materials Under Shock Compression, Applied Physics Letter, 118, p. 101902,1-3 (2021)
- M. Mursalat**, M. Schoenitz, E.L. Dreizin, Effect of premilling Al and CuO in acetonitrile on properties of Al-CuO thermites prepared by arrested reactive milling, Combustion and Flame 214, p.57-64 (2020)

- M. Mursalat**, D.L. Hastings, M. Schoenitz, E.L. Dreizin, Microspheres with Diverse Material Compositions Can be Prepared by Mechanical Milling, *Advanced Engineering Materials* 22, p.1901204,1-4 (2020)
- M. Mursalat**, M. Schoenitz, E.L. Dreizin, Custom particle morphology in energetic nanocomposites prepared by arrested reactive milling in immiscible liquids, *Powder technology* 359, p.238-246 (2020)
- M. Mursalat**, M. Schoenitz, E.L. Dreizin, Composite Al-Ti powders prepared by high-energy milling with different process controls agents, *Advanced Powder technology* 30, p.1319-1328 (2019).

Presentations:

- M. Mursalat**, M. Schoenitz, and E.L. Dreizin, Ignition and Combustion of Spherical Boron by Ball Milling, Spring technical Meeting of Eastern State Sections of Combustion Institute, Orlando, FL, March 2022 (oral)
- M. Mursalat**, M. Schoenitz, and E.L. Dreizin, Spherical Powders with Improved Rheology Prepared by Ball Milling, presented at the Annual Meeting of Society of Tribologists and Lubrication Engineers (STLE), February 2022 (virtual invited talk)
- M. Mursalat**, M. Schoenitz, E.L. Dreizin, Tuning Reactivity of Al-CuO Thermites Prepared by Arrested Reactive Milling Using Liquid Process Control Agents, presented at the Materials Research Society (MRS) Fall Meeting & Exhibit, Boston, MA, December 2019 (oral).
- M. Mursalat**, D.L. Hastings, M. Schoenitz, E.L. Dreizin, Spherical Composite Powders Prepared by Mechanical Milling, presented at the Materials Research Society (MRS) Fall Meeting & Exhibit, Boston, MA, December 2019 (oral).
- M. Mursalat**, M. Schoenitz, E.L. Dreizin, Aluminum-Based Thermites Prepared By Staged Milling with Different Process Control Agents, presented at the American Institute of Chemical Engineers (AIChE) Annual Meeting, Orlando, FL, November 2019 (oral).
- M. Mursalat**, D.L. Hastings, M. Schoenitz, E.L. Dreizin, Filled Spherical Composite Particles Prepared By Mechanical Milling, presented at the American Institute of Chemical Engineers (AIChE) Annual Meeting, Orlando, FL, November 2019 (oral).
- M. Mursalat**, M. Schoenitz, E.L. Dreizin, Effect of Liquid Hydrocarbon-Based Process Control Agents on Characteristics of mechanically Alloyed Al-Ti Powders,

presented at the American Institute of Chemical Engineers (AIChE) Annual Meeting, Pittsburg, PA, October 2018 (oral).

M. Mursalat, M. Schoenitz, E.L. Dreizin, Effects of Liquid Hydrocarbon based Process Control Agents on Characteristics of Nanocomposite Thermites Prepared by Arrested Reactive Milling, presented at the Defense Threat Reduction Agency (DTRA) Technical Review, McLean, VA, July 2018 (poster).

M. Mursalat, M. Schoenitz, E.L. Dreizin, Effects of Liquid Hydrocarbon based Process Control Agents on Characteristics of Nanocomposite Thermites Prepared by Arrested Reactive Milling, presented at the Gordon Research Seminar (GRS) on Energetic Materials, Newry, ME, June 2018 (poster).

M. Mursalat, M. Schoenitz, E.L. Dreizin, Effects of Liquid Hydrocarbon based Process Control Agents on Characteristics of Nanocomposite Thermites Prepared by Arrested Reactive Milling, presented at the Gordon Research Conference (GRC) on Energetic Materials, Newry, ME, June 2018 (poster).

Patents:

M. Mursalat, M. Schoenitz, E.L. Dreizin, Method of preparation of spherical composite powder, US provisional patent application 62738046, 2018 (renewed 2019).

M. Mursalat, M. Schoenitz, E.L. Dreizin, Method of preparation of spherical composite powder, US non-provisional patent application 62738046, 2020.

I dedicate this dissertation

To my parents:

Dr. Shaila Hossain (Ammu) and Dr. A.T.M. Mosharef Hossain (Abbu)
There is no me without you and what I am today is all because of you

To my grandparents:

Late Md. Siddique Hossain (Nana), Mrs. Syeda Khatoon (Nanu), Late Md. Adam Ali
(Dada), Late Mrs. Anwara Begum (Dadi)
You are the pillars of our wonderful family and my continued success is a result of your
prayers and blessings

To my beloved motherland:

Bangladesh

You taught me to dream, you taught me to strive and I will continue to adhere to the
values you instilled in me InshaAllah

আমার সোনার বাংলা আমি তোমায় ভালবাসি

ACKNOWLEDGMENT

I would like to thank the Almighty for crossing my path with my advisor, Dr. Edward Dreizin. In a time of despair when I was struggling with uncertainties and indecision, Dr. Dreizin allowed me to be a part of his Advanced Energetic Lab in spring 2018. His constant guidance and care have not only helped me grow as a researcher but a strong individual embarking into a new chapter of life. I thank him with all my heart for being by my side and supporting me through my good times and bad times.

I would like to offer my utmost gratitude to my co-advisor Dr. Mirko Schoenitz for enriching my research with his constructive feedback. He has always been the go-to person whenever I encountered any problem with experiments or needed help understanding certain concepts. I greatly admire his patience and willingness to help.

I am thankful to my dissertation committee members Dr. Lisa Axe, Dr. Stephen Tse and Dr. Murat Guvendiren for their time and feedback.

I would also like to acknowledge NJIT CME faculty and staff, staff members from material characterization facilities at Otto H. York Centre for Environmental Engineering and Sciences, US Defense Threat reduction Agency, Office of Naval research, Airforce office of Scientific Research for facilitating my research at NJIT.

I would like to further extend my gratitude to my fellow lab mates in the Advanced Energetics Group for always supporting me. And of course, I greatly appreciate two of my very talented undergraduate mentees Agata Skura and Holly McCann for driving the projects through.

Some of the names I simply cannot miss out are Dr. Esha Khoshnu, Andrew House, Dr. Farzana Zaki, Dr. Mahbubur Rahman, Samiha Hossain, Dr. Irina Molodetsky, Dr.

Kerri-lee Chintersingh, Dr. Xinhang Liu, Ci Huang and Fatima Enam. You all made my journey in the USA worth cherishing forever.

I would never have reached this milestone unless my parents, Shaila Hossain (Ammu) and Mosharef Hossain (Abbu) had pushed me off my limits. Their hard work, vision and core values have always inspired me to strive through my journey with honesty, integrity and dignity. I am the luckiest daughter in the world.

I strongly believe the prayers and blessings from my grandparents, the late Md. Siddique Hossain (Nana), Mrs. Sayeda Khatoon (Nanu), late Md. Adam Ali (Dada) and late Mrs. Anwara Begum (Dadi) who have always protected me from all adversities and will continue to be my pillar of strength.

My Aunt Dr. Maheen Hossain, cousins, Akash and Arko are my family in this foreign land, seven thousand miles away from home. I would also like to acknowledge my aunts, Ms. Ishrat Jahan (Boroapu) and Mrs. Yasmin Hossain (Achchi) for being instrumental in my life in many different ways that I cannot even express.

I crossed path with my husband, Daniel Hastings during our doctoral journey. His role in this journey has been instrumental as a co-author, a critique, a travel buddy and most importantly as my best friend and a true confidant. I thank you for introducing me to the wonderful Hastings family who have embraced me with great love and affection. I am excited to explore many new chapters of our lives together in the coming days.

Last but not the least, I am extremely indebted to my beloved motherland, Bangladesh. No matter wherever I am, I am always inseparable from you. And I will bear Bangladesh in my heart and soul as long as I live.

TABLE OF CONTENTS

Chapter	Page
1 INTRODUCTION	1
1.1 Background.....	1
1.2 Synthesis Methods of Reactive Materials	3
1.2.1 Mixing of Nanopowders.....	4
1.2.2 Electrodeposition.....	5
1.2.3 Self-assembly	6
1.2.4 Sol-gel Synthesis.....	7
1.2.5 Layer Deposition.....	8
1.2.6 Mechanical Milling	10
1.3 Types of Interfaces between Reactive Components	11
1.4 Advantages of Mechanical Milling.....	13
1.5 Role of Process Control Agent (PCA) in Mechanical Milling.....	14
2 CUSTOM PARTICLE MORPHOLOGY IN ENERGETIC NANOCOMPOSITE BYARRESTED REACTIVE MILLING.....	17
2.1 Abstract	17
2.2 Introduction	17
2.3 Experiment	19
2.3.1 Sample Preparation	19
2.3.2 Characterization of Prepared Powders	20

TABLE OF CONTENTS (Continued)

Chapter	Page
2.4 Results	23
2.4.1 SEM Image Analysis.....	23
2.4.2 XRD Analysis	25
2.4.3 Thermal Analysis	27
2.4.4 Surface Areas	32
2.4.5 Ignition.....	33
2.4.6 Constant Volume Explosion (CVE).....	35
2.5 Discussion	36
2.6 Conclusions	42
3 EFFECT OF PREMILLING ALUMINUM AND COPPER (II) OXIDE IN ACETONITRILE ON PROPERTIES OF ALUMINUM-COPPER OXIDE THERMITES PREPARED BY ARRESTED REACTIVE MILLING.....	43
3.1 Abstract	43
3.2 Introduction	43
3.3 Experimental.....	44
3.3.1 Sample preparation.....	44
3.3.2 Characterization	45
3.4 Results	48
3.4.1 Component Premilling (Stage 1).....	48

TABLE OF CONTENTS (Continued)

Chapter	Page
3.4.2 Composite Formation (Stage 2)	50
3.4.3 Thermal Analysis	56
3.4.4 Ignition.....	60
3.4.5 Kinetics of Exothermic Reactions.....	61
3.5 Discussion	63
3.6 Conclusions	69
 4 LOW TEMPERATURE EXOTHERMIC REACTIONS IN Al-CuO NANOTHERMITES PRODUCING COPPER NANODOTS AND ACCELERATING COMBUSTION	 70
4.1 Abstract	70
4.2 Introduction	71
4.3 Experimental.....	74
4.3.1 Reactive Composite Powder	74
4.3.2 Material Characterization	75
4.4 Results	77
4.4.1 Combustion.....	77
4.4.2 Morphology and Phase Characterization of Composite Powders.....	81
4.5 Discussion	88
4.6 Conclusions	93

TABLE OF CONTENTS

(Continued)

Chapter	Page
5 COMPOSITE Al-Ti POWDERS PREPARED BY HIGH ENERGY MILLING WITH DIFFERENT PROCESS CONTROL AGENTS	95
5.1 Abstract	95
5.2 Introduction	96
5.3 Experimental.....	97
5.3.1 Sample preparation.....	97
5.3.2 Material Characterization	100
5.4 Preparation of Reactive Composite Al-Ti Powders with Fine Particle Sizes.....	104
5.4.1 Powders Prepared by One-stage Milling	104
5.4.2 Powders Prepared by Two-stage Milling	106
5.5 Exothermic Reactions	113
5.6 Results of Ignition and Combustion Experiments	114
5.6 Discussion	118
5.8 Conclusions	123
6 MICROSPHERES WITH DIVERSE MATERIAL COMPOSITIONS PREPARED BY MECHANICAL MILLING	124
6.1 Abstract	124
6.2 Introduction	124
6.3 Experimental.....	126
6.4 Results	127

TABLE OF CONTENTS (Continued)

Chapter	Page
6.5 Conclusion.....	133
7 SPHERICAL BORON POWDERS PREPARED BY MECHANICAL MILLING IN IMMISCIBLE LIQUIDS	134
7.1 Abstract	134
7.2 Introduction	135
7.3 Experimental.....	136
7.3.1 Materials Preparation	136
7.3.1 Material Characterization	137
7.4 Results	141
7.5 Effects of Milling Parameters on Properties of the Produced Spheres	152
7.6 Conclusion.....	161
8 EFFECT OF PARTICLE MORPHOLOGY ON REACTIVITY, IGNITION AND COMBUSTION OF BORON POWDERS	162
8.1 Abstract	162
8.2 Introduction	163
8.3 Experimental.....	164
8.3.1 Material Preparation	164
8.3.2 Material Characterization	166
8.4 Results	170

TABLE OF CONTENTS (Continued)

Chapter	Page
8.4.1 Powder morphology and size distributions.....	170
8.4.2 Oxidation of Boron Powders	174
8.4.2 Low-temperature Oxidation of Boron Powders in Air at Controlled Humidity	176
8.4.4 Heated Filament Ignition	178
8.4.5 Constant Volume Explosion (CVE).....	178
8.4.6 Combustion of Boron KNO ₃ Blends.....	180
8.5 Discussion	181
8.6 Conclusion.....	189
9 FUTURE WORK AND CONCLUSION	190
APPENDIX A STEM- EELS ANALYSIS OF Al-CuO NANOTHERMITES PRODUCING COPPER NANODOTS AT 650K	193
APPENDIX B DENSELY FILLED POWDER PREPARED BY MECHANICAL MILLING.....	195
APPENDIX C SPHERICAL BORON MORPHOLOGY, SIZE DISTRIBUTION.....	198
APPENDIX D EFFECT OF SPHERICAL MORPHOLOGY ON BORON COMBUSTION	201
REFERENCES.....	205

LIST OF TABLES

Table	Page
2.1	Compositions of Mixed Solvents Used for Preparation of $8\text{Al}\cdot 3\text{CuO}$20
3.1	Combinations of Milled/Unmilled Starting Materials45
3.2	Results of XRD Whole-pattern Refinement of As-milled Materials.....55
3.3	Mass Loss Encountered by Samples Heated in Ar to 1073 K.....57
3.4	Activation Energies Determined from DSC and DTG Measurements63
4.1	Phase Composition in wt-% of Materials Recovered from 650 K83
5.1	Milling Parameters for One stage Milling of $\text{Al}_{0.8}\text{Ti}_{0.2}$ Alloys.....98
5.2	Milling Parameters for Milling of $\text{Al}_{0.8}\text{Ti}_{0.2}$ at the 2nd stage99
5.3	Heating Rates Achieved in Ignition Experiments with Number of Batteries ...102
7.1	Milling Parameters Used to Prepare Different Boron Powders.....139
7.2	Characteristics of Particle Size Distribution, Surface Area, and Bulk Density 147
7.3	Coefficients of Linear Model 1.....157
7.4	Coefficients of Linear Model 1 with Outlier Removed158
8.1	Materials Used and Prepared with Respective Milling Conditions.....166
8.2	Maximum Pressure and Pressurization Rate from CVE Experiments.....180

LIST OF FIGURES

Figure	Page
1.1	Enthalpies of combustion of different reactive materials.....2
1.2	Scanning electron microscopy (SEM) image of Al/CuO thermite prepared by ultrasonic mixing.....4
1.3	FESEM image of the WO _{2.9} nanowire6
1.4	TEM image of self-assembled Fe ₂ O ₃ –Al nanothermite.....7
1.5	TEM image of Al-Fe ₂ O ₃ thermite system prepared by sol-gel method.....8
1.6	Elemental distribution images of CuO _x /Al multilayer foils.....9
1.7	Different materials prepared by mechanical milling.....11
1.8	Possible Interface geometry of different types of thermite systems13
1.9	Effect of the amount of stearic acid on particle size15
2.1	Backscattered electron SEM images of milled 8Al·3CuO thermites.....24
2.2	Cross-sections of 8Al·3CuO composites25
2.3	XRD patterns and Aluminum mass fractions26
2.4	DSC traces and Reaction onset for 8Al·3CuO samples28
2.5	A Kissinger processing and activation energies29
2.6	TG and MS results for milled composites31
2.7	Mass loss encountered by samples heated in Ar32
2.8	Specific surface area of milled composites33
2.9	Characteristic sequence of video frames showing ignition of S433
2.10	Ignition temperatures of 8Al·3CuO thermites at different heating34
2.11	CVE Pressure trace for 8.64 mg of the composite milled with 25% ACN35

LIST OF FIGURES (Continued)

Figure	Page
2.12	Peak CVE pressures and peak pressurization rates vs. sample mass36
3.1	Back-scattered electron images of cross-sections of Al and CuO49
3.2	Particle size distributions of the individual starting materials49
3.3	Back-scattered electron images of the composites after stage 2 milling.....50
3.4	Particle size distributions of the prepared 8Al·3CuO thermite powders.....52
3.5	Size distribution of CuO inclusions53
3.6	Specific surface areas for the prepared 8Al·3CuO thermite powders54
3.7	XRD patterns for 8Al·3CuO thermite powders.54
3.8	DSC traces for the prepared 8Al·3CuO thermite powders at 5 K/min.....56
3.9	Phase composition of quenched materials.....58
3.10	Phase composition of all composite materials.....59
3.11	Ignition temperatures of 8Al·3CuO thermites prepared with premilled Al.....60
3.12	Kissinger plots correlating ignition temperatures with DSC peaks62
4.1	Previously reported DSC curves for Al/CuO nanofolios with Au inclusions73
4.2	Two-stage milling procedure used to prepare nanocomposite75
4.3	High-speed video frames showing the ESD-induced combustion.....79
4.4	Integrated time-resolved emission traces80
4.5	Time-resolved flame height profiles of combustion by ESD81
4.6	XRD patterns of quenched ARM-prepared 8Al·3CuO thermite powders83
4.7	Cross-sectional STEM-HAADF images and ELNES spectra85
4.8	Cross-sectional STEM-HAADF images of A-C- and ApC- materials86

LIST OF FIGURES (Continued)

Figure	Page
4.9	Cross-sectional STEM-HAADF images and ELNES of Cu L _{2,3} -edge.....87
4.10	Schematic diagram illustrating the low-temperature redox reactions92
5.1	Backscattered electron SEM images of as-milled Al-Ti composites105
5.2	XRD traces for samples prepared by one-stage milling of Al and Ti106
5.3	Backscattered electron SEM images of samples with 2-stage milling.....107
5.4	Particle size distributions for a powder milled at different stages109
5.5	XRD traces of Al-Ti samples 3-6 prepared by 2-stage milling110
5.6	Backscattered electron SEM images of samples in planetary mill.....111
5.7	Particle size distributions for samples milled in planetary mill.....112
5.8	XRD traces of Al-Ti samples by 2-stage milling with different PCAs.....113
5.9	DSC traces of Al-Ti composites heated at 15 K/min.....114
5.10	Heated filament ignition temperatures for different Al-Ti powders115
5.11	Pressure traces of typical CVE experiments.....116
5.12	Pressurization rate (dP/dt) _{max} and b) time of P _{max} vs P _{max} /P ₀ for CVE118
5.13	Arrhenius plot showing ignition temperatures at different heating rates122
6.1	Scanning electron images of starting materials and resulting microspheres...128
6.2	Backscattered electron images of cross sections of microspheres.....129
6.3	Compositional map of solvent for all materials.....129
7.1	SEM images of powders prepared with different milling parameters141

LIST OF FIGURES (Continued)

Figure	Page
7.2	Particle size distributions for different boron powders 143
7.3	Specific surface areas and bulk density of selected boron powders 144
7.4	Granupack measurements of bulk density for SB-95 and prepared powders.. 146
7.5	Cohesive index using GranuDrum for SB-95 and powders 150
7.6	Initial and final charge densities measured by GranuCharge 151
7.7	Coarse correlation of the mode of the particle size distribution and ACN. 152
7.8	Relative change in the mode of the particle size distribution..... 153
7.9	Histogram of spherical particles with modes under 40 μm 154
7.10	Number-surface means and sphere surface areas for particles 155
7.11	Comparison of sphere surface areas and results of the linear model 157
7.12	Predictions of linear model with the coefficients 160
8.1	SEM images of different boron powders 171
8.2	Particle size distributions of boron powders and effect of sonication 173
8.3	Backscattered electron images of B-KNO ₃ powder blends 174
8.4	TG and DTG traces for different oxidizing boron powders o 176
8.5	Normalized heat flow traces for different boron powder 178
8.6	Characteristic pressure traces recorded in CVE experiments..... 179
8.7	Snapshots from high-speed videos capturing B-KNO ₃ combustion 181
8.8	Combustion characteristics for boron/KNO ₃ blends ignited by laser. 181
8.9	Earliest oxidation onset for spherical and irregular boron powders 183

CHAPTER 1

INTRODUCTION

1.1 Background

Reactive materials are high energy density solids capable of generating highly exothermic reactions [1]. They are non-detonable solids that encompass a variety of metal-based systems, such as powders of metals (Al, B, Zr, etc.), alloys (Al-Ni, Al-Ti, Al-Mg, etc.) and thermites (Al/CuO, Al/Fe₂O₃, Al/MoO₃, etc.)[2-7]. Figure 1.1 is a comparative plot showing combustion enthalpies of metals and some common explosives. Clearly, metal combustion releases substantial energy per unit mass or volume presenting an attractive alternative to organic energetic materials in many applications. Specific applications, where metals are used as components of energetic formulations include propellants, explosives, pyrotechnics, welding and custom energetics for MEMS (Micro-Electro-Mechanical Systems) [1, 8-10]. Due to its relatively high oxidation enthalpy (-1675.7 kJ/mol at 25 °C), low melting point (660 °C) and abundance in nature, aluminum tops the list of potential metal fuels for different reactive materials [11, 12].

Commonly, the global reaction rate in metal-based reactive materials is controlled by mass diffusion of reactive components towards each other [13]. Hence, the resulting rates of energy release are lower than those attained in combustion of common energetic compounds with reaction rate limited by kinetics of decomposition of metastable molecules. The acceleration of combustion in reactive materials is often associated with use of finer powder particles, leading to an increased reaction interface area. However, it has been observed that in certain applications, such as solid propellants, conventional

micron-sized aluminum powders tend to coalesce and form agglomerates. This leads to high ignition temperatures and prolonged ignition delays limiting their benefits [14]. Apart from aluminum, Mg, Zr, Ti, Ta and B based fuels were also developed [11, 15-17]. Still, a number of issues, mostly affecting the rate and completeness of reaction achieved in practical configurations, limit their applications. For instance, despite a very high volumetric energy density (138 kJ/cm^3) boron particles exhibit delayed ignition due to the presence of an oxide (B_2O_3) layer [18-20]. Magnesium powders tend to age fast in humid environment [21], making them difficult to store and handle.

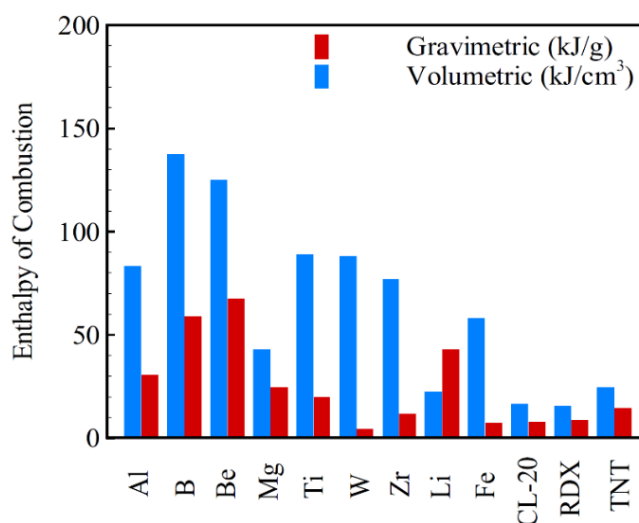


Figure 1.1 Enthalpies of combustion of different reactive materials.

Source: Sundaram, D., V. Yang, and R.A. Yetter, Metal-based nanoenergetic materials: Synthesis, properties, and applications. Progress in Energy and Combustion Science, 2017.

Studies suggest that shrinking the particle size from conventional micron range to the nanometer scale enhances their reactivity by several orders of magnitude [13]. This boost in reactivity is due to the decreased diffusion distances and high interfacial surface area between the reactive components [13]. However, agglomeration and sintering of

nanoparticles restrict the advantages associated with using nanopowders. With an effort to overcome the limitations, several systematic methods have been developed for the synthesis of reactive nanocomposites. Interestingly, these novel materials show many features which include very high burn rates, higher flame speeds, and accelerated ignition compared to their micron-sized counterparts [3].

1.2 Synthesis Methods of Reactive Materials

The easiest and the most common approach to form an intimate mixture between the reactive components is simple physical mixing of particles or nanoparticles. More sophisticated methods of synthesis include layered deposition, electrodeposition, sol-gel processing, self-assembly synthesis and arrested reactive milling [11, 22-25]. With each of these methods introducing specific structural characteristics and reaction dynamics, the ultimate focus has been to increase the interfacial contact between the components capable of highly exothermic reactions. It is interesting to note that materials with the same compositions prepared by different methods show different ignition and combustion characteristics. For instance, the ignition temperature recorded for electro sprayed Al/CuO powders was around 930 K. Mixed powders with the same composition and particle sizes ignited at 1000 K [26]. The ignition of the electro sprayed sample also occurred 0.15 ms earlier than that of mixed powder [26]. This change in behavior can be attributed to the formation of interfaces with different structural properties for each method. Different methods of synthesizing reactive nanocomposites are described further in the following sections.

1.2.1 Mixing of Nanopowders

Nanocomposites are commonly prepared by ultrasonic mixing of nanosized reactive components in an organic solvent (typically hexane, isopropyl alcohol), where the solvent is eventually evaporated [27, 28]. The produced materials, often referred to as metastable intermolecular composites (MICs), appear to be porous and their properties can be tuned by altering different parameters like fuel/oxidizer composition, exposure time in solvent and size of the starting particles [3]. A variety of aluminum-based mixed thermite powder were prepared using different oxidizers (CuO , Fe_2O_3 , WO_3 , BiO_3)[29]. Even though the preparation of composite material is relatively straightforward and simple, mixed powders are prone to agglomeration[30]. Sometimes, the mixing is non-uniform, which leads to a low rate of reaction [31]. Figure 1.2 shows a scanning electron microscopy (SEM) image of an Al/CuO thermite prepared by ultrasonic mixing [30]. The bright parts of the image correspond to oxide particles while the dark gray shaded particles are aluminum.

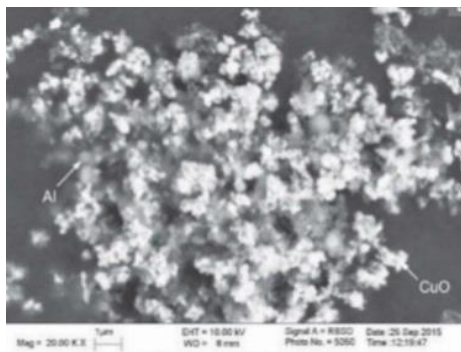


Figure 1.2 Scanning electron microscopy (SEM) image of Al/CuO thermite prepared by ultrasonic mixing.

Source: Monk, I., et al., Combustion characteristics of stoichiometric al-cuo nanocomposite thermites prepared by different methods. Combustion Science and Technology, 2017.

A modified method ensuring a more homogeneous mixing was developed, where uniformly sized droplets of mixed suspended nanoparticles are formed upon dispersing the mixture into an aerosol using an electrospray [26, 30]. An organic binder is added to the ultra-sonicated mixture of nanopowders. As the solvent evaporates, composite particles are formed and held together by the binder. The product formed turns out to be porous micron-sized agglomerates referred to as mesoparticles, which contain mixed nanoparticles and a small amount of binder. The binder gasifies upon ignition at a lower temperature and causes particle separation. This reduces loss of surface areas and prevents sintering. However, one of the major disadvantages is decrease in energy density due to the binder.

1.2.2 Electrodeposition

In this method, the metal to be deposited is contained in an ionic liquid. The nanostructured composite is formed upon electrodeposition of the ionic liquid on oxide nanowires [25]. Dong et al., [25] fabricated $\text{WO}_{2.9}/\text{Al}$ co-axial nanowires using the ionic liquid consisting of aluminum chloride and 1-ethyl-3-methylimidazolium chloride. First, a tungsten wire with well-aligned tungsten oxide nanowires attached to its surface was prepared by flame synthesis. This wire served as the cathode, which remained immersed in the ionic liquid. A DC potential was applied for 15 min for the aluminum coating to form on the tungsten oxide nanowires. Figure 1.3 shows different stages of the co-axial $\text{WO}_{2.9}/\text{Al}$ formation process. Upon ignition, the energetic nanocomposite exhibited strong exothermicity. It is of particular interest that the interface between metal and oxidizer is prepared using a low-temperature process; thus, the intermixing between reactive components at such interfaces is minimized. However, the method is presently difficult to scale up for bulk material synthesis.

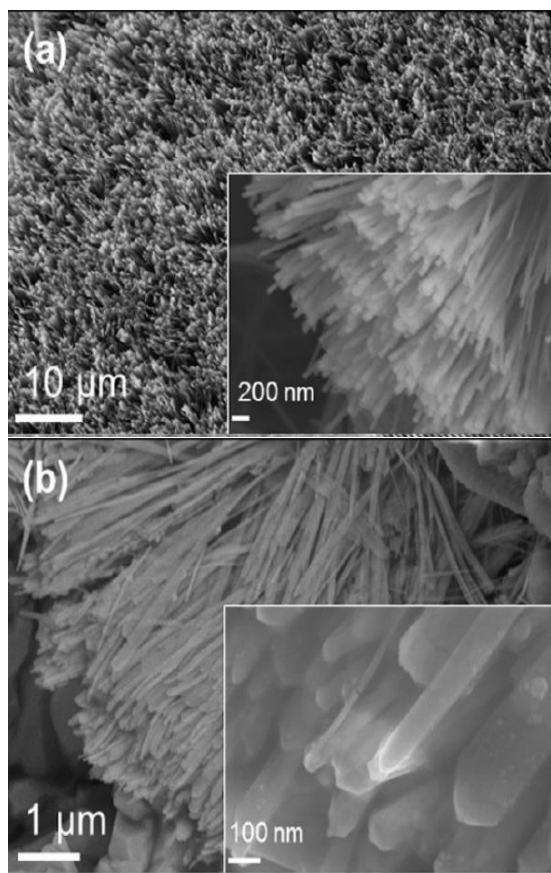


Figure 1.3 a) FESEM image of the WO_{2.9} nanowire grown by flame synthesis. b) WO_{2.9}/Al nanowires after electrodeposition.

Source: Dong, Z., et al., Combined Flame and Electrodeposition Synthesis of Energetic Coaxial Tungsten-Oxide/Aluminum Nanowire Arrays. *Nano Letters*, 2013.

1.2.3 Self-assembly

In self-assembled composites, functionalization of oxide surface enables nanosized metal particles to arrange themselves at the surface of the oxide [24, 32]. Metal nanoparticles adhering to the functionalized oxide particles form ordered structure, which optimizes mixing and thus maximizes utility of the surface available in nano-structured composites. Self-assembled Al–CuO system was synthesized where CuO nanorods were functionalized by a monofunctional polymer, poly(4)-vinyl pyridine (P4VP) [24]. It has been reported that

self-assembled thermites exhibit higher flame speed compared to nanocomposite materials with the same compositions prepared by ultrasonic mixing [32]. Figure 1.4 shows a TEM image of self-assembled Al/Fe₂O₃–nanothermite where the Al nanoparticles are attached at the exterior surface of Fe₂O₃ nanotube [32]. This approach, however, has some shortcomings which include expensive custom-made oxides and the presence of functionalizing agents that generally reduce the energy density [3].

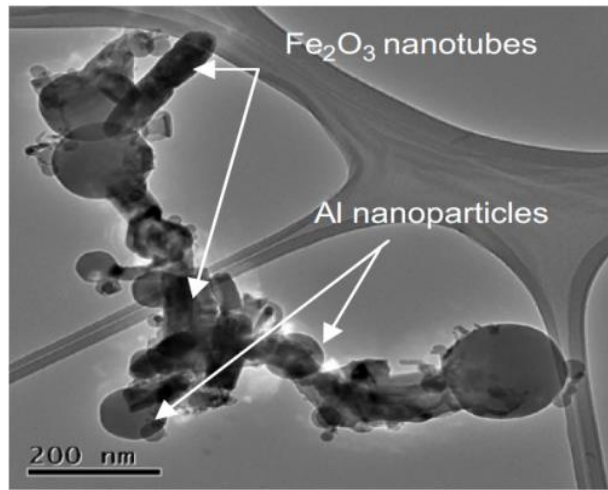


Figure 1.4 TEM image of self-assembled Fe₂O₃–Al nanothermite.

Source: Cheng, J.L., et al., Synthesis and characterization of self-assembled nanoenergetic Al–Fe₂O₃ thermite system. *Journal of Physics and Chemistry of Solids*, 2010.

1.2.4 Sol-gel Synthesis

Thermites prepared by sol-gel method consist of a nanoscale porous network of sol-gel-based metal oxide with dispersed metal fuel particles [33]. The synthesis strategy for sol-gel thermite involves a simple mixing of hydrated salts of metals in polar, protic solvents (methanol, ethanol) in the presence of propylene oxide, which serves as a gelation agent [34]. Immediately before the onset of gelation, the metal particles are added and further mixed to yield a uniform distribution. The removal of the pore fluid from the system is

achieved either by slow evaporation or by supercritical extraction with CO₂ [3]. The precursors can then be processed into aerogels, xerogels, or nano powders. Figure 1.5 illustrates Al-Fe₂O₃ thermite system prepared by sol-gel method. These composites achieve intimate contact between the constituents compared to mixed powders. This leads to favorable ignition and combustion properties. However, limitations regarding the applicability of different oxides and porosity make it unsuitable for some applications [3].

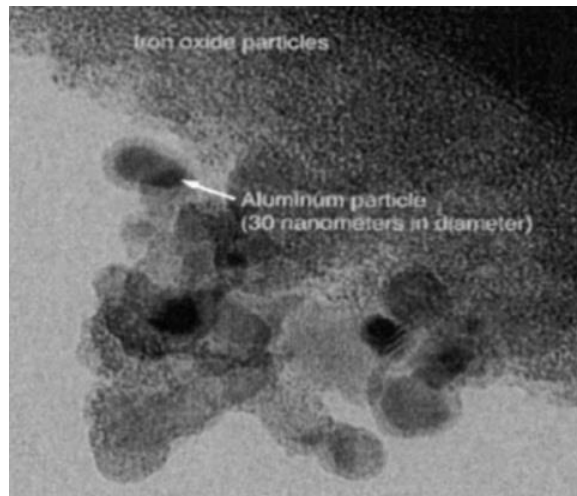


Figure 1.5 TEM image of Al-Fe₂O₃ thermite system prepared by sol-gel method.

Source: Tillotson, T.M., et al., Nanostructured energetic materials using sol-gel methodologies. Journal of Non-Crystalline Solids, 2001

1.2.5 Layer Deposition

Nanolayers of fuel and oxidizer deposited by physical deposition methods ensure a good control over purity [35]. These composites are fully dense and provide a well-defined geometry [23]. During material deposition, chemical intermixing naturally occurs at the interface between the two reactive layers, resulting in a relatively thick interfacial layer.

Al/CuO nanofoils were reported to have a narrow region at the interface identified as amorphous and nanocrystalline Al_2O_3 [23]. Figure 1.6 shows a) Cu, b) Al c) O and d) plasmon loss image of the as-deposited CuO_x /Al multilayer foils. The nature of the interface formed by nanofoils impacts their exothermic response [35]. Researchers aimed at engineering alumina-based interfaces in Al/CuO through atomic layer deposition (ALD), e-beam evaporation and sputtered deposition. The interface regions were found to be inhomogeneous with irregular thickness of about 5 nm maximum due to an intermixing of elements at the rough CuO surface region. The interfacial layer is composed of a mixture of Al, Cu, and O with a high density of defects, which enhances reactivity. These well-controlled nanosized layers of materials are capable of generating highly exothermic reactions [36]. Additionally, a layered system with a core-shell structure synthesized using ALD has been reported [37].

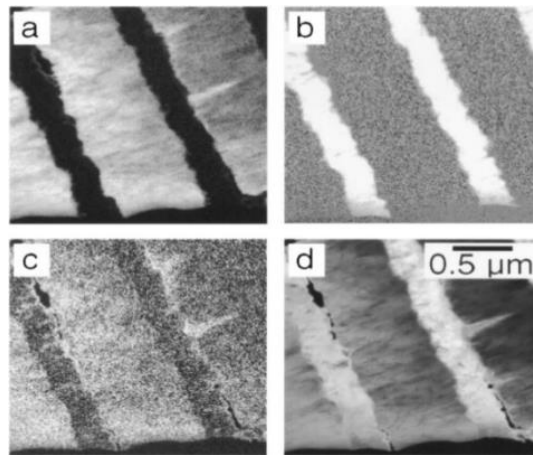


Figure 1.6 Elemental distribution images of the as-deposited CuO_x /Al multilayer foils. a) Cu b) Al map c) O map d) plasmon loss image of this region.

Source: Blobaum, K.J., et al., Deposition and characterization of a self-propagating CuO_x /Al thermite reaction in a multilayer foil geometry. *Journal of Applied Physics*, 2003.

1.2.6 Mechanical Milling

Powders are processed in high energy ball mills (planetary, shaker or attritor mill) [38]. Ball material, sizes and quantity are chosen based on the type of powder to be milled. Usually milling is stopped or reaction is arrested before ignition. Hence, this process is also termed Arrested Reactive Milling (ARM) [13]. The powder processing is tuned by adjusting specific milling parameters such as milling time, the powder batch size, the mass ratio of powder sample to that of the milling media, the process temperature, and so on [17, 22, 38]. During milling, a reaction between the components may be locally triggered due to mechanical perturbation; this could lead to self-sustaining reaction damaging the milling equipment [39]. This issue can be overcome by adjusting the milling conditions and using proper process control agents (PCAs); some liquid PCAs are capable of quenching a locally initiated reaction. Milling parameters were explicitly studied previously by Umbrajkar et al., where different temperature regimes were explored during mechanical milling of Al-Mg alloys [40]. The effect of milling media and ball to powder mass ratio on Al/MoO₃ were also considered in order to affect the structural refinement [41].

To further understand milling mechanisms, Santhanam et al., performed simulation to quantify the energy imparted by the milling media at different conditions [42]. As the refinement mechanisms for diverse materials subjected to mechanical milling were clarified, it was suggested that ARM decreases the length scales of the reactants by intimately mixing the composites through fracture and cold welding of constituent powders, eventually setting the mixing scale at nano level [43, 44]. However, quantifying the mixing scale has been a challenge for lack of in situ instrumentation during high energy milling. Monk et al., [45] attempted to quantify scale of mixing by analyzing cross-

sectioned composite particles using SEM and measuring the distance between two adjacent CuO inclusions in Al matrix prepared in a milled Al/CuO composite. Recently, Al, Mg, Ti, and B based composites were synthesized by mechanical milling; their ignition and combustion characteristics were studied [17, 22, 38]. Figure 1.7 displays different types of particle morphologies and sizes achieved as a result of varying milling parameters for different metal-based systems.

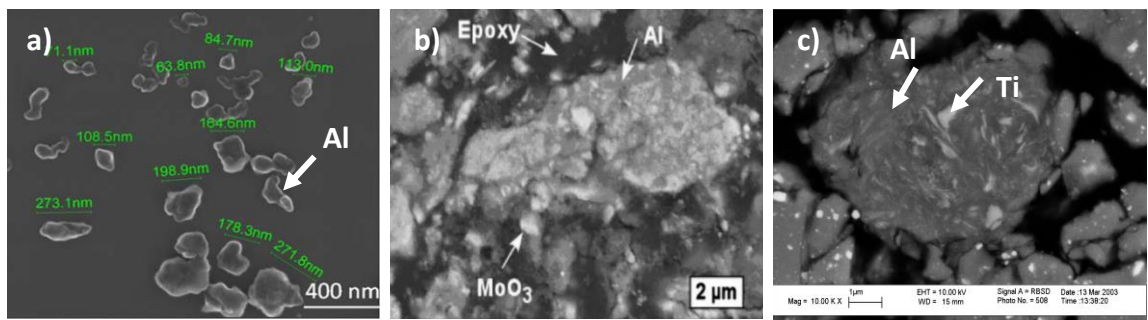


Figure 1.7 Different materials prepared by mechanical milling. a) nano aluminum b) Al-MoO₃ thermite powder c) Al-Ti alloy.

Sources:

Schoenitz, M., S.M. Umbrajkar, and E.L. Dreizin, Kinetic Analysis of Thermite Reactions in Al-MoO₃ Nanocomposites. *Journal of Propulsion and Power*, 2007.

Yu, J., et al., Aluminum Nanoparticle Production by Acetonitrile-Assisted Milling: Effects of Liquid- vs Vapor-Phase Milling and of Milling Method on Particle Size and Surface Chemistry. *The Journal of Physical Chemistry C*, 2016.

L. Shoshin, Y., et al., Ignition of aluminum-rich Al-Ti mechanical alloys in air, 2006.

1.3 Types of Interfaces between Reactive Components

Interfaces are believed to play a crucial role in determining the reaction kinetics and ignition characteristics of nanocomposite systems. It is generally agreed that reactivity of these nanocomposites increases significantly upon intimate interfacial contact between the

components [35]. The extent of interfacial contact between the components with same composition varies with their method of synthesis.

In Figure 1.8, we categorized reactive materials into two classes. This applies to most of the metal-based reactive materials. Here, for the sake of simplicity, different interfaces of thermites are being discussed. In class I type, the fuel and oxidizer are reported to remain in contact over a relatively small portion of the total surface area. As a result, high porosity and low material density is observed in such composites. High porosity leads to low energy density. However, enhanced gas release and reduced heat transfer facilitate thermal runaway, consequently accelerating ignition [48]. Some of the relevant composites include mixed powders, sol-gel and self-assembled systems [11, 24, 29, 30]. On the other hand, class II category lists the composites, which ensure the maximum possible interfacial contact between fuel and oxidizer, minimizing porosity. Such interfaces effectively enhance uniform mixing of solid reactants and greatly reduce the diffusion distance. Consequently, the reactivity of material is improved. Layered systems, core-shell and ARM prepared powder fall under this category [22, 23, 37]. These composites are very dense and possess well-defined geometry.

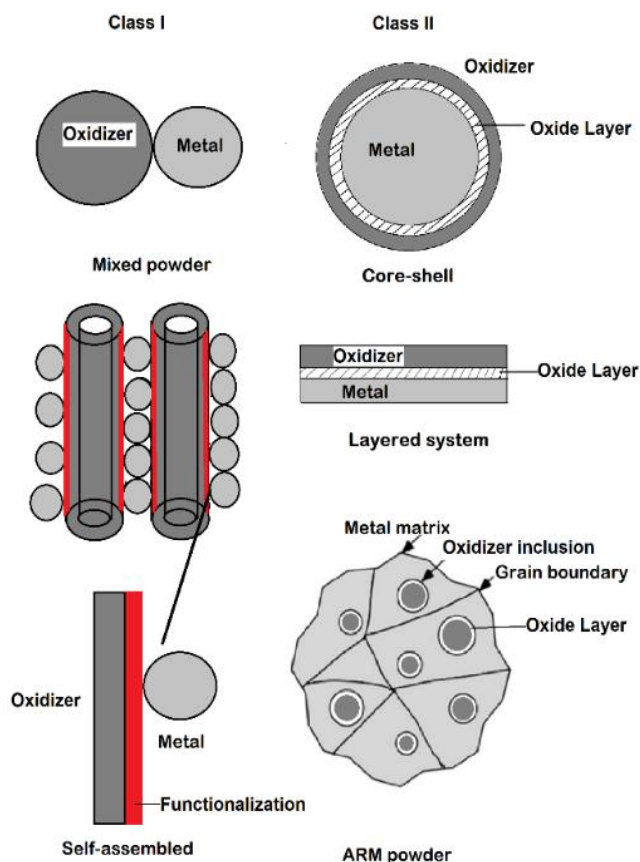


Figure 1.8 Possible Interface geometry of different types of thermite systems.

1.4 Advantages of Mechanical Milling

Upon analyzing different types of interfaces of reactive materials in the above section it can be asserted that mechanically milled composites have maximized interfacial contact among the components, while being readily made on a practical scale. One of the major advantages of ARM is the formulation of fully dense materials unlike composites formed by mixing or sol-gel [3]. The formed products are chemically unbound condensed materials where individual particles are reported to have a density close to their theoretical maximum density (TMD) [39]. The starting materials need not be nano-sized, as is necessary in case of powder mixing. This top down approach employing readily available inexpensive

micron-sized powders does not require extensive instrumentation, which is mandatory for composites prepared by layered deposition or electrodeposition. This makes ARM a readily scalable and cost-effective method. Hence, it is deemed a very versatile method for synthesis of reactive materials.

1.5 Role of Process Control Agent (PCA) in Mechanical Milling

Sometimes, the advantages of mechanical milling cannot be fully exploited because of particle agglomeration due to cold welding, which, in turn, decreases the overall reactivity of the synthesized material. One effective approach to avoid cold welding is to introduce surface active substances as process control agents, or PCAs. A number of non-oxidizing liquid hydrocarbon PCAs, such as hexane, pyridine, benzonitrile, and acetonitrile have been explored as lubricants [12, 49, 50]. Shaw et al., [51] performed study on the effect of stearic acid (SA) as PCA on mechanical alloying of $\text{Al}_{93}\text{Fe}_3\text{Ti}_2\text{Cr}_2$. As illustrated in Figure 1.9(a), the size of the aluminum particles increases with milling time in presence of 1 wt% SA for up to 5 hours as a result of cold welding [51]. The particle size decreases at longer milling times as fracturing of agglomerates becomes dominant. Interestingly, upon introducing 2 wt% SA, there was no jump in particle size because at this point, the amount of PCA was adequate to effectively prevent cold welding. Similar findings were reported by Machio et al.,[52] during mechanical alloying of Ti-Mg in presence of SA. Their study further concludes that upon increasing the PCA amount beyond an optimum point, the particle surface energy becomes very high that they re-agglomerate. From Figure 1.9(b) it is evident that cold welding again dominates at 6 wt% SA [52].

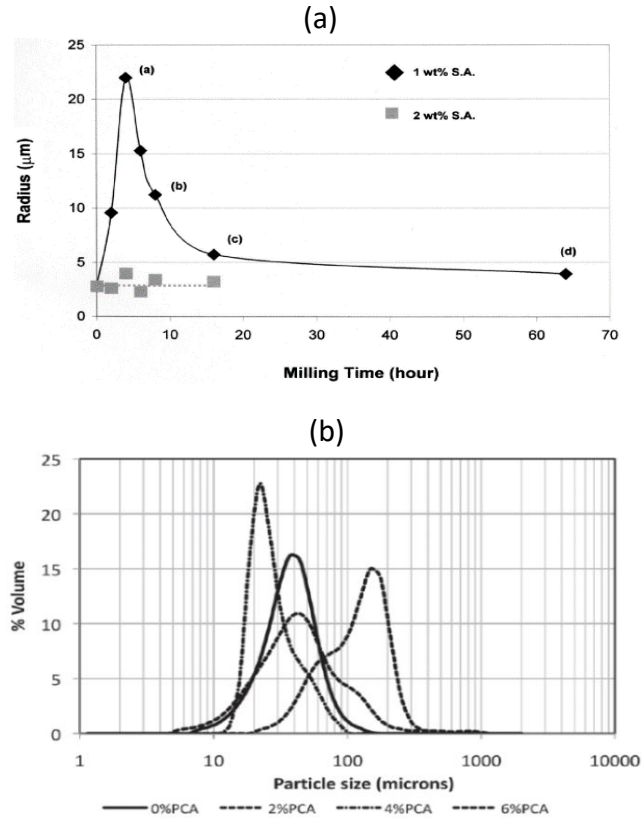


Figure 1.9 Effect of the amount of stearic acid on particle size during mechanical alloying of a) Al₉₃Fe₃Ti₂Cr₂ and b) Ti-Mg.

Sources:

Shaw, L., et al., Effects of process-control agents on mechanical alloying of nanostructured aluminum alloys. *Metallurgical and Materials Transactions A*, 2003.

Machio, C., H.K. Chikwanda, and S. Chikosha, Effect of process control agent (PCA) on the characteristics of mechanically alloyed Ti-Mg powders. *Journal of the Southern African Institute of Mining and Metallurgy*, 2011.

Al-Ti alloys were also milled with SA as PCA. It was observed that the ignition and combustion behavior of the samples improved to some extent [47]. One recent study involving acetonitrile (ACN)-assisted milling of aluminum indicates that PCAs can significantly alter interface chemistry along with particle size and morphology [46]. It is suggested that the ACN used during milling may modify aluminum surface leading to formation of carbide and nitride layers fully or partially replacing common surface oxide

film. Such altered surface properties may prove conducive to ignition. In addition, a small amount of PCA can be chemically or physically adsorbed by the prepared composite; its release at different temperatures is expected to affect combustion of the heated composite particles.

The effect of PCA on mechanochemical synthesis and manipulation of interfacial properties of reactive nanocomposites has been addressed in this study; which led to an extensive investigation of how particle size, mixing scale, and overall particle morphology can be altered and how those parameters affect powder reactivity, stability, and ease of handling. The work also delivers mechanistic understanding of reaction mechanisms of the prepared composite materials triggering ignition and combustion. In an effort to improve the powder morphology, a novel method of synthesizing spherical energetic powders by mechanical milling was introduced, where a pair of immiscible liquids served as a PCA. Specifically, an emulsion of hexane and ACN served as PCA in most such experiments. The chapters in this dissertation thoroughly discuss the experimental findings of different energetic systems prepared by PCA-assisted mechanical milling.

CHAPTER 2

CUSTOM PARTICLE MORPHOLOGY IN ENERGETIC NANOCOMPOSITE BY ARRESTED REACTIVE MILLING IN IMMISCIBLE LIQUIDS

2.1 Abstract

The effect of polar and nonpolar liquid process control agents (PCA) on properties of metal rich Al/CuO thermites prepared by Arrested Reactive Milling was studied. Acetonitrile and hexane, and their mixtures were used as PCA. Milling in nonpolar hexane results in fully dense, micron-sized composite particles of 100 nm-scale CuO inclusions in an Al matrix. Using polar acetonitrile results in a mixture of nano-sized, largely unagglomerated Al and CuO particles. Porous composites, agglomerated to different degrees, formed in hexane-acetonitrile mixtures. In particular, micron-sized porous spherical composite particles formed in a mixture with 25% acetonitrile. Such spherical composites may result from interaction of suspended powder particles with stressed droplets of a Pickering emulsion forming when immiscible liquids serve as PCA. Despite dramatic changes in the powder morphology, all composites were reactive. Systematic differences, discussed in the text, were observed in their ignition temperatures and oxidation kinetics.

2.2 Introduction

Thermites composed of a metal fuel and metal oxide oxidizer undergo a highly exothermic redox reaction upon heating [3]. Such reactions find applications in propellants, explosives, pyrotechnic, infrastructure demolition and MEMS technology [1, 8-10]. Lately, thermite synthesis methods focused on preparing nanocomposite systems using mixed

nanopowders, layered vacuum deposition, sol-gel processing, self-assembly, and arrested reactive milling (ARM) [11, 22-24]. With each of these methods introducing specific structural characteristics and reaction dynamics, the ultimate focus has been to increase the thermite reactivity. Mechanical milling, in particular, is deemed a versatile way of synthesizing nanothermites due to its operational simplicity and cost effectiveness.

Among several types of reactive composites synthesized by ARM, Al–CuO nanocomposite thermites have garnered a great deal of interest owing to their highly exothermic reactions and transient gas generation. Effect of several ARM parameters, including milling time, milling media, and ball to powder mass ratio were explored [53-55]. The correlations of these parameters with composite particle size, inclusion size and characteristics of their ignition and combustion were reported in literature [12, 22, 53, 54, 56, 57]. However, properties of the prepared composites are also affected by process control agent (PCA) using during milling. PCA can serve as a lubricant and as a cooling agent; it can also functionalize surface of the prepared powders. Presently, systematic studies addressing the effect of PCA on properties of nanocomposite thermites are lacking.

Many non-oxidizing hydrocarbons such as hexane, pyridine, benzonitrile, and acetonitrile have been used as PCAs [12, 49, 50] while preparing metal-based composites by high-energy milling. One recent study involving acetonitrile (ACN) assisted milling of aluminum suggests that PCAs can significantly alter interface chemistry along with particle size and morphology [46]. It is likely that PCAs affect the interfacial reaction kinetics of the thermites causing changes in their ignition and combustion characteristics.

In this work, a non-polar (hexane) and polar (ACN) fluids served as PCAs for preparing a metal rich Al-CuO thermite powder by ARM. Samples were ball-milled in pure

hexane and ACN as well as in a set of their mixtures. In addition to the effect on reactions leading to ignition, pronounced changes in the morphology of the prepared materials were observed, as discussed.

2.3 Experiment

2.3.1 Sample Preparation

Aluminum-rich $8\text{Al}\cdot 3\text{CuO}$ nanocomposite powders (with $8/3$ molar ratio between Al and CuO, forming a thermite with the equivalence ratio of 4) were prepared in a Retsch PM400 planetary mill. The composition was chosen complying with safety considerations since stoichiometric ratio yield pyrophoric materials unsafe to handle. The starting powders were -325 mesh (less than $44\text{ }\mu\text{m}$), 99.5% pure aluminum (by Atlantic Equipment Engineers), and $25\text{ }\mu\text{m}$, 99+ % pure copper (II) oxide (by Sigma–Aldrich). Process control agents (PCA) were the pure solvents hexane (Alfa Aesar, 99.5% pure) and acetonitrile (Alfa Aesar, 99.5 pure), and mixtures of the two. Table 2.1 shows compositions of solvent mixtures, and the assigned sample IDs.

Custom-made hardened steel milling vials were used with a capacity of 175 ml and with 17 mm thick walls, capable of withstanding high pressure in case of an accidental initiation of the thermite reaction during milling. Each vial was charged with 30 g of powder and 24 ml PCA. The amount of the PCA was selected to ensure that the entire powder charge remained submerged in the fluid. Hardened steel balls with 9.525 mm ($3/8''$) diameter served as the milling media. A ball to powder mass ratio of 3:1 was maintained for all the samples. The vials were loaded and sealed in an Ar-filled glovebox. All samples were milled for 60 min at 350 RPM.

Table 1.1 Compositions of Mixed Solvents used for Preparation of 8Al·3CuO Nanocomposite Powders

Acetonitrile volume fraction (balance is Hexane)	Sample ID
100 %	A100
75 %	A075
50 %	A050
25 %	A025
12.5 %	A012
6.25 %	A006
0 %	A000

2.3.2 Characterization of Prepared Powders

Particle size and surface morphology of the samples were characterized using a LEO 1530 field emission scanning electron microscope (SEM). Carbon tape was used as a substrate during SEM imaging for as-milled powder. Prior to SEM analysis, the liquids in the samples were evaporated. Also, as-milled powders were embedded in epoxy, cross-sectioned, and imaged. The back-scattered electrons were used for imaging cross-sections to observe the compositional contrast between Al and CuO.

X-ray diffraction was performed using a PANalytical Empyrean multipurpose research diffractometer. The samples were dried and exposed to air for 24 hours before the

XRD runs. The diffractometer was operated at 45 kV and 40 mA, using unfiltered Cu K α radiation ($\lambda = 1.5438 \text{ \AA}$). HighscorePlus software (version 3.0e) along with PDF-4+ 2018 database was used to identify the peaks. Peak refinement based on the Rietveld method [58] was performed to quantify the concentration of aluminum present in the samples after they were dried and exposed to air and could, therefore, partially oxidize. The built-in code for Rietveld analysis was based on reference [59].

The thermite reactions were characterized by differential scanning calorimetry (DSC) and thermogravimetry (TG) using a Netzsch STA409PC thermal analyzer. The powders were loaded in an alumina crucible without removing them from liquid PCA in order to prevent their oxidation in air. The crucible with samples immersed in liquid was loaded into the analyzer. Prior to measurement, the furnace was evacuated and then flushed with argon three times. The liquid was allowed to evaporate in a flow of argon before the heating program started. The final mass was recorded when the internal balance showed a stable reading for about 10 min. This final mass ranged from 10 to 15 mg for every sample. The experiments were performed under the flow of argon (99.998% pure, supplied by Airgas) at a flow rate of 50 ml/min. DSC traces were recorded at four different heating rates (2, 5, 10 and 20 K/min). During each run, the samples were heated twice to the maximum temperature set in the program (800 °C). Prior to the second heating, the sample was allowed to cool down from 800 °C to 50 °C. The traces were baseline-corrected by subtracting the signal recorded during the second heating and then normalized by the sample mass. In selected experiments, the gas exhaust from the DSC/TG furnace was connected to the inlet of a quadrupole Mass Spectrometer (MS) by Extrel.

Specific surface areas were determined using an Autosorb iQ (model no: ASIQM000000-6) BET by Quantachrome Instruments. Samples were degassed at 30 °C for 48 hours in a 0.9 mtorr vacuum.

2.3.3 Ignition and Combustion Experiments

Ignition was characterized in experiments involving a thin coating of the thermite powder on an electrically heated, 0.5-mm diameter nickel-chromium (Ni-Cr) wire. The powders were suspended in either ACN or hexane to prepare the wire coating. A thin layer of the suspension was deposited on the wire using a small brush. The solvent was dried off the coated wire prior to each run. Rechargeable large-cell 12-V batteries by McMaster Carr were used as the source of DC voltage. One, two, and three batteries were connected in series, resulting in heating rates of 4160 ± 310 K/s, 17200 ± 1600 K/s, and 34700 ± 1500 K/s, respectively.

The ignition time was recorded simultaneously by a MotionPro 500 high-speed video camera and a photodiode based on optical emission. The temperature of the heated powder was not measured directly but inferred from the measured filament temperature. An infrared pyrometer comprising a germanium switchable gain detector (PDA30B2 by Thorlabs) coupled with a fiber optics cable and a lens was focused on an uncoated portion of the wire to obtain the wire temperature as a function of time. Rigol DS1054Z digital oscilloscope was used in order to record the photodiode and pyrometer readings. The pyrometer was calibrated in the temperature range of 300 to 950°C using a BB-4A black body emission source by Omega Engineering.

A spark induced constant volume explosion (CVE) experiment was performed to measure pressure release during thermite reaction. A custom-made, miniature steel

combustion chamber (180 ml) with an in-built pin-electrode was used for the experiment. The electrode's tip was located approximately 1 mm above the surface of the powder sample placed in the chamber. The powder was placed in a 0.635-mm-deep, 3.05-mm-diameter cylindrical cavity in a grounded brass plate mounted inside the spark chamber. Mass of the powder loaded into the sample holder varied in the range of 1-12 mg. A capacitor was charged to 8 kV and was then discharged through the high-voltage pin electrode and the grounded powder holder. The pin electrode was connected to the positive plate of the capacitor while the negative plate of the capacitor was grounded. ESD ignition experiments were performed with different amounts of powder. The chamber was sealed properly prior to any discharge. Real-time measurements of voltage signatures produced by the sample during sparks were translated to pressure release. A factory-calibrated ICP 113B28 pressure sensor by PCB Piezotronics with a 0-50 psi pressure range was used in the experiment. Further details of the set-up has been described elsewhere [60].

2.4 Results

2.4.1 SEM Image Analysis

SEM images of the as-milled 8Al·3CuO powders synthesized with different PCAs are presented in Figure 2.1. For brevity, only three materials are shown. Images taken at higher magnification show that the material milled in pure hexane (A000) formed coarser composite particles (Figure 2.1(a)). The material milled in pure acetonitrile (A100, figure. 2.1(c)) formed a very fine powder, which appeared to contain mostly individual Al and CuO rather than composite particles. An unusual particle morphology was observed for the material milled with 25 vol-% acetonitrile (A025, Figure 2.1(b)). It contained multiple, relatively coarse spherical or spheroidal particles mixed with fine particles of random

shapes. To a lesser extent, formation of spheroidal composite particles was also observed for sample A012

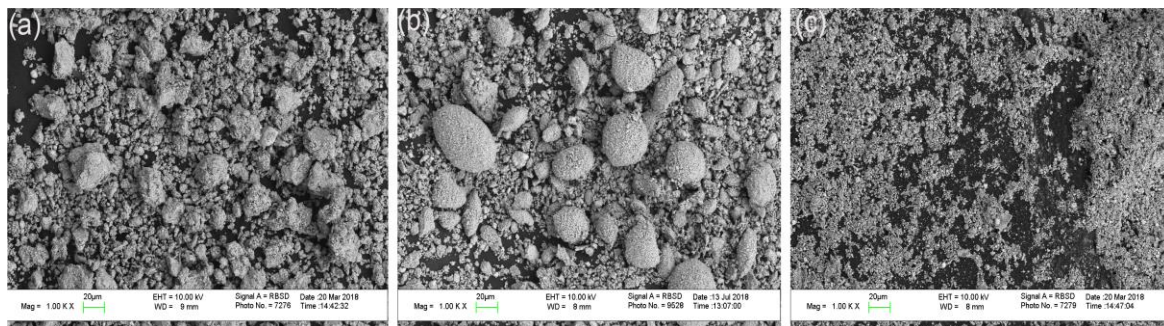


Figure 2.1 Backscattered electron SEM images of 8Al·3CuO thermites milled in different PCAs: (a) pure hexane; (b) solvent mixture with 25 vol-% acetonitrile; (c) pure acetonitrile.

The striking differences in the powder morphologies are also well visible in the images of cross-sectioned powders in Figure 2.2. The material milled in pure hexane (A000) contains coarser, fully dense composite particles. Aluminum appears as a darker matrix and CuO is seen as brighter inclusions, and CuO is mixed homogeneously with Al. Consistent with the image in Figure 2.1(b), the material milled with 25 vol-% acetonitrile (A025) formed spherical or spheroidal composite particles with noticeable porosity and multiple cracks. The composite spheres appear to be aggregates of fully dense composite particles (as in A000), fine oxide particles (as in A100), and relatively large fragments of aluminum. The material milled in pure acetonitrile (A100), again consistent with observation from Figure 2.1, formed a very fine powder containing aluminum particles and flakes as well as CuO particles mixed with aluminum but not forming many dense agglomerates.

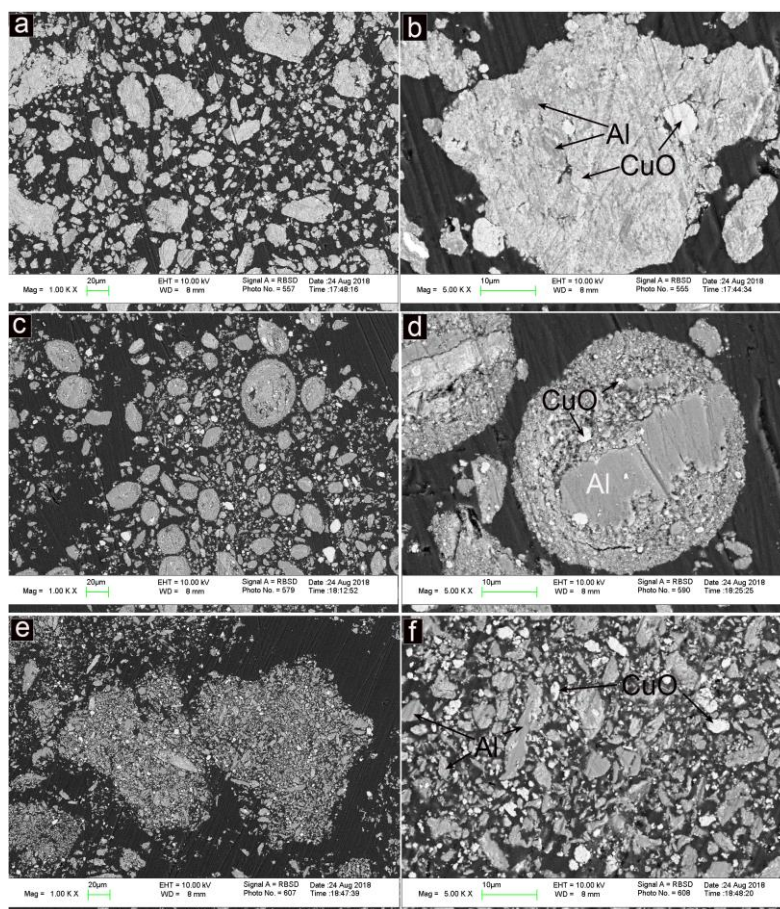


Figure 2.2 Cross-sections of 8Al:3CuO composites. a, b: milled in pure hexane; c, d: milled with 25% acetonitrile, and e, f: milled in pure acetonitrile.

2.4.2 XRD Analysis

Figure 2.3A shows XRD patterns for samples A100, A025, and A000. Omitted XRD patterns are qualitatively similar to those shown. The major peaks correspond to aluminum and tenorite (a polymorph of CuO). No trace of reacted species such as Cu₂O or Cu, was found in the patterns. Although amorphous Al₂O₃ may form during milling or upon drying the samples in air prior to the XRD measurement, it is not detectable by XRD.

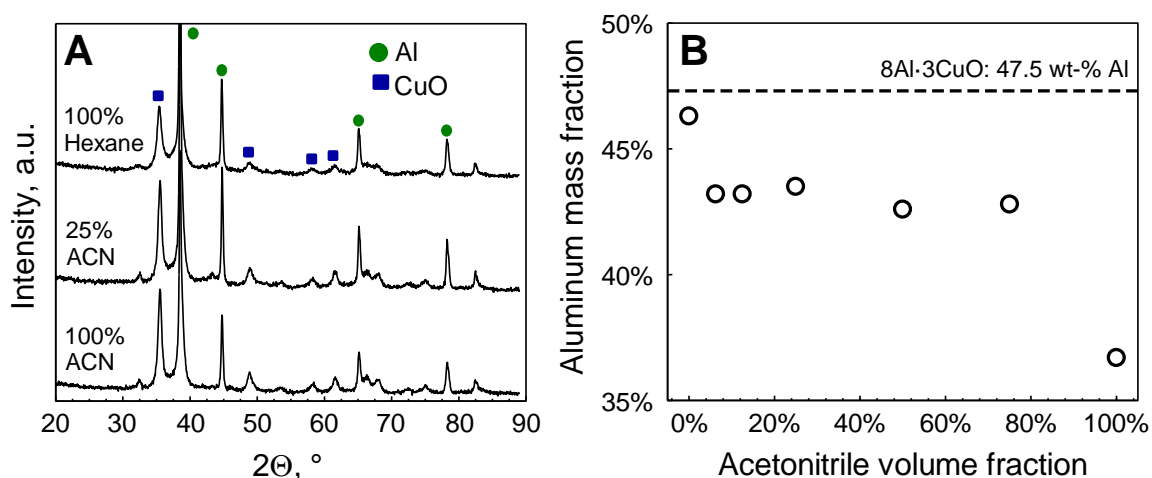


Figure 2.3 (A) XRD patterns of selected 8Al-3CuO composites milled with different PCA compositions. (B) Aluminum mass fractions estimated by quantitative phase analysis of milled composites exposed to air

While there was no qualitative difference among XRD patterns for different samples, the relative amplitude of aluminum peaks varied. A set of samples was systematically dried and exposed to air for 24 hours and analyzed. Whole-pattern analysis showed variation in the mass percentage of metallic, unreacted aluminum as shown in Figure 2.3B. The material milled in pure hexane (A000) contains 46.3 wt-% aluminum. The detectable aluminum content decreases to 36.7 wt-% for the sample milled in pure acetonitrile. The detectable aluminum content for samples milled in ACN-hexane mixtures ranges between 41 and 43%. The reduction in the content of metallic aluminum is likely due to oxidation in air. As noted above, the product of this reaction, amorphous or poorly crystalline Al_2O_3 will not be detected in the XRD patterns. Nominally, for 8Al-3CuO composite, the mass fraction of aluminum is 47.5 wt-%. Thus, A000, milled in hexane, has minimal aluminum oxidized. However, as much as 35% of the aluminum has been oxidized from A100, milled in ACN. For samples A006 – A075, milled in the mixed solvents, about 15% of the metallic aluminum oxidized upon exposure to air.

2.4.3 Thermal Analysis

In addition to the XRD results in Figure. 2.3B suggesting that aluminum oxidizes upon exposure to air, an indication of sample aging was observed following initial DSC experiments, using dried powder samples.

In preliminary experiments, samples milled in pure hexane showed exothermic heat flow due to the thermite reaction in a first heating cycle, and endothermic peaks attributable to melting transitions in the Al-Cu binary system (primarily Al, and Al_2Cu , and the respective eutectic). This is expected because elemental copper is a product of the redox reaction, and should alloy with the excess aluminum in the Al-rich composite. Conversely, the material milled in 100% ACN, after exposure to air, showed no such intermetallic peak in a second heating cycle. This strongly suggests that during handling in air, a significant fraction of aluminum was oxidized so that no excess aluminum remained available to alloy with the reduced copper. This initial observation served to modify the experimental protocol. Samples were stored and loaded into the thermal analyzer under liquid, so they would not be directly exposed to air prior to measurements. With this procedure, the intermetallic melting peaks were observed for all materials during repeat heating cycles.

DSC traces of the samples heated in argon at 5 K/min are presented in figure 2.4A. A broad exothermic feature begins for all samples below 400 K. All materials exhibit a relatively sharp exothermic peak between 800 and 900 K. Additionally, one or two weaker exothermic peaks can be distinguished at lower temperatures. The weak first exothermic event was only observed for samples A006 - A075, prepared using mixed solvents as PCA. Eutectic melting of CuAl_2 (endothermic at 813 K, 540 °C) was only clearly observed for the material milled in pure hexane.

Proteus[®] thermo-analytical software by Netzsch was used to identify the exothermic peak temperatures. The tool detects the peak temperature analyzing the first derivative of the DSC trace with respect to temperature. The onset temperatures for the initial, low-temperature exotherms were identified by fitting tangents to the baseline and the peak slope of the DSC traces. The temperature corresponding to the intersection point of the two tangents was considered the onset temperature. Temperatures of the reaction onset and of exothermic peaks became higher at greater heating rates. These results are further discussed below.

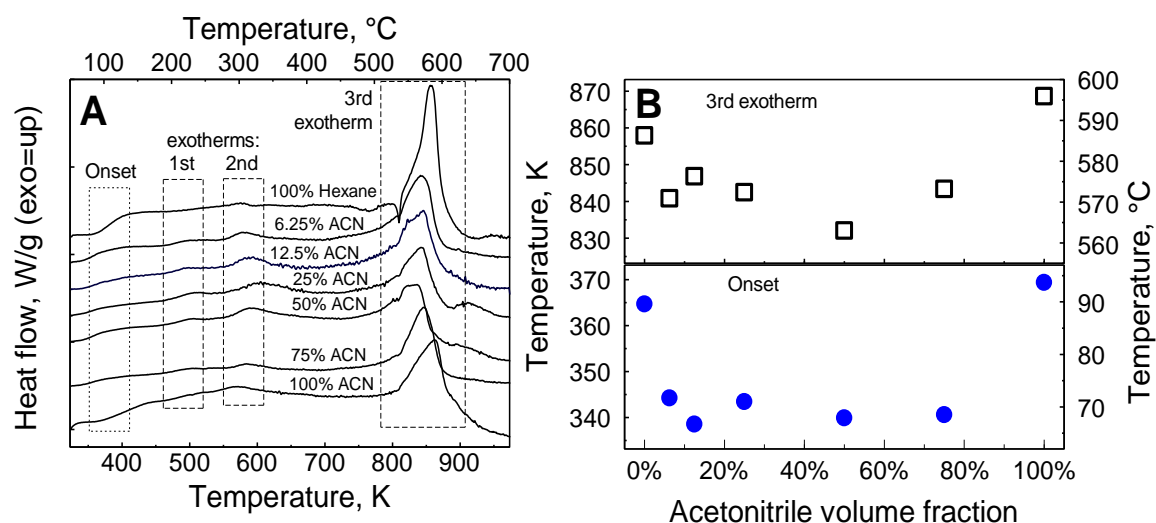


Figure 2.4 A DSC traces for 8Al·3CuO samples heated in Ar at 5 K/min. B Reaction onset and peak temperatures of the strongest exotherm vs solvent composition.

Identified onset temperatures for the broad exothermic feature and the temperatures for the strongest exothermic peak are plotted in figure 2.4B as a function of the ACN volume fraction. Both characteristic temperatures are higher for the samples milled in pure ACN and hexane compared to the materials prepared using mixed fluids as PCA.

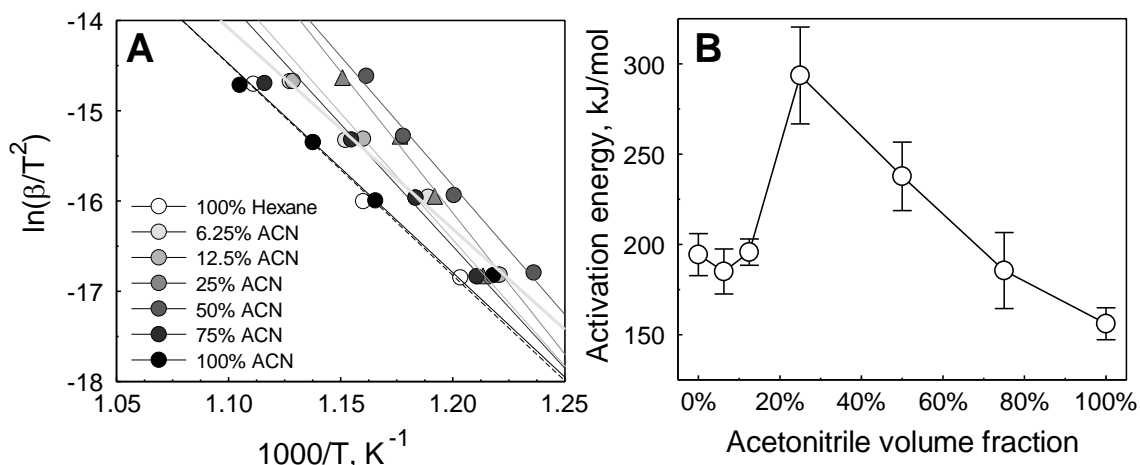


Figure 2.5 A Kissinger processing of the strongest exothermic peak temperatures observed in DSC traces. B Activation energies for the reaction represented by the strongest exothermic peaks observed in DSC experiments (cf. figure 2.4A).

Measurements performed at different heating rates showed that the strongest exotherm shifted consistently to higher temperatures at greater heating rates. Shifts in weaker exothermic events have also occurred but were difficult to quantify. Figure 2.5A shows Kissinger plots [61] of $\ln(\beta/T^2)$, where β is the heating rate vs. the inverse temperatures ($1000/T$) for the strongest exothermic peaks for different samples.

The slopes of the straight lines fitted to each group of data points representing individual samples give an estimate for the respective apparent activation energies. These activation energies are plotted in figure. 2.5B. The activation energies are near 200 kJ/mol for the material milled in hexane, and with low amounts of acetonitrile. It peaks for A025, and decreases again to near 150 kJ/mol for the sample milled in pure acetonitrile.

A small mass loss was measured by TG, which accompanied weak, low-temperature exothermic reactions observed in different prepared materials. This mass loss, along with respective time derivative (DTG) and associated MS measurements are shown in figure. 2.6 for sample A025. Because of non-linear change in temperature at the

beginning of the heating program, figure 2.6A shows temperature, and figure 2.6B shows TG and DTG as a function of time. The initial mass loss occurs at about the same temperatures at which the DSC signal in figure 2.4A becomes weakly exothermic. The strongest peak in the DTG, corresponding to the highest mass loss rate occurs around 550 K or 300 °C, where the second exotherm (see figure 2.4A) is observed by DSC. A couple of weaker features are noted in the DTG at lower temperatures, in the vicinity of the first weak exotherm marked by squares in figure 2.4A.

In the MS signals, collected during DSC/TG experiments, peaks corresponding to CO_2 ($m/z=44$), CH_3CN ($m/z=41$), and CO (or N_2) ($m/z=28$) were observed. The formation of CO_2 and CO can be attributed to the reaction of oxygen released by decomposing CuO with residual hexane or ACN . The CH_3CN peak could be assigned to the release of residual ACN . The evolution of these peaks as a function of time is shown in figure 2.6C. The CO and CO_2 peaks appear to correlate with each other, although the CO peak is generally weaker and barely resolved at lower temperatures. The possibility that $m/z=28$ indicates N_2 from ACN decomposition instead of CO remains, but simultaneous evolution of CO and CO_2 in an otherwise inert atmosphere is more plausible. The evolution of different gas species upon heating correlates with features observed in the DTG. The first significant feature (or first step of the observed mass loss) is associated with a relatively weak first peak of CO_2 (and likely CO) release. The second step of the observed mass loss correlates with the release of residual ACN . Finally, the third, and the strongest mass loss step is associated with the simultaneously occurring peaks for CO_2 and CO .

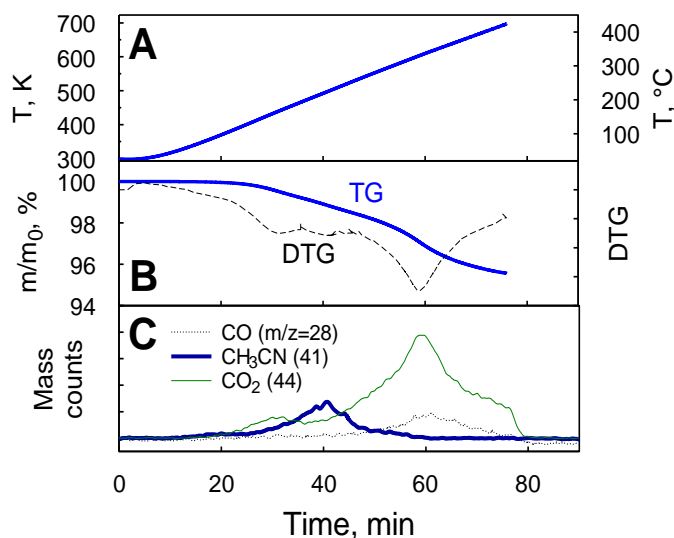


Figure 2.6 TG and MS results for composite milled with 25% ACN, heated to 800 °C at 5 K/min

The average total mass loss obtained from TG traces for samples heated to 1073 K (800 °C) at different heating rates are plotted against ACN volume fraction in figure 2.7. Although results are somewhat scattered, a general trend of increased mass loss with an increase of ACN volume from 0 to 25% is noted. The mass loss then decreases with further increase in ACN volume. Considering our materials as 8Al·3CuO composites with low levels of carbon contamination, a theoretical reduction of all CuO to Cu₂O could lead to reaction of released oxygen with carbon, and eventual evolution of CO₂. This would result in an observed mass loss of about 7.1 % as an upper limit of expectable mass losses during TGA. Figure 2.7 is therefore consistent with at least partial reduction of the CuO contained in the composite by the reducing atmosphere (Ar) in the TG. The general trend of higher mass losses at intermediate solvent compositions suggests that for those, the CuO is more exposed to the TG atmosphere. In pure hexane the composites are nearly fully dense and CuO is more encapsulated in the Al matrix (cf. figure 2.2a,b), while in pure ACN the

smaller particles are possibly more densely settled in the TG crucible, reducing pore space and exposure to Ar as well.

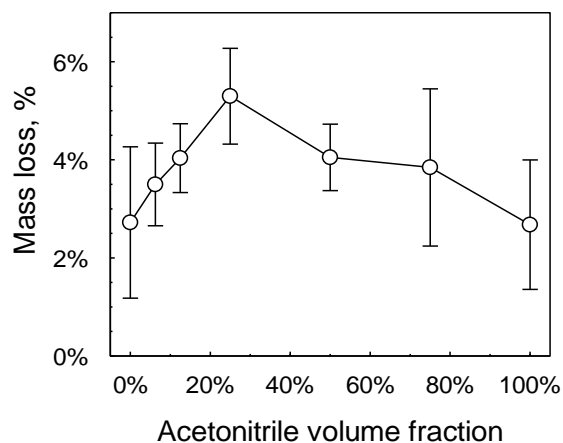


Figure 2.7 Mass loss encountered by samples heated in Ar to 1073 K at different rates as a function of the volume fraction of ACN used in PCA.

2.4.4 Surface Areas

Specific surface areas are shown in figure 2.8. Composites milled with different solvent mixtures are shown as open symbols, while filled symbols show the samples milled with 100 % hexane and 100 % acetonitrile, respectively. The specific surface area is relatively low for the material milled in pure hexane. It increases by <50 % if small amounts of acetonitrile are used in the PCA, but then nearly quadruples for a solvent composition of 25 % acetonitrile. For higher amounts of acetonitrile, the surface area decreases again. The material milled in pure acetonitrile has a surface area comparable to the sample milled in the 20% ACN mixed solvent.

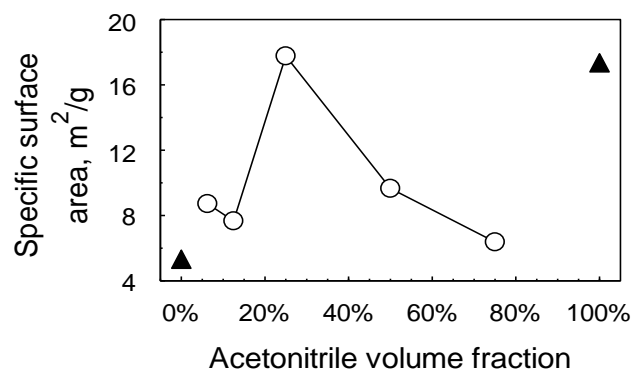


Figure 2.8 Specific surface area of composites milled with mixed solvents. Filled symbols show the materials milled in pure solvents.

2.4.5 Ignition

All prepared samples readily ignited as coatings on an electrically heated filament. A characteristic sequence of high-speed video frames illustrating ignition is shown in figure 2.9. Each frame is labeled with the time elapsed from the instant the wire heating started. The wire, crossing the images horizontally, is not luminous and thus remains invisible while the powder ignites and produces bright emission. Following ignition, there are bright streaks of particles ejected from the sample. Once started locally, the reaction propagates along the filament rapidly and the size of the luminous zone ejecting burning particles increases.



Figure 2.9 A characteristic sequence of video frames showing ignition of S4 (milled in 25% ACN). Heating rate is 34700 ± 1500 K/s.

The ignition temperatures of 8Al:3CuO nanocomposites milled with different solvent mixtures, and heated at different rates are shown in figure 2.10. Figure 2.10 A shows the ignition temperatures vs. the applied heating rate. The error bars represent the standard deviations for at least five repeat measurements. A linear regression of all experiments accounting for heating rate and individual solvent compositions gives an estimate of $dT/d\log\beta = 1.4 \pm 6.4$, with an uncertainty that effectively rules out any dependence of the ignition temperature, T , on the heating rate, β . The results for different heating rates were therefore averaged, and plotted vs. solvent composition in figure 2.10 B. The error bars shown in figure 2.10 B represent the standard deviations of the mean.

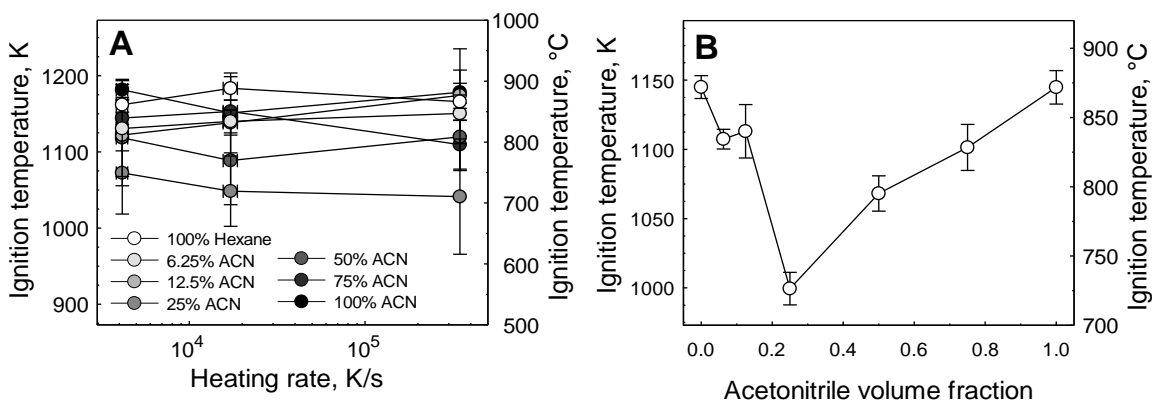


Figure 2.10 Ignition temperatures of 8Al:3CuO thermites at different heating rates obtained from heated filament experiment plotted against volume fraction of ACN.

Solvent composition has a distinct effect on the observed ignition temperatures. The samples milled with mixed solvents exhibit lower ignition temperatures than both samples milled with pure acetonitrile and hexane, respectively. The average ignition temperature for A000 was 1145 K (872 °C); it decreased with increasing volume of ACN and appeared to be lowest at 1000 K (723 °C) for A025, a reduction of about 150 K. With greater ACN volumes, the average ignition temperature increased again to reach a value

for the composite milled in pure acetonitrile that is nearly identical to that of the material milled in pure hexane.

2.4.6 Constant Volume Explosion (CVE)

An example of a pressure trace recorded in a typical experiment is shown in figure 2.11. Following ignition at $t=0$, the pressure is observed to increase for about 20 ms, which suggests the duration of the combustion event. Considering the approximate mass of the sample placed in the holder, this translates into roughly 0.432 g/s as the mass burn rate.

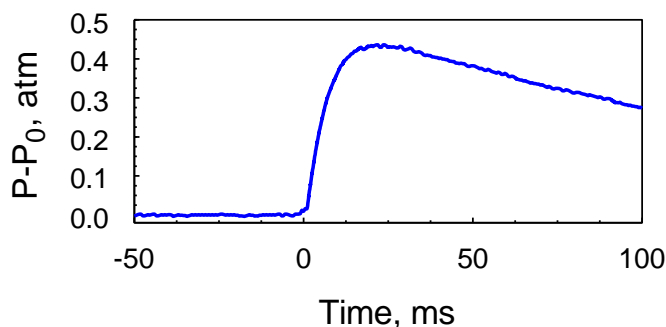


Figure 2.11 Pressure trace for 8.64 mg of the composite milled with 25% ACN in a constant volume explosion (CVE) experiment.

Maximum pressures, P_{\max} , recorded for different 8Al·3CuO samples from CVE experiments are shown in figure 2.12 as a function of the mass loaded into the sample holder for materials prepared at different ACN/hexane ratios in PCA. In addition, the respective values of dP/dt_{\max} are plotted. A linear increase of pressure with mass of the powder is observed, which appears to be the same for all samples, independently of the milling conditions. Similarly, no distinct effect of milling conditions on dP/dt_{\max} can be observed, although these data are more scattered, and the trend is less clear than for P_{\max} .

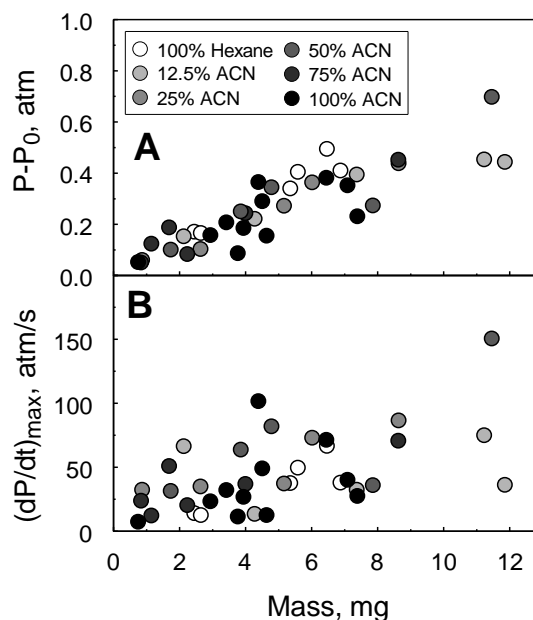


Figure 2.12 Peak CVE pressures and peak pressurization rates vs. sample mass.

2.5 Discussion

The results show that the PCA composition significantly affects the morphology and properties of the nanocomposite thermite powders. Milling with hexane yielded materials similar to those prepared earlier (figure 2.1a, figure 2.2 a, b) and comprising fully dense nanocomposite particles [53, 62]. Such particles are stable in air (figure 2.3B) and highly reactive upon heating (figures 2.4 and 2.10), as shown in many previous studies. Milling with ACN yields a blend of fine Al and CuO particles (figures. 2.1 c, 2.2 e, f), which are mostly de-agglomerated, which is consistent with previous work where ACN was used to mill aluminum [50], [46]. It was proposed that CH₃CN is chemisorbed to aluminum forming surface molecular complexes, which impede the re-consolidation during milling of fine particles produced by attrition [50]. Apparently, the same considerations apply when both Al and CuO particles are milled, as was done here. Assuming that the fine aluminum particles formed by milling in ACN (A100) are not oxidized, they are expected

to be highly reactive upon exposure to air. Indeed, rapid oxidation is observed, leading to a loss of about 35 % of the metallic aluminum (figure 2.3B). Based on that, and assuming that the formed oxide thickness is 2.5 nm (in the range, reported in Refs. [63, 64]), we estimate that the average diameter of the produced particles is close to 40 nm. Such fine particles are not resolved in figure 2.1c and figure 2.2e and f, however.

Using mixed hexane and ACN leads to distinctly different particle morphologies, especially for compositions close to that containing 25% of ACN (A025). Formation of distinct, porous spherical particles (figure 2.1b, figure 2.2c and d) as a product of high energy milling was unexpected, but can be explained considering processes leading to formation of so-called colloidosomes [65]. Colloidosomes, of hollow spheres with shells comprising weakly bonded fine particles form due to interfacial adsorption of colloidal particles at the liquid interface of emulsions formed in agitated immiscible binary liquids containing solid powders. The solids adsorbed at the liquid interface play the key role in stabilizing the droplets of one liquid phase emulsified in another, referred to as Pickering emulsions [66, 67]. A solid particle stabilized at the interface of two liquids can hardly be removed from that interface. Thus, particles are accumulated at the interface until the entire surface of the droplet is populated with fine particles. When such emulsions are dried, colloidosomes form. It is proposed that a similar process leads to formation of spherical particles in the present experiments. An emulsion is formed upon mixing hexane and ACN. The droplet size and stability are affected by the hexane/ACN ratio as well as by the energy introduced into the emulsion by the milling tools (balls) and powder. These energies are expected to be much greater than in systems that do not involve milling tools. It is also possible that stable emulsion form only for a certain range of milling conditions, e.g.,

affected by the hexane/ACN ratio. For the material milled with 25 vol-% acetonitrile, for which formation of spherical particles was most pronounced, it is likely that droplets of ACN formed in hexane. Milled particles were likely to become immobilized at the surface of such droplets, as in Pickering emulsion. Unlike other reported studies describing formation of colloidosomes, however, milling tools used in the present experiments introduced a much higher energy of agitation in the three-phase system (emulsion of immiscible liquids with suspended particles), causing ballistic interaction of particles and droplets. Thus, particles stabilized at the interface could become pushed inside the droplet while being replaced by other particles impinging upon the droplets at high speeds. Particles trapped inside the droplets can no longer interact directly with the milling tools; thus, their refinement is effectively stopped. This may explain relatively coarse and less refined particles observed inside composite spheres in figure 2.2 c and d. This is also consistent with less rapid aging observed for such particles compared to those prepared in pure ACN (figure 2.3B). Assuming again the oxide thickness of 2.5 nm and accounting for the loss of ca. 10% of metallic aluminum (figure 2.3B), an average aluminum particle diameter of 145 nm is estimated for these powders.

Based on the present observations, it can be hypothesized that the ratio of the immiscible solvents, the relative amount of emulsified fluid (e.g., ACN), and the solid loading need to be in certain ranges in order for the spherical particles to be effectively produced. Preliminary estimates suggest that the volume of ACN was approximately equal to the volume of the loaded solid powders for A025, for which the formation of spheres was most noticeable. Further work is certainly of interest examining closer mechanisms of formation of spherical composite particles, expanding the range of their respective

compositions, and ways of fine-tuning their structures. Such particles are expected to have a better flowability than conventional composites; they may also be advantageous when the solid reactive powder needs to be mixed with a polymeric binder and/or when the reactive materials need to be ordered or packed in certain ways.

In addition to the significant differences in morphologies of the prepared powders, there are differences in their reactivity as determined by both, thermo-analytical and ignition experiments. In DSC experiments, the intermetallic eutectic melting was only observed for the material milled in pure hexane (figure 2.4a). This is consistent with the fully-dense structure of nanocomposite particles in A000. In other samples, chemisorbed ACN generated a different interface structure between Al and CuO, preventing or delaying reaction of Al with reduced Cu.

Results presented in figures 2.4, 2.5, 2.7, and 2.10 show complex effect of PCA composition on the reactivity of obtained composites. The reactivity is affected by the scale of mixing between reactive components, uniformity of this mixing, porosity of the material, and the specific nature of the interface separating Al from CuO. All of the above parameters change for the samples prepared with different compositions of PCA. Quantifying all such changes is important, but it is outside the scope of this study. Thus, only preliminary discussion can be proposed here, while it is clear that fine-tuning properties of nanocomposite thermites is possible varying PCA. In particular, a lower ignition temperature for A025 (figure 2.10) combined with the higher apparent activation energy for the redox reaction for the same material (figure 2.5B) may be of interest.

Direct comparisons between the DSC and ignition experiments reported here cannot be readily made. Indeed, in ignition tests, the powders were exposed to air and thus

oxidized, at least partially. This oxidation was prevented in DSC experiments using samples loaded under a protective liquid, and dried in argon inside the DSC furnace before heating. Extrapolating the trends from Kissinger plots shown in figure 2.5A to the range of heating rates achieved in heated wire experiments points to higher temperatures than the observed ignition temperatures for all samples. Additionally, the measured ignition temperatures were not affected by the heating rates (figure 2.10A). Thus, the ignition was likely associated with a phase transformation occurring in the interfacial layer separating Al and CuO, and not by a thermally activated redox reaction. These transformations must have been affected by the structure and composition of this interfacial layer, which in turn was affected by the PCA composition used. Additionally, partial oxidation of Al upon exposure to air at ambient temperature, when the prepared porous samples were dried before the tests, could have further altered properties of Al/CuO interfaces.

Effect of interface structure on the reactivity can be inferred from the results of MS analysis correlated with TG shown in figure 2.6 for A025. The release of oxidation products, CO and CO₂ does not correlate with release of residual ACN. One interpretation may be that hexane is adsorbed to the powder surface physically and is thus readily oxidized when oxygen becomes available as a result of CuO decomposition. Conversely, ACN is chemisorbed and is not readily reacting with oxygen. However, release of ACN upon heating may disturb the powder surface and generate defects; such defects would be important when the sample is heated in an oxidizing environment and thus a source of oxygen other than decomposing CuO is available. Note also that the decomposition of CuO is significantly accelerated by presence of aluminum, a strong reducing agent. At the same time, the interface between Al and CuO, affected by chemisorbed ACN, in particular, may

be substantially different for samples prepared with different PCA compositions. Thus, decomposition of CuO can proceed differently in samples containing aluminum functionalized by different adsorbed PCAs.

The results suggest that both, ignition and reactions during thermal analysis are affected not only by properties of the interface, but also by the particles' porosity. BET surface area measurements offered a method to characterize the composites' overall accessibility to an external gas, without the rigor required to quantify pore size distributions. In this measurement, A025 stands out as the composite milled in mixed solvents with the highest surface area, and therefore presumably with the greatest porosity (figure 2.8). Pore space between the reactants Al and CuO is consistent with a higher activation barrier for the reaction, as observed by DSC (figure 2.5B). Open porosity is also consistent with a stronger evolution of gaseous species, whether due to CuO decomposition in an Ar atmosphere, or due to evaporation of solvent remnants (figures 2.6 and 2.7). Seeing the greatest reduction in ignition temperature for the composite material with the greatest porosity (figure 2.10B) is, therefore, not surprising. The surface area measurement showed the material milled in pure acetonitrile, A100, had a similar surface area as A025. However, the geometry is different: no coherent composite particles form under these conditions, as well as A100 is most likely aged during handling in air (figure 2.3B), and consequently did not ignite as readily as the material milled with 25 vol-% of acetonitrile.

Future work should focus on a better characterization of the Al-CuO interfaces and on protection of freshly formed surface of composite materials from oxidation upon their exposure to air. This can be achieved by coating the prepared composites. It is possible that the lack of detectable differences between composites in the combustion experiments

(figure 2.12) could be associated with oxidation of aluminum, reducing reactivity of all prepared composites occurring for all but the traditionally prepared powder, A000. Because similar reactivity was observed in these combustion experiments for all materials despite substantially reduced fraction of crystalline aluminum for samples milled in ACN and mixed fluids, there is potential for a substantial improvement of reactive properties of the composites, when their freshly made surface is properly protected from ambient air.

2.6 Conclusions

Preparing nanocomposite 8Al:3CuO thermite powders by ARM using different liquid PCAs dramatically affects the surface morphology and structure of the prepared composites. Fully-dense composite particles comprising micron-sized particles with Al and CuO mixed on the scale of 100 nm are formed when the starting materials are milled in hexane. A mixture of nano-sized, largely un-agglomerated particles of Al and CuO is produced when milling is performed in ACN. The surface of the formed fine Al particles is not protected with alumina and when ACN is dried, the material oxidizes in air rapidly consuming close to 20% of available aluminum. Porous composites agglomerated to a different degree are prepared when hexane and ACN are mixed in PCA.

Using different PCAs affects the reactivity of the prepared composites; however, these effects are complex and involve multiple changes in the prepared composites. It is proposed that hexane and ACN are respectively physically and chemisorbed to milled powders. They influence the structure of the formed Al/CuO interfaces and thus affect kinetics of the respective redox reactions.

CHAPTER 3

EFFECT OF PREMILLING ALUMINUM AND COPPER (II) OXIDE IN ACETONITRILE ON PROPERTIES OF ALUMINUM-COPPER OXIDE THERMITES PREPARED BY ARRESTED REACTIVE MILLING

3.1 Abstract

Thermite powders with molar composition $8\text{Al}\cdot 3\text{CuO}$ were prepared in two stages by Arrested Reactive Milling (ARM). In the first stage, the starting materials Al and CuO were milled separately in acetonitrile. Composite powders were then prepared in the second milling stage with hexane as process control agent and in the four possible combinations of one, both, or neither starting material being premilled in acetonitrile. Composites were characterized for morphology, size distribution, surface area, and reactive properties at low heating rates (thermal analysis) and high heating rates (ignition). Whether or not CuO was premilled, dense composites formed without premilling of Al. If Al was premilled in acetonitrile, however, loose agglomerates of refined Al and CuO particles formed in the second milling stage. Premilling changed the low-temperature reactions leading to ignition in the $8\text{Al}\cdot 3\text{CuO}$ thermites. These changes are attributed to increased porosity of the formed composites if aluminum is premilled with acetonitrile. It is shown that greater refinement and lower ignition temperatures are achievable using two-stage milling.

3.2 Introduction

Mechanical milling is a scalable, cost effective, and operationally simple method of preparing reactive nanocomposites [68]. In particular, thermites with Al as fuel and CuO as oxidizer have been prepared by Arrested Reactive Milling [69] and extensively

characterized [30, 56, 62, 70-74]. Typical operating parameters of mechanical milling including ball to powder mass ratio, milling time, and choice of process control agent (PCA) affect distribution of components in the prepared composite materials. This is important for their reactivity, energy density, and particle morphology. Preparing nanocomposite thermites with solid PCA, such as stearic acid, may lead to initiation of the powder during milling, which may damage equipment and thus is undesirable. Using a liquid PCA, such as hexane was adopted in most recent studies [30, 72]. Even if the thermite reaction is locally mechanically triggered during milling, it is quenched by the vaporization of the endothermic liquid and prevented from propagating throughout the milling container. In such cases, it is therefore observed that greater refinement of the prepared nanocomposite thermites is accompanied by formation of small amounts of reaction products, which diminishes the energy density of the prepared materials. This issue motivated the current effort to improve refinement in nanocomposite thermite powders prepared by ARM without sacrificing energy density. The approach used here is to mill separately the starting components used in ARM. The premilling step uses acetonitrile (ACN) as PCA, which has been shown recently to be effective in refining milled metal powders [75, 76].

3.3 Experimental

3.3.1 Sample preparation

Metal rich $8\text{Al}\cdot 3\text{CuO}$ nanocomposite powders (8/3 molar ratio; equivalence ratio of 4) were prepared. The specific fuel-rich composition was chosen for safety of handling, and in order to remain consistent with our previous work [71]. The composites were prepared using a Retsch PM400 planetary mill. Custom-made, hardened steel milling vials (175 ml)

with 17-mm thick walls capable of withstanding high pressure in case of any thermite reaction triggered during milling were used. Hardened steel balls with 9.5 mm (3/8") diameter served as milling media. The ball to powder mass ratio (BPR) was 3. The starting materials included aluminum (Atlantic Equipment Engineers, –325 mesh, 99.5 %), and CuO (Sigma–Aldrich, 10 μm and 5 μm , 98+ %). Hexane (95 %) and acetonitrile (99.5 %, both Alfa Aesar) served as PCAs. Milling vials were always loaded in an Ar-filled glove box. For the first milling stage, 30-g batches of Al and CuO were loaded and sealed with 12 ml ACN in separate milling vials inside the glovebox. The samples were then milled for 60 min at 350 RPM. Prior to 2nd stage milling, the premilled powders containing vials were transferred to the glovebox and dried in Ar for 24 hours to evaporate any remaining ACN. In the second milling stage, 14.25 g of Al and 15.75 g of CuO – each either premilled or not premilled – were loaded and sealed with 24 ml hexane under Ar and milled for an hour. The material prepared with unmilled components used CuO with nominal size of 5 μm , while all other materials were prepared with 10 μm CuO due to availability. The resulting samples are listed in Table 3.1. After preparation all samples were stored under hexane.

Table 3.1 Combinations of Milled/Unmilled Starting Materials and Assigned Material ID

Material ID		CuO	
		as- received	premilled
Al	as-received	A-C-	A-Cp
	premilled	ApC-	ApCp

3.3.2 Characterization

Particle size distributions were determined by light scattering using a Malvern 3000 Mastersizer with ethylene glycol as a dispersant. The obscuration throughout the entire

experiment was maintained between 5 to 8%. Suspensions were continuously stirred at 2500 RPM with ultrasonic agitation to avoid particle settling and to break up loosely-held agglomerates.

Specific surface analysis by nitrogen adsorption was performed using an Autosorb iQ (model ASIQM000000-6) BET by Quantachrome Instruments. Prior to analysis, 250 – 350 mg of sample were degassed at 30 °C under vacuum for 48 hrs to remove remaining PCA and any other adsorbed gases.

A JEOL JSM 7900F field emission scanning electron microscope (SEM) operated at 10 kV was used to characterize particle morphology and CuO inclusion sizes. Particles were embedded in epoxy resin and cross-sectioned. Backscattered electron images were processed using FIJI software [77] to obtain CuO inclusion size distributions within the composite particles. Ten images were processed for each material. After scaling, a single threshold value of 170 out of 255 was applied. The threshold was consistent for all images as they were obtained under the same brightness and contrast in the SEM. Each thresholded image was converted into a binary image with CuO inclusions as black particles in a white matrix. A recursive median filter was applied (using the Biovoxxel toolbox [78]) to minimize noise while retaining particle features, effectively eliminating single-pixel particles as artifacts. CuO size distributions were obtained using the built-in analyze-particles feature of FIJI. Particles on the edges of the images were not excluded as preliminary tests showed that this had no effect on the obtained size distributions.

To investigate the presence of reacted species, X-ray diffraction (XRD) analysis was performed. The samples were dried and exposed to air for 24 hours. A PANalytical Empyrean multipurpose research diffractometer was operated at 45 kV and 40 mA, with

unfiltered Cu K α radiation ($\lambda = 1.5438 \text{ \AA}$). Whole-pattern refinement was performed using the X'Pert Highscore software package [79].

Reactions occurring in the composite powders were characterized by differential scanning calorimetry (DSC) and thermogravimetry (TG) using a Netzsch STA409PC thermal analyzer. Powders were loaded as suspension in hexane in alumina crucibles in order to prevent oxidation in air. After loading, the liquid was allowed to evaporate in a flow of argon, followed by three cycles of evacuation and flushing with argon. Samples were not allowed to come in contact with air throughout the entire process. The dry sample mass was recorded after the internal balance showed a stable reading for 10 min. Masses ranged from 15 to 20 mg. All measurements were conducted under 99.998 % argon, (Airgas) at a flow rate of 50 ml/min. DSC traces were recorded at 2.5, 5, and 10 K/min. Samples were heated twice to the maximum temperature set in the program, 1073 K (800 °C) for each run. To correct for baseline effects, the signal recorded in the second heating cycle was subtracted from the signal recorded in the first heating cycle, and then normalized by sample mass. Peak temperatures were determined using Proteus[®] thermo-analytical software by Netzsch.

Ignition temperatures were obtained in heated filament experiments. In a custom experiment, a thin coating of suspensions of the powders in hexane was applied to an electrically heated, 0.5-mm diameter nickel-chromium wire [75]. The hexane was dried prior to each run. Rechargeable large-cell 12-V batteries (Kinetikpower.com) served as the source of DC voltage. Heating rates of $3,500 \pm 340 \text{ K/s}$, $13,100 \pm 1,300 \text{ K/s}$, and $28,100 \pm 3,100 \text{ K/s}$ were achieved by using one, two, or three batteries in series, respectively.

The time of ignition was recorded by a photodiode and a MotionPro 500 high-speed video camera simultaneously. The filament temperature was obtained by focusing an infrared pyrometer based on a germanium switchable gain detector (PDA30B2, Thorlabs) on an uncoated portion of the wire. A BB-4A black body emission source by Omega Engineering was used to calibrate the pyrometer at temperatures ranging from 300 to 950 °C. The pyrometer and photodiode signals were recorded using a Rigol DS1054Z digital oscilloscope. The filament temperature at the time of ignition was interpreted as the powder ignition temperature.

3.4 Results

3.4.1 Component Premilling (Stage 1)

Cross-sections of as-received and pre-milled powders of Al and CuO are shown in figure 3.1. After one hour of milling, the roughly equiaxial Al particles (figure 3.1, top left) form flakes reduced to submicron thickness for some particles (figure 3.1, bottom left). The flakes have length on the order of several microns; some flakes with greater lengths (10-30 μm) have also been observed. As-received copper oxide (figure 3.1, top right) also includes roughly equiaxial particles, which, unlike ductile Al, contain multiple cracks. After premilling, CuO particles are reduced in size (figure 3.1, bottom right); however, they remain equiaxial.

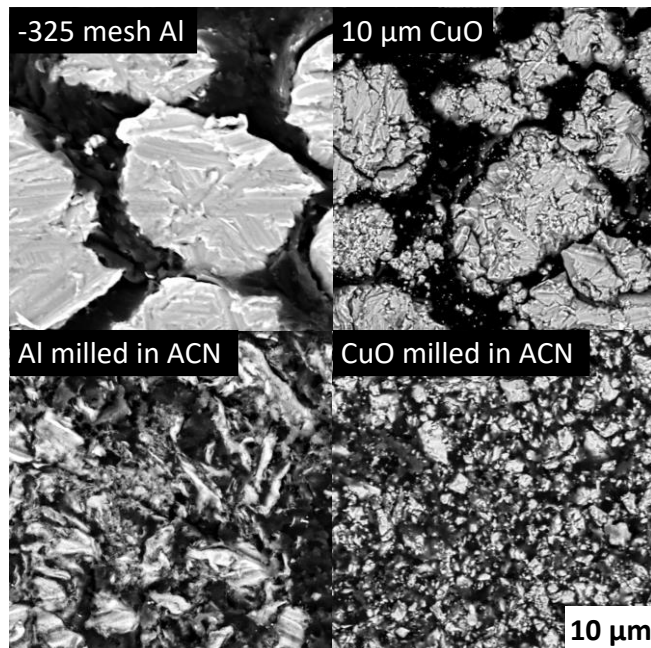


Figure 3.1 Back-scattered electron images of cross-sections of Al and CuO before and after milling in acetonitrile.

Particle size distributions are shown in figure 3.2. After milling in acetonitrile for an hour, both aluminum and copper oxide powders decrease in size. For CuO the mode shifts from 10.5 to 3 μm . For aluminum, the mode does not shift, but additional fine particles appear in the size distribution. However, the particle size measurement for the flake-like particles observed for Al is biased to larger sizes and thus may not adequately represent the particle volumes.

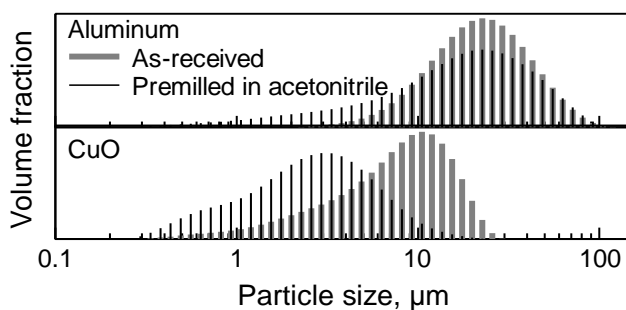


Figure 3.2 Particle size distributions of the individual starting materials Al and CuO before and after milling in acetonitrile for an hour.

3.4.2 Composite Formation (Stage 2)

Back-scattered electron images of the composites after stage 2 milling are shown in figure 3.3. The lower-magnification images in the left column show particle/agglomerate morphology. Higher-magnification images in right column illustrate the scale of mixing between Al and CuO and the types of Al/CuO interfaces formed in the composites. In all images, epoxy appears black, Al appears dark gray and CuO appears light gray. Brighter CuO particles or inclusions are readily distinguished from Al.

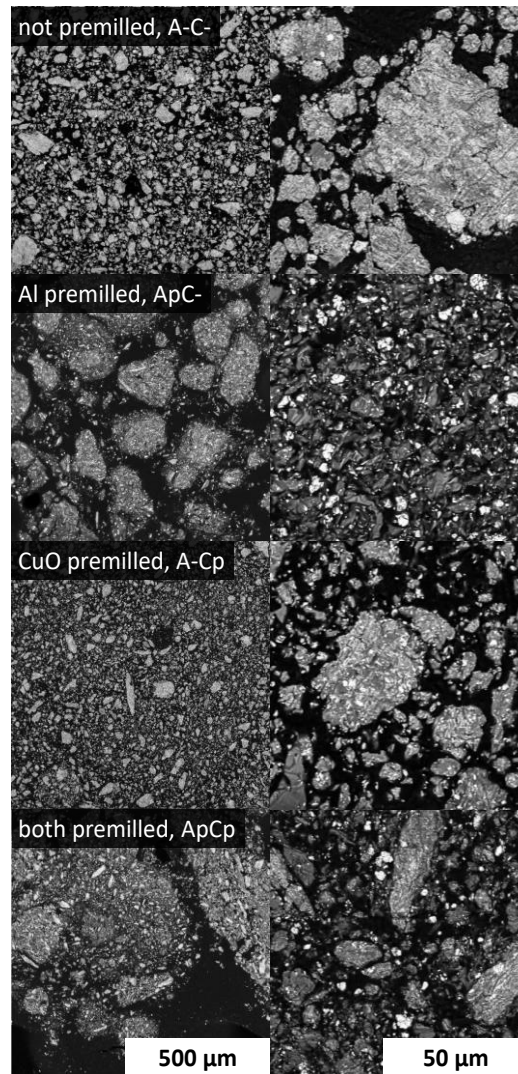


Figure 3.3 Back-scattered electron images of the composites after stage 2 milling.

Sample A-C- (see Table 3.1) is the reference material prepared by one-stage milling. As reported in previous work, it comprises nearly fully-dense, approximately equiaxial composite particles. CuO inclusions are fully embedded into the Al matrix [71]. Sample ApC- prepared with premilled aluminum forms large and relatively loose agglomerates. The high magnification image shows that most CuO particles are not embedded in Al; instead, fine Al and CuO particles are mixed without forming a fully-dense composite. Sample A-Cp with premilled CuO forms finer particles than the reference material A-C- although the particle interiors show a fully-dense composite structure, similar to that observed for A-C-. Most CuO is embedded into composite particles. Finally, sample ApCp using both Al and CuO that were premilled forms large, loose agglomerates similar to those observed for ApC-. Also similar to ApC-, many CuO particles appear to be separated from Al, although formation of relatively large, flattened composite particles is also observed.

Figure 3.4 shows particle size distributions for all composite materials prepared. Sample ApC- using premilled Al shows a significant size reduction relative to the reference sample A-C- with a distinct increase in fine particles. The size reduction for A-Cp with premilled CuO is less pronounced, although particles on the coarse end are reduced as well. ApCp with both components premilled has a size distribution similar to ApC-, but with fewer fines.

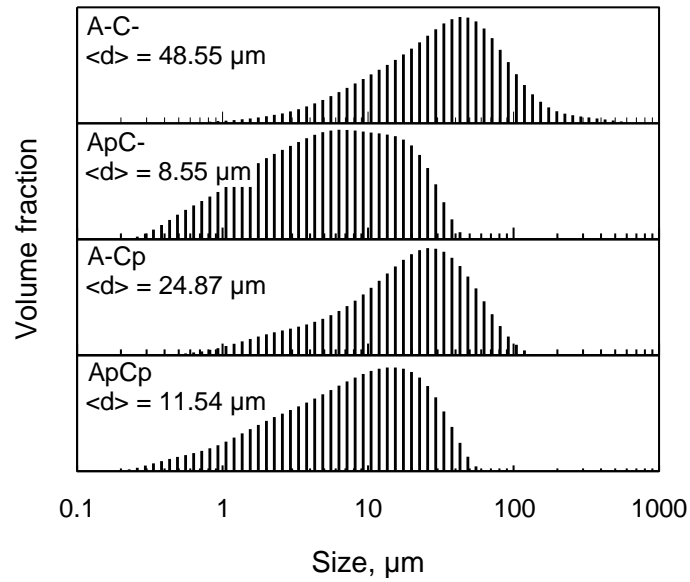


Figure 3.4 Particle size distributions of the prepared 8Al·3CuO thermite powders.

Figure. 3.5 shows the volume-based size distribution of CuO inclusions in the prepared composites. Since the reference material A-C- was prepared using CuO with a smaller starting particle size (nominally 5 μm), the resulting inclusion sizes are smallest compared to the other composites. Among the composites prepared with the larger starting material (nominally 10 μm), the material prepared without premilling CuO (ApC) shows the largest inclusion size. Premilling CuO (A-Cp) reduces the inclusion size slightly. Premilling Al in addition to CuO (ApCp) results in further reduction of the CuO inclusions and a more prominent fine fraction.

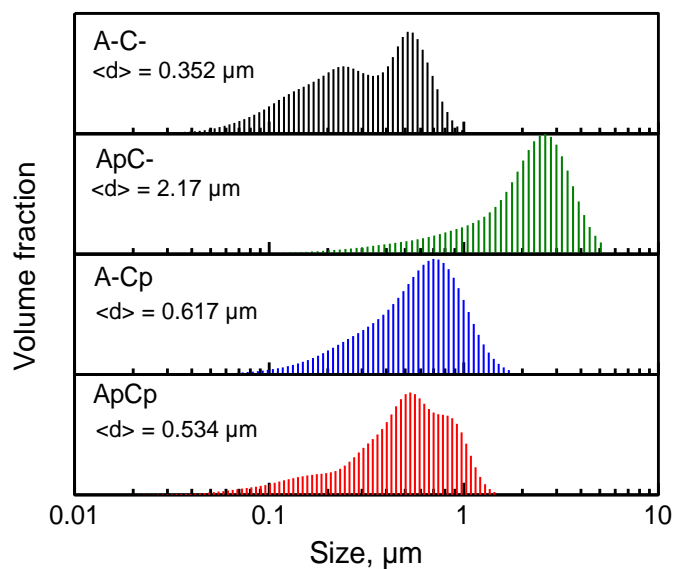


Figure 3.5 Size distribution of CuO inclusions.

The specific surface areas obtained from N_2 absorption are shown in figure 3.6. The samples containing premilled Al show larger specific surface areas compared to samples without premilled Al. The sample prepared with both, premilled Al and CuO has the largest specific surface area with $10.3 \text{ m}^2/\text{g}$. The lowest surface area was observed for A-Cp, while the reference material A-C- had a surface area of around $5.3 \text{ m}^2/\text{g}$. These measurements are generally consistent with the particle size distribution measurements shown in figure 3.4.

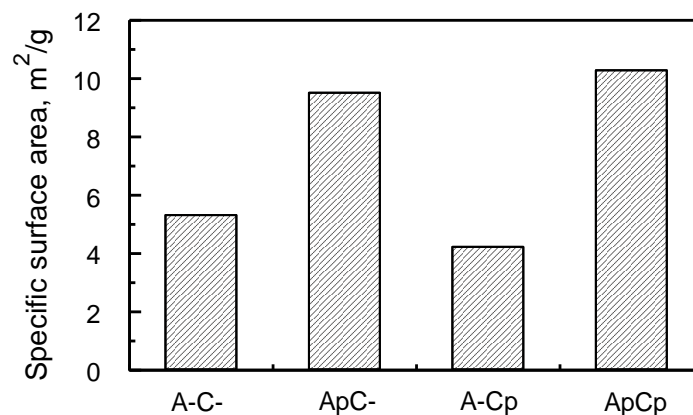


Figure 3.6 Specific surface areas for the prepared 8Al·3CuO thermite powders.

XRD patterns of the as-milled materials are shown in figure 3.7. All patterns are qualitatively similar with peaks corresponding to aluminum (marked) and tenorite, CuO (all remaining unmarked peaks). Processing these patterns by whole-pattern refinement resulted in estimates for crystallite sizes as well as apparent composition. Results are shown in Table 3.2.

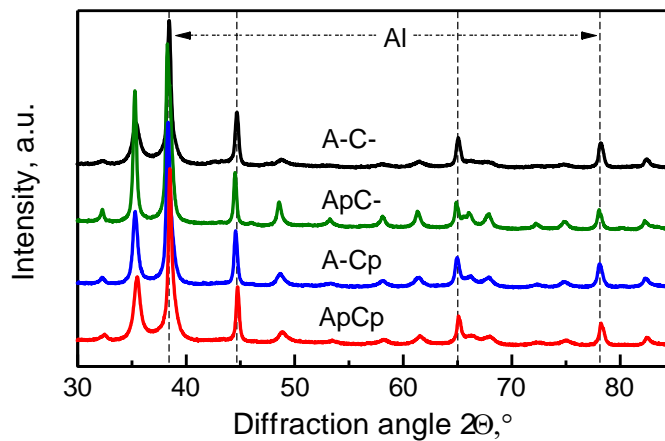


Figure 3.7 XRD patterns for 8Al·3CuO thermite powders. All unmarked peaks correspond to CuO, tenorite.

Table 3.2 Results of XRD Whole-pattern Refinement of As-milled Materials

Material	Cryst. size, nm		Microstrain, %		w_{Al} , wt-%	Reaction products	w_{prod} , wt-%	$N_{Al}/(N_{Al}+N_{Cu})$ [8/(8+3) = 0.727]
	Al	CuO	Al	CuO				
A-C-	31.7	27.6	0.046	0.84	45.7	Cu, Al ₂ Cu	3.40	0.714
ApC-	79.4	>1	0.14	0.37	37.0	Cu	0.602	0.633
		μm						
A-Cp	37.2	44.3	0.082	0.54	46.0	Cu	0.958	0.715
ApCp	52.3	27.6	0.12	0.64	39.6	Cu	1.51	0.658

Comparing materials with premilled Al (ApC- and ApCp) to those with as-received Al (A-C- and A-Cp), apparent crystallite sizes are greater, but lattice strains are also greater. For CuO, the analogous comparison of A-C- and ApC- to A-Cp and ApCp suggests that premilling CuO also results in slightly larger crystallite sizes as well as marginally higher microstrain. Note that A-C- was prepared from a starting material with smaller nominal CuO particle size, as stated in section 2.1. The composition estimates suggest a decrease in metallic Al for samples with premilled Al; premilling CuO has negligible effect on overall composition. Reaction products, formed during preparation, are present for all materials. The highest concentration is observed in the material where neither Al nor CuO were premilled (A-C-), and the second highest in the material where both were premilled (ApCp). The overall compositional balance is expressed as the atomic ratio $N_{Al}/(N_{Al}+N_{Cu})$, accounting for the elements in all observed phases. It is expected to be $8/11 = 0.727$ for the targeted composition of 8Al·3CuO. Observed values are consistently lower, but particularly the materials prepared with premilled Al (ApC- and ApCp) are deficient in metallic aluminum and must contain Al in some form that is not detected by XRD.

3.4.3 Thermal Analysis

Results of thermal analysis are shown in figure 3.8. A relatively weak and broad exothermic process starting at ca. 400 K in the reference material A-C-, and previously described for similar materials [62], is either diminished (A-Cp) or not observed at all for the composites prepared with premilled Al (ApC- and ApCp). Similarly, an endothermic peak representing the Al-Al₂Cu eutectic is only visible for A-C-.

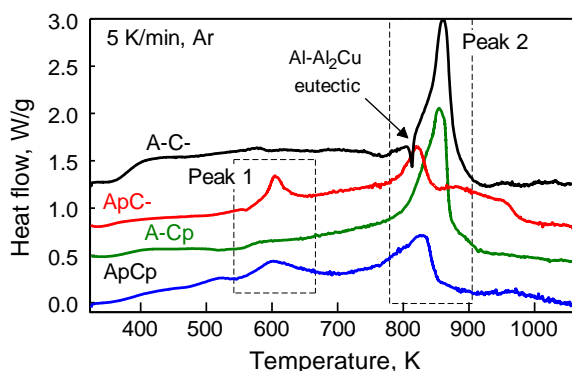


Figure 3.8 DSC traces for the prepared 8Al-3CuO thermite powders heated in Ar at 5 K/min.

The strongest exothermic peak, labeled peak 2 in figure 3.8, occurs at about 850 K for materials prepared with as-received aluminum (A-C- and A-Cp). For materials prepared with premilled aluminum (ApC- and ApCp), it is reduced to about 815 K. These materials also show an exothermic peak near 600 K, labeled peak 1 in figure 3.8. This pronounced exothermic peak is absent in the materials prepared with as-received aluminum. A small endothermic feature is observed before peak 1 for ApC-; it appears less clearly for ApCp. This feature is observed consistently at different heating rates.

Mass loss was recorded simultaneously to the heat flow measurements. The highest mass loss rate was observed to coincide with peak 1 (figure 3.8) for all materials, even for

A-Cp, where peak 1 is nearly absent. The total mass loss observed after heating to 1073 K is shown in table 3.3. The values shown represent averages and standard deviations of three measurements each material, performed at different heating rates. The mass loss is lower (1-2 %) for materials prepared with as-received aluminum, and higher (near 6 %) for materials prepared with premilled aluminum, corresponding to a 3-4 fold increase. Premilling CuO causes a comparatively smaller increase in the observed mass loss.

Table 3.3 Mass Loss Encountered by Samples Heated in Ar to 1073 K

Sample	Mass loss, %
A-C-	1.3 ± 0.3
ApC-	5.3 ± 0.3
A-Cp	2.0 ± 0.2
ApCp	6.2 ± 0.2

To elucidate details about the processes observed by DSC, samples of the material prepared with premilled Al and as-received CuO (ApC-) were heated to intermediate temperatures, recovered, and analyzed by XRD. The recorded XRD patterns were processed by whole-pattern refinement. Figure 3.9 shows estimated phase compositions (bars) as well as the observed compositional balance $N_{Al}/(N_{Al}+N_{Cu})$ (open circles).

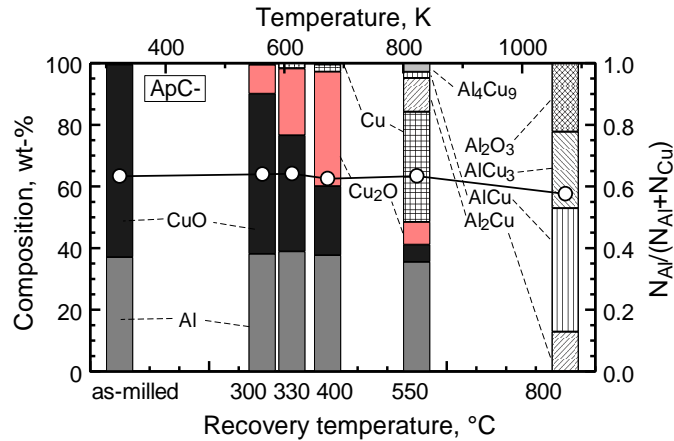


Figure 3.9 Phase composition of material prepared with premilled Al (ApC-) and heated to intermediate temperatures. The material at 1073 K (800 °C) was recovered after two heating cycles.

The results suggest that the reaction associated with the DSC peak 1 near 600 K is the reduction of CuO to form Cu₂O. This reaction is not accompanied with a detectable change in the measured fraction of Al. Peak 2 near 850 K is characterized by the next reduction step of Cu₂O to form Cu. Once again, the fraction of metallic aluminum detected by XRD remains nearly unaffected. The formed metallic Cu proceeds then to alloy with the metallic Al to form intermetallic compounds. Under idealized conditions, complete reaction of the available CuO with the available Al in an 8Al-3CuO composite would result in a metallic phase with an Al/Cu ratio of 2. The expected stable intermetallic phase with this composition is \square -Al₂Cu [80]. While some Al₂Cu is indeed observed in material recovered from 823 K (550 °C) and 1073 K (800 °C), several other phases are observed as well, and the majority of phases containing reduced copper are more copper rich. This is generally consistent with the lower-than-expected values of $N_{Al}/(N_{Al}+N_{Cu})$ in the as-prepared material (table 3.2), and after heating (open symbols in figure 3.9). However, the number and compositional range of the phases observed also suggests a degree of compositional inhomogeneity.

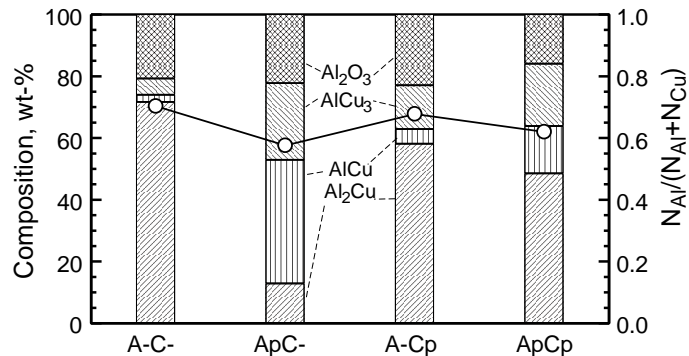


Figure 3.10 Phase composition of all composite materials after two complete heating cycles to 1073 K (800 °C).

This indicator was used to further compare the different prepared composites. Figure 3.10 shows the phase composition and elemental balance $N_{Al}/(N_{Al}+N_{Cu})$ for all materials recovered after two complete heating cycles to 1073 K (800 °C, see section 3.3.2).

After two complete heating cycles to 1073 K, the material prepared with as-received components, A-C-, consists primarily Al₂Cu with minor amounts of AlCu and AlCu₃. Al₂Cu is also the most abundant metallic phase in the other material prepared with unmilled Al, A-Cp. The other, more Cu-rich phases become more prominent in ApCp where both components were premilled, and the least amount of Al₂Cu is observed in the material prepared with premilled Al and unmilled CuO, ApC-. Taking this measure as an indicator of homogeneity, the results suggest that in the as-milled state, A-C- was the most homogeneous with the most contact area between the components, and ApC- was the least homogeneous with the least contact between the components.

3.4.4 Ignition

The ignition temperatures of different 8Al-3CuO nanocomposites coated on a heated filament are shown in figure 3.11. Materials prepared with unmilled Al showed a weak (A-C-) or no (A-Cp) dependence of ignition temperature on heating rate, although the ignition temperatures were slightly lower for the material with premilled CuO. Premilling Al on the other hand resulted in a noticeable effect of heating rate on ignition temperature. Additionally, the ignition temperatures are lower, and the effect of premilling CuO is more pronounced if Al is also premilled.

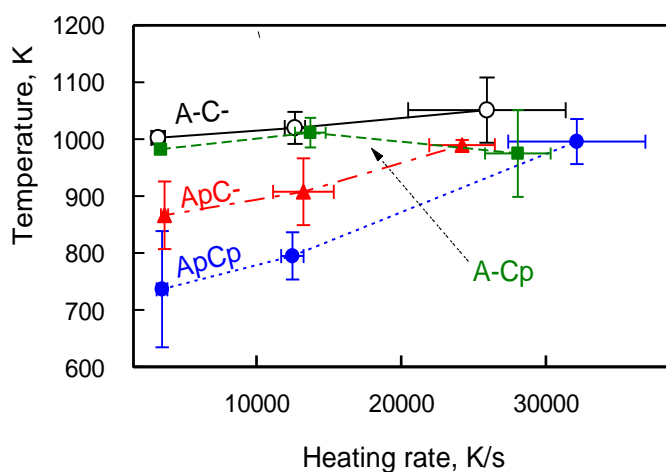


Figure 3.11 Ignition temperatures of 8Al-3CuO thermites prepared with premilled components in a heated filament experiment.

In addition, for both materials prepared with premilled Al (ApC- and ApCp) secondary ignition was observed at low heating rates. After the samples had ignited and appeared to burn out, the filament temperature continued to increase until at temperatures between 950 and 1000 K, a small light emission appeared from the burnt-out powder. This suggests that the first, low-temperature ignition did not consume all of the material even

though it was accompanied by a bright flame and ejection of burning particles. The temperature of the secondary ignition was effectively the same as the ignition temperature measured for the composites prepared with unmilled Al (A-C- and A-Cp).

3.4.5 Kinetics of Exothermic Reactions

The data obtained from thermal analysis are processed using an isoconversion method by Kissinger [61]. Figure. 3.12 correlates DSC and DTG peak temperatures with ignition temperatures observed at different heating rates. The vertical axis is $\ln(\beta / T^2)$, where β is the heating rate in K/min, and the horizontal axis is the reciprocal temperature $1/T$. Broken lines show linear fits to the DSC data; slopes of these fits represent the apparent activation energy. Extrapolating to high heating rates enables one to assess how likely each exothermic reaction observed by DSC is to lead to ignition. The ignition temperature of materials prepared with as-received aluminum (A-C- and A-Cp) did barely vary with heating rate (figure. 3.11). The respective points in the Kissinger plot (figure. 3.12) are grouped near 1000 K. For all samples, the straight-line extrapolation of the main exothermic event, peak 2, point to a temperature range higher than the experimental ignition temperatures, and is therefore unlikely to be relevant for ignition. Extrapolating peak 1 for materials with premilled Al, ApC- and ApCp, on the other hand, roughly points to the temperature range where ignition was observed.

Activation energies for different reactions observed by thermal analysis are summarized in Table 3.4. For the materials using premilled Al, ApC- and ApCp, the activation energies derived from DSC peak 1 are consistent with the values derived from simultaneous DTG. However, the activation energies appear to differ noticeably between these two materials. For peak 2, all activation energies vary in the relatively narrow range

of 179 – 204 kJ/mol. Premilling CuO appears to cause the activation energy to decrease slightly (A-Cp vs A-C- and ApCp vs. ApC-), while premilling Al causes a slight increase (ApC- vs A-C- and ApCp vs A-Cp).

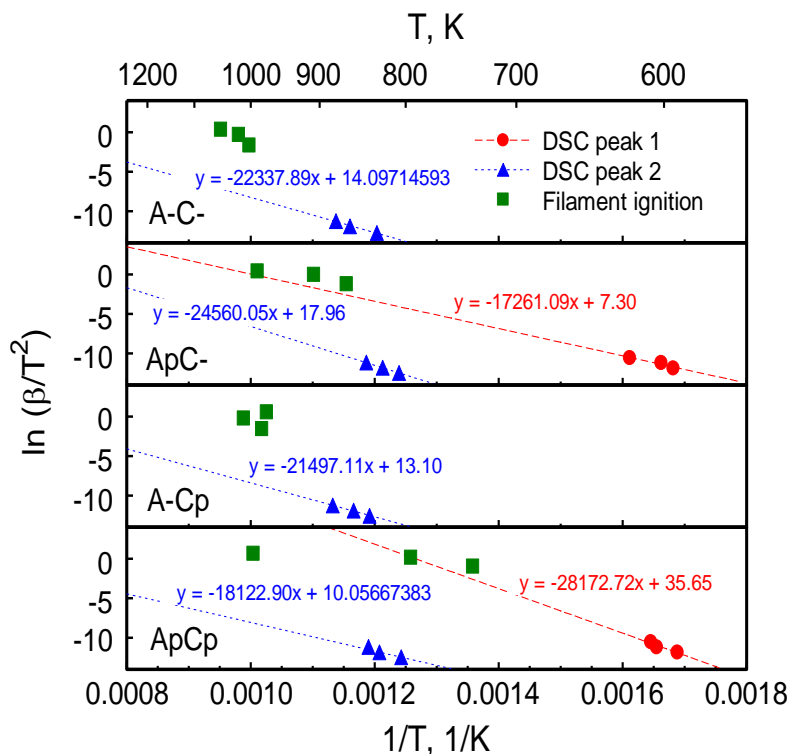


Figure 3.12 Kissinger plots correlating ignition temperatures with DSC peaks at different heating rates.

Table 3.4 Activation Energies Determined from DSC and DTG Measurements

Material	Apparent activation energy, kJ/mol		
	Peak 1	Peak 1	Peak 2
	(DSC)	(DTG)	(DSC)
A-C-	N/A	N/A	194 ± 11
ApC-	144 ± 39	157 ± 7	204 ± 1
A-Cp	N/A	N/A	179 ± 15
ApCp	234 ± 78	203 ± 6	197 ± 40

3.5 Discussion

The results show that premilling Al and CuO in ACN affects both physical and chemical properties of the prepared composite powders. Al particle size reduction was expected based on earlier reports [50]. The proposed mechanism of this refinement involves ACN chemisorption to aluminum generating molecular complexes at the surface. The binding presumably takes place at crack tips where free dangling bonds of Al clusters get capped by ACN. This impedes agglomeration of fine particles produced by attrition. Because of their ductility, the resulting fine Al particles are flake-like as seen in figure 3.1. Presumably, a similar process yields refinement of CuO, for which premilling produces finer size equiaxial particles (also figure 3.1). Present results show that the same surface modifications that assist refinement of premilled Al and CuO also affect morphology of Al-CuO composites prepared by ARM as well as mechanisms of ensuing redox reactions.

The material A-C-, which used starting components with no premilling, consists of fully-dense composites, as prepared by ARM previously [30, 62, 70, 72, 73]. Conversely, Al and CuO remain largely separated in ApC- and ApCp where premilled Al was used (figure 3.3), although large and loose agglomerates form. For A-Cp, using premilled CuO but as-received Al, the formed agglomerates are denser again, similar to A-C-. This suggests that exposing CuO to acetonitrile does not impede cold-welding and composite formation expected for as-received Al while the fine premilled CuO particles are effectively embedded in the forming composite particles.

Sizes of composite particles are coarser for materials prepared with as-received Al, and finer for materials prepared with premilled Al. Whether CuO is premilled has a minor effect on the sizes of the resulting composites. However, sizes of CuO inclusions are affected by premilling of CuO. Comparing ApC-, prepared with as-received CuO with ApCp, prepared with premilled CuO, the resulting inclusions are smaller by almost an order of magnitude. The effect of premilling Al on the CuO inclusion sizes is minor.

Specific surface areas estimated from the particle size distributions shown in figure 3.4 vary from about 0.1 m²/g (A-C-) to about 0.6 m²/g (ApC-). The measured, much greater specific surface areas shown in figure 3.6 therefore reflect both, particle sizes and considerable particle porosities. Composites prepared with premilled Al, ApC- and ApCp, have a greater specific surface area by about a factor of two compared to the corresponding materials prepared with as-received Al.

The analysis of the powder XRD patterns of the as-milled materials is somewhat tentative in that crystallite sizes and microstrain as determined from fitted peak profile parameters are correlated. The crystallite size reduction in CuO after premilling (Table

3.2, comparing ApC- to ApCp) is unambiguous and parallels the observed reduction in inclusion sizes (figure 3.5), but has little effect on the material's surface area or reactivity. Aluminum in materials where it was premilled show larger apparent crystallite sizes but also higher microstrain, probably reflecting the greater cumulative milling time. Reactivity is not expected to be significantly affected; strain relaxation and coarsening in milled/mechanically alloyed materials have weak thermal effects and occur at lower temperatures than the peaks observed in the DSC measurements here [81].

The reactive behavior of the materials as judged from thermal analysis and corresponding phase analysis suggests that premilling Al has a stronger effect than premilling CuO. Materials prepared with premilled Al consistently show a diminished thermal effect at the low-temperature onset, a distinct thermal effect near 600 K (peak 1), and a shift of the strongest peak (peak 2) to lower temperatures. The mass loss occurring simultaneously with peak 1 is greater if Al is premilled. XRD phase analysis of samples of the material prepared with premilled Al (ApC-) that were recovered from intermediate temperatures (figure 3.9) shows that DSC peak 1, when it is observed, is associated with the formation of Cu_2O . This is consistent with previous observations of reduction of CuO in 8Al·3CuO composites prepared in hexane-acetonitrile mixtures [82]. There, evolved gas analysis showed that the strong DSC peak near 600 K correlated with release of CO_2 , which was explained by the reduction of CuO to form Cu_2O by the argon atmosphere in the DSC and the ensuing reaction of the produced oxygen with residual carbon in the material that was introduced by the PCA during milling. A mass balance shows that in an ideal 8Al·CuO composite reduction of CuO to Cu_2O with no other reaction leads to a mass loss of 5.3 %, and a proportional loss of carbon in the form of CO_2 leads to a mass loss of 7.1 %. The

mass losses observed here (see table 3.3) therefore suggest that reduction of CuO by the atmosphere in the thermal analyzer occurs to a greater degree in the composites prepared with premilled Al. This is also consistent with the observed greater BET surface areas (figure 3.6) in that in the denser composites prepared with as-received Al, A-C- and A-Cp, less CuO surface is exposed to the environment, and therefore less oxygen is lost to the gas phase.

XRD phase analysis estimates show a reduced Al-Cu balance in the as-milled materials prepared with premilled Al (table 3.2), suggesting the presence of X-ray amorphous Al phases. This could be in the form of a surface layer generated by the interaction of acetonitrile with aluminum during premilling [50, 76]. Previous work on 8Al·3CuO composites prepared in hexane-ACN mixtures showed that composites with a large surface area age more rapidly when exposed to air, suggesting that amorphous aluminum oxide formed when the materials were exposed to air prior to XRD data collection as an alternative cause of the decrease in observed Al. A future microscopic targeted surface analysis would be instrumental resolving this issue.

Phase analysis of the materials recovered after thermal analysis (figure 3.10) allows two principal observations. First, the apparent Al deficiency observed in the as-milled materials (table 3.2) persists after complete reaction: materials prepared with premilled Al have reduced $N_{Al}/(N_{Al}+N_{Cu})$ values. Second, these materials also show reduced Cu present in the form of more Cu-rich Al-Cu intermetallics, particularly in comparison with the material prepared with as-received Al and CuO. As compositional equilibration across the material, governed by diffusion, takes time, and as the materials were exposed to the temperatures of the DSC heating program for relatively short times, the amount of Al-Cu

intermetallic phases other than Al_2Cu can be interpreted as semiquantitative indicator for the degree of contact between the components. The fully dense material prepared from unmilled Al and CuO, A-C- has CuO fully embedded in Al with minimal porosity and exposure of CuO to the environment. The reduction of CuO occurs at the same rate as the (inferred) oxidation of Al. Any Cu reduced to the metallic state is in immediate contact with the remaining Al, and reacts to form Al_2Cu as the predominant intermetallic product phase. This leads directly to the observation of the endothermic peak at about 808 K, consistent with the Al- Al_2Cu eutectic [80].

Conversely, materials prepared with premilled Al, ApC- and ApCp, both with high surface areas and apparent Al deficiencies, show larger amounts of the more Cu rich Al_3Cu and AlCu phases. Here, some of the oxygen generated by the reduction of CuO, and at higher temperatures of Cu_2O , enters the gas phase, and reacts with the available Al via its growing surface oxide layers. The reduction of CuO forming Cu_2O is endothermic by about 141 kJ per mole of oxygen [83] while the oxidation of Al is strongly exothermic. DSC peak 1 is exothermic, indicating Al is oxidizing. However, it is preceded by a very weak endothermic feature, most visible for the material where only Al is premilled, ApC- (figure 3.8), suggesting that CuO reduction via the gas phase precedes Al oxidation. The metallic Cu forming as the final product of the copper oxide reduction has less contact area with the remaining Al, and the compositional equilibration of the intermetallic products is slower. The endothermic peak of the Al- Al_2Cu eutectic is not observed because the metallic phase is more Cu rich than Al_2Cu . Aluminum still oxidizes, and the bulk of the reaction observed by thermal analysis still occurs at a lower temperature than in the fully dense material (A-C-) because of the increased Al surface area available for reaction. Nevertheless, the greater

mass loss and the phase composition of the products suggest that more of the reaction occurs in pore spaces via the gas phase.

The observed activation energies for (table 3.4) can only be systematically compared for peak 2, occurring in all materials. Here, premilling Al appears to increase the activation energy, while premilling CuO appears to decrease it. The increase can be explained by the increased reaction barrier if the oxygen transport from the copper oxides to the metallic Al proceeds via the gas phase in addition to the developing surface oxide layers. The cause of the apparent decrease if CuO is premilled is not clear.

The ignition temperatures of the denser composites prepared with unmilled Al (A-C- and A-Cp) are relatively higher, and not affected by the heating rate, suggesting that for those materials, ignition may be caused by a phase change without thermal activation. The observed ignition temperatures for A-C- and A-Cp near 1000 K exceed the Al melting point of 933 K, however, making it unlikely that the phase transition leading to ignition is Al melting.

The double ignition observed for ApC- and ApCp at lower heating rates suggests that a portion of the powder could be ignited by the same exothermic reaction causing DSC peak 1, i.e., reduction of CuO to produce a more oxygen-rich gas phase in the material's porosity, which then reacts with the increased Al surface area. The remainder of the powder could ignite as a result of the higher temperature phase transition. This assignment of reactions causing ignition in the prepared composites is preliminary; a more detailed and quantitative analysis of the results would be needed to validate this assignment, which is beyond the scope of this experimental study.

3.6 Conclusions

Premilling powders of Al and CuO in acetonitrile effectively reduces particle sizes and likely adds a nitrogen bearing surface layer to the produced powders, which affects their mechanical and chemical properties. Premilling Al yields fine flake particles, while equiaxial refined particles are formed by premilling CuO. Milling such premilled powders together using hexane as a process control agent yields composites with a reduced scale of mixing and properties distinct from those prepared by ARM using as-received starting materials. Composite thermite powders prepared by ARM using premilled Al do not form fully dense composite particles. Instead they form porous agglomerates, in which components are refined on the nanoscale. Release of oxygen from decomposing CuO and ensuing redox reaction via the gas phase becomes significant in these materials. In the fully-dense thermites prepared without premilling Al, the redox reaction occurs in the condensed phase and begins at lower temperatures. Premilling CuO does not prevent formation of fully dense composite powders, but increases dispersion of CuO inclusions in the resulting composites. In materials prepared from both, premilled Al and premilled CuO, some Al oxidizes via the gas phase in the particles' pore space, but the material is also more homogeneous than if CuO is not premilled, improving reactivity. Aluminum oxidation via the gas phase leads to ignition if Al is premilled. If aluminum is not premilled, a higher temperature phase transition likely leads to ignition in fully-dense powders. At higher heating rates, that transition may trigger ignition for all materials.

CHAPTER 4

LOW TEMPERATURE EXOTHERMIC REACTIONS IN Al-CuO NANOTHERMITES PRODUCING COPPER NANODOTS AND ACCELERATING COMBUSTION

4.1 Abstract

Several Al-CuO nanocomposite reactive materials, prepared recently by arrested reactive milling were found to exhibit a distinct low-temperature exothermic peak around 600 K seen by differential scanning calorimetry. This work is an experimental study aimed to establish whether this low-temperature reaction affects combustion and why it is observed in some but not all materials with identical compositions. The peak is only observed when aluminum is initially separately milled in acetonitrile. Electron microscopy showed resulting composite powders to be porous unlike fully-dense powders obtained without pre-milling aluminum. As-prepared and partially reacted powders recovered after heating just past the peak to 650 K were examined using high-angle annular dark-field scanning transmission electron microscopy and electron energy loss spectroscopy. Additionally, x-ray diffraction measurements were performed for all materials. Finally, the reactive powders were ignited using plasma and shock generated by an electrostatic discharge. Results show that the low-temperature exothermic peak is associated with a redox reaction pathway involving release of oxygen by CuO that is not in direct contact with Al and free-molecular transport of that oxygen to nearby surface of Al. This reaction pathway inhibits formation of Al-Cu intermetallic phases. Instead, nanometer-scale metallic Cu particles are formed due to CuO reduction. It is also found that this reaction pathway accelerates ignition of reactive powders, which in turn leads to a higher burn rate of aerosolized powder.

4.2 Introduction

Al/CuO nanothermites have been the subject of many recent studies because of their high energy density and transient gas combustion products attractive for many applications in pyrotechnics and other energetic formulations [1, 8-10]. Different preparation methods, including mixing nanopowders [84], electrospray assembly [26, 30, 85], vacuum layer deposition [86-90], electro-chemical synthesis [91], sol-gel processing [92], self-assembly [93-95], and arrested reactive milling (ARM) [72, 73] were used to prepare such thermites, in which Al and CuO are mixed at the nano-scale. Despite similar scale of mixing, different methods (or even different variants of the same method) yield materials in which interfaces between reactive components have different structures and characteristics. Such differences are expected to affect ignition and combustion of the nanothermites; thus, modifying reactive interfaces could be an effective way of controlling reactions in nanothermites even if their chemical compositions remain the same [96-98].

Vacuum layer deposition offers the most ordered (often planar) interface structures and direct methods of tuning chemical properties of the produced interfaces, i.e., by altering the sequence in which the layers are grown or by embedding sublayers or inclusions [99, 100]. For example, nano-inclusions of gold resulted in corrugated layers and altered the redox reaction [100]. Differential Scanning Calorimetry (DSC) showed an unusual, distinct low-temperature exothermic peak around 600 K. It was attributed to accelerated decomposition of CuO in the presence of surface defects at the CuO/Al interface. A similar low-temperature exothermic peak was reported for vacuum-deposited Al/CuO nanofoils when a thin intermediate Cu layer was added [101]. In the latter case, the Cu layer was thought to prevent evaporation of Cu during combustion, but was proposed to not offer a

substantial obstacle for gaseous oxygen formed during CuO decomposition. In related work, it was observed that the process control agents (PCA) used for ARM, such as stearic acid, hexane, or acetonitrile affect the reactive behavior of nanocomposite powders prepared by ARM [22, 46, 102], likely by altering the interface properties. In a recent study [103], nanothermites with 8/3 molar Al/CuO ratio, (equivalence ratio 4) were prepared by ARM with hexane serving as PCA while using Al and/or CuO powders preliminarily milled in acetonitrile. Like for the modified nanofoils [100, 101], DSC traces for some of these composite powders showed distinct exothermic reactions near 600 K. This reaction was only observed for nanothermites using Al powder that was pre-milled in acetonitrile. In materials prepared with as-received (not pre-milled) aluminum, the low-temperature reactions are represented by a broad, relatively flat signal with no peak around 600 K; additionally, an endotherm indicative of Al-Al₂Cu eutectic is observed before the main redox reaction occurring at ≈ 850 K. These previous results for $x\text{Al}-y\text{CuO}$ (x and y representing respective mole parts) nanofoils and nanocomposite powders are summarized in figure 4.1. It was also reported that the nanocomposite powders exhibiting the low-temperature DSC peak ignited at a reduced temperature when coated on an electrically heated wire [103].

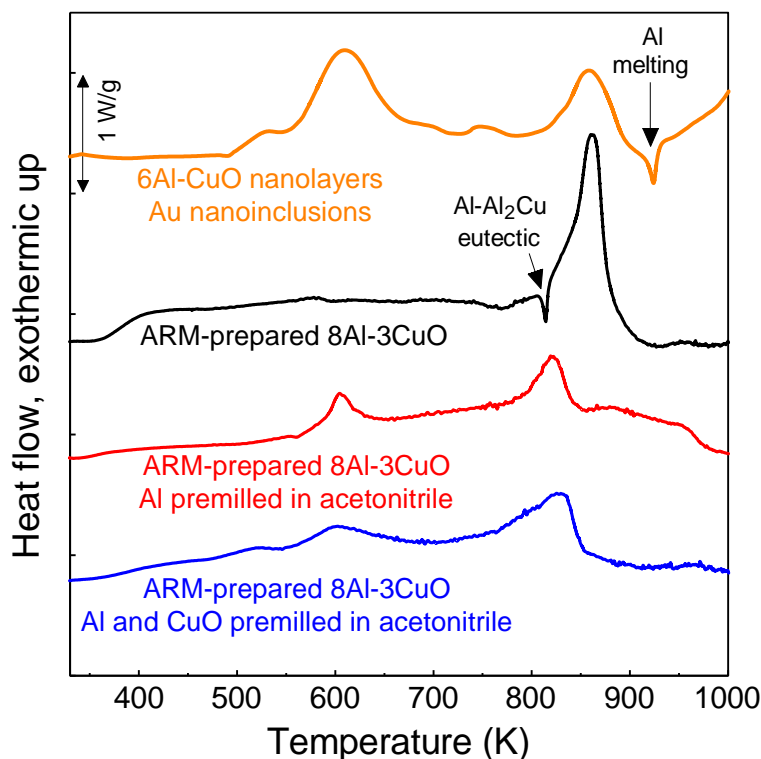


Figure 4.1 Previously reported DSC curves for Al/CuO nanofuels with Au nano-inclusions (top curve, equivalence ratio 9, heating rate 20 K/min) and Al/CuO nanocomposite powders prepared by ARM, bottom three curves (equivalence ratio 4, heating rate 5 K/min).

Sources:

Julien, B., et al., Integration of Gold Nanoparticles to Modulate the Ignitability of Nanothermite Films. ACS Applied Nano Materials, 2020

Mursalat, M., M. Schoenitz, and E.L. Dreizin, Effect of premilling Al and CuO in acetonitrile on properties of Al-CuO thermites prepared by arrested reactive milling. Combustion and Flame, 2020

The goal of the present study is to determine whether the low-temperature exothermic reactions detected in the nanothermites with altered interfaces prepared by ARM affect their bulk burn rates. It is further of interest to understand the nature of the low-temperature exothermic reactions observed when aluminum pre-milled in acetonitrile is used to prepare the nanocomposite powders. To that end, it is necessary to characterize the reaction products generated by these unique low-temperature exothermic process.

4.3 Experimental

4.3.1 Reactive Composite Powder

Materials used in this work, 8Al·3CuO powders (respective 8/3 mole ratio), are the same as prepared in Ref. [103]. Briefly, -325 mesh 99.5% pure aluminum (Atlantic Equipment Engineers), and 10 μm , 99+% pure copper (II) oxide (Sigma–Aldrich) served as the starting components. PCA were either 95% pure hexane (Alfa Aesar) or 99.5% pure acetonitrile by Alfa Aesar. A Retsch PM400 planetary mill operated at 350 RPM was used with custom-made 175-ml milling vials capable of withstanding high pressure that could develop in case of accidental mechanical initiation of the milled thermite. Powder load per vial was 30 g; 3/8 in (9.53 mm) hardened steel balls were used; ball to powder mass ratio was 3. A diagram illustrating the milling sequence used to prepare powders is shown in figure 4.2. Aside from the powder prepared in 1 stage milling using as-received Al and CuO with 24 ml of hexane as PCA, referred to as A-C- (see dashed arrows in figure 4.2), two materials including pre-milled Al with as-received CuO (ApC-) and both pre-milled Al and CuO (ApCp) were prepared in two stages, including the initial milling step in acetonitrile. For each stage, the milling time was 60 min. After the first milling stage, the powders were dried in Ar for 24 h to remove any remaining acetonitrile. For the second stage milling, each vial was loaded with 14.25 g of Al and 15.75 g of CuO. All powders prepared for this study were stored in hexane.

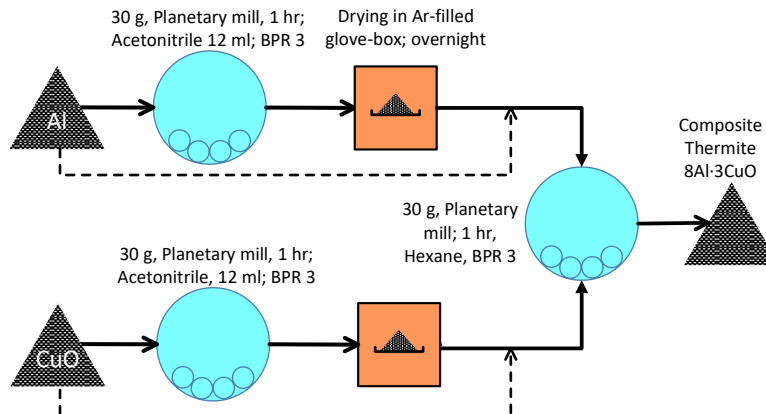


Figure 4.2 Two-stage milling procedure used to prepare nanocomposite thermite powders with pre-milled Al and/or CuO.

4.3.2 Material Characterization

Reactions occurring in the ARM-prepared nanocomposite thermite powders were characterized by differential scanning calorimetry (DSC) using a Netzsch STA409PC thermal analyzer. 15 to 20 mg of powders immersed in hexane were loaded in an alumina crucible in order to prevent oxidation in air. Upon loading the crucible in the analyzer, the liquid was allowed to evaporate in argon (Airgas, 99.98 %). Next, the furnace was evacuated and then flushed with argon three times before heating at 5 K/min under a 50 mL/min Ar flow.

Phase composition was determined by X-ray diffraction (XRD) on a PANalytical Empyrean multipurpose research diffractometer operated at 45 kV and 40 mA, with unfiltered Cu K α radiation ($\lambda = 1.5438 \text{ \AA}$). Phases were identified using the PDF-4+ database [104] and the tools built into the Highscore Plus software (version 3.0e) [59] for the whole-pattern refinement.

Morphology and chemical composition of the nanocomposite powders were analyzed by Transmission Electron Microscopy (TEM), Scanning Transmission Electron Microscopy (STEM) and Electron Energy-Loss Spectroscopy (EELS) using a JEOL cold-FEG JEM-ARM200F operated at 200 kV equipped with a probe Cs corrector reaching a spatial resolution of 0.078 nm. EELS data were acquired on a Gatan Imaging Filter Quantum (energy resolution of 0.3 eV) using a dispersion of 0.5 eV/channel, a collection semi-angle of 19.4 mrad and a convergence semi-angle of 14.8 mrad. The spatial resolution is estimated at 0.5 nm. STEM samples were prepared by ultramicrotomy, i.e., the powders were embedded in epoxy resin (MA2+, Presi) before being cut in 50 nm slices, placed in Ni hexagonal grids and then coated with a 20 nm carbon layer for analysis.

Electron Probe Micro-Analysis was also used to quantify the chemical composition of powders using a Cameca SXFive FE microprobe operated at low voltage (7 kV) to have a sub- μm X-ray generation volume. Quantitative analysis was accomplished by comparing the intensities of characteristic X-rays for elemental Al, Cu and O with respective intensities for standard natural minerals. For combustion tests, the ARM-prepared powders were ignited in air by the shock and plasma produced by an electrostatic discharge (ESD) initiated near the sample. The ESD was produced using a model 931 Firing Test System by Electro-Tech Systems, Inc. A 10-nF capacitor charged to 20 kV and discharged between two pin-electrodes set 1-mm apart served to generate the ESD. Precision point steel pins (0.9 mm diameter) by Super Steel Microground, Dritz, were used as electrodes. A detailed description of the set up can be found elsewhere [105]. A Photron FASTCAM Nova high-speed camera (type: 800K-M-8GB) operated at 50,000 fps with an exposure time of 20 μs was used to capture the images of the ignited powder. Each recorded video includes five

frames before the trigger signal and 4995 frames after the trigger, providing a time span of 100 ms. The camera was operated with a 0.7 – 4.5 x Zoom Monocular lens by Hayear Corp. Ltd. An FL532-10 laser line filter by Thorlabs, ensuring only the passage of 532 ± 10 nm wavelength, was used to avoid saturation and to protect the image sensor in the camera. The camera was triggered by a pulse from an induction coil by Pearson Electronics (model 110A) measuring the ESD current.

The composite powder was placed in a recession in a 1.6-mm thick aluminum alloy (6061-T1) plate (by McMaster-Carr) about 1 mm below the pin electrodes. The recession with approximately 2.6 mm length, 0.4 mm width, and 0.4 mm depth was made on the plate by hammering a flat-tip screwdriver onto its surface. Approximately 3 – 4 mg of the powder were loaded into the recession with a spatula. Using the tip of the spatula, any large loose agglomerates were broken. The powder surface was then flattened and excess powder removed with a glove-covered fingertip.

4.4 Results

4.4.1 Combustion

Combustion of the differently prepared nanocomposite thermites (A-C-, ApC-, ApCp) exposed to the shock and plasma produced by ESD includes events that are qualitatively similar to those reported recently for zirconium powder, ignited using the same method [106]. For all powders, weak emission from igniting particles initiates effectively immediately. A much stronger combustion event is observed following a substantial delay on the order of 1 ms. Example sequences of the recorded high-speed videos are shown in figure 4.3. The images were taken every 20 μ s; only selected images are shown for each experiment. For each powder, at least five combustion runs were recorded and examined.

Differences in the emission produced by the initial (instant) flame immediately following the ESD are difficult to discern among different powders. However, differences in the dynamics and appearance of the delayed flames are clear. For A-C- powder, the flame appeared after a longer delay and existed longer than for either ApC- or ApCp powders. For the latter two powders, a faster flame propagation is also noted based on the recorded videos. Many individual particle streaks are observed for the flame produced by A-C- powder, whereas almost no such streaks is noted for either ApC- or ApCp powders. Flames produced by ApC- and ApCp powders comprise rather uniform central core and diffuse cloud with a sharp boundary, suggesting substantial gas release. A luminous cloud suggesting gas release can also be distinguished at later times for the A-C- powder flame; however, its boundary is fuzzy.

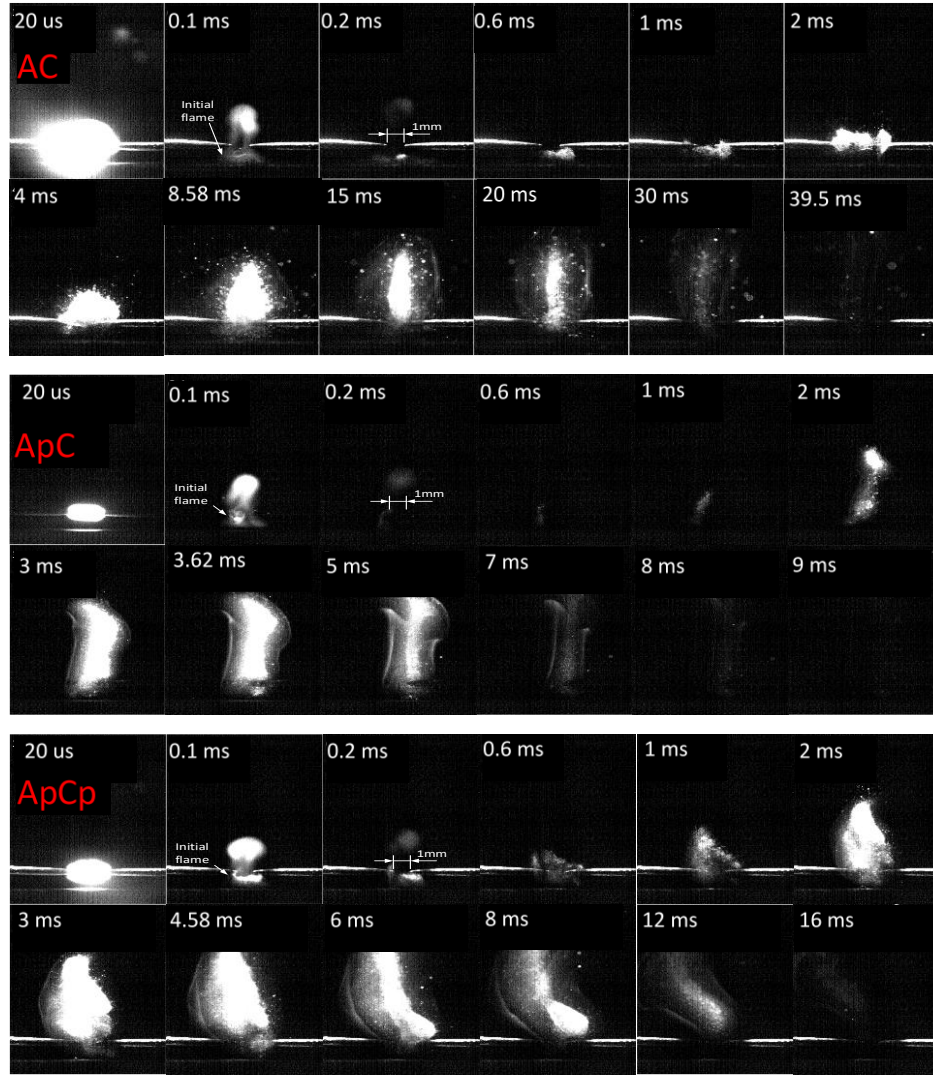


Figure 4.3 High-speed video frames showing the ESD-induced combustion of powders A C , ApC and ApCp on an aluminum substrate 1 mm below the electrode gap.

To quantify the differences between combustion characteristics of different powders, the total emission intensity for each video frame is integrated over the entire field of view. Such integral intensity values are shown in figure 4.4 as a function of time and clearly show the development of the delayed flames. The initial decay, largely similar for all powders is mostly caused by the diminishing emission produced by the plasma kernel associated with ESD. The characteristic time for such a decay is 200 μ s. A larger peak

appearing with ms delay is produced by the delayed powder flame. This peak appears later and lasts longer for A-C- powder compared to the peaks produced by burning ApC- and ApCp powders. Thus, the powders exhibiting a distinct low-temperature exotherm in their DSC traces (figure 4.1) also ignite sooner and burn faster.

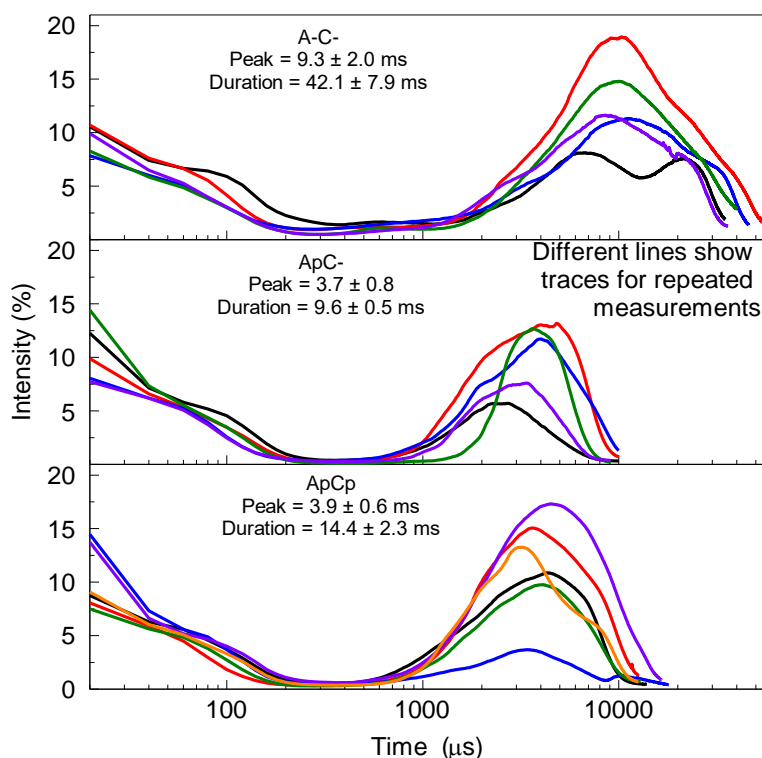


Figure 4.4 Integrated time-resolved emission traces obtained by processing the high-speed video frames for different powders A-C-, ApC-, ApCp.

The video frames were further processed to identify the flame height using image binarization [107]. For each tested powder, the flame height profiles were averaged among 5 tests. The results are shown in figure 4.5. The flames propagate fastest for ApCp, followed by ApC- and then by A-C-.

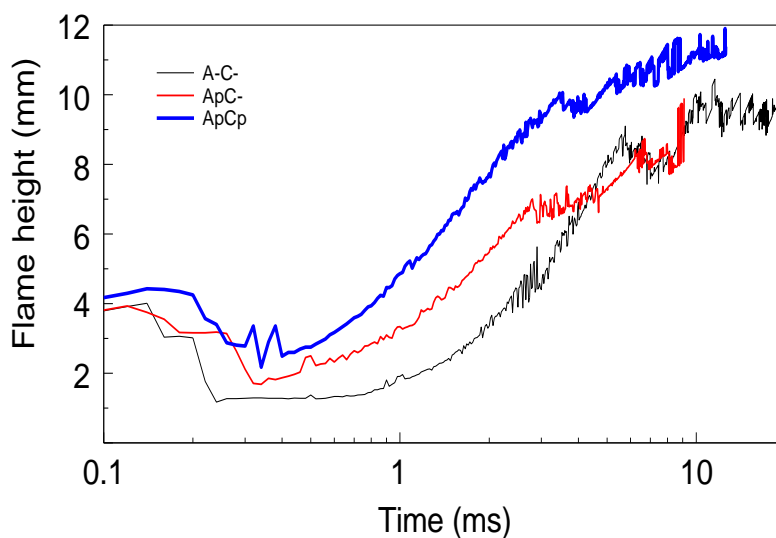


Figure 4.5 Time-resolved flame height profiles of A C , ApC and ApCp powders combustion by ESD. Each profile was average among at least five repetitions

The ignition and combustion results clearly indicate that pre-milling Al has an effect on the reactive behavior of the Al/CuO nanocomposite powders. Powders prepared with pre-milled Al initiate sooner and burn faster than those made with regular Al, indicating a correlation between the low-temperature exothermic reaction and higher burn rates.

4.4.2 Morphology and Phase Characterization of Composite Powders

To determine how using pre-milled Al to prepare the nanothermite affects the low-temperature exothermic reaction, the morphology, microstructural and chemical features of the different Al/CuO nanocomposite powders were investigated. A-C-, ApC- and ApCp powders were heated in the thermal analyzer to 650 K (end of the low-temperature exotherm, cf. figure 4.1) under argon at a rate of 5 K/min (same conditions as DSC experiments) and recovered. As-prepared and partially reacted powders were further

analyzed using XRD and STEM. When necessary, complementary elemental compositions of powder phases were quantified using an electron microprobe.

4.4.2.1 Bulk Composition of the As-prepared and Partially Reacted Powders.

The XRD patterns for all as-prepared powders are shown in Figure 3.7 (Chapter 3). They look qualitatively similar to one another with major peaks corresponding to aluminum and tenorite (a polymorph of CuO). Although amorphous Al_2O_3 may be difficult to detect by XRD, no trace of reduced crystalline species, such as Cu_2O or Cu, were found, suggesting that any reaction occurring during milling is negligible. XRD patterns for partially reacted powders recovered from 650 K are shown in figure 4.6. Table 4.1 shows the compositions obtained from the whole pattern refinement. Cu_2O and Al_2Cu are the most abundant reaction products formed prior to 650 K. The amount of Al_2Cu in A-C- prepared without pre-milling Al is much higher than in other samples. The powder ApC- contains the greatest amount of unreduced CuO, which is readily understood considering that this material contains a relatively large number of CuO particles that are not in immediate contact with Al [103] (discussed later).

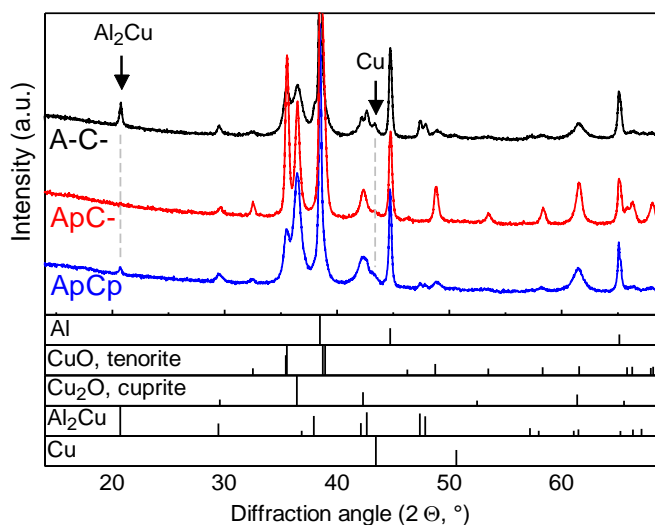


Figure 4.6 XRD patterns of ARM-prepared 8Al·3CuO thermite powders quenched from 650 K. The strongest peaks of Al₂Cu and Cu are indicated with arrows.

Table 4.1 Phase Composition in wt-% of Materials Recovered from 650 K

ID	Al	CuO (Tenorite)	Cu ₂ O (Cuprite)	Cu	Al ₂ Cu	Al ₄ Cu ₉	AlCu
A-C-	45.3	20.9	25.5	1.27	7.02	-	-
ApC-	39.0	37.6	21.6	1.34	0.20	-	0.21
ApCp	40.9	19.4	36.4	1.41	1.67	0.27	-

4.4.2.2 Near Surface and Interface Composition of the As-prepared and Partially Reacted Powders.

In complement to bulk XRD analysis, atomically resolved STEM-HAADF and STEM-EELS were performed in ARM-prepared powder with pre-milled Al and as-received Al, i.e. ApC- and A-C-, in as-prepared condition and after recovering from 650 K. EELS here is used to monitor the evolution of the oxidation state of Cu and Al oxides in order to

unravel the reaction pathway associated with the low-temperature exothermic reaction seen in ApC- powders. Hence, electron loss near edge structure (ELNES) of Cu $L_{2,3}$ -edges@932-953 eV, O K-edges at 532eV and Al K edges at 1560 eV were acquired on different zones near and across Al/CuO interfaces. EELS core loss edges were background subtracted using a power law fit before being plotted.

The ELNES of the Cu oxides in both A-C- and ApC- as-prepared powders is characterized by sharp and symmetric peaks at 932 eV L_3 ($2p_{3/2} \rightarrow 3d$) and 953 eV L_2 ($2p_{1/2} \rightarrow 3d$) lines which correspond to cupric oxide (figure 4.7). No CuO reduction is observed near surfaces for both as-prepared powders. Elemental composition quantified by electron microprobe confirmed EELS analyses: CuO phases are composed of 49 ± 1 % of O and 50 ± 1 % of Cu.

However, differences between Al-bearing phases are detected for samples prepared using as received and pre-milled Al. In A-C- powders, pure Al is detected (grey lines in ELNES spectra of figure 4.7a and 4.7b) and Al oxide is only present in contact with CuO, unlike ApC- powders in which Al is oxidized over a much thicker zone (≈ 30 nm measured in ELNES spectra of figure 4.7c). Quantification of the oxygen content in Al by the electron microprobe gave 9 ± 1 % of O and 91 ± 1 % of Al.

Finally, both as-prepared materials, A-C- and ApC- form interfacial layers made of atomic mixture of Al, Cu and O (yellow lines in spectra of figure 4.7).

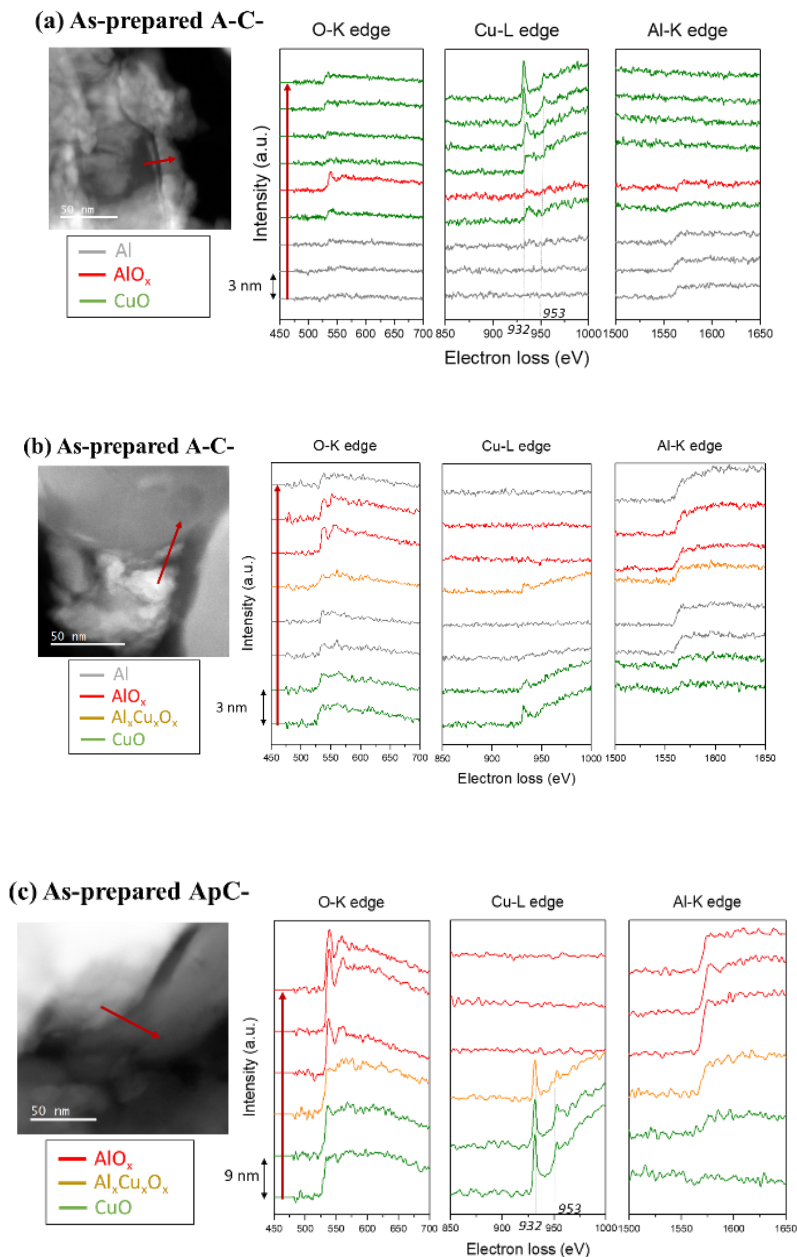


Figure 4.7 As prepared samples: Cross-sectional STEM-HAADF images and EELS spectra of Cu L2,3-edge, Al L2,3-edge and O K-edge acquired across (a) Al/CuO interface, and, (b) CuO/Al interface in A-C- (c) CuO/Al interface in ApC-. EELS spectra was acquired every 1 nm but plotted every 3 nm for (a), (b) and 9 nm for (c).

After heating to 650 K and respective partial reaction, there is a clear evolution in both microstructures and EELS signatures. The STEM-HAADF image of ApC- (figure

4.8) gives direct evidence of formation of copper dots (5 – 10 nm in dimension) in the AlO_x phase. The Cu-L_{2,3} edge spectra acquired across a dot (figure A.1 in Appendix A) confirms the sole presence of Cu. Neither oxygen nor Al are detected in the dots.

In contrast, in these analyses targeting surfaces of the particles for partially reacted A-C- powders, no pure copper but cuprous oxide is detected (figure 4.9a) close to AlO_x zones. Looking in detail at the interfacial zone, pre-edge O K peaks at 530 eV were observed (figure 4.9b) which reveal the presence of gaseous oxygen that could have liberated from the decomposing CuO upon heating and accumulated at the interface [108]. Finally, we also see in quenched A-C- the growth of an intermetallic phase (yellow lines in ELNES spectra of figure 4.9b) which is consistent with both XRD (figure 4.6) and DSC analyses (figure 4.1, presence of the endotherm at ≈ 820 K).

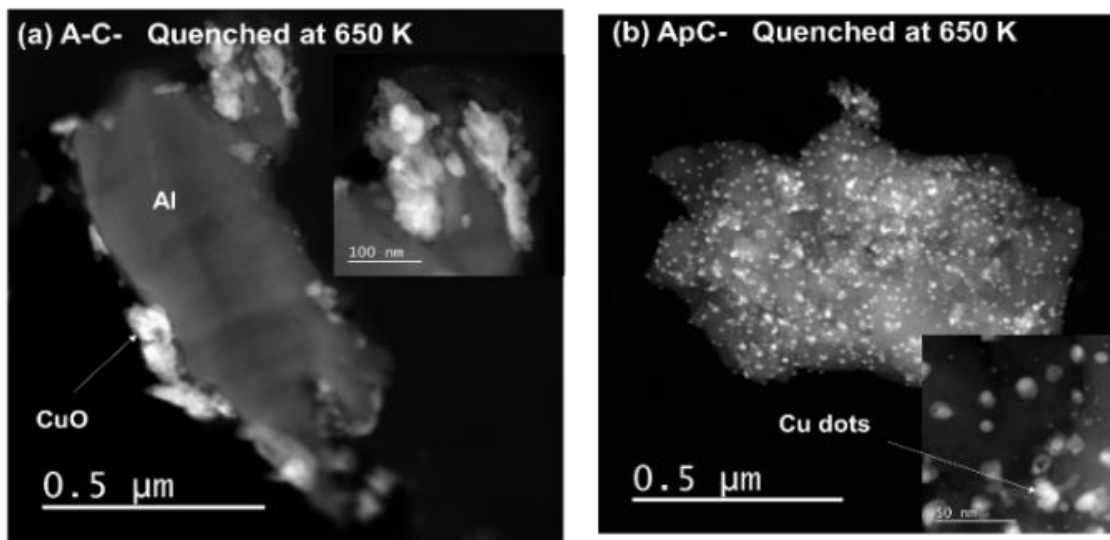


Figure 4.8 Samples heated to and recovered from 650 K: Cross-sectional STEM-HAADF images of A-C- and ApC- materials. The insets in (a) and (b) shows a magnified view.

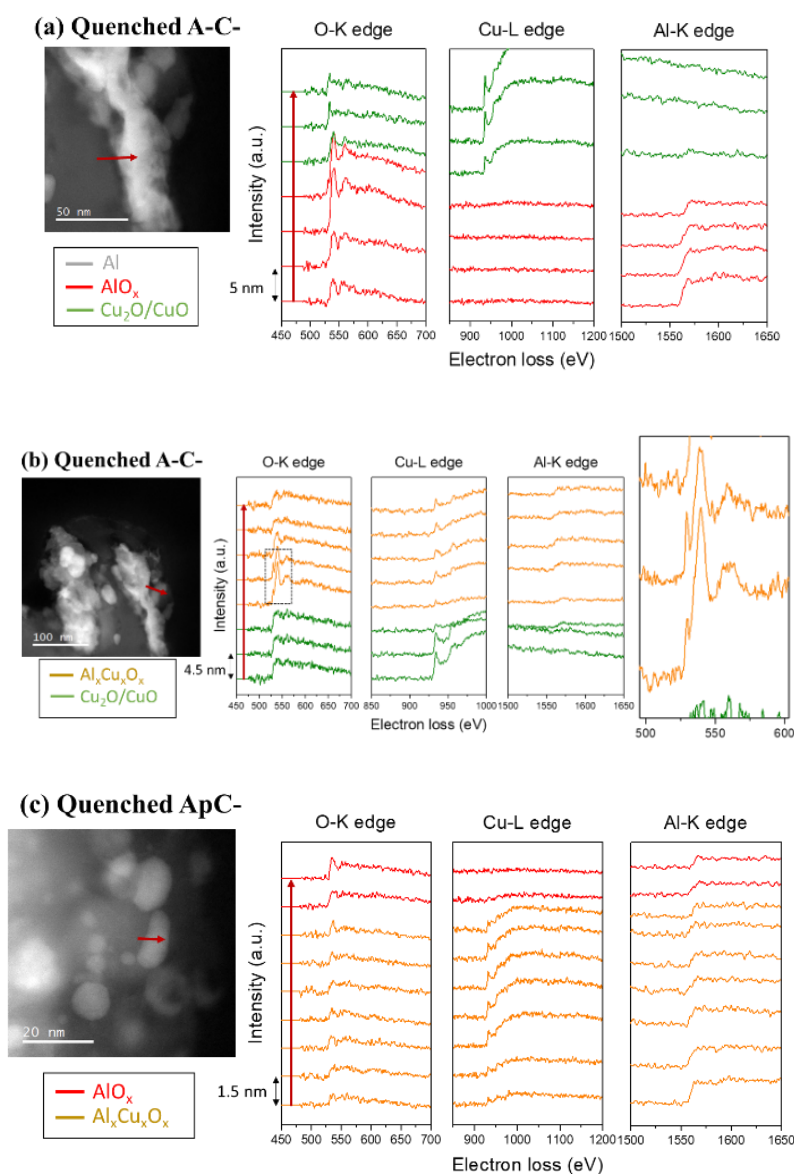


Figure 4.9 Samples heated to and recovered from 650 K: Cross-sectional STEM-HAADF images and ELNES spectra of Cu L2,3-edge, Al L2,3-edge and O K-edge acquired across (a) $\text{AlO}_x/\text{Cu}_2\text{O}$ in quenched A-C-, (b) $\text{Cu}_2\text{O}/\text{AlO}_x$ interface showing a pre-edge O K peak at 530 eV in quenched A-C-, and, (c) across a ApC zone being reacted. EELS spectra was acquired every 0.5 nm but plotted every 5 nm, 4.5 nm, and 9 nm for analysis (a),(b) and (c), respectively.

4.5 Discussion

Differences in the morphology of the Al/CuO interface induced by pre-milling Al in acetonitrile were observed to affect the low-temperature reaction mechanism in the nanocomposite thermites and subsequent reactivity. To interpret the present results, it should be first recognized that a continuous range of interfaces with different structures is present in all nanocomposite prepared by ARM. Scanning electron microscopy results reported elsewhere [103] consistently with the present STEM work suggest a near full-density mixing between Al and CuO for A-C- powders, whereas fully-dense composite structures are combined with porous particles in ApC- and ApCp powders. This is confirmed by cross-sectional STEM images of the as-prepared powders (figure A.2, Appendix A) showing differences in reactant intimacy and CuO distribution when Al is pre-milled: CuO and Al are mixed intimately in A-C- powders whereas porosity is observed in ApC- powders with Al and CuO separated from each other. The presence of these nano-voids between Al and CuO phases modifies the low-temperature reactions pathway as evidenced by DSC and supported by STEM-EELS results (Sec. 3.2). Paradoxically, separation of Al and CuO by nano-voids forming in ApC- and ApCp powders accelerates the low-temperature reaction and leads to the complete reduction of CuO to metallic Cu (yielding the observed Cu nanodots), at least close to the particle surface. The mechanisms of such reactions are qualitatively discussed below.

In a fully-dense nanocomposite, reaction occurs at the CuO/Al₂O₃ interface and is controlled by diffusion of ions of Al through the growing layer of Al₂O₃ as was proposed earlier [71]. Indeed, transport of Al directly to CuO explains the formation of greater amounts of Al₂Cu detected in the products (figure 4.6 and table 4.1) and the eutectic

melting peak observed only for the A-C- material in figure 4.1. Counter-diffusion of oxygen from decomposing CuO must be slower. If the reaction occurred at the Al/Al₂O₃ interface, Al and Cu would always be separated by a layer of Al₂O₃ preventing formation of the alloys. The schematic diagram in figure 4.10a shows the discussed above reaction in fully-dense composites. For simplicity, such composites are shown as planar layers. Initially, CuO is reduced to Cu₂O, as supported by STEM-EELS (figure 4.9a and 4.9b) which detect cuprous oxides and gaseous oxygen trapped near Al/CuO interface in A-C- powders after partial reaction and recovery from 650 K. Continuing reaction causes formation of Al-Cu intermetallic inclusions along the Al₂O₃/Cu₂O interface (observed in STEM-EELS diagrams in figure 4.9b). This is the proposed reaction scenario for the fully dense A-C- powders.

The same reaction can occur in ApC- and ApCp powders for the part of the material, in which CuO is in intimate contact with Al. However, because part of CuO is separated from Al (or Al₂O₃ covering Al surface), as shown in figure 4.10b, an alternative reaction pathway becomes available. The schematic simplifies the structure, assuming it to be similar to that of the fully-dense material, but including parts of CuO surfaces that are not in contact with Al or Al₂O₃. Clearly, different geometries are possible having the common feature of CuO surface slightly removed from Al. Upon heating, CuO begins to decompose releasing oxygen. This oxygen must be transferred through the voids to nearby surfaces of Al₂O₃. It then can react with Al ions diffusing outward, to the Al₂O₃/gas interface [109]. If such reaction continues, the CuO domain that released oxygen can be reduced to metallic Cu, completely avoiding formation of Al-Cu intermetallics. This can explain formation of multiple Cu nanodots embedded into alumina observed to form by 650 K on the surface of

both ApC- and ApCp powders (figure 4.8 and figure A.3 in Appendix A), which include significant portion of CuO that is not in direct contact with Al. The rate of the reaction described here depends on how fast oxygen released by CuO can be transported across the void separating it from Al. In the present materials, such voids have dimensions of 10 – 100 nm, which is comparable or less than the mean free path of the gas molecules at the temperatures of interest. Thus, gas phase diffusion is not a factor affecting the reaction rate. Instead, oxygen released by decomposing CuO is transported in the free molecular regime to Al ions at the surface of Al₂O₃, where it is immediately consumed. In this case there exists effectively no gas phase, which helps accelerate decomposition of CuO.

As noted above, the morphology illustrated schematically in figure 4.10b is just an example; any CuO particle or inclusion having an exposed surface in the vicinity of Al can be precursor to one or more Cu nanodots. Based on the present experimental observations, it is proposed that the redox reaction occurring via release of oxygen from CuO that oxidizes Al at the nearby exposed Al₂O₃ surface explains formation of the low-temperature peak observed in figure 4.1. No gaseous oxygen was detected in STEM-EELS of quenched ApC- powders, suggesting that all such oxygen released in the voids reacted readily upon adsorbing to Al or Al₂O₃ surface. This is consistent with the STEM-EELS analysis shown in figure 4.7c which reveals slightly oxidized aluminum (8 % O and 92 % Al) in ApC- near Al/CuO interface. Conversely, observed traces of gaseous oxygen for A-C- suggest that Al is oxidized at the Al₂O₃/CuO (or Cu₂O) interface, and not at the Al₂O₃ part exposed to gas (where there is no nearby decomposing CuO surface).

The proposed reaction mechanism involving free-molecular transport of oxygen released by CuO into nano-voids may be dominant, at least at low temperatures, for

powders containing CuO and Al₂O₃ surfaces that are not in direct contact with each other while the separation between such surfaces remains sufficiently small. The predominant nature of such reaction is consistent with the STEM observations suggesting the presence of Cu₂O near the surface of the A-C- powders, but only detecting elemental Cu for the ApC- powders (STEM-EELS spectra in figure 4.9). Oxygen leaving the condensed phase, and entering the pore space in measurable quantities is further supported by previous observations of oxygenated gas release near 600 K observed by thermogravimetry with coupled mass spectrometry in similar 8Al-3CuO nanocomposites prepared by a related ARM technique [82].

Because separating CuO from Al removes the kinetic pathway enabling formation of intermetallics, it leads to a reaction producing only Al₂O₃ and Cu, which is more thermodynamically favored compared to that producing additionally Cu₂O and Al-Cu intermetallics. On the other hand, this reaction may begin at a higher temperature, because it requires release of oxygen by CuO. Conversely, in fully-dense systems, Al diffusing to CuO may begin reacting directly with condensed CuO before any oxygen is released. Thus, when the temperature is sufficiently high for CuO to begin releasing oxygen, the reaction that started earlier in the fully-dense systems may have led to growth of a thicker alumina layer (see reaction for A-C-, schematically represented by figure 4.10a) compared to the case with CuO separated from Al. A thicker alumina layer in the fully-dense thermites thus serves to slow down the reaction at higher temperatures, when release of gas oxygen by CuO begins. Conversely, the lack of very low-temperature condensed phase reaction in materials containing nano-voids leads to a greater redox reaction rate when the temperature

increases to trigger release of oxygen by CuO. This explains a relatively sharp peak observed for such materials in DSC (figure 4.1).

The same mechanism can also be applied to describe the low-temperature exothermic reaction observed in Al/CuO nanolayers with embedded gold nanoparticles (see figure 4.1) [100]. Indeed, it was observed that multiple defects were formed around such nanoparticles upon heating, causing voids around the Al/CuO interface. It is proposed here that the presence of voids generated due to heating of a corrugated interface led to separation of Al (and growing Al_2O_3) from CuO, thus prompting release of gaseous oxygen reacting with Al. Interestingly, Cu nanodots were not detected in Ref. [100], where electron microscopy was done with cross-sectioned multilayered structures, making it difficult to resolve the nanodots that might have formed on the surface of growing voids.

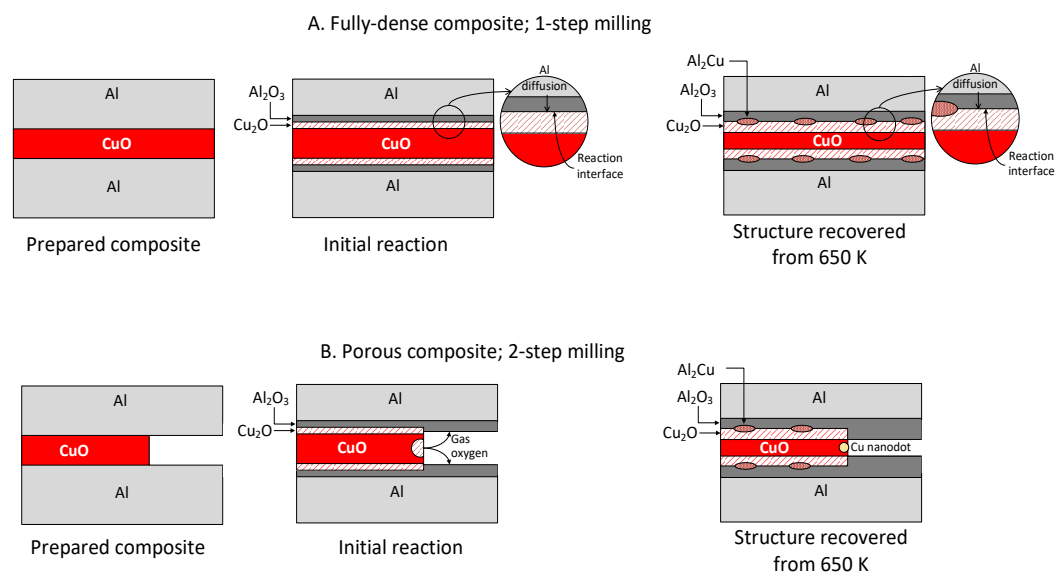


Figure 4.10 Schematic diagram illustrating the low-temperature redox reactions and formation of products in materials with different initial morphology.

It is further interesting that the low-temperature reactions detected in DSC measurements and causing formation of Cu nanodots discussed above appear to affect

combustion of the nanocomposite powders, as implied from the reported experiments (figures 4.3-4.5). Both qualitative differences in the flame appearance and quantitative differences in the flame propagation and the bulk burn rate suggest that the low-temperature reactions lead to an accelerated ignition and faster combustion. Because combustion of these Al-rich thermites involves much higher temperatures (typically, >2000 K) than those relevant to the discussed exothermic reactions, it is suggested that the observed bulk effect on the burn rate is due to an earlier ignition of the composite particles. An earlier ignition accelerates the heat release, which, in turn can further accelerate combustion of the aerosolized powders tested here. In other words, the effect is unlikely to be detectable when single particle burn times are measured in experiments, in which combustion of each particle occurs independently. Conversely, for collective combustion of multiple interacting particles, the acceleration of the bulk burn rate can be significant.

4.6 Conclusions

In this work, atomically resolved STEM-HAADF and STEM-EELS were performed on reactive nanocomposite powders prepared by ARM using Al pre-milled in acetonitrile, and unmodified Al. As-prepared and partially reacted materials were analyzed in order to unravel their low-temperature reaction pathway. In the fully-dense material prepared with unmodified Al, the reaction occurs at the $\text{Al}_2\text{O}_3/\text{CuO}$ interface where gaseous oxygen is trapped after CuO decomposition. This causes the formation of Al-Cu intermetallic inclusions along the $\text{Al}_2\text{O}_3/\text{Cu}_2\text{O}$ interface. When Al is pre-milled in acetonitrile, the prepared Al/CuO powders contain nano-sized pores. Separating Al and CuO phases modifies the reaction pathway involving the formation of gaseous oxygen by reduced CuO

that is not in direct contact with Al. The generated gaseous oxygen moves, in free-molecular regime, through the nano-voids to nearby surfaces of $\text{Al}_2\text{O}_3/\text{Al}$ grains where it and reacts with Al diffusing outward through the formed oxide layer. The reaction continues i.e., the CuO domain around the voids is reduced to metallic Cu. Thus, somewhat unexpectedly, introduced small separation between Al and CuO removes the kinetic pathway enabling formation of Al-Cu intermetallic phases as byproduct of the redox reaction. This leads to a more thermodynamically preferred scenario yielding only Al_2O_3 and Cu. This reaction triggered by release of oxygen by CuO begins at slightly higher temperatures than that proceeding in the fully-dense phase with Al reaching CuO directly by diffusion through Al_2O_3 . Because the redox reaction in the material containing nano-voids is delayed to higher temperatures, once started, it proceeds faster because of a thinner pre-existing layer of Al_2O_3 . This explains the relatively sharp low-temperature exothermic peak observed by DSC of Al/CuO powders prepared with Al pre-milled in acetonitrile. Once such reaction pathway is enabled, the ignition delays of reactive material particles are reduced and the bulk burn rate increased. This work emphasizes the major role of the interface structure between reactive components in controlling reactions in nanothermites.

CHAPTER 5

COMPOSITE Al-Ti POWDERS PREPARED BY HIGH ENERGY MILLING WITH DIFFERENT PROCESS CONTROL AGENTS

5.1 Abstract

Aluminum rich Al-Ti composite powders were prepared by mechanical milling using different polar (acetonitrile, stearic acid) and non-polar (hexane) hydrocarbon process control agents. Stearic acid was introduced at the initial stage of milling in order to prevent caking. Hexane and acetonitrile were introduced in a 2nd milling stage. Particles agglomerated for powders processed with hexane or a hexane-acetonitrile mixture, while particles were finer and remained dispersed when milled with acetonitrile. X-ray diffraction did not identify intermetallics in the prepared composite powders comprising elemental Al and Ti. Differential thermal analysis showed low-temperature exothermic events assigned to the formation of intermetallics; such events started at a lower temperature for the composite prepared using acetonitrile in the second milling stage. Ignition experiments showed lower ignition temperatures (below the Al melting point) for powders milled with acetonitrile in the second stage, compared with powders prepared using stearic acid during both first and second milling stages. All composite powders ignited at a much lower temperature than pure aluminum. Constant volume explosion tests showed a higher energy release rate with comparable energy content compared to the reference fine spherical aluminum powder. Staged milling with increasingly polar process control agents, introduced in this work, suggests a viable method to control particle size distributions in mechanically milled, metal-based energetic composite powders.

5.2 Introduction

Aluminum, owing to its high combustion enthalpy, has garnered a great deal of interest as a high energy density fuel additive for propellants. In a common solid propellant, aluminum particles are mixed with ammonium perchlorate (AP) and an elastomeric binder. Upon heating of such materials, the binder melts and AP is gasified, while aluminum particles tend to melt and form large sized agglomerates prior to ignition [110-112]. Such large agglomerates may encounter very long ignition delays or may even remain completely unburned [110, 113, 114]. Hence, reducing agglomeration of aluminum powders becomes vital for enhancing propellant efficiency. Agglomeration can be reduced if metal particles ignite at lower temperatures. In turn, ignition temperatures can be reduced if pure aluminum is substituted by some of its alloys [3, 111, 115]. Al-Ti, Al-Mg, Al-Zr, Al-Li are some of the binary alloys, which have been explored as possible replacements for pure Al powders in energetic formulations [3, 116-120]. It was observed that particles of such Al-Ti alloys ignite at lower temperatures and burn faster than pure aluminum particles of the same sizes [121]. It was proposed that the phase changes associated with relaxation of metastable structures in such alloys accelerated their ignition [122]. Mechanically alloyed Al-Ti powders were milled previously with stearic acid as a process control agent (PCA) [123]. Both ignition and combustion behavior of the mechanically alloyed powders was improved compared to pure aluminum. However, the mechanically milled powders were relatively coarse and could not be effectively reduced in size for useful practical applications [123] where finer aluminum powders are typically used.

This study aims to investigate the effects of liquid hydrocarbon PCAs on properties of mechanically milled Al-Ti powders, specifically focusing on the feasibility of

combining the attractive reactive particle structures with practically desired fine particle sizes. Both one and two-stage milling protocols were explored using different PCAs. In particular, the use of acetonitrile as a PCA was explored, for which it was observed that milling may lead to formation of nanoparticles of Al [117]. 5-micron spherical aluminum powder widely used as a fuel additive was chosen as the reference material for the combustion experiments in this study.

5.3 Experimental

5.3.1 Sample preparation

Commercially available –325 mesh (less than 44 μm), 99.5% pure aluminum and titanium powders (by Atlantic Equipment Engineers) were used for sample preparation. A composition of 80 at% Al and 20% at% Ti (70 wt% Al, 30 wt% Ti) was maintained in all experiments. Initially, one stage milling was conducted in a Retsch PM400 planetary mill (PM) using 95% pure hexane (Alfa Aesar) and 99.5% pure acetonitrile (Alfa Aesar, "ACN" hereafter) as PCAs preparing samples 1 and 2, respectively. Both PCAs are hydrocarbon fluids with significantly different polarity. Hexane is non-polar, while ACN is polar. 20 g of powder was charged with 24 ml PCA. The PCA amount was selected so that the powders would be fully immersed in it. Standard Retsch hardened steel 500-ml vials were used for milling. The samples were milled at 350 RPM for 10 hours using 9.525-mm (3/8") diameter hardened steel balls at a ball-to-powder mass ratio (BPR) of 15. Prior to milling, the metal powders were loaded into the vials inside a glove box filled with argon. table 5.1 shows the milling parameters of Al-Ti samples 1 and 2 using, respectively, hexane and ACN as PCAs.

Table 5.1 Milling Parameters for One-stage Milling of Al_{0.8}Ti_{0.2} Alloys

ID	Mill Type	Sample Mass (g)	Time (hr)	BPR	PCA amount	
					Hex	ACN
					(ml)	(ml)
1	PM	20	10	15	24	-
2	PM	20	10	15	-	24

Preliminary examination of the samples prepared in one-stage milling showed, as discussed below, that the materials milled in ACN for 10 hrs (table 5.1) reacted with the PCA during milling. Hence, a 2-stage milling protocol was tested in order to produce finer composites which are not altered chemically. For this 2-stage protocol, stearic acid (SA) served as PCA during the 1st stage milling in the same planetary mill with the same steel balls. The samples were milled for 3 hours with stearic acid at BPR 10. The 2nd stage milling of this powder was first explored for small powder batches using a SPEX Certiprep 8000 series shaker mill (SM). Hexane, ACN, a combination thereof, and stearic acid served as PCAs for samples 3-6, as shown in table 5.2. In all cases, the second stage milling in the SM was 30 min. Upon recovery, the samples were stored without separating them from the used PCAs. Once promising materials were identified for small batches prepared in the shaker mill, larger amounts (samples 7 and 8) were prepared using a similar protocol but using the planetary mill for both 1st and 2nd milling stages (see table 5.2 for details).

Table 5.2 Milling Parameters for Milling of Al_{0.8}Ti_{0.2} at the 2nd Stage

Sample ID	PCA amount			Mill type	Powder mass (g)	Time (hr)	BPR
	Hex (ml)	ACN (ml)	SA (wt%)				
3	4	-	-	SM	5	0.5	10
4	-	4	-				
5	-	-	2				
6	2.8	1.2	-				
7	-	-	2	PM	50	1	
8	-	40	-				

The powders selected for the final combustion testing (samples 7, 8) were prepared by two-stage milling in the planetary mill. For both powders, the first stage lasted 3 hours, and the second stage lasted 1 hour. Ball to powder mass ratio was 10. For one of the samples (sample 7), both first and second stages used stearic acid as PCA. For the second sample (sample 8), ACN served as PCA during the second stage milling.

5.3.2 Material Characterization

5.3.2.1 Scanning Electron Microscopy (SEM). A LEO 1530 field emission scanning electron microscope (SEM) operated at 10 kV was used for characterizing particle size and surface morphology of the samples. SEM stubs were prepared using carbon tape as the substrate. Prior to transferring trace amount of sample on the substrate for SEM analysis, the liquids in the samples were evaporated. Some milled samples were embedded in epoxy and cross-sectioned to image the internal structures of the prepared composites. The compositional contrast between Al and Ti was achieved using back-scattered electrons for their SEM imaging.

5.3.2.2 X-ray Diffraction. X-ray diffraction (XRD) analysis of the milled samples was performed using PANalytical Empyrean multipurpose research diffractometer. The milled samples were allowed to dry in air before XRD measurements. Unfiltered Cu K α radiation ($\lambda = 1.5438 \text{ \AA}$) was used. The voltage and current used to generate x-rays were set at 45 kV and 40 mA, respectively. Analytical software HighscorePlus (version 3.0e) combined with the PDF-4+ (2018) database was used to identify the peaks.

5.3.2.3 Particle Size Distributions. Particle size distributions were obtained using a low-angle laser light scattering technique employing a Malvern 3000 Mastersizer. Ethylene glycol was used as the dispersant for the alloy samples. 5 to 8% obscuration was maintained throughout the experiment. Samples were continuously stirred at 2500 RPM to avoid particle settling. Further, 10% ultrasonication was introduced for breaking up loosely held agglomerates.

5.3.2.4. Thermal analysis. Differential scanning calorimetry (DSC) using a Netzsch STA409PC thermal analyzer was conducted on sample 7 and 8 to characterize their reactions upon heating. Sample 8 was loaded dry into the analyzer. However, sample 7 was loaded as a suspension in acetonitrile to prevent aging as it contained fine powder in the submicron range. The liquid was allowed to evaporate under argon in order to avoid contact with air. The furnace was evacuated and then flushed with argon three times before every measurement. The dry powder mass was recorded when a stable reading in the internal balance was observed after liquid evaporation. The dry mass of the samples ranged from 20 to 25 mg. The experiments were performed under the flow of argon (99.998% pure, supplied by Airgas) at a flow rate of 50 ml/min with an assigned heating rate of 15 K/min. During each run, the samples were heated to 800 °C twice. Prior to the second heating, the samples were allowed to cool down from 800 °C to 50 °C. The traces were finally baseline-corrected by subtracting the signal recorded during the second heating and then normalized by sample mass.

5.3.2.5 Heated Filament Ignition. Heated filament experiments were conducted to obtain ignition temperatures. Samples milled in two stages in planetary mill were explored in these experiments. A very thin coating of sample was observed to ignite on an electrically heated, 0.5 mm diameter nickel-chromium (Ni-Cr) wire. The samples were suspended in either ACN or hexane prior to coating. The coating was applied as a thin layer of the powder suspension using a fine brush. The solvent was dried off the wire before each run. 12-V rechargeable large-cell batteries by McMaster Carr were used as the DC source. Table 5.3 shows the heating rates achieved with one, two and three batteries connected in series.

Table 5.3 Heating Rates Achieved in Ignition Experiments with Different Number of Batteries Connected in Series

No. of batteries	Average heating rate (K/s)
1	3370 ± 160
2	11700 ± 1500
3	27800 ± 2000

A MotionPro 500 high-speed video camera as well a photodiode focused on the coated heated filament served to register the powder ignition in real time. However, the photodiode readings were significantly affected by the emission from the heated filament, making them difficult to use to identify the time of ignition. Thus, all ignition times in this study were determined from analysis of the recorded high-speed videos. Simultaneously, the temperature of the heated wire was measured using an infrared pyrometer comprising a germanium switchable gain detector (PDA30B2 by Thorlabs) coupled with a fiber optics cable and a focusing lens. The lens was focused on an uncoated portion of the wire so that the measured temperature as a function of time was unaffected by the varied emissivities of the powder coatings. The pyrometer was calibrated in the temperature range of 573 – 1223 K (300 – 950 °C) using a BB-4A black body emission source by Omega Engineering. A Rigol DS1054Z digital oscilloscope was used to read the signals from the photodiode and pyrometer. The wire temperature recorded at the instant of the powder ignition was registered as the powder ignition temperature in these experiments. This measurement neglects the difference in temperatures of the heated filament and the igniting powder; this difference was minimized maintaining very thin coating thickness in all experiments.

5.3.2.6 Constant Volume Explosion (CVE). The constant volume explosion apparatus consists of a 9.2-liter chamber with an aerosolizing nozzle positioned at the bottom. Two schedule-40-type 304 stainless steel 40-cm i.d. welded caps were used to construct the chamber. Four clamps hold the two halves of the chamber (sealed with an O-ring) together. The upper, removable half has an igniter, which is located near the center of the closed chamber. The igniter is constructed by coiling a 10-cm long, 0.2 mm diameter tungsten wire. The lower half is stationary and is equipped with gas ports, a Honeywell pressure transducer PX2AN1XX500PSA, and a nozzle located at its bottom. Samples are loaded in a pipe elbow placed under the nozzle. Initially, the explosion chamber is evacuated to 0.25 atm. The powder is then injected in the chamber with an air blast coming from a 7.6-liter reservoir tank filled to a high pressure. When the powder is injected, a desired starting pressure for the combustion test is also achieved in the explosion vessel. The gas blast is produced using a solenoid valve, and the duration of the pulse is selected to achieve the desired starting pressure. In these experiments, the target initial pressure in the explosion vessel was 1 atm. To achieve this, the duration of the gas blast was set at 200 ms and the pressure in the reservoir was 5.85 atm. The igniter is initiated after a 300 ms delay following the powder injection. That delay was consistent with previous work using the same experimental setup [117]. The delay is necessary to reduce the effect of turbulence produced by the injection gas flow on the combustion of aerosol produced in the chamber. A Rigol DS1054Z digital oscilloscope was used to record the measured pressure traces as well as electrical pulses controlling the pressure pulse and initiation of the igniter. For each run, the initial pressure (P_o), maximum pressure (P_{max}) exerted by the aerosol combustion event, and the maximum rate of pressure rise, (dP/dt_{max}) were determined by processing

the recorded pressure traces. Further details about the explosion chamber set-up have been described elsewhere [117].

5.4 Preparation of Reactive Composite Al-Ti Powders with Fine Particle Sizes

Milling conditions were selected analyzing powders prepared using one-stage milling and then two-stage milling using planetary and shaker mills. Results of these analyses are discussed below.

5.4.1 Powders Prepared by One-stage Milling

Figure 5.1 presents SEM images of powders prepared by one-stage milling in hexane and ACN. Images indicate that sample 1 (milled in hexane, figure 5.1 a, b) contained coarser particles, similar to those prepared in earlier work [124]. Sample 2 (milled in ACN, figure 5.1 c, d) had much finer particles, consistently with the results expected for milling using ACN based on previous work [125]. Particles in sample 2, however, appeared less as composite particles, but rather as loosely mixed unattached fines of Al and Ti. Aluminum particles generally appear darker and titanium particles brighter in these images acquired using a backscattered electron detector.

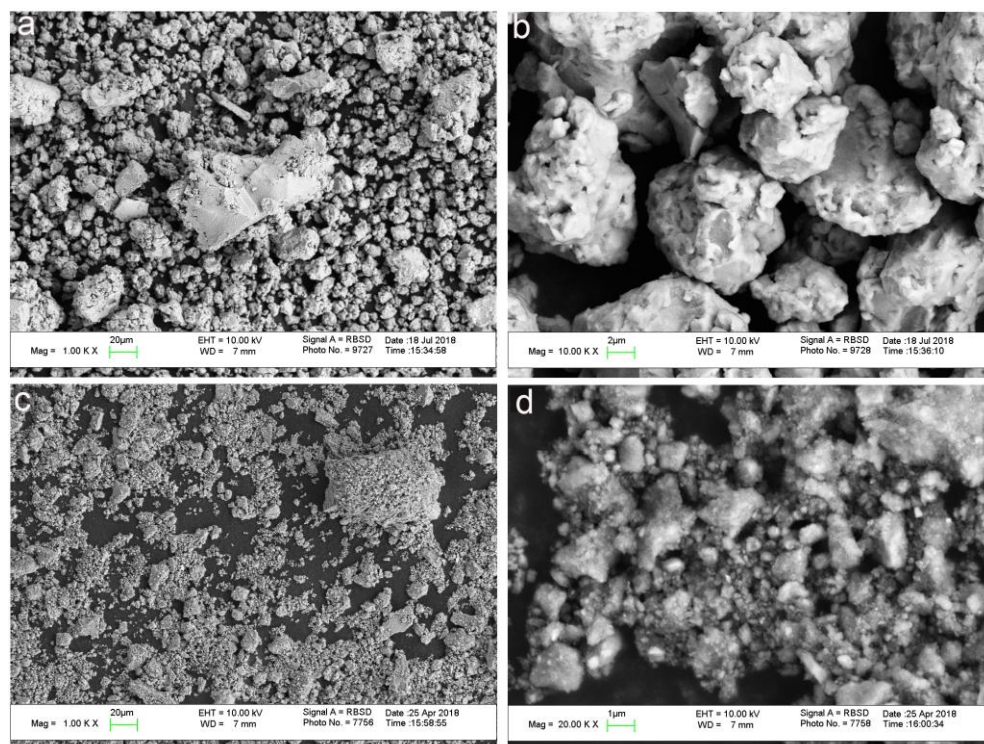


Figure 0.1 Backscattered electron SEM images of as-milled Al-Ti composites samples 1 and 2 after single-stage milling in hexane and ACN. Low and high magnification images show respectively: a, b: sample 1; c, d: sample 2.

Figure 5.2 illustrates XRD patterns for the Al-Ti powders synthesized by one stage milling in the presence of hexane and ACN. The major peaks for sample 1 milled in hexane corresponded to *fcc*-aluminum. Titanium peaks are not distinguished, although no traces of reacted species were found in that sample. Sample 2 milled in ACN showed no aluminum or titanium peaks. There was clear evidence of reactions during milling; respective XRD results show the presence of aluminum nitride, AlN, and a titanium carbonitride, $\text{TiC}_{0.51}\text{N}_{0.12}$ (cf. JCPDS ref. 98-003-9942). Such reactions are undesirable suggesting that long time milling in acetonitrile is impractical. Therefore, the two-stage milling protocol was further explored, as discussed below.

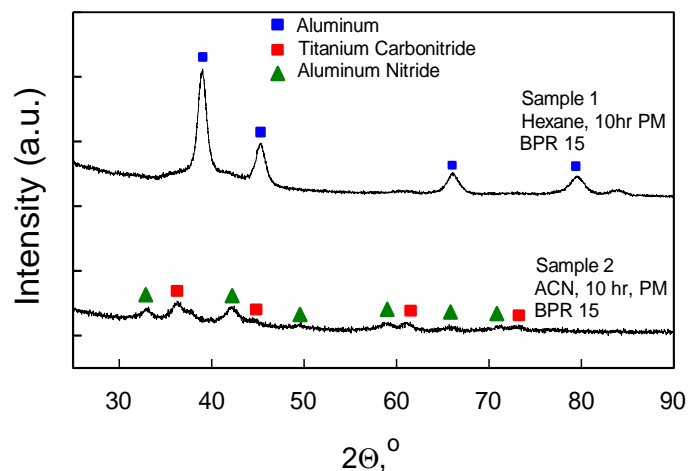


Figure 5.2 XRD traces for samples 1 and 2 prepared by one-stage milling of Al and Ti powders in hexane and acetonitrile, respectively.

5.4.2 Powders Prepared by Two-stage Milling

SEM images of samples 4-6 synthesized by two-stage milling in the shaker mill are presented in figure 5.3. Only in sample 4 (figure 5.3 c, d) milled in ACN during the second stage, most of the final particles have dimensions of ca. 1 – 2 μm or less. Many such particles appear as flakes. For all other samples, a broad particle size distribution including substantial fraction of coarse particles (exceeding 10 – 20 μm) are observed. For all powders except those prepared with ACN as PCA in the second stage, the powder particle shapes are difficult to distinguish from those prepared during single stage milling.

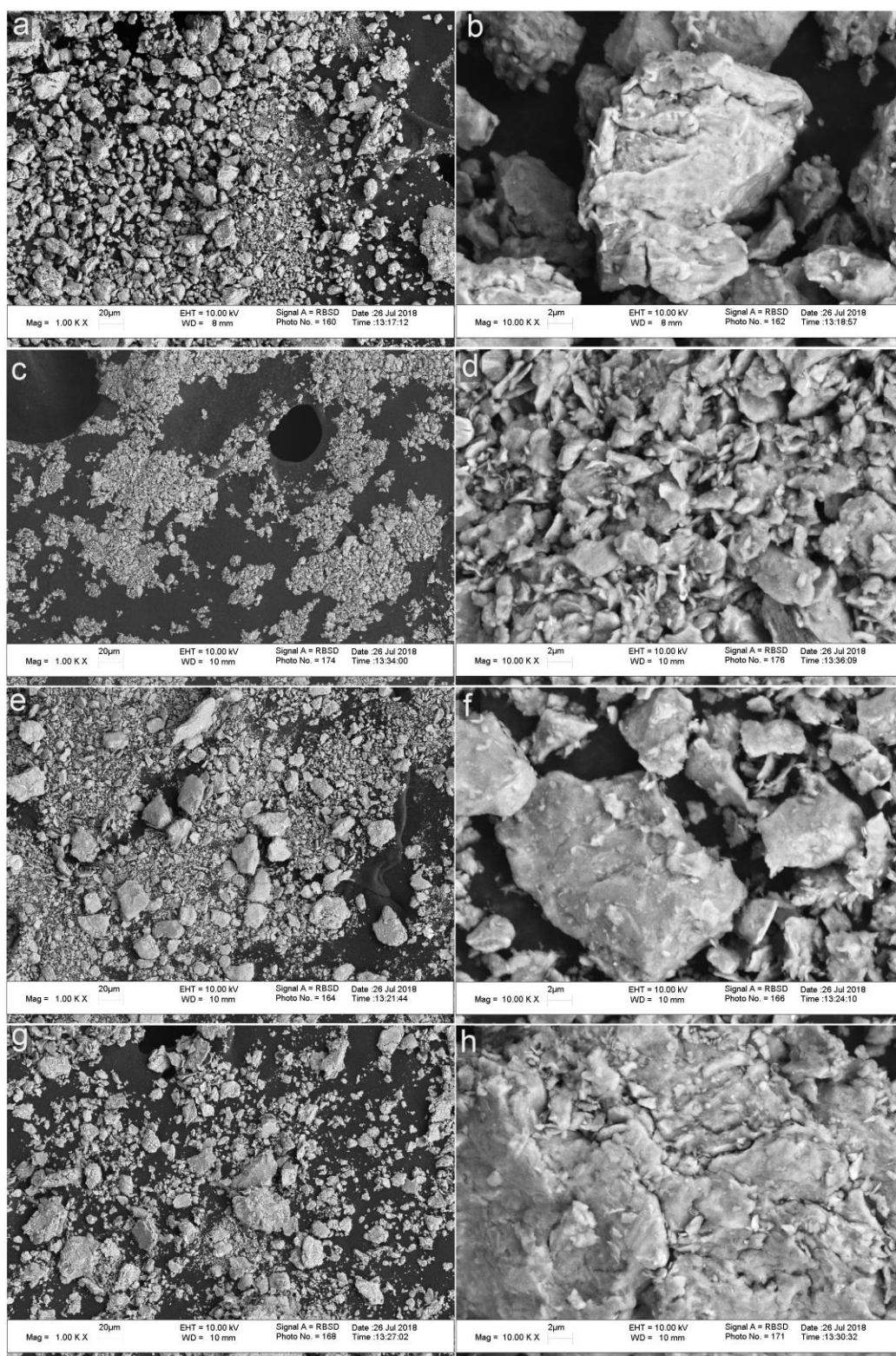


Figure 5.3 Backscattered electron SEM images of samples synthesized by 2-stage milling in shaker mill. Low and high magnification images show respectively: a, b: Sample 3; c, d: Sample 4; e, f: Sample 5; g, h: Sample 6.

Particle size distributions obtained using low angle laser scattering for samples 3-6 milled in the shaker mill during the 2nd stage are plotted in figure 5.4. For comparison, a particle size distribution is also shown for the powder prepared during the first milling stage, serving as a starting material for the second milling stage for all these samples. For that starting powder, the particles remain coarse, with the distribution peak around 50 μm . The plot clearly shows that upon introducing 2nd stage milling with different PCAs, the particles become finer. Figure 5.4 also suggests that among all the PCA conditions introduced during 2nd stage milling, ACN is significantly more effective in reducing the particle sizes, in agreement with images shown in figure 5.3. Sample 5 prepared with the 2nd stage milling using ACN shows a broader size distribution with significantly increased number of fine particles. Considering, that the particle shapes are flaky, it is likely that this measurement is overestimating the number of large particles. Indeed, large flat particles may scatter the laser light similar to spheres with comparable diameters, while the volume and mass of the respective particles are significantly smaller than those of such spheres.

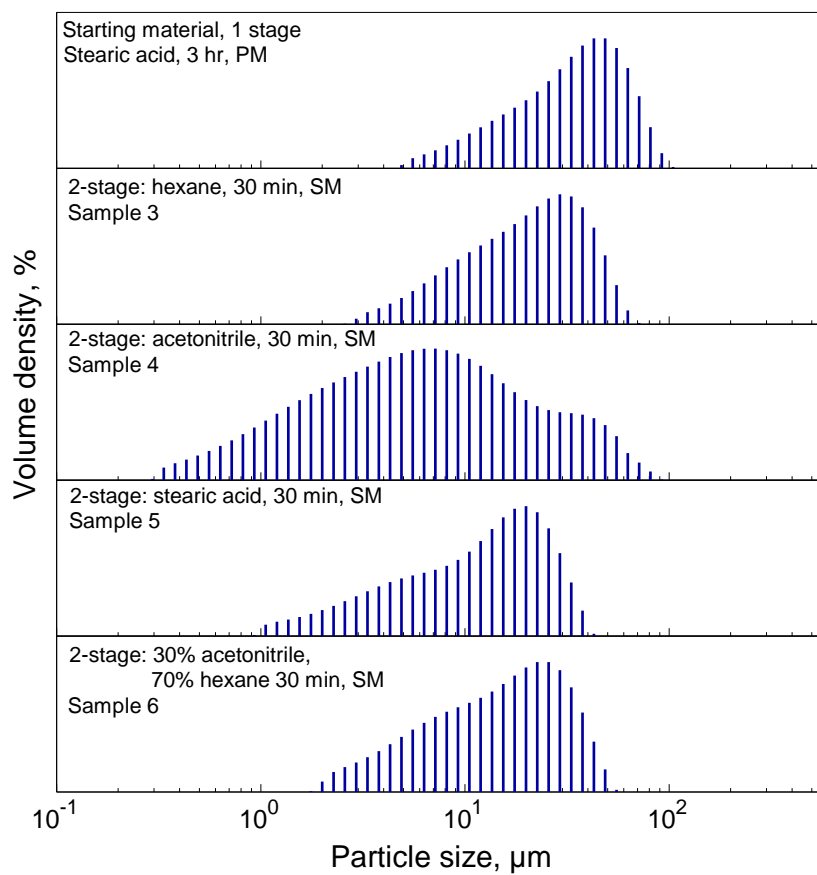


Figure 5.4 Particle size distributions for a powder milled in the first stage in the planetary mill and samples 3-6 prepared using that powder milling during 2-nd stage in the shaker mill with different PCAs

Figure 5.5 illustrates the XRD results for Al-Ti powders, samples 3 – 6, prepared using the shaker mill in the second stage. For comparison, the XRD pattern is also shown for the powder prepared during the first milling stage, serving as a starting material for the second milling stage for all these samples. No traces of reaction products were observed that could have formed during milling. Only peaks of Al and Ti are detected. The differences between XRD patterns for the powders recovered after the first stage and those milled further with different PCAs are minor. Peaks of both Al and Ti broaden and peaks

of Ti become noticeably weaker after the second stage milling. Both changes are likely due to continuing refinement of the material by milling.

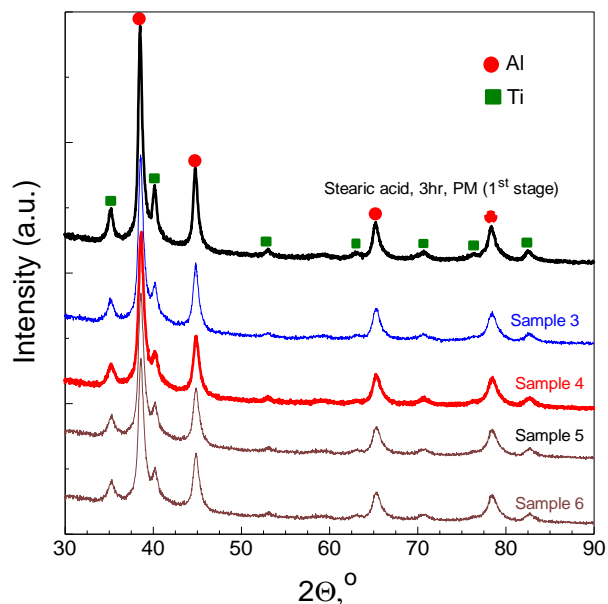


Figure 5.5 XRD traces of Al-Ti samples 3-6 prepared by 2-stage milling with different PCAs using shaker mill during the second stage.

Based on the results shown in Figures 5.3 – 5.5, preparation of composite powder samples on a larger scale was attempted using the planetary mill for both stages. Details are given in table 5.2. Samples 7 and 8 were prepared using the 2-stage protocol and employing planetary mill for both stages. Both samples were milled for 3 hours during the first stage using stearic acid as PCA. Both samples were milled for 1 hour during the second stage. For sample 7, stearic acid remained the PCA. For sample 8, ACN was added for the second milling stage. Both prepared materials were embedded in epoxy and cross-sectioned. Figure 5.6 shows SEM images of the obtained cross sections. Coarser composites were formed for sample 7 (figure 5.6, a, b). The bright areas in the particle cross-sections correspond to inclusions of titanium, which can be distinguished from dark

grey Al matrix. Sample 8 (figure 5.6 c, d), experiencing an hour of milling in ACN at the 2nd stage formed fine composite particles instead, although few large agglomerated particles were also observed. Cross-sections of powder particles for sample 8 show little compositional contrast. Apparently, the scale of mixing between the elements is finer than the compositional resolution of images shown in figure 5.6c, 5.6d.

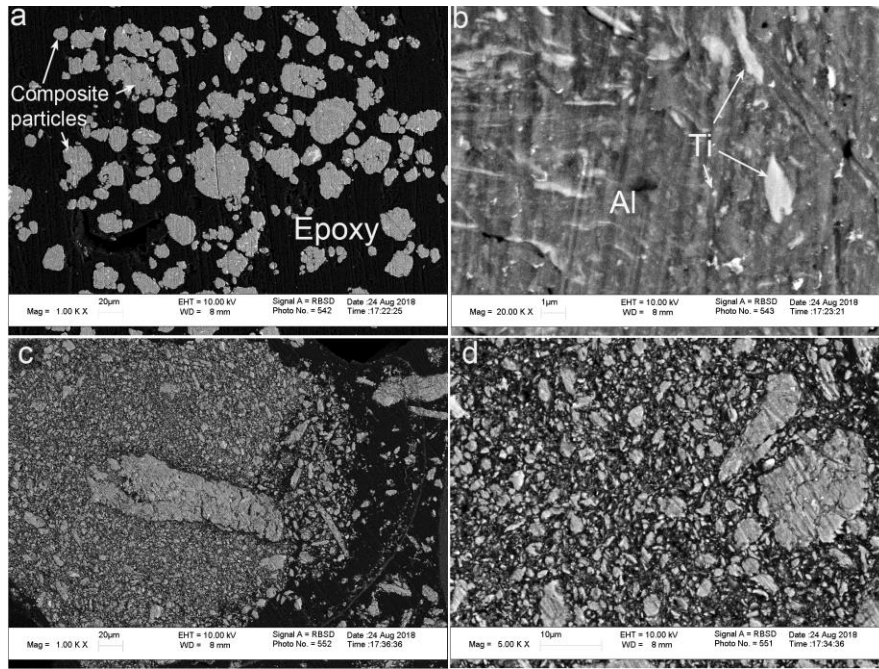


Figure 5.6 Backscattered electron SEM images of samples synthesized by 2-stage milling in planetary mill. Low and high magnification images show respectively: a, b: Sample 7; c, d: Sample 8.

Particle size distributions for samples 7 and 8 milled in the planetary mill during both first and second stages are shown in figure 5.7. For clarity, the size distribution for the powder prepared during first stage milling (the same as in figure 5.4) is also shown. The powder particle size distributions for samples 7 and 8 are similar to those of samples 5 and 4, respectively. For either shaker or planetary mill used during the second stage milling, continued milling in stearic acid during the 2nd stage reduced the number of coarse

particles; however, the change in the particle size distribution was not significant. For the sample using ACN during the second stage milling, the size distribution became broader with a significant shift towards fine sizes for both samples 4 (figure 5.4) and 8 (figure 5.7). Similar to sample 4, for sample 8 a substantial fraction of coarse particles is implied by the particle size analysis shown in figure 4.7, which is, as discussed previously, likely a superficial effect of the presence of relatively large but thin flakes in the prepared powder. For reference, a powder particle size distribution for the nominally 5- μm spherical aluminum powder used in combustion experiments discussed below is also shown. The sample using ACN as PCA in the second milling stage appears to be finer than aluminum.

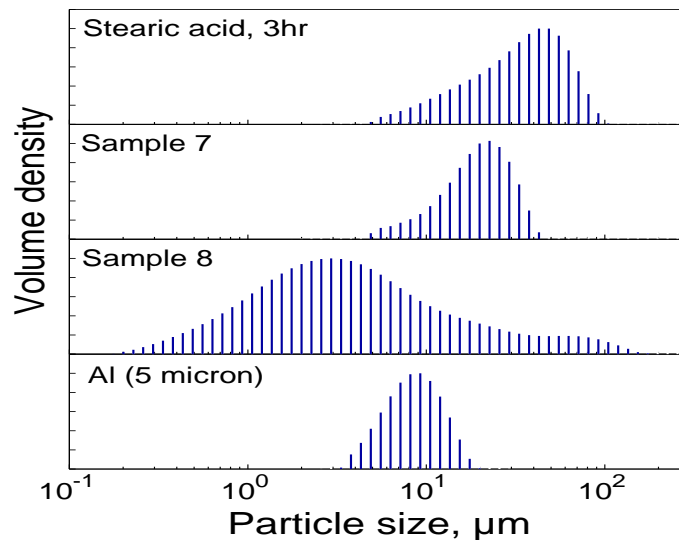


Figure 5.7 Particle size distributions for samples milled in planetary mill during 3 hours (one stage) and during 4 hours (two stages) using different PCAs and for the reference spherical Al powder.

XRD patterns for samples 7 and 8 are shown in figure 5.8. The pattern for sample 7 includes peaks of both Al and Ti and is essentially the same as the patterns shown in

figure 5.5 for samples 3 – 6. For sample 8, peaks of Al become weaker and broader and peaks of Ti are nearly indistinguishable. This could be simply due to the reduction in the sizes of composite particles, observed in Figs. 5.6 and 5.7. No intermetallic formation is observed. Further ignition and combustion tests used only samples 7 and 8.

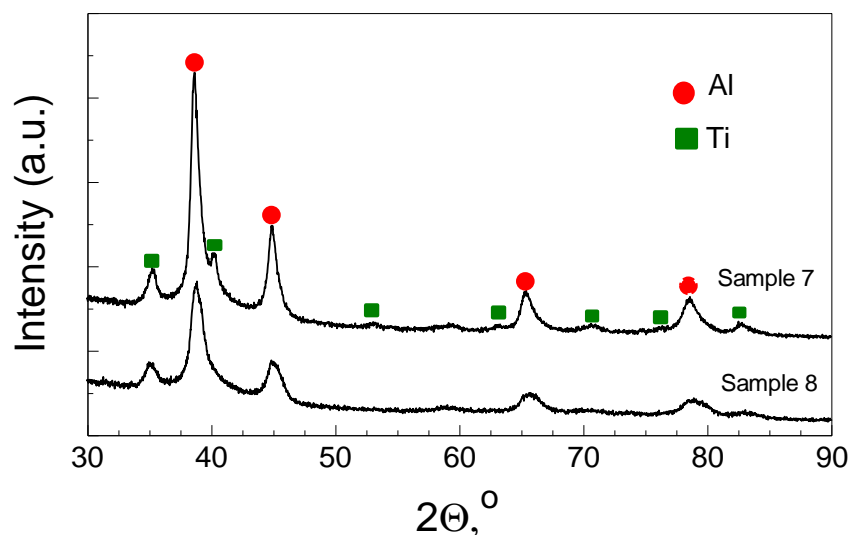


Figure 5.8 XRD traces of Al-Ti samples 7 and 8 prepared by 2-stage milling with different PCAs using planetary mill during the second stage.

5.5 Exothermic Reactions

Figure 5.9 shows DSC traces of samples 7 and 8 heated at 15 K/min up to a maximum temperature of 1073 K (800 °C). The signal for sample 8, milled in ACN in the 2nd stage, is distinctly exothermic starting at 373 K (100 °C) with the first peak under 474 K (200°C). The trace shows exothermic peaks near 600, 725, and 850 K (or, respectively, 325, 450 and 575 °C) marked with black dots in figure 5.9. However, the peaks are not well resolved and the signal is generally noisy. Aluminum melting, or an Al-Al₃Ti eutectic melting peak at 933 K (660 °C) cannot be detected reliably. For sample 7 (milled in stearic acid for 4

hrs) the signal becomes exothermic at a higher temperature, around 423 K (150 °C). A strong, well-resolved peak is observed at 623 K (350 °C); it is followed by a weaker peak at around 773 K (500 °C); both marked with black triangles. In sample 7, aluminum melting (or a eutectic melting peak) was observed at 933 K (660 °C).

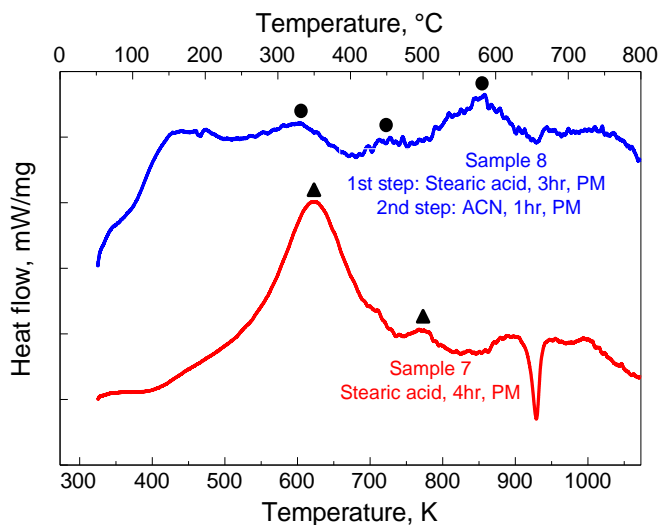


Figure 5.9 DSC traces of Al-Ti composites heated at 15 K/min to a maximum temperature of 1073 K (800 °C).

5.6 Results of Ignition and Combustion Experiments

From the heated filament experiment results shown in figure 5.10, it is observed that sample 7 milled in stearic acid for 4 hrs (both first and second stage milling) ignited at relatively high temperatures ranging from 1123 to 1223 K (850 to 950 °C). These ignition temperatures exceed the aluminum melting point. Conversely, sample 8 milled in ACN during the second stage ignited at very low temperatures. The ignition temperature ranged approximately from 763 to 853 K (490 to 580 °C). An increase in the ignition temperature was observed with increasing heating rate. The average ignition temperatures recorded for

that sample for all three different heating rates were below the aluminum melting point. The present results were compared with those published previously [117] for mechanically alloyed Al-Ti powders prepared using a shaker mill with zirconia vials and milling balls and milled for 15 hours with stearic acid as PCA [125]. Three exothermic events accompanied ignition in those experiments. Respective temperatures are shown in figure 5.10 for the mechanically alloyed powder with the same composition as used in this work. The ignition of the mechanically alloyed powder was assigned to the most significant event 2, occurring at intermediate temperatures, relatively close to the melting point of aluminum. Event 1, reported in Ref. [117] and reported to be rather weak, coincides nearly exactly with the ignition temperature measured here for sample 8.

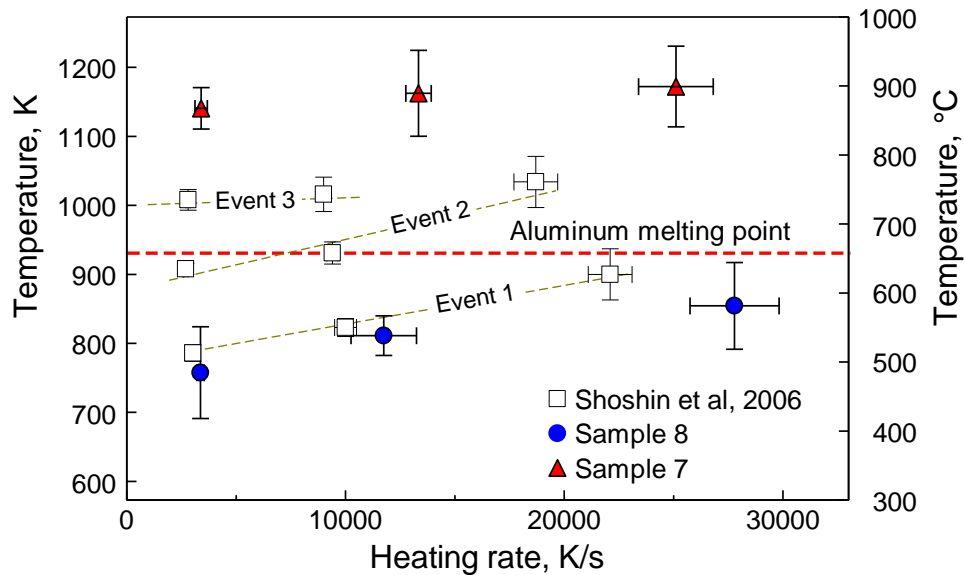


Figure 5.10 Heated filament ignition temperatures for different Al-Ti composite powders and for mechanically alloyed powder prepared in previous work

Source: Shoshin, Y., L., et al., Ignition of aluminum-rich Al-Ti mechanical alloys in air. Combustion and Flame, 2006

Combustion of samples 7 and 8 was explored in CVE experiments. Traces shown on figure 5.11 are marked to illustrate the experimental sequence. The pressure in the vessel is initially low. A gas blast, during which the powder is dispersed in the chamber leads to a nearly linear pressure rise. The pressure P_0 achieved after the gas blast is the starting experimental pressure, typically close to 1 atm. The gas blast is followed by a delay needed to reduce the turbulence level in the vessel. Ignition, caused by a heated tungsten wire placed in the center of the vessel begins the aerosol combustion event leading to the main pressure rise to P_{\max} observed in figure 5.11. Sample 7 prepared by milling using only stearic acid as PCA did not ignite and thus is not discussed here. From the typical pressure traces in figure 5.11 it is observed that sample 8 milled in ACN burns faster, and with a slightly greater pressure rise than the reference Al powder. Both a reduced delay in ignition (the pressure rise starting sooner after the ignition pulse) and a greater rate of pressure rise are observed for the prepared milled composites as compared to the Al powder.

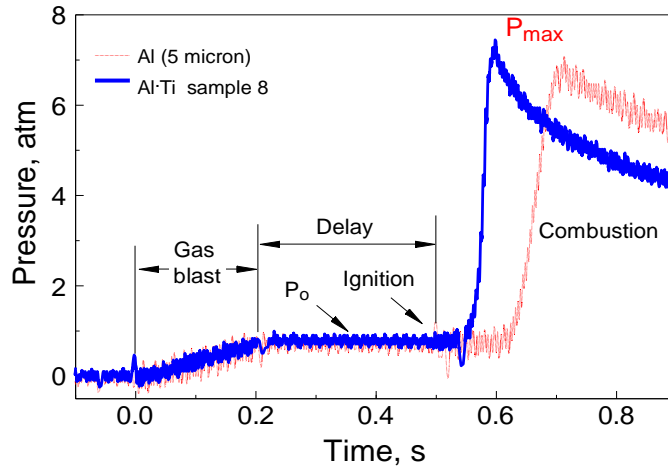


Figure 5.11 Pressure traces of typical CVE experiments with sample 8 and reference 5- μm aluminum powder.

Figure 5.12 shows a summary of the present CVE experiments. Open symbols in figure 5.12 represent Al, and closed symbols represent sample 8. For both plots shown in

figure 5.12, the horizontal axis represents the ratio of the maximum pressure to the initial pressure, P_{\max}/P_0 . This ratio is expected to be higher for samples burning more efficiently and thus generating more heat. The vertical axis in the top plot is $(dP/dt)_{\max}$, representing the rate of combustion achieved in the present experiments. Higher burn rates are advantageous, and thus the most attractive experimental points are expected to be positioned in the upper right corner of that plot. The points representing runs with the aluminum powder form a trend suggesting a greater rate of pressure rise corresponding to a greater achieved pressure. It is likely that the discrepancy between individual runs is caused by some inconsistency in dispersing the powder in the vessel prior to ignition. A better-dispersed powder forming a denser and more homogeneous dust cloud is expected to lead to both greater pressure and rate of pressure rise. The data points representing the sample 8 composite lie above the trend representing reference aluminum. Thus, a greater rate of pressure rise is observed for the same maximum pressure achieved. Note also that the pressures achieved with sample 8 are comparable to the highest pressures observed for aluminum.

For the bottom plot in figure 5.12, the vertical axis is the time of P_{\max} . This time is affected by both the rate of pressure rise and by ignition delay observed after the igniter wire was initiated. The shorter this time, the greater is the bulk reaction rate, affected by both ignition delay and burn rate of the aerosolized powder. Thus, the most attractive experimental points are expected to be in the lower right corner of this plot. While there is substantial scatter in the experimental data points, there is a clear indication that, in agreement with the example shown in figure 5.11, the prepared composite powders

outperform reference Al. For the same experimental pressures, shorter times of $(dP/dt)_{\max}$ are observed for sample 8 compared to the reference aluminum.

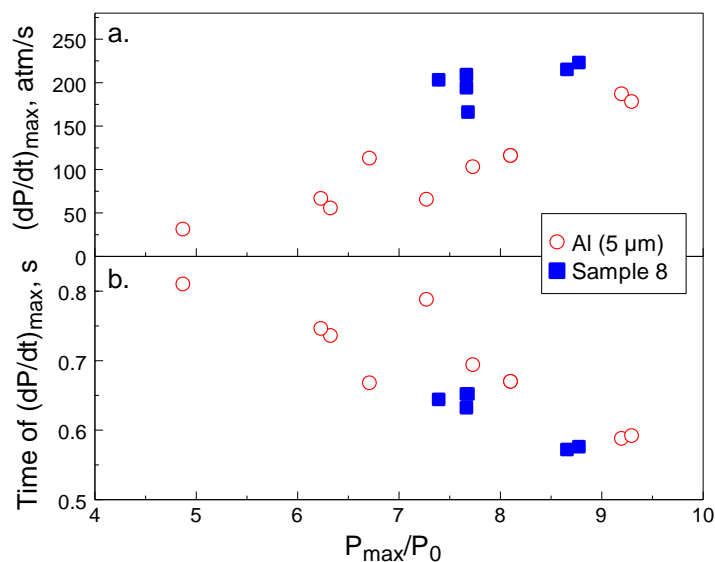


Figure 5.12 a) Pressurization rate $(dP/dt)_{\max}$ and b) time of P_{\max} vs P_{\max}/P_0 for CVE experiments with sample 8 and reference 5- μm aluminum powder.

5.6 Discussion

The objective of this effort was to find a way of preparing reactive Al-Ti powders with micron-sized particles, comparable to the size of aluminum commonly used in energetic formulations. It was observed that extended milling in a liquid polar PCA, such as ACN is effective in reducing particle sizes, but also alters the powder chemically (figure 5.2). This is not desirable for applications in energetic materials. Conversely, the two-stage milling including preparing a powder with a desired composite structure in the first milling step without using a polar PCA, and then refining that powder achieving finer particle sizes in a relatively short second milling step with polar PCA is feasible for preparing reactive Al-Ti composites. Interestingly, the effect caused by ACN as a polar PCA during the second milling step is qualitatively similar for the samples prepared using either shaker

(sample 4) or planetary (sample 8) mills. The similarities are observed for particle sizes and shapes (figure 5.3 c and d vs. figure 5.6 c and d), for particle size distributions (figure 5.4 vs. figure 5.7), and for material structures inferred by XRD (figure 5.5 vs. figure 5.8). Milling in a non-polar PCA (hexane), mixture of hexane and ACN, as well as in stearic acid during the second milling stage does not change size or structure of the material appreciably.

Based on previous work describing milling of aluminum using ACN [76], it can be proposed that interaction of ACN and aluminum involves a chemical reaction which alters the aluminum surface. This interaction most likely leads to the formation of carbon-aluminum and nitrogen-aluminum bonds (figure 5.2), which dramatically change the interaction between powder particles, reducing their agglomeration. Thus, milling time or the amount of ACN need to be limited to avoid bulk conversion of aluminum to its nitride, carbide or other passivated phases. Further studies are desired to elucidate the mechanisms of interaction between aluminum and other metals with acetonitrile (and other polar solvents) serving as PCA during high-energy milling.

The present results show that when the powder particle size is effectively reduced due to additional milling in ACN, there is also a significant change in the powder structure. Unlike samples 3, 5, and 6, for which brighter inclusions of Ti can be distinguished in a darker matrix of Al in SEM images taken using backscattered electrons (figures. 5.3b, 5.3f, and 5.3h) and sample 7 (figure 5.6b), no such distinction could be made for samples 4 and 8 (figure 5.3d and Fig 5.6c, respectively). The XRD patterns also show diminished peaks of Ti and broader peaks of Al for samples 4 (figure 5.5) and especially 8 (figure 5.8), milled in ACN during the second stage.

Apparently, the differences in the sample structure affect the exothermic reactions occurring upon heating and ignition. Sample 7, prepared using stearic acid for both stages 1 and 2 milling, shows the first pronounced exothermic effect (figure 5.9), likely corresponding to the formation of thermodynamically stable $\text{D0}_{22} \text{Al}_3\text{Ti}$, consistent with the first exotherm observed at 623 K (350 °C) in the DSC measurements for mechanically alloyed powders [123, 126]. Interestingly, the exothermic event at this temperature appears to be stronger for the present measurements for sample 7 than reported earlier for the mechanically alloyed powders [123, 126]. This can be attributed to shorter milling times used here compared to references. [123, 126]. A longer milling time leads to mixing between Al and Ti at nearly atomic scale, causing formation of metastable precursors for the intermetallic Al_3Ti . In contrast, shorter milling times cause formation of a composite structure, where the mixing between Al and Ti occurs at the scale of ca. 0.1 – 1 μm (figure 5.6b), while formation of the metastable precursors to intermetallics is suppressed. Therefore, when the temperature is increased and the intermetallic phase forms, a composite structure releases a greater amount of heat compared to the more intimately mixed and thus partially reacted mechanically alloyed powder.

For sample 8, using ACN in the second milling stage, exothermic reactions begin at a significantly lower temperature (figure 5.9). Once the reaction starts, multiple, poorly resolved exothermic events are observed. It is possible that the equilibrium phase of Al_3Ti is only formed via intermediate steps, possibly involving the L1_2 and D0_{23} forms [123]. It is also possible that the large surface area, in combination with acetonitrile adsorbed to it, stabilizes other phases, particularly considering that Al (or Al- Al_3Ti eutectic) melting is not observed in this case.

The low-temperature exothermic reactions observed by DSC (figure 5.9) and leading to formation of Al_3Ti are likely leading to ignition described in figure 5.10, similarly to mechanically alloyed Al-Ti powders [117]. Despite a stronger first exothermic peak (occurring at the same temperature for sample 7 and mechanically alloyed powder), ignition temperatures for sample 7 shown in figure 5.10 are higher than for mechanically alloyed powder explored previously [117]. This can be understood considering that the heat of intermetallic reaction, detected in DSC is never sufficient to drive the powder ignition directly. Instead, the weakly exothermic intermetallic reaction serves as a trigger generating new structure, defects, and surface exposed to the external oxidizer. It is that reaction with the external oxidizer occurring at the newly formed surface that leads to a temperature runaway and ignition. For the composite material, the generated surface is apparently smaller than that for the mechanically alloyed powder, leading to a longer ignition delay and, respectively higher ignition temperature. For sample 8, however, for which the milling time is also much shorter than for mechanically alloyed powders tested in reference. [117], the ignition occurs at a lower temperature, effectively coinciding with the first, very weak exothermic event observed to accompany ignition for the mechanically alloyed powders (cf. figure 5.10). This suggests that the reaction, triggering ignition is similar for both sample 8 and mechanically alloyed powder. However, for sample 8 milled using ACN as PCA, even the initial reaction occurring at lower temperature generates enough defects and new surface to lead to ignition.

Experimental ignition temperatures for sample 8 shown in figure 5.10, for which a clear effect of heating rate on ignition was observed, are plotted in Arrhenius coordinates in figure 5.13. A straight-line fit is also shown, which is extrapolated to the range of low

heating rates. A horizontal line shows the heating rate used in the DSC experiments (figure 5.9). At that heating rate, the extrapolated line points to a temperature of 223 °C or 500 K, at which the event, triggering ignition is anticipated in the DSC measurement. This temperature is just slightly higher than the first, poorly resolved exothermic event observed for sample 8 in figure 5.9. Considering experimental uncertainties and the extrapolated range, this supports the correlation between the very low-temperature reactions forming intermediate intermetallic species serving as precursors to formation of Al_3Ti and ignition of the prepared composite.

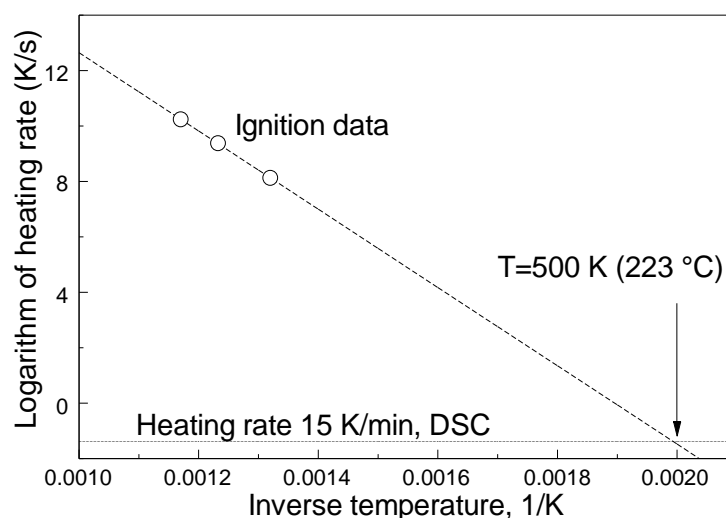


Figure 5.13 Arrhenius plot showing ignition temperatures recorded for sample 8 at different heating rates and linear fit for these data extrapolated to the range of low heating rates used in DSC experiments.

Finally, CVE experiments illustrated in figure. 5.11 and 5.12 show that a direct comparison between combustion of aerosolized powders of Al and Al-Ti composite is possible. Furthermore, this comparison suggests an advantageous performance of the Al-Ti composites. This is consistent with earlier reports showing that the mechanically alloyed

powders burned faster than the same size Al powder [123]. However, previous comparisons could only be made for individual particle burn times for relatively large particles. Coarse mechanically alloyed powders, which could be prepared previously, could not be ignited in CVE. Similarly, sample 7 prepared using stearic acid as PCA could not be ignited. Such coarse metal powders are not commonly used in practical energetic formulations. Reducing the particle size for the prepared composites achieved using ACN during the second milling stage generated sample 8, fine enough to be readily ignited in CVE. Thus, such materials, which are as or even more energetic than pure aluminum, hold promise for their practical utilization in energetic formulations.

5.8 Conclusions

A two-stage milling offers an effective way of preparing Al-Ti composites with tunable fine powder particle sizes. The first milling stage can use common PCAs, such as stearic acid or hexane to produce the desired scale of mixing or structure. The second milling stage uses ACN, a polar fluid, to reduce the particle sizes effectively. Further modification of the powder structure also occurs during the second stage milling, which should thus be restricted in time to avoid formation of metal nitrides or carbonitrides. Powders prepared by two-stage milling in this work have particle size distributions comparable to those of fine Al powders typically used in energetic formulations. Ignition and combustion tests show that the ignition temperatures for the prepared composite powders can be reduced below the Al melting point. The ignition is likely triggered by the initial intermetallic reactions forming precursors for Al_3T intermetallic phases. The powders are readily aerosolized and ignited in CVE. They demonstrate shorter ignition delays and higher burn rates than the reference fine spherical aluminum powder.

CHAPTER 6

MICROSPHERES WITH DIVERSE MATERIAL COMPOSITIONS PREPARED BY MECHANICAL MILLING

6.1 Abstract

Spherical particles with dimensions in the range of ca. 1 – 100 μm are prepared by mechanical milling of precursor materials in the presence of a blend of immiscible liquids. Microspheres with a broad range of compositions are prepared including hard and ductile elements, metals, metalloids, oxides, organic compounds, and composites. The proposed mechanism leading to formation of spheres includes formation of a Pickering-Ramsden emulsion coexisting with a dense suspension of solids in the continuous phase. Milling continuously transfers energy to the multiphase mixture, destabilizing particles located on the liquid interface. This causes a net transport of solids from the continuous phase into the emulsion droplets where solids accumulate and form microspheres that can be recovered after milling. The process continues until the solid loading of the droplets exceeds a limit, or until the continuous phase suspension is depleted. Microspheres prepared by this method may be of interest as feedstock for additive manufacturing, for drug formulations, catalysts, membranes, and in various other technologies.

6.2 Introduction

Mechanochemical processing and synthesis of new materials has attracted significant attention because of the versatility and simplicity of this approach.[127-130] Products are typically powders. Their compositions and structures are often metastable and not attainable by other synthetic routes. Particle shapes can be described as roughly equiaxial

rock-like compacts or flakes.[131] while compositions of materials prepared by milling are effectively unlimited, control of particle morphology is difficult. Indeed, the powders form by repeated fracturing and cold welding or agglomeration, starting typically from solid powder precursors. Common but relatively ineffective ways to affect particle sizes are to change the size of milling balls, e.g., [55, 132, 133] and to select process control agents [134-136] that affect cold welding. However, particle shapes are mostly determined by mechanical properties of the material milled, and evolve during milling until a steady state size is reached. Yet, particle shapes are important for many applications [137-143]. Spherical particles are often desired for flowability, ease of transport, processing, packing, and mixing.

Spherical particles in the micrometer size range are most commonly prepared by cooling droplets of melts [144, 145]. However, challenges arise for refractory compounds or composites comprising components with diverse melting temperatures. This method is also inapplicable to materials sensitive to heating, as they may react before they melt. We introduce a new technique of preparing spherical composite powders by mechanical milling. It is shown that mechanical milling in the presence of a liquid process control agent comprising two immiscible liquids can produce nearly perfect microspheres that consist of densely compacted micro- or nano-particles of one or more material components. There are multiple potential applications for such microspheres, including feedstock powders for additive manufacturing (when flowability attained with spherical particles is of critical importance), materials for drug formulation, materials for joining, multifunctional porous components, catalysts, membranes, etc. Mechanical milling used to prepare the microspheres is a readily scalable, industrially flexible and adaptable technology,

suggesting that practical quantities of the microspheres can be readily produced once the mechanism of their formation is fully elucidated.

6.3 Experimental

Two types of ball mills were used to prepare microspheres from different materials. A SPEX Sampleprep 8000D Mixer/Mill with 50-mL flat-ended steel vials was used to prepare aluminum-copper(II) oxide thermite microspheres. A Retsch PM 400 MA planetary mill was used to prepare microspheres of aluminum, titanium, boron, iron (III) oxide, fumed silica, melamine and sucrose, as well as composite microspheres of aluminum-copper(II) oxide, aluminum-iron (III) oxide, and aluminum-boron. The planetary mill was equipped with custom hardened steel milling jars, designed to withstand accidental combustion of reactive composite materials, such as thermite compositions (although no such accidents occurred during this effort). Samples were milled at 350 RPM with 90 g (25 g for the shaker mill) of 9.525 mm (3/8") diameter hardened steel balls, typically for an hour. Milling time for selected materials (aluminum, boron, iron oxide) varied up to 4 hours.

Starting materials included powders of aluminum and titanium (both by Atlantic Equipment Engineers, -325 mesh, 99.5 %), copper oxide (Sigma Aldrich, 10 μ m, 99+%), fumed silica (Sigma-Aldrich, 99.5%), iron oxide (Alfa Aesar, 99.5 %), boron (SB95 by SB Boron, 95 %), melamine (Sigma Aldrich, 99 %), and food grade sucrose. For the process control agents, hexane and acetonitrile (both by Alfa Aesar, 99.5%) were used. In most experiments involving the planetary mill, each milling jar was charged with a total of 24 ml PCA. In experiments with aluminum, the total volume of PCA was 37 ml. Mixed solvent compositions ranged from 6.25 vol-% to 75 vol-% acetonitrile. Milling containers

were loaded in a protective argon atmosphere. A parameter found to be important for formation of spherical particles was solid to acetonitrile volume ratio. This ratio varied from 0.06 to >99 (for milling in pure hexane); microsphere formation was observed in the range 0.75-2.

6.4 Results

Electron images of microspheres prepared by mechanical milling in the presence of a blend of hexane and acetonitrile are shown in figure 6.1, and compared to their precursor powders. Images for additional materials are shown in figure B.1 (appendix B). The microspheres consist of densely packed fine precursor particles but have a strikingly different morphology. The sizes of the spheres vary in the range of ca. 1 – 100 μm (see Figure B.2 in Appendix B). Precursor materials tested in this work include metals, metalloids, oxides, and organic compounds. Mechanical properties vary from very hard (boron) to ductile (aluminum) or brittle (melamine). Composite microspheres have been prepared by mechanical milling as well, e.g., combining a metal and oxide powders and combining metal and metalloid. For some precursors, e.g., fumed silica, the resulting spheres are fragile and tend to break upon recovery and drying. However, none of the microspheres prepared to date, including those that retain their shapes after drying, as shown in figure 6.1, have included any binder, which can be readily added when structural integrity of the microspheres needs to be improved. The spherical particles shown in figure 6.1 consist of smaller primary particles that could represent the starting material directly such as in the case of the iron oxide used here, or that could form from initially coarser starting powder, such as in the case of Al. A comparison of particle size

distributions for initial materials and resulting spherical particles is shown in figure B.2 (see Appendix B).

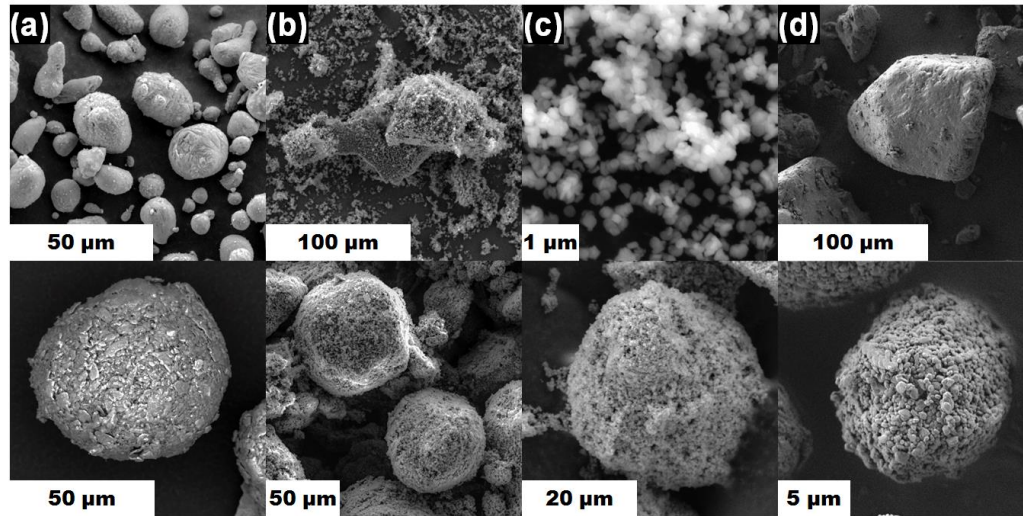


Figure 6.1 Electron images of starting materials (top) and resulting microspheres (bottom) of (a) Al, 1.25 h (b) B, 4 h (c) Fe₂O₃, 1 h (d) melamine, 1 h after premilling

Figure 6.2 shows cross-sections of microspheres of Al, Fe₂O₃, and composite microspheres of Al·CuO, Al·Fe₂O₃, and Al·B. For the ductile aluminum, typically forming flakes during mechanical milling, the microspheres contain packed flakes, which are, however, not fused together. The flakes packed inside the spheres are positioned at different angles to the sectioning plane, explaining a significant spread of their cross-section areas seen in figure 6.2. For iron oxide, consisting of nano-sized primary particles, such particles are packed to nearly full density inside the microspheres. Among the composites, the Al·CuO thermites assumed spherical shape with visible pores while Al·Fe₂O₃ and Al·B appear denser in comparison. For all materials, porosity of the microspheres is found to depend on the milling time. Longer milling times typically lead to finer and denser microspheres. However, longer milling times can lead to finer and denser microspheres; supporting evidence is shown in Figure B.2 (see Appendix B).

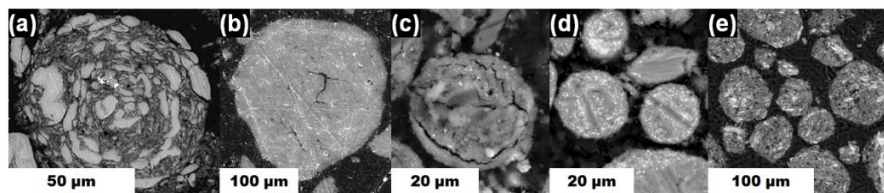


Figure 6.2 Backscattered electron images of cross sections of microspheres of (a) Al, 1.25 h (b) Fe₂O₃, 1 h (c) Al·CuO, 1 h (d) Al·Fe₂O₃, 1 h (e) Al·B, 1 h.

The formation mechanism of microspheres is not presently understood. Microspheres are observed with about equal volume fractions of solid powder precursor and acetonitrile, and with a hexane volume fraction greater than 50 %. An overview of solvent compositions and solid volume fractions where microsphere formation was observed is shown in figure 6.3a. In the resulting emulsion, the mildly polar acetonitrile typically wets the solids better than hexane. Particles suspended in acetonitrile tend to deagglomerate, while solids suspended in hexane agglomerate readily. The specific pattern of mechanical agitation does not appear to be important because spheres are observed in both shaker and planetary mills. The milling times needed to generate microspheres vary for different precursors. However, proper conditions for microsphere formation were found for all precursor powders tested so far.

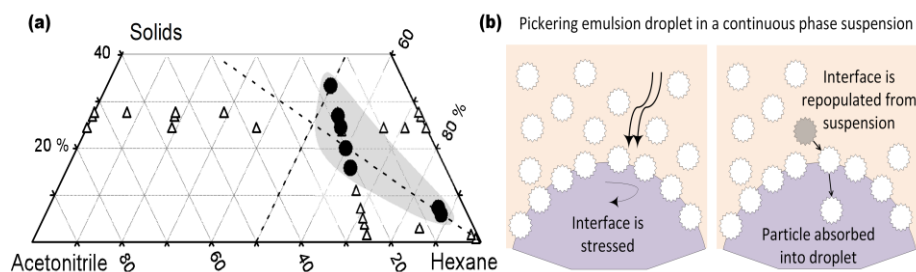


Figure 6.3 Summary compositional map of solvent compositions for all materials discussed in the text. Filled symbols show where microsphere formation was observed, open symbols show where microspheres did not form. Dashed lines indicate 50 vol-% hexane, and an acetonitrile/solids volume ratio of one, respectively. (b) Schematic illustration of microsphere formation mechanism.

Formation of composite spherical particles when a powder is combined with two immiscible liquids bears similarity to formation of Pickering-Ramsden (PR) emulsions [146] and colloidosomes [147, 148]. In all such cases, emulsion droplets are stabilized by solid particles located at the liquid interface. These particles, partially wetted by both liquids, become immobilized and are difficult to remove from the interface. In PR emulsions, there are no solids in the droplet interiors. Partially filled droplets or colloidosomes were formed using double emulsions [148, 149]. In contrast, microspheres prepared here are filled to much greater extent and have distinctly different structures.

We propose that microspheres form as a result of high-energy, high-shear interactions of a PR emulsion and a high-concentration suspension. A PR emulsion forms quickly when two immiscible liquids are combined and agitated if both partially wet the powder(s) being milled. Because the volume fraction of acetonitrile in the present effort is always smaller than that of hexane, it is proposed that acetonitrile forms droplets in the continuous phase of hexane. Considering typical mass load of powder found to be suitable to prepare the microspheres, solid particles stabilized at the liquid interface account for only a small fraction of the powder loaded in the mill. The rest of the powder remains suspended in the continuous phase. The resulting system including both a PR emulsion and a dense suspension in the continuous phase is unusual and has not been studied previously.

Milling subjects the liquid interface to significant shear stress. This has been reported to generate defects and lead to removal of particles from the liquid interface, and destabilization and destruction of PR emulsion droplets.[150] However, in this work the interface is stressed in a continuous liquid densely filled with suspended particles; such particles are expected to rapidly replace particles at the liquid interface, and to effectively

“repair” any damage to the PR emulsion droplets. This process is schematically illustrated in figure 6.3b. As the droplet surface is strained, a particle from the surface may move to the droplet interior. If the particle does not return to the surface, the remaining particles rearrange. As continued energy input removes more particles from the surface, the number density of particles at the surface decreases until the droplet either breaks up, or other particles from the bulk liquid become trapped at the liquid interface. It is proposed that in the presence of an agitated, densely loaded suspension, particle movement from the bulk suspension to the interface may be faster than either breakup of the droplet, or return of particles from the droplet interior to the liquid interface. As a result, solid particles accumulate in acetonitrile droplets and eventually form filled microspheres as shown in figure 6.1 and 6.2.

There could be both thermodynamic and rheological (kinetic) reasons supporting the proposed mechanism of formation of filled microspheres. If the liquid inside the droplet wets the particle better than the continuous liquid, there is an energetic benefit of transferring the particles from the continuous phase into the droplet. Additionally, when the concentration of particles in the droplet is sufficiently high, capillary forces may hold these particles together.

Kinetically, particles in the continuous phase and those in droplets have different motion patterns and thus have a different likelihood of interacting with the surface. Within the continuous phase, particles follow the fluid flow, while particles in the droplet move with the droplet. With any slip between droplets and the suspension in the continuous phase, the speed of particles relative to droplets can be substantial, as expected to occur during mechanical milling. Internal flows are much weaker than the flows in the continuous

phase, and increasingly impeded as more particles accumulate in the droplets. As a result, the emulsion droplets may become mechanically stable as the particles in the droplet accumulate. Additionally, if the suspended particles are substantially denser than the liquid of the continuous phase, they could move by inertia, impacting droplets ballistically. A related mechanism was recently proposed to explain penetration of suspended oil droplets by solid debris subject to a turbulent flow[151].

During milling, the amount of powder suspended in the continuous fluid progressively diminishes. Mechanical agitation may lead to destabilization and repair of the liquid interface as long as the concentration of the suspended particles in the continuous phase remains sufficiently high. In a batch process, once the suspension becomes used up, the droplets may break more readily. For a given powder mass load, the filled spherical particles can form in a specific time interval during processing. Once the destabilized droplets break apart, it is unlikely for the released and rather agglomerated particles to be suspended again. Instead, they may form clusters of suspended particles too large to stabilize the liquid interface and to form emulsion droplets.

Observation of any of the described processes in situ is challenging due the complex motion of the milling containers and lack of optical access. Experiments investigating transport of particles across strained liquid interfaces may help in developing a model. In the first step, PR emulsion droplets were formed from hexane, acetonitrile, and suspended aluminum particles by ultrasonic agitation, as shown in figure B.4 (see appendix B). It may be possible in future work to immobilize such droplets in a microfluidic device and observe the interaction with a suspension directly.

6.5 Conclusion

This work shows that the preparation of filled composite spherical particles is feasible using ball milling in presence of PCA comprising immiscible liquids for a broad range of powders. We hypothesize that the process is universal and is suitable for preparing both organic and inorganic spherical particulates with tunable compositions, sizes and porosities. The solid to liquid ratio, specifically focusing on the liquid forming emulsion droplets is critical. While preliminary in nature, these findings suggest ways to tune and control properties of the prepared spherical particulates. In addition to the parameters explored here, one can certainly vary the intensity of agitation, e.g., changing the type and size of milling media, RPM for the mill, and ball to powder mass ratio. Exploring PCAs comprising of different immiscible liquids and further tuning the PCA properties adding customized surfactants may add effective ways of further controlling the material synthesis process proposed here.

CHAPTER 7

SPHERICAL BORON POWDERS PREPARED BY MECHANICAL MILLING IN IMMISCIBLE LIQUIDS

7.1 Abstract

Spherical boron powders with sizes ranging from 4 to 100 μm were prepared by ball milling a commercial boron powder. A planetary mill was used with a process control agent consisting of two immiscible fluids: hexane and acetonitrile. The spherical powders formed when the volume of the loaded boron was close to that of acetonitrile in presence of excess hexane. Particle sizes were measured using low-angle laser light scattering, they were examined using scanning electron microscopy, and their specific surface area was measured using nitrogen adsorption. The size distributions of the prepared spheres were much narrower than is common for solids processed by high-energy milling. Spherical particles were fragile; their mechanical stability was improved when a small amount of Fluorel®, a fluorocarbon binder, was preliminarily dissolved in acetonitrile. Experiments showed that the prepared spherical powders exhibited a higher bulk density and much better flowability than starting boron powder. Process-property relations were explored by systematically varying milling parameters and analyzing their effect on the size distribution of the formed spheres. The size of spherical particles was found to decrease with the decrease in the amount of acetonitrile used; it was also decreased with an increase in milling time, number of milling balls, and speed of milling.

7.2 Introduction

Boron powders are attractive fuel additives having the gravimetric and volumetric heats of combustion exceeding those of any hydrocarbon fuels and most other metals. However, boron powders are cohesive and hard to process. Mixing boron with common binders, such as hydroxyl-terminated polybutadiene (HTPB) is often difficult because of an increased viscosity of the binder with added boron [152]. An increase in viscosity upon heating [153] is particularly problematic as affecting proper curing of the energetic formulations. Boron powders prepared by different methods comprise nano-sized primary particles forming agglomerates with broad size distributions [154]. These broadly sized agglomerates exhibit poor flowability and cause undesirable slag formation during combustion [155]. This irregular self-agglomeration greatly hampers uniform and stable burning of propellants [156]. Boron agglomerates are also clogging nozzles of the propulsion systems [157]. To improve mixing boron with binders, such as HTPB, their rheological properties have been modified by mixing of coating with LiF [158], adding pre-processing agents, such as acetic ether [159], or by surface treatment with ammonia or sodium hydroxide [160]. In addition, rheological properties and size distributions of boron powders were manipulated using granulation [152], extrusion-spheronization [161], and wet milling [162], all with limited success. Studies involving electrospray to prepare boron-bearing composites have also been reported [156, 163], however, they involve additional stages of chemical processing, undesired residues and typically are hard to scale up for practical applications [164]. In this study, a simple, scalable and cost-effective way of improving rheological properties of boron is introduced. Micron sized boron spheres were prepared by mechanically milling a common, commercial boron powder. The spheres have a narrow size distribution and a

dramatically improved flowability. The preparation method is developed based on recent research showing that porous spherical powders can be obtained by mechanical milling diverse solid precursors in presence of a blend of immiscible liquids: hexane and acetonitrile introduced as a process control agent [165]. Our work demonstrates how tunability of particle size and sphere stability can be achieved by varying the volume ratio of the immiscible liquids, the mass of the milling media, milling speed and milling time. We further extend the focus of this study to address property correlations of the prepared spherical boron with the associated milling parameters. Correlating properties of the resulting powders with the milling conditions used to prepare the powder is complex. Even though some studies investigated this aspect for regular powder, very little has been done quantitatively [42]. Given the importance of spherical powders for efficient material processing, this study lays the basic groundwork for quantitatively predicting powder properties based on milling parameters.

7.3 Experimental

7.3.1 Materials Preparation

Boron spheres were prepared using a Retsch PM400 planetary mill. Boron powder SB-95 (95% purity) supplied by SB Boron Corp., was loaded into milling vials inside a glove box filled with argon. Hexane (95% pure) and acetonitrile (99.5% pure) by Alfa Aesar were used as process control agents for all materials. For most materials, Fluorel®, a fluorocarbon by 3M was dissolved in acetonitrile (0.5 or 1 %) preliminarily to serve as a binder improving the mechanical integrity of the produced spheres. Two types of hardened steel vials were used. Type 1 was a custom-made 175-mL vial with diameter of 6.35 cm (2.5 inch). Type 2 was a regular, 500-mL vial with diameter of 10.16 cm (4 inch). The

milling media used were hardened steel balls with diameter of 9.525 mm (3/8 inch). The overall liquid process control agent volume was constant (24 ml for vial type 1, 48 ml for vial type 2). A number of milling parameters such as time, RPM, mass of milling media, and liquid ratio (LR, volumes of hexane to acetonitrile: $V_{\text{Hex}} / V_{\text{ACN}}$) were varied as shown in table 7.1. For each material, the volumes of acetonitrile and powder were the equal to each other. Theoretical density of boron (2.37 g/cm^3) was used to determine the volume of powder loaded based on the volume of acetonitrile used. The loaded mass of boron ranged between 7.11 to 14.22 g. To produce mechanically stable spheres, the powders recovered from the milling vials were dried in air for 72 hours, while the binder was cured.

7.3.1 Material Characterization

After milling the materials were dried for 72 hr under vacuum. Particle morphology was investigated using JEOL JSM 7900F field emission Scanning Electron Microscope (SEM) operated at 10 kV. Particle size distributions were measured using a Malvern 3000 Mastersizer. With ethylene glycol as the dispersant, the obscuration ranged between 4 to 6 % throughout all measurements. The suspended samples were continuously stirred at 2500 RPM. In separate measurements, ultrasonic agitation at 20% was additionally introduced to examine the mechanical stability of the spherical powder particle. Three consecutive measurements were recorded first without, then with sonication.

An Autosorb iQ (model ASIQM000000-6) analyzer by Quantachrome Instruments was used to measure specific surface areas of the prepared powders by nitrogen adsorption. Samples were degassed at 200°C under vacuum for 12 hr. The sample charge for surface area measurement ranged from 150 to 250 mg.

To characterize material properties particularly relevant for powder flowability and packing, the following properties were determined for a subset of materials prepared: bulk tapped density, electrostatic charge buildup due to agitation, and a cohesive index as further expanded below. A preliminary measurement of bulk density for all prepared powders used the mass of solid loaded in a 2-mL vial. A more accurate measurement of the bulk density for the reference boron and for selected spheres (IDs 4 and 5, cf. table 7.1) of powders was performed using a GranuPack high resolution tapped density analyzer by Granutools [166]. After 35 ml of the powder were automatically poured into a holder, 1-mm taps were applied to the sample. Bulk density was measured after each tap by use of an inductive sensor with sufficient resolution to measure the entire range of densities. The Hausner ratio, defined as the ratio of the tapped bulk density $\rho(\infty)$ to the initial (loose) bulk density $\rho(0)$ is used as a flowability index [167]. A dynamical parameter $n_{1/2}$, corresponding to the number of taps to reach half of the packing amplitude $(\rho(\infty)+\rho(0))/2$, gives information on the kinematics of packing [168]. Cohesive index, a measure of powder cohesiveness, was quantified using GranuDrum by Granutools employing the rotating drum principle [169]. Additionally, tribocharging properties of powder samples were measured using GranuCharge electrostatic charge analyzer, also by Granutools [170]. Electrostatic charging causes agglomeration of particles, which leads to poor flowability. In other words, this charge density is an additional measure of particle cohesiveness.

Table 7.1 Milling Parameters Used to Prepare Different Boron Powders. 5% Fluorel® Solution in Acetonitrile was used unless Noted Otherwise

Mass of boron (g)	Volume of acetonitrile (ml)	ID	Volume of hexane (ml)	LR ($V_{\text{Hex}}/V_{\text{ACN}}$)	Milling media mass (g)	Milling time (hr)	RPM	Vial Type
14.22	6	1*	--	--	90	1	350	1
		2**	18	3	90	1	350	1
		3	18	3	90	1	350	1
		4	42	7	180	1	275	2
		5***	42	7	180	1	275	2
		6	42	7	180	1	220	2
		7	18	3	90	1	400	1
		8	18	3	90	1	400	1
		9	18	3	90	1	350	1
		10	18	3	77	1	400	1
		11	18	3	105	1	400	1
		12	18	3	77	1	350	1
		13	18	3	105	1	350	1
		14	18	3	90	0.75	350	1
		15	18	3	90	1.5	350	1
11.85	5	16	19	3.8	90	1	350	1
		17	19	3.8	90	1	250	1
9.48	4	18	20	5	90	1	400	1

		19	20	5	90	1	350	1
		20	20	5	90	1	350	1
		21	20	5	77	1	400	1
		22	20	5	105	1	400	1
		23	20	5	77	1	350	1
		24	20	5	77	1	400	1
		25	20	5	105	1	350	1
		26	20	5	90	0.75	350	1
		27	20	5	90	1.5	350	1
7.11	3	28	21	7	90	1	400	1
		29	21	7	90	1	350	1
		30	21	7	90	1	250	1
		31	21	7	90	1	250	1
		32	21	7	105	1	300	1
		33	21	7	90	1	300	1
		34	21	7	77	1	300	1
		35	21	7	105	1.5	300	1
		36	21	7	90	1.5	300	1
		37	21	7	77	1.5	300	1
		38	21	7	105	1.5	250	1
		39	21	7	77	1.5	250	1

* milled in 6 ml acetonitrile with 0.5% Fluorel® solution and no hexane

** milled with no Fluorel® dissolved in acetonitrile

*** milled in acetonitrile with 1% Fluorel® solution

7.4 Results

Powder particle shapes and the tunability of the powder particle sizes achieved by varying milling parameters are illustrated in figure 7.1. It appears that the size of spherical powder particles decreases with increase in both LR and RPM. It is also apparent that most particles have spherical shapes and that the particle sizes are rather uniform. Boron powder exhibiting such uniform and narrow size distribution has not been reported previously. Commercial boron, (see appendix C, figure C.3) shows irregularly shaped, fractal boron aggregates with a wide size distribution and consisting of nanosized primary particles[17].

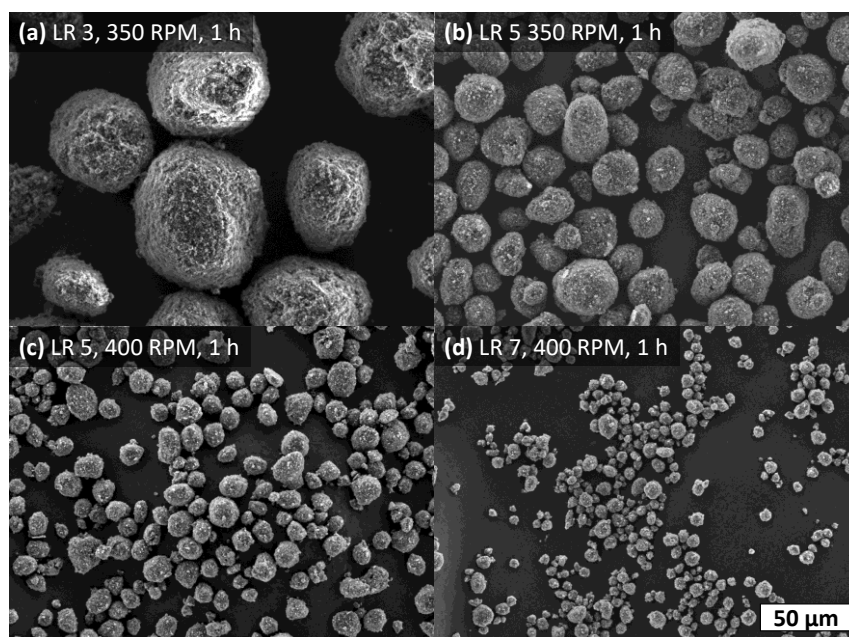


Figure 7.1 SEM images of powders prepared in vial type 1 using different milling parameters. Powder IDs refer to table 7.1. (a) 12; (b) 23; (c) 18; (d) 28

The relationship between milling parameters and produced powder particle size distribution is further illustrated in figure 7.2 for a set of representative powders. For each material, two size distributions are shown. The first one is measured without sonicating the powder suspension in the Mastersizer. After that measurement was obtained, the

suspension was sonicated to assess mechanical stability of spherical particles. For stable powders, both measured size distributions were close to each other. If particles disintegrated, the second size distribution became broader and included finer particles. For reference, the size distribution for the starting SB-95 boron powder is shown on top of figure 7.2. It is rather broad and bimodal. Particles with sizes from 0.25 to 95 μm are observed. Labels for size distributions of the milled powders in figure 7.2 refer to the ID from table 7.1. Powder 1, milled in acetonitrile (6 ml) without hexane does not contain spherical particles. The size distribution is very broad. Upon sonication, large agglomerates break apart yielding a powder with broad range of particle sizes, which is somewhat finer than the starting material. Powder 12 (LR 3, 350 RPM) consists of large spherical particles with a mode at 92 μm before sonication. The size distribution is symmetric and rather narrow. After sonication, the particles largely disintegrate, forming a broad bimodal distribution of much finer particles. Powder 23 (LR 5 350 RPM) contains somewhat finer particles with the mode around 30 μm before sonication; the size distribution is broader and less symmetric than for powder 12 before sonication. It also includes a significant fraction of larger particles or agglomerates. Upon sonication, the agglomerates break while the position of the original size distribution mode remains unchanged. The size distribution becomes narrower, although significant portion of very fine particles is also detected. The other two powders illustrated in figure 7.2, 18: LR 5, 400 RPM and 28: LR 7, 400 RPM, show almost no change in the particle size distribution upon sonication. Powders 18 and 28 prepared at higher LR values exhibit narrow particle size distributions with modes at 13 and 7 μm , respectively. Generally, the particle size distributions shown in figure 7.2 are in good agreement with the particle sizes observed in the SEM images shown in figure 7.1.

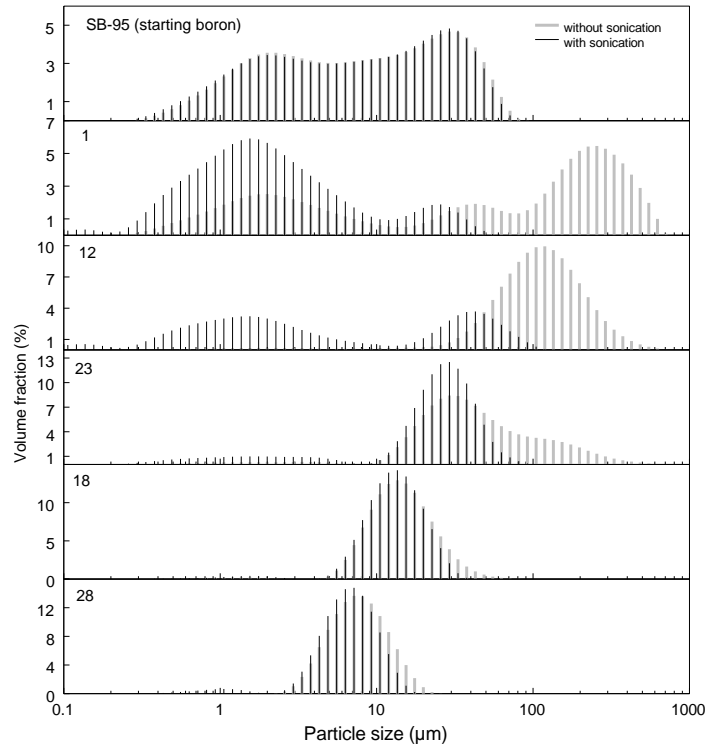


Figure 7.2 Particle size distributions for different boron powders (IDs as in table 7.1) measured by low-angle laser light scattering without and with sonication of the powder suspension.

Nitrogen adsorption measurements show that the specific surface areas for milled powders are higher than that of the starting boron, results are shown in figure 7.3 (a). All spherical powders packed better than starting boron, yielding greater bulk density based on the mass of powder placed in a 2-mL vial, as shown in figure 7.3(b). Characteristics of the measured particle size distributions, surface areas, and bulk densities preliminarily assessed for all powders are shown in table 7.2. Consistent with figure 7.3(b), all milled spherical powders pack better than the starting boron yielding greater bulk densities. To quantify differences in the measured particle size distributions observed before and after sonication, a parameter quantifying relative shift in the mode is introduced. It is calculated as relative change in the mode, $\frac{d_{m1}-d_{m2}}{d_{m1}}$, where d_{m1} and d_{m2} are modes before and after

sonication, respectively. Illustrations of the change in size distributions of some of the spherical particles due to sonication is shown in appendix D (figure C.4). The width of the measured size distribution was quantified using span calculated as $\frac{d_{90}-d_{10}}{d_{50}}$, where d_{10} , d_{50} , and d_{90} are the particle diameters representing 10, 50, and 90 % in the measured distributions, respectively.

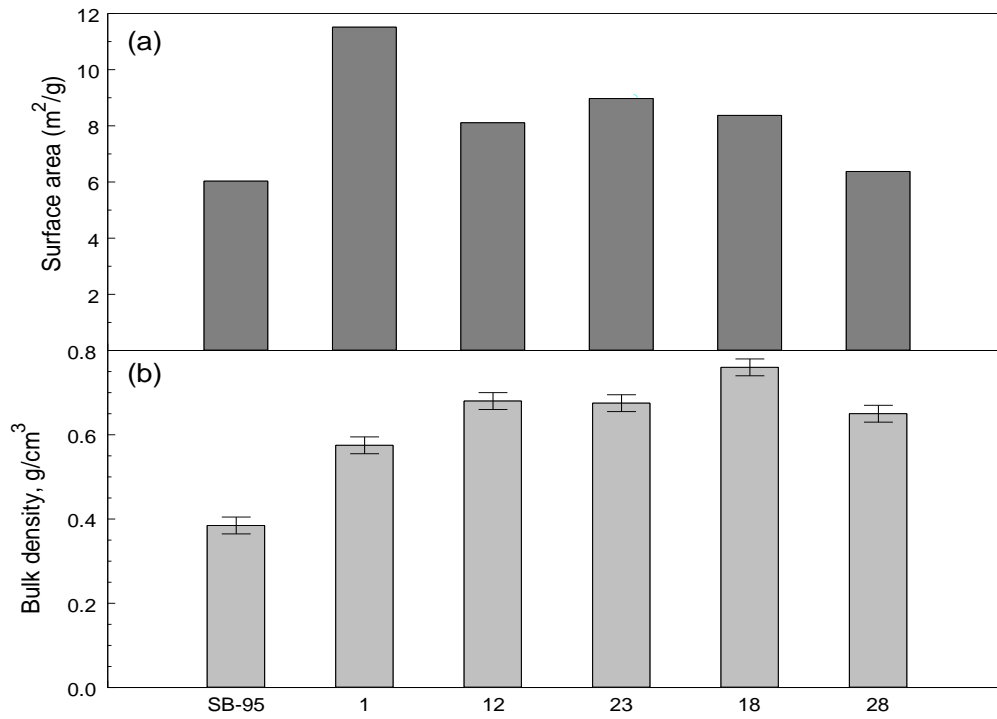


Figure 7.3 Specific surface areas (a) and bulk density (b) of selected boron powders

The measurements of packing curves, cohesive index, and tribocharging required larger amounts of material. Therefore, spheres prepared in the larger, type-2 milling vials were chosen as representative. The packing curves measured for selected powders (4 and 5), and for the reference SB-95, using Granupack are shown in figure 7.4. Consistently with figure 7.3, the initial bulk density of SB-95 is lower than that of the milled powders. Only small difference is detected between characteristics of the two milled powders

prepared with 0.5 and 1% solutions of Fluorel® in acetonitrile. The tapped density achieved after 500 taps is substantially higher for the spherical powders than for SB-95 . For spheres, it reaches ca. 0.72 g/cm^3 , which is more than 30 % of theoretical maximum density (TMD). For SB-95, only 0.49 g/cm^3 is reached by the end of measurement, which represents just over 20 % of TMD for boron. Even for spherical powders, the density is less than one half of that expected for the densest packing for spheres, close to 0.74 TMD. A significantly higher Hausner ratio is measured for SB-95 (1.50) than for powders 4 (1.26) and 5 (1.27). This indicates a stronger cohesive behavior of SB-95, arising from interactions between the particles. These cohesive interactions oppose the free reorganization of the grains preventing the powder from minimizing its potential energy by better packing. The $n_{1/2}$ parameter gives information on the dynamics of packing. SB-95 exhibits a $n_{1/2}$ value of 43, two times higher than for spheres, denoting slower packing dynamics. Therefore, the spherical shape of the milled powders leads to faster and better packing.

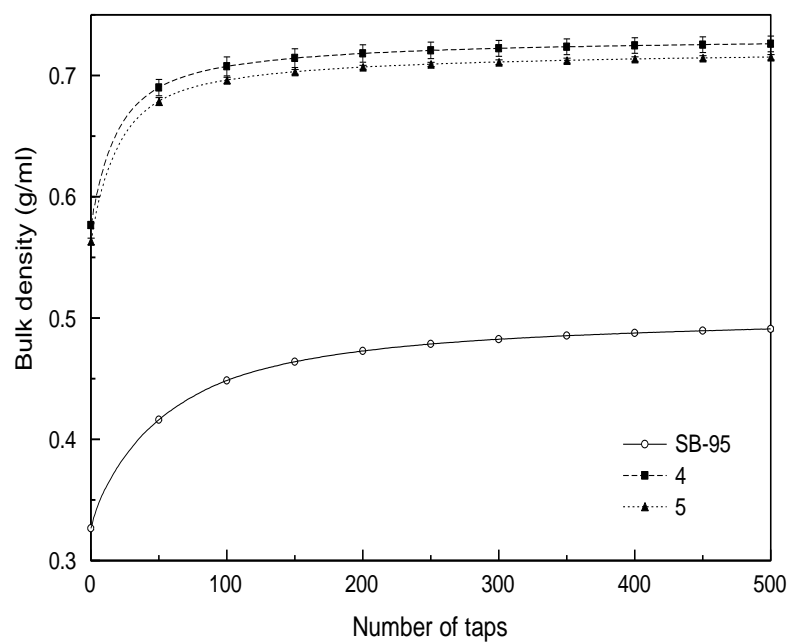


Figure 7.4 Granupack measurements of bulk density for SB-95 and prepared powders 4 and 5. Error bars are standard deviations around the mean computed over three independent tests for clarity, only selected experimental points are marked by symbols.

Table 7.2 Characteristics of the Particle Size Distributions, Surface Areas, and Bulk Densities Evaluated based on the Mass of a Powder-filled 2-mL vial

ID	Mode* before sonication d_{m1} (μm)	$\frac{d_{m1}-d_{m2}}{d_{m1}}$	Span	Specific surface area (m^2/g)	Bulk density** (g/cm^3)
1	255	0.99		11.51	0.57
2	92	0.98	2.3	13.53	0.75
3	92	0.98	2.1	13.32	0.77
4	8	0.11	1.1	13.71	0.61
5	9	0	1.5		0.60
6	10	0	1.0	14.29	0.64
7	224	0.85	2.2	19.46	0.78
8	174	0.99	2.1	11.08	0.81
9	92	0.63	2.1	13.53	0.77
10	81	0.63	2.9	8.98	0.74
11	197	0.83	2.2	11.35	0.70
12	118	0.63	1.7	8.10	0.68
13	92	0.63	1.8	11.10	0.68
14	92	0.68	1.8	8.215	0.79
15	71	0.47	1.4	11.12	0.74
16	135	0.68	1.9	16.44	0.74
17	135	0.53	1.6		0.70

18	13	0	1.3	8.36	0.76
19	71	0.11	1.4	11.73	0.77
20	11	0	2.8		0.57
21	42	0.11	2.9	11.31	0.75
22	8	0.11	2.1	9.08	0.55
23	29	0	3.5	8.97	0.67
24	92	0.31	1.6		0.76
25	29	0.11	2.9	10.10	0.64
26	42	0.11	2.0	9.61	0.76
27	11	0	1.2	11.11	0.74
28	7	0	1.1	6.37	0.65
29	13	0	0.8	13.16	0.61
30	17	0.11	2.4	18.61	0.62
31	19	0	2.8		0.53
32	8	0	1.4		0.59
33	13	0	1.3		0.51
34	25	0	1.2		0.61
35	6	0.11	1.1		0.61
36	22	0	6.5		0.67
37	17	0.11	1.8		0.60
38	174	0.68	1.8		0.70
39	62	0.22	2.2		0.74

* Uncertainty of the mode: ± 0.06 log units

** Uncertainty of the bulk density: ± 0.02 g/cm³

Results of the cohesive index measurements performed using GranuDrum are shown in figure 7.5 for the same powders as used for measurements shown in figure 7.4. The cohesive index measure is based on the temporal fluctuations of the powder/air interface and is directly related to the intensity of cohesive forces acting between the grains [171]. At the lowest rotating speed of 2 rpm the SB-95 and milled powders exhibit a similar cohesive index around 40. However, upon increasing the rotating speed the behavior of SB-95 becomes qualitatively and quantitatively different from that of the prepared spherical powders. Indeed, the spherical powders show a shear-thinning behavior, i.e., a decrease of cohesiveness with increasing rotating speeds. At the opposite, the SB-95 remains very cohesive and could not usefully be measured with the drum speed increasing above 20 rpm due to heavy clogging of the powder. These results demonstrate the major improvement of flowability for the milled spherical powders compared to starting boron SB-95. Upon the end of these experiments, performed by Granutools in Belgium, the particles used in experiments were shipped back to the USA and evaluated using SEM and Mastersizer. It was found that spherical shapes and particle sizes were largely preserved despite the aggressive mechanical agitation during measurements and overseas shipping.

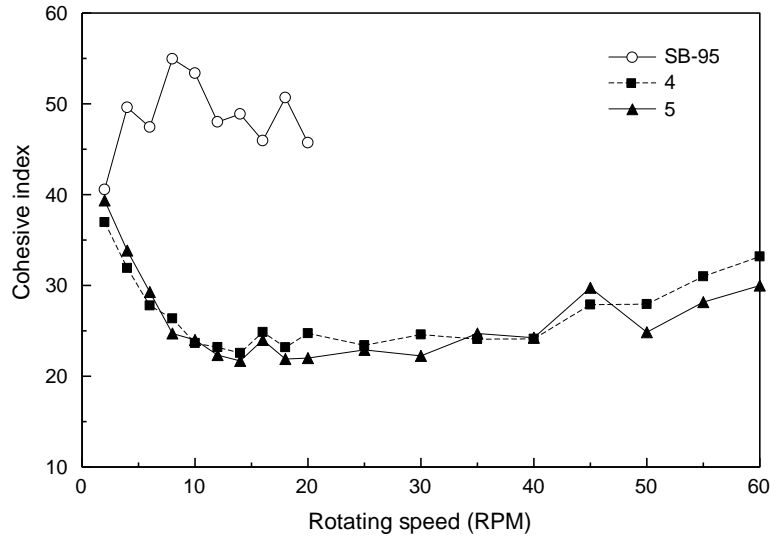


Figure 7.5 Cohesive index using GranuDrum for SB-95 and powders 4 and 5.

Finally, the sensitivity of the powders to charge buildup has been investigated with the GranuCharge [17]. The instrument is composed of a Faraday cup allowing to measure low charge density in powders. Initially, 55 ml of powder is poured inside the cup to measure its initial charge density q_0 . Then, the powder is taken from the cup and poured in a vibrating feeder. The feeder pours the powder through a stainless steel (SS316L) V-shape tube to the Faraday cup to measure its final charge density q_f . The difference between q_0 and q_f gives the variation of charge density Δq arising from triboelectric effect due to the flow through the tube. Obtained charge densities are presented in figure 7.6. All powders exhibit a negative initial charge density (q_0), slightly lower for SB-95. The initial charge density may be affected by how the powder was handled prior to the measurement. After flowing through the steel tube, spherical powders exhibit a negative charge buildup. Conversely, the charge density of SB-95 is reduced with the final charge density close to zero. This result indicates that the spherical powders are more sensitive to tribocharging than the starting boron. Exchange of charges arise mainly at the surface of the particles

during frictional contact, thus a higher specific surface area for spherical particles (which are also less agglomerated) may have led to the observed higher charge build-up compared to SB-95.

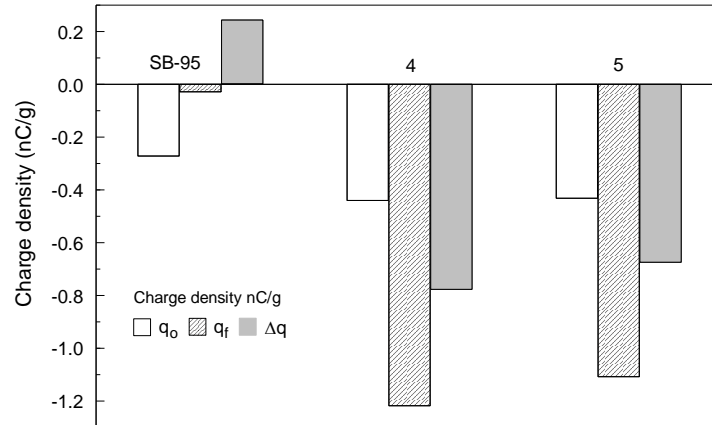


Figure 7.6 Initial q_0 and final q_f charge densities and the difference Δq for SB-95 and powders 4 and 5 measured by GranuCharge.

An additional indicator of mechanical stability of the prepared powders was obtained examining the powders 4 and 5, which were shipped from the USA to Belgium for analyses and shipped back. Particle size distributions for the powders experiencing experimentation at Granutools and shipment overseas were measured and shown in appendix C, figure C.1. It is apparent that the particle size distributions for spheres were largely preserved.

Another interesting observation was obtained when the prepared spherical powder was attempted to be sieved. Powder 29 was placed on a 20- μm sieve. It was observed that the entire sample readily passed; the sieved particles are shown in Appendix C Figure C.2. It is apparent that the particles are unaffected by the sieving.

7.5 Effects of Milling Parameters on Properties of the Produced Spheres

In experiments described in table 7.1, the following milling parameters were systematically varied: acetonitrile volume (or LR), ball mass, RPM, and milling time. The results of these experiments were evaluated in terms of particle size distribution, specific surface area, and particle packing density (table 7.2). From the aggregated data, some coarse trends can be observed. As an example, figure 7.7 shows that the particle size depends noticeably on the amount of acetonitrile used.

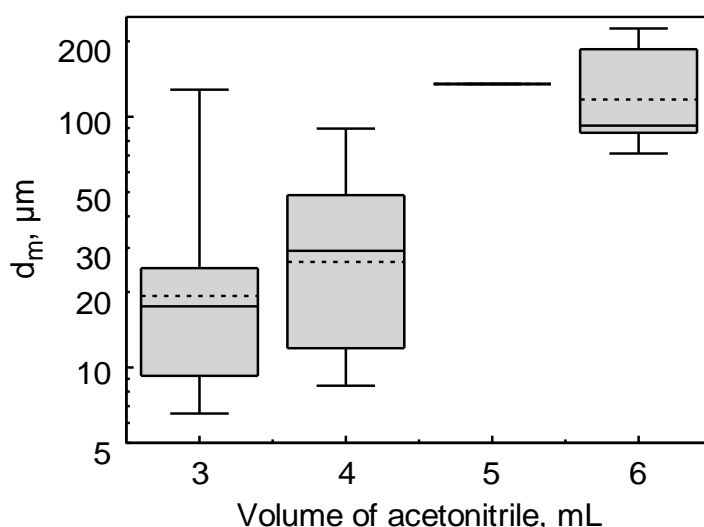


Figure 7.7 Coarse correlation of the mode of the particle size distribution and the amount of acetonitrile used. Horizontal elements indicate 10th, 25th, 50th, 75th, and 90th percentiles. The average is indicated by dashed lines.

Mechanical stability served as an additional characteristic of the materials: some particles disintegrated when the suspension in the size analyzer was sonicated. This is reflected in the difference between two subsequent measurements, first without, then with sonication applied (figure 7.2 and table 7.2). Particle size distributions that became wider and shifted to smaller sizes and those that did not change significantly were considered mechanically unstable and stable, respectively. The ratio of the mode of the volume-based

particle size distribution after sonication, $d_{m,2}$, relative to the mode before sonication, $d_{m,1}$ is shown in figure 7.8 as a function of $d_{m,1}$. Differences close to 1 are the effect of a shift of one size bin; lower values represent a more significant change. Two trends are evident: the size distributions of smaller particles with $d_{m,1}$ below about 40 μm in size generally do not change when sonicated, while larger particles disintegrate, at least partially.

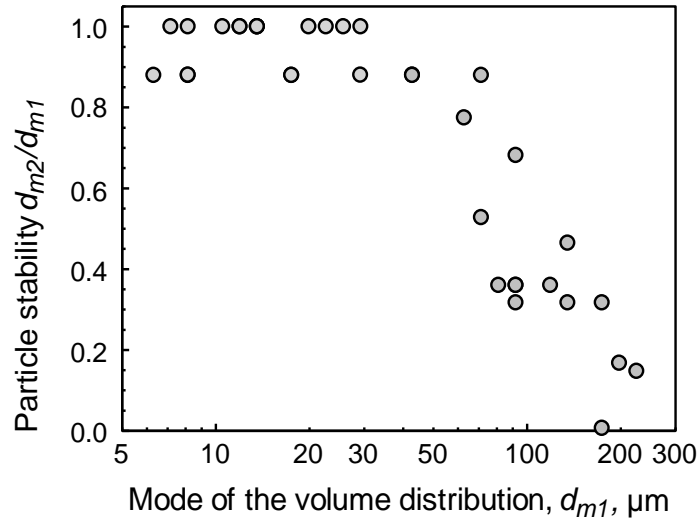


Figure 7.8 Relative change in the mode of the particle size distribution as a result of sonication during the size distribution measurement

To draw a pragmatic distinction between “mechanically stable” particles, and those that do not survive sonication, one can consider particles with a mode of less than 40 μm separately from particles with a larger mode. These smaller, apparently more robust particles, are not uniformly observed over the four-dimensional parameter space covered in the milling experiments (see table 7.3). One possible way to visualize where in the milling parameter space smaller spheres were produced is to consider a histogram of the frequency, with which particles under 40 μm were observed. This is shown in figure 7.9 the three bar plots show the fraction of particles with modes under 40 μm as black bars. All remaining particles are shown as gray bars. Milling conditions that were not covered

experimentally show no bar at all. The three plots (back to front) show the three different milling times used. The horizontal axis shows the volume of acetonitrile used. The other milling parameters, ball mass and milling speed, are not distinguished here. The numbers shown within bars indicate the proportion of experiments where particles with modes under $40\text{ }\mu\text{m}$ were observed. The numbers in parentheses show the total number of experiments performed. It is evident that the smaller particles tend to be observed at longer milling times, and when smaller amounts of acetonitrile are used, notwithstanding the fact that the parameter space is not uniformly covered by experiments. There is also some variability in the observed data. An experiment (powder 19, table 7.1) with milling time of 60 min at 350 RPM with 90 g of balls and 4 mL of acetonitrile resulted in a mode of $11.9\text{ }\mu\text{m}$, while a repetition at identical conditions (powder 20, table 7.1) resulted in a mode of $71.3\text{ }\mu\text{m}$.

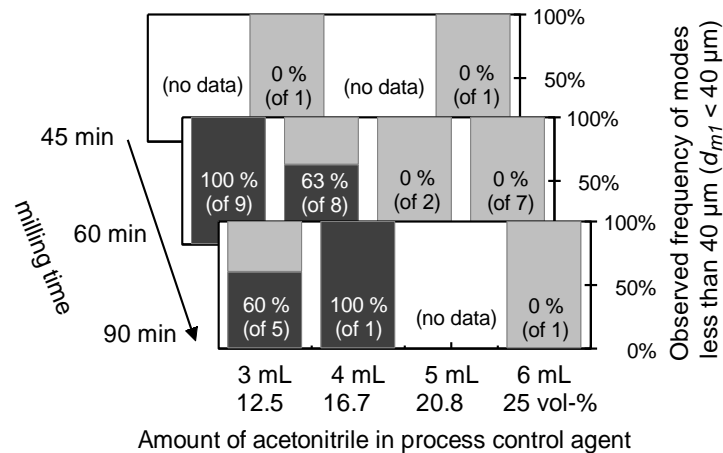


Figure 7.9 Histogram of spherical particles with modes under $40\text{ }\mu\text{m}$ (dark gray bars) at different milling conditions.

For the purpose of exploring how particle sizes depend on milling conditions, only particles with modes under $40\text{ }\mu\text{m}$ were considered, as the size measurements of particles prone to disintegration were deemed unreliable. Further, the mode of the size distribution is not a particularly instructive quantity; at the least it does not reflect the entirety of the

particle size distribution. A more comprehensive representation is found in the sphere surface area SSA (in units of m^2/mL .) In the present analysis, SSA is the spheres' surface area as calculated from the particle size distribution determined by light scattering assuming a spherical particle shape. It reflects the entire powder with contributions from all particle sizes as opposed to the mode representing only a singular particle size. A related measure is the number-surface mean, $d(2,0)$, the particle size with a specific surface area equal to SSA . Both measures are shown in figure 7.10 vs. the mode of the volume distribution, d_{m1} . Despite the rough, and expected correlation, there are significant deviations that primarily reflect differences in the widths of the size distributions.

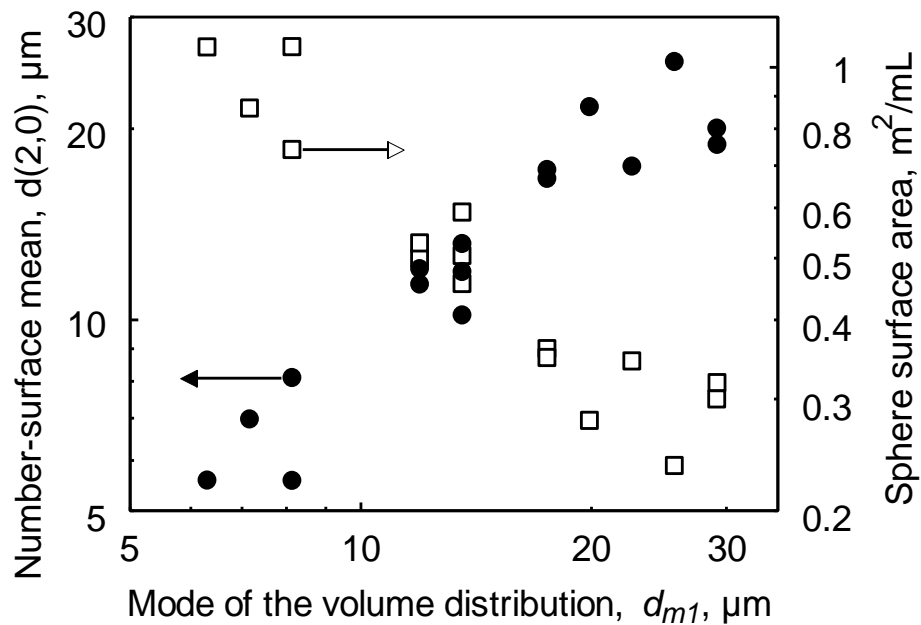


Figure 7.10 Number-surface means and sphere surface areas for particles with modes under $40 \mu\text{m}$.

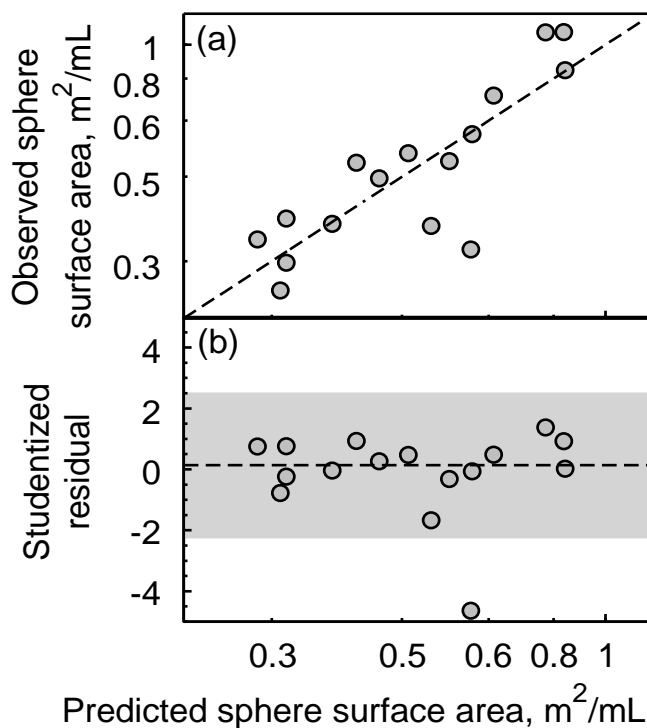
Correlations between milling conditions and the sphere surface areas were explored using a linear model of the form:

$$\ln(SSA) = c_0 + \sum_{i=1}^4 c_i \cdot \xi_i \quad (7.1)$$

Where ξ_i are the milling parameters that were systematically varied, and c_i are the associated coefficients. The resulting coefficients of the model are shown in table 7.3. The model fit is poor, with an adjusted R^2 value of 0.593. Predictions would have large errors as compared with the observed variations. To examine the poor model fit visually, figure 7.11(a) shows the observed sphere surface areas *vs.* the sphere surface areas predicted by the linear model (1). Considerable deviations from a direct correlation, shown as the dashed line, are observed. figure 7.11(b) shows the studentized residuals of the fit, a measure of how far any given observation differs from a prediction that is based on all other observations [172]. The dashed line in figure 7.11 (b) shows the median of the residuals, and the gray band shows ± 3 scaled median absolute deviations around the median [173]. One of the observations clearly falls outside these limits. This outlier result for an experiment milled for 60 min at 350 RPM with 105 g of balls and 4 mL of acetonitrile (powder 25, table 7.1), according to figure 7.9 falls in the boundary region where spherical particles with a mode under 40 μm are observed, and is adjacent to the above mentioned observation of different d_{ml} under identical conditions. Therefore, this outlier may represent the inherent variability associated with milling experiments and, for the purpose of describing the remaining observations, can be removed from consideration.

Table 7.3 Coefficients of Linear Model (1)

Coefficient	Milling parameter, ξ_i	Value	<i>t</i> -value
c_0	-	-4.68 ± 1.03	4.52
c_1, min	ω, RPM	$7.09\text{e-}3 \pm 2.14\text{e-}3$	3.32
c_2, g^{-1}	ball mass, g	$2.91\text{e-}2 \pm 8.25\text{e-}3$	3.52
c_3, mL^{-1}	acetonitrile volume, mL	-0.441 ± 0.204	2.16
c_4, min^{-1}	time, min	$6.60\text{e-}3 \pm 5.95\text{e-}3$	1.11

**Figure 7.11** Comparison of observed sphere surface areas and the results of the linear model (1). See text for details.

The results of the linear model fit without the outlier are shown in table 7.4. The fit has improved with an adjusted R^2 value of 0.858.

Table 7.4 Coefficients of linear model (1) with outlier removed

Coefficient	Milling parameter, ξ_i	Value	t -value
c_0	-	-5.64 ± 0.64	8.75
c_1, min	ω, RPM	$5.99\text{e-}3 \pm 1.28\text{e-}3$	4.67
c_2, g^{-1}	ball mass, g	$3.83\text{e-}2 \pm 5.26\text{e-}3$	7.28
c_3, mL^{-1}	acetonitrile volume, mL	-0.238 ± 0.128	2.16
c_4, min^{-1}	time, min	$4.53\text{e-}3 \pm 3.54\text{e-}3$	1.23

It may be possible to physically interpret the observed correlations. One potential relation lies in the amount of acetonitrile used and the total interface area of the emulsion present during milling, A_{int} , which is reflected in the total surface area of particles, which form inside emulsion droplets. This relation could show how the total energy dissipation rate from the milling tools E_d is balanced by the energy cost of maintaining the total interface area created between the immiscible liquids A_{int} ,

$$A_{\text{int}} \propto \dot{E}_d \approx f(t, \omega, m_b) \quad (7.2)$$

From the sphere surface area of the powder after recovery, SSA and the total volume of the droplet phase, V_{droplets} , the interface area in the emulsion during milling can be estimated as $A_{\text{int}} = SSA \cdot V_{\text{droplet}}$. Assuming that all of the solids enter the emulsion droplets, the total volume of the droplet phase is the sum of the volumes of acetonitrile, V_{ACN} , and milled solids, V_{solids} . Under the constraints used in the present experiments these two are equal to each other, so that

$$A_{\text{int}} = SSA \cdot 2V_{\text{ACN}} \quad (7.3)$$

Using A_{int} instead of the (particle size distribution derived) sphere surface area removes the volume of acetonitrile from the linear model, and therefore eliminates one coefficient. This new linear model is

$$\ln(A_{\text{int}}) = c_0 + \sum_{i=1}^3 c_i \cdot \xi_i \quad (7.4)$$

Where the symbols are defined as in (1), but only operating speed ω , ball mass, m_b , and milling time, t , are used as milling parameters ξ_i . The results of this model fit are shown in

Table 7.5 Coefficients of Linear Model (4)

Coefficient	Milling parameter, ξ_i	Value	t -value
c_0	-	-4.64 ± 0.59	7.87
$c_1, \text{ min}$	$\omega, \text{ RPM}$	$6.31\text{e-}3 \pm 9.48\text{e-}4$	6.65
$c_2, \text{ g}^{-1}$	ball mass, g	$3.81\text{e-}2 \pm 5.03\text{e-}3$	7.57
$c_3, \text{ min}^{-1}$	time, min	$4.54\text{e-}3 \pm 3.40\text{e-}3$	1.34

The model fit (4) is a minor improvement over (1) with an adjusted R^2 of 0.888. Interestingly, the coefficients for the milling parameters remaining in (4) and shown in table 7.5, are nearly identical to the corresponding coefficients of model (1) shown in table 7.4. This suggests that the assumption that the volume of acetonitrile primarily governs the total interface area during milling is reasonable.

All coefficients in table 7.5 associated with different milling parameters are positive, indicating that increasing milling speed, ball mass, or milling time result in smaller particles. The coefficients for milling speed and ball mass are statistically significantly different from zero; all t -values exceed 4, for 11 degrees of freedom (4.024 indicates 99.9 % confidence [174]). The coefficient for milling time has wider confidence

limits and a corresponding lower t -value, however. Most experiments were performed with a milling time of 60 minutes (26), while relatively fewer were performed at 90 minutes (7), and 45 minutes (2), with no d_{m1} of less than 40 μm observed at 45 min. More experiments with a wider time base would be required for a more strongly supported relation between emulsion interface and therefore particle size and milling time.

With the coefficients in table 7.5, it is possible to predict the particle size. The observations and the model predictions at selected milling conditions are shown in figure 7.12. Since the model is based on the emulsion interface area, the resulting predicted particle size is the number-surface mean $d(2,0)$.

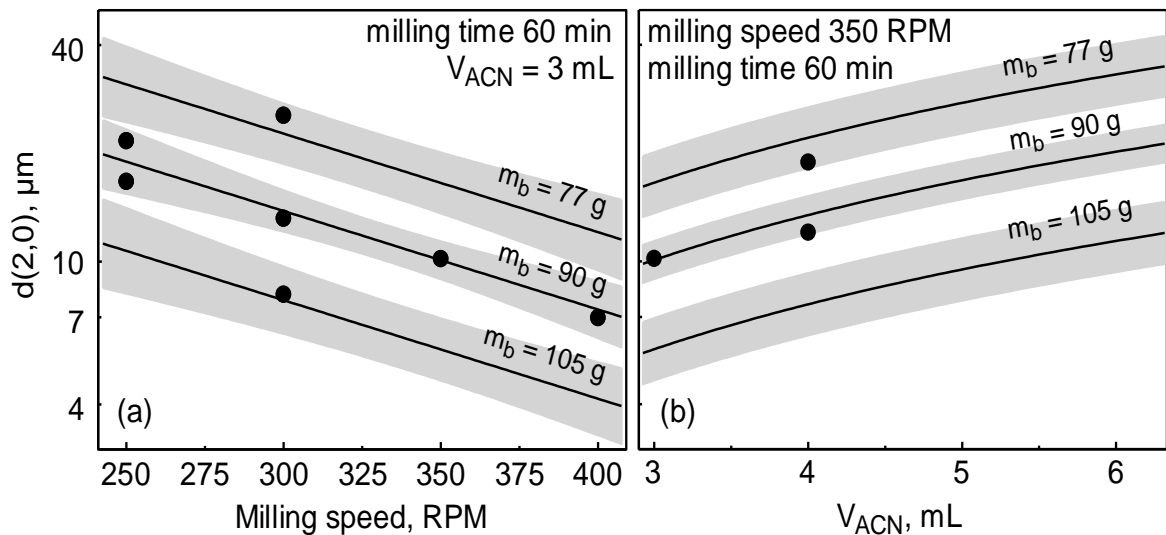


Figure 7.12 Predictions of the linear model (4) with the coefficients shown in table 7.5, compared to observations at the same conditions (a) constant milling time and volume of acetonitrile (b) constant milling speed and milling time. The error bands indicate 95 % confidence intervals.

From the number-surface mean $d(2,0)$ the particle size distributions can be estimated. The size distributions of stable particles (cf. figure 7.2), are close to log-normal, and the width, σ of the size distribution of stable particles is relatively constant, therefore

volume and number averages can be obtained using the Hatch-Choate transformations [175].

7.6 Conclusion

Using mechanical milling and varying process parameters while employing process control agent comprising immiscible liquids made it possible to prepare spherical powders of boron with different sizes. The size distributions of the obtained spherical powders were more symmetric and much narrower than that of the starting commercial boron powder. All particles were stabilized mechanically using a small amount of Fluorel® serving as binder. The particles smaller than 40 μm were sufficiently stable to survive being sonicated in a suspension. It is observed that the flowability of the prepared spherical powders was improved dramatically compared to the starting boron. In particular, a greater bulk density, reduced cohesive index, and altered charging behavior were observed for the milled spherical powders. It is observed that the particle sizes scale with the size of the emulsion droplets, and respectively with the volume of the droplet phase of the immiscible liquids serving as process control agent. Further, decrease in particle size was observed with increase in milling time, ball mass, and speed of milling. With the planetary mill used here, most consistent results with tunable particle sizes were obtained at milling times of 60 min and above, with amounts of 4 mL acetonitrile or less, and over the entire range of milling speeds and ball masses considered. These observed effects of process parameters on the particle size can be approximately predicted using the obtained, data-based model.

CHAPTER 8

EFFECT OF PARTICLE MORPHOLOGY ON REACTIVITY, IGNITION AND COMBUSTION OF BORON POWDERS

8.1 Abstract

Spherical boron powders with 2-20 μm sized particles were prepared by ball milling commercial boron in the presence of an emulsion of hexane and acetonitrile as continuous and droplet phases, respectively. The acetonitrile contained a small amount of Fluorel®, a fluorocarbon serving as binder. For comparison, boron powder was prepared by milling commercial boron with the same acetonitrile/Fluorel® solution. Reactivity of the spherical boron powders were compared to those of milled and as received commercial powders containing irregularly-shaped particles. Thermo-gravimetric measurements in Ar/O₂ gas flow showed that milling boron with or without Fluorel® shifts the onset of boron oxidation to lower temperatures. The rate of initial oxidation was greater for finer spherical boron powders compared to coarser spheres and irregularly shaped milled reference powder. It is observed that the milling does not appreciably change the activation energy of oxidation of boron and the observed accelerated oxidation is associated with its increased specific surface area. Two of the finer prepared spherical powders could be ignited when coated on an electrically heated filament in the temperature range of about 600 – 1000 °C. Commercial powders, irregularly-shaped milled powder, and coarser spherical powders did not ignite. All boron powders aerosolized and ignited in an enclosed vessel in air generated similar pressures. In another experiment, blended boron and potassium nitrate powders were heated to ignition in room air using a laser beam. The ignition delays for the blends made with spherical powders were substantially shorter vs. similar blends with

commercial powder. Combustion of the blends with spherical powders was more vigorous than with commercial boron. Particles were ejected more rapidly, and had shorter apparent burn times.

8.2 Introduction

Boron is an attractive fuel for air breathing propulsion based on its high energy density and low density [176-178]; it is also a common pyrotechnic fuel [179-182]. However, there are well-recognized challenges associated with its delayed ignition and slow combustion. Often, reduced burn rate of boron can be traced to its agglomeration and slag formation in the respective formulations [155, 183]. These effects are associated with rheological properties of boron powders, often comprising broadly sized agglomerates of submicron primary particles [154]. Powder morphology affects rheological characteristics of the boron-loaded propellant precursors, which are important for both their safety and performance [184]. Both flowability and curing characteristics of propellants depend on the powder particle size distributions and surface properties.

For composites of boron with hydroxyl-terminated polybutadiene (HTPB), which is a common binder, the viscosity was reported to be rather high [153, 185], limiting the mass loading of boron. Further, rheological properties were found to be strongly affected by surface impurities and aging of the boron powders [186]. Limited success in improving rheology of boron-based formulations was achieved using various coatings [187, 188]; although such coatings make the formulation more complex and, often, less safe. Altering boron particle morphology while preserving their chemical characteristics might be another attractive approach to prepare highly loaded, high energy density solid propellants. In our recent study, spherical boron powder with enhanced flowability and narrow particle size

distribution was synthesized by mechanical milling using a liquid process control agent (PCA) comprising an emulsion with hexane as a continuous and acetonitrile as droplet phases [189]. The spherical powders were produced when precursor particles were deagglomerated and packed inside acetonitrile droplets during milling [82, 165, 189]. A small amount of Fluorel®, a copolymer of hexafluoropropylene and vinylidene difluoride, was dissolved in acetonitrile to improve mechanical integrity of the prepared spherical particles [190, 191]. In this effort, exothermic reactions and ignition and combustion characteristics of the prepared spherical boron powder are compared to those of the starting, commercial boron and boron powder modified by milling in presence of Fluorel® but without using the milling conditions leading to the formation of spheres.

8.3 Experimental

8.3.1 Material Preparation

Table 8.1 gives a summary of all powders studied here, including specific parameters used to prepare different batches. Commercial boron powder SB-95, (SB Boron, 95 %) served as the starting material. Two nominally identical batches were used. One (designated C1) was stored in air for more than 10 years and is described as “aged”. The other (C2) was purchased for this project in 2020 and is described as “fresh”. Acetonitrile (95 %) and hexane (95 %, both Alfa Aesar) served as emulsion forming PCA. A small amount of 0.5 wt-% of Fluorel® (3M) was dissolved in acetonitrile as binder in the spherical powder particles. This addition introduced nominally 0.17 wt-% of Fluorel® in all final milled powders, except for the powder designated as S0. To observe the effect of the added fluorocarbon while retaining the morphology of the commercial boron, a sample F1 was

prepared by milling powder C1 in the acetonitrile-Fluorel® solution for 1 h without adding hexane and thus without emulsion.

A Retsch PM400/MA planetary mill was used to prepare spherical boron. Two types of hardened steel milling vials were used: a standard 500-mL vial (Retsch) and a custom-made 180-mL vial. Milling media were 9.525-mm (3/8”) diameter hardened steel balls (Frantz Mfg.). For the preparation of spherical particles (S0 – S3) conditions were selected based on the previous work [189]. The milling time was always 1 h, and the ball to powder mass ratio was 12.5. The volumes of acetonitrile and of boron were kept equal. Powders were recovered as slurries from the vials after milling. Any clear liquid was decanted, and the powder was allowed to dry in air for 72 h. This allowed any remaining acetonitrile to evaporate, and the contained Fluorel® to solidify.

For selected combustion experiments, powder blends of boron with KNO₃ (Mil-Spec Industries, MIL-P-156, Class 2, 30 µm max) were prepared using a 1:3 mass ratio of B to KNO₃. The powders were blended by stirring a suspension of 1g boron and 3 g KNO₃ in 500 mL hexane for 2 h.

Table 8.1 Materials used and prepared in this study and respective milling conditions

Description	Mill RPM	Vial volume , mL	Boron mass, g	Ball mass , g	Ball to powder mass ratio	PCA components, mL		Fluorel added	Sample ID
						Hex	ACN		
SB95 (aged)	--	--	--	--	--	--	--	N/A	C1
SB95 (fresh)	--	--	--	--	--	--	--	N/A	C2
Irregularly shaped, milled C1	350	180	14.22	90	6.3	--	6	Yes	F1
Spheres, milled C1	350	180	14.22	90	6.3	18	6	No	S0
	350	180	7.11	90	12.6	21	3	Yes	S1
	275	500	14.22	180	12.6	42	6	Yes	S2
Spheres, milled C2	275	500	14.22	180	12.6	42	6	Yes	S3

8.3.2 Material Characterization

A JEOL JSM 7900F field emission scanning electron microscope (SEM), operated at 5-10 kV was used to examine the powders. A Malvern 3000 Mastersizer was used to analyze

particle size distributions with ethylene glycol serving as the dispersant. The obscuration range varied between 4 and 6 %. The dispersed powder suspensions were stirred continuously at 2500 RPM. After initial measurements, the suspensions were ultrasonicated (20 % of maximum intensity) and the powder particle size distributions were re-measured to observe whether the produced agglomerated particles were mechanically stable and capable of withstanding such agitation.

For thermogravimetric (TG) analysis, a Netzsch STA409PC thermal analyzer was used, operated with the dedicated TG sample carrier. The powder load varied from 5 to 10 mg. The furnace of the analyzer was evacuated to 0.05 atm and flushed with argon three times prior to the measurement to ensure that the gas environment during the heating was well controlled. In most of the measurements a mixture of argon and oxygen were used at 80 and 20 mL/min, respectively. In selected runs, argon was replaced with nitrogen, which was observed to have no effect on the results. Materials were heated to 1173 K (900 °C) with baseline correction performed using an empty TG plate.

Specific surface areas of the prepared powders C2 and S3 were determined by nitrogen adsorption using an Autosorb iQ (model ASIQM000000–6) analyzer by Quantachrome Instruments. Samples were subjected to degassing under vacuum at 200 °C for 12 h. The mass of the powders for surface area measurement ranged from 150 to 250 mg. Similar specific surface area measurements for other powders were reported previously [189].

To assess stability of boron, commercial powders C1 and C2 and spheres S2 and S3 were exposed to humid oxidizing environments at a constant temperature of 343 K (70 °C) using a TAM III isoperibolic heat flow calorimeter by TA Instruments operated with a

5-mL RH perfusion ampoule. This enabled experiments with samples exposed to either dry air or air with 80% relative humidity. The relative humidity and the total gas flow rate over the sample were controlled using TAM Assistant™ software. Prior to measurements, and in order to insure reproducible starting conditions, powders were dried in vacuum at 80 °C for 12 hours. The samples were then placed into the calorimeter. Constant flow of nitrogen was ensured. Each measurement was programmed to start once a relatively stable heat flow signal was reached. Humid gas was added after 1 h of the initial recording. Both, nitrogen and hydrated air were charged at a flow rate of 100 ml/h.

For heated filament ignition measurements, dry powders were placed on a nickel–chromium ribbon with a 0.8×0.1 mm cross-section (Nichrome 80 Flat, WIREOPTIM). The ribbon was heated electrically using a 12-V battery (Kinetikpower.com). The wire temperature as function of time was determined using a calibrated pyrometer based on a PDA30B2 germanium switchable gain detector (Thorlabs) connected via an optic fiber. Ignition was detected by light emission from the powder, recorded at 500 fps using a Redlake MotionPro 500 camera. The heating rate in this experiment was 4130 ± 300 K/s. More details of this experiment were published previously [192].

Boron powder combustion in air was characterized using a constant volume explosion apparatus consisting of a 9.2-liter, nearly spherical vessel used in previous studies [125, 193-195]. The powder (2g) was loaded in a ½ inch pipe elbow below an aerosolizing nozzle. The vessel was initially evacuated to 0.25 atm, and an air blast was used to disperse the powder through the nozzle into the vessel. Final pressure in the vessel after the blast was 1 atm. After a 200 ms delay to reduce turbulence, the aerosol was ignited at the center of the vessel using a custom pyrotechnic igniter. The igniter consisted of 0.85

g of 4Al·3CuO nanocomposite contained in a 2.5 cm × 0.5 cm (L×D) paper cylinder sealed with Fluorel® at the ends, and wrapped in a 20 cm long 200 μm diameter tungsten wire. The internal pressure was measured using a pressure transducer (PX2AN1XX500PSA by Honeywell) and recorded using a Rigol DS1054Z digital oscilloscope. This experiment was repeated at least five times for each material.

For combustion experiments using KNO₃ as solid oxidizer, blends of KNO₃ with C1 or S3 were loaded as suspensions in hexane into a cavity (0.5 mm wide × 0.07 mm deep) in an aluminum block. The cavity depth was measured using an optical microscope, focusing the objective at the top and bottom of the cavity and reading the displacement from the micrometer moving the lens. Hexane was allowed to dry and excess powder removed, aiming to keep the powder volume as constant as possible. Powders were ignited using a 450-nm 20-W laser diode (NEJE®, 5.5 W output) located 9 cm away from the powder surface. The laser beam projected onto the sample holder produced a 0.73 × 0.5-mm oblong spot, covering the sample cavity entirely. Combustion was recorded using a Photron FASTCAM Nova high-speed video camera (type: 800K-M-8GB) operated at 10,000 and 20,000 fps with shutter speeds of 20 and 3.3 μs respectively. A schematic diagram of this experiment can be found in appendix D (figure D.1). The powders ignited following a certain delay after being illuminated. Once ignited, the powders produced an expanding bright plume consisting of burning ejected particles. In some instances, several such plumes were observed until the loaded powder eventually burned out. Image analysis using ImageJ and Matlab was used to threshold the images at saturation level and to track the leading edge of the plume of ejected particles. The following descriptive parameters were determined: the ignition delay time as the onset of light emission, the initial velocity

with which particles were ejected as the speed of the leading edge of the plume over up to 10 frames, the maximum distance particles were ejected, the time to reach this distance, and the time at which no light emission was detected after the powder had burned out.

8.4 Results

8.4.1 Powder morphology and size distributions

SEM images of different boron powders are shown in figure 8.1. Commercial boron C1 consists of agglomerates of submicron primary particles. Milled, irregularly shaped sample F1 has a morphology similar to that of the starting powder C1, with fewer large agglomerates. The morphology for spherical powders S1 and S2 is distinct from that of C1. All particles in samples S1 and S2 are round with similar particle sizes within each powder. Some sphere fragments forming finer irregularly shaped particles are noted for sample S1 but not for S2. SEM images of powders C2 and S3 are similar to those of C1 and S2, respectively, and are shown in appendix D, figure. D.2 SEM images for powder S0 showing that it is spherical, similar to S1-S3, were reported earlier [189].

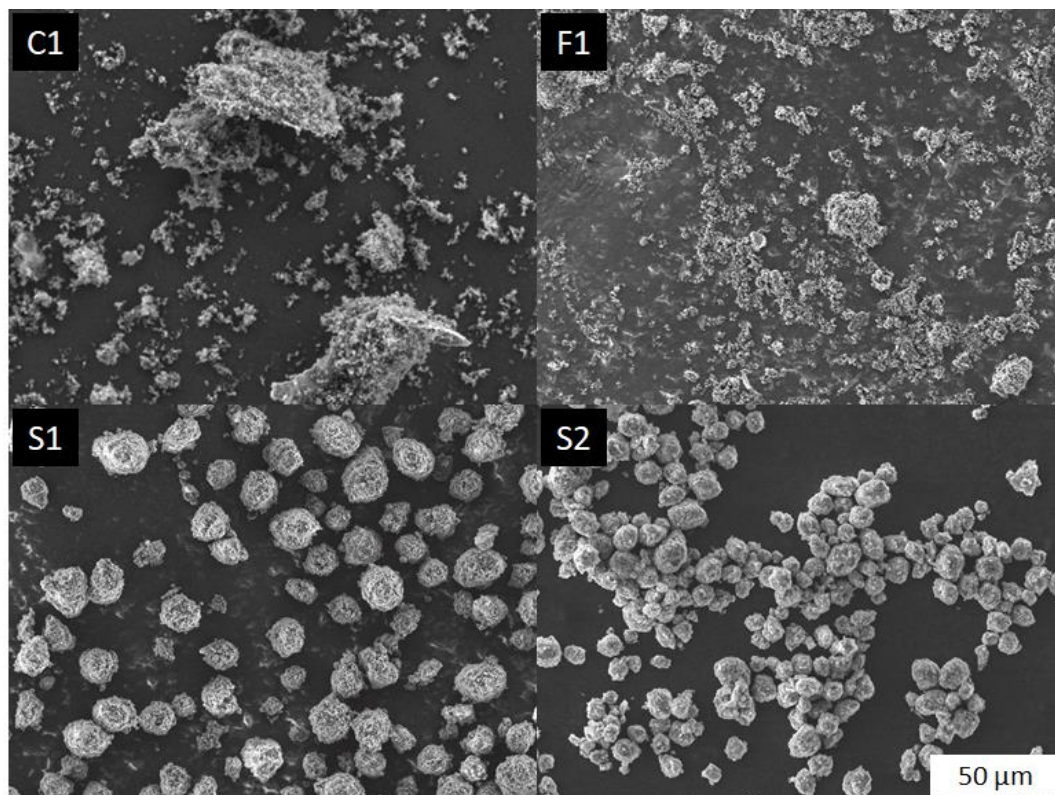


Figure 8.1 SEM images of different boron powders: aged commercial boron C1, boron milled with acetonitrile and Fluorel® F1, and spherical powders with different particle sizes, S1 and S2

Figure 8.2 shows particle size distributions for different boron powders. Initial measurements are shown as thin dark bars, measurements after sonication are shown as wide gray bars. The aged commercial boron C1 has a bi-modal distribution with peaks around 2 and 30 μm . Fresh commercial boron C2 only shows one peak around 2 μm , lacking large agglomerates present in the aged sample. For milled, irregularly shaped powder, sample F1, the peak around 2 μm (as in the starting powder C1) is preserved. Two more peaks appear for sample F1 in the size ranges around 40 and 250 μm , suggesting additional agglomeration induced by milling in the presence of Fluorel®. However, sonication breaks down most agglomerates; even the finer peak is shifted down to about

1.5 μm , showing that milling destabilized the initial, relatively well-packed agglomerates in the boron powder. For all spherical samples, S1, S2, and S3, the particle size distributions are relatively narrow and symmetric with small numbers of fine unattached particles. The modes of the main size distributions are 13.5, 7.2, and 13.2 μm and the width, $\frac{d_{90}-d_{10}}{d_{50}}$ of the same are 0.88, 1.08 and 1.5 for samples S1, S2, and S3, respectively. Sonication during the measurement did not lead to noticeable changes in the size distribution of any of the spherical samples. Size distribution for a coarser powder S0 is qualitatively similar to those of other spherical powders, and was shown elsewhere[165]; the mode of the distribution is 92 μm . Upon sonication, powder particles of the sample S0 disintegrated, leading to a substantial growth of the fine fraction.

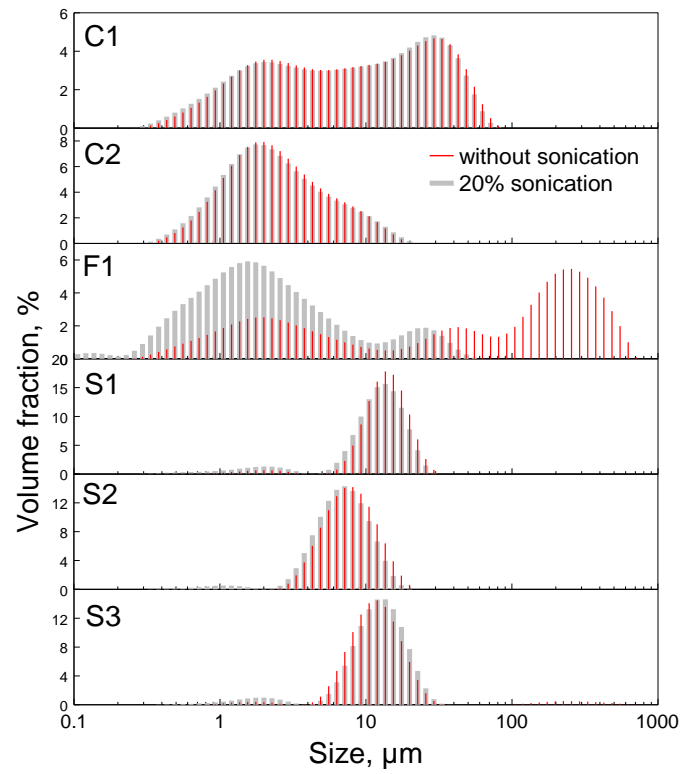


Figure 8.2 Particle size distributions of different boron powders and effect of sonication on their stability.

Figure 8.3 shows particle blends of selected boron powders with KNO_3 oxidizer. The blend using commercial powder C2 generally shows more loose boron particles than the blend with spherical boron S3.

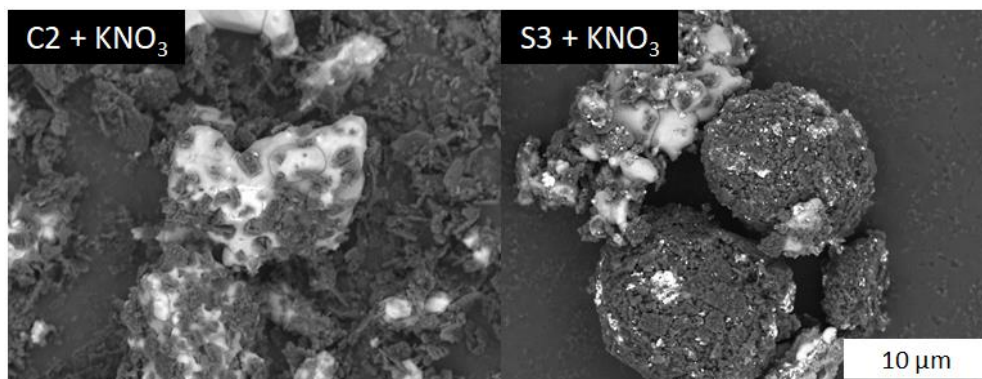


Figure 8.3 Backscattered electron images of C2+KNO₃ and S3+KNO₃ powder blends

8.4.2 Oxidation of Boron Powders

TG and differential DTG traces recorded at 5 K/min in the presence of oxygen are shown in figure 8.4. All irregularly shaped powders are represented by dashed lines of different thickness and color. Conversely, spherical powders are represented by solid lines with different thickness and color. Insets show magnified low-temperature portions of the TG and DTG traces where the onset of oxidation occurs.

Aged commercial powder C1 and both powders prepared using it as a starting material, irregularly shaped F1 and spherical S1, show a low-temperature mass loss around 100 °C. This mass loss is due to dehydration of boric acid. It is not noted for fresh powder C2 and spheres S3 prepared using that powder.

At temperatures below ≈ 400 °C, all materials behave similarly and oxidation rates are negligible. Between 400 °C and 500 °C the commercial powders C1 and C2 start to oxidize, recognizable as an onset in the DTG. The oxidation rate of the fresh powder C2 increases until it reaches a maximum at about 656 °C. Conversely, the oxidation rate of the aged powder remains low until the onset of the main oxidation event in the 600 °C – 650 °C range, and it peaks near 736 °C. The final degree of oxidation in the covered temperature

range and the maximum rate of oxidation are both higher for the fresh C2 powder compared to its aged counterpart C1.

All milled powders oxidize faster than the commercial boron starting around 400 °C. The oxidation rates rise and reach a region resembling plateau. This is distinct from the relatively sharp DTG peaks observed for the commercial boron powders. For the milled, irregularly shaped powder F1, the DTG peak is narrower than for spheres. The oxidation rates for the milled powders become nearly constant sooner for finer spheres S2 prepared using aged boron as a starting material, followed by spheres S3 prepared using fresh boron. The much coarser milled spherical powder containing no Fluorel, S0, begins oxidizing at about the same temperature as other milled samples. The peak rate of oxidation is somewhat higher for smaller spheres, S2 and S3, compared to coarser spheres S0 and S1. For irregularly shaped milled powder F1, the maximum achieved oxidation rate was slightly lower than any of those observed for spheres.

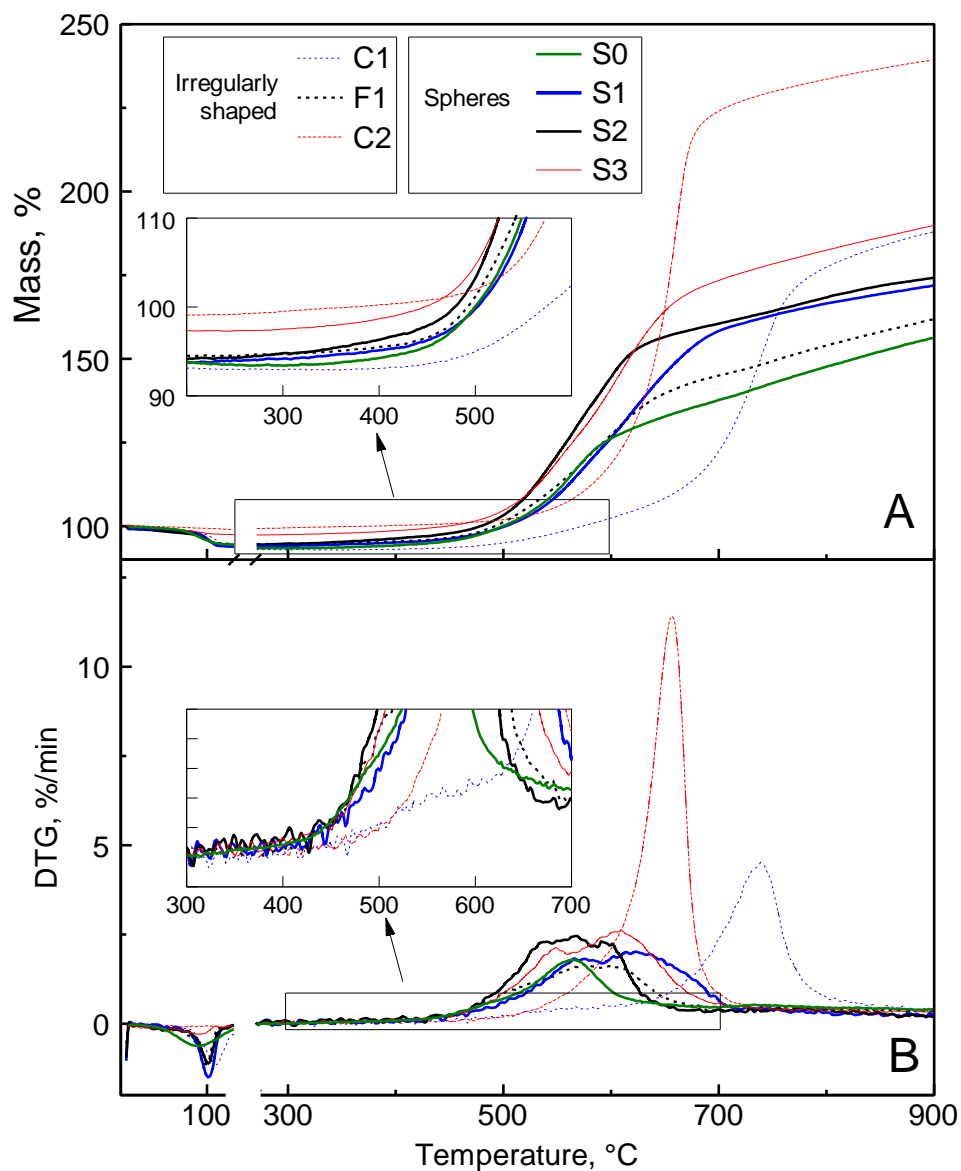


Figure 8.4 TG (A) and DTG (B) traces for different boron powders oxidized while being heated at 5 K/min.

8.4.2 Low-temperature Oxidation of Boron Powders in Air at Controlled Humidity

Normalized heat flow traces measured in air at 80% humidity at 70 °C for different powders are shown in figure 8.5. The traces are grouped to compare the starting powders with the respective milled materials. Qualitatively, both starting powders, C1 and C2, show similar reactions: the reaction proceeds fast in the beginning and the rate of reaction slows down

with time. However, the heat flow is much higher for the aged C1 powder. Irregularly-shaped milled powder F1 reacts at a lower rate than the starting powder C1. The decay in the reaction rate also occurs somewhat slower. Both spherical powders, S1 and S3 used in these experiments exhibit a more complex reaction process showing at least two peaks in figure 8.5. For spheres S2 prepared using aged boron C1, the first peak is smaller than for the starting powder and is very similar to that observed for the milled irregularly shaped powder F1. The second peak, observed clearly at longer times results in a significantly greater overall oxidation occurring for this material following its exposure to humid air. For spheres S3 prepared using fresh boron C2, the first peak is nearly the same as for the starting powder. Once again, the second peak occurring at longer times leads to a greater powder oxidation.

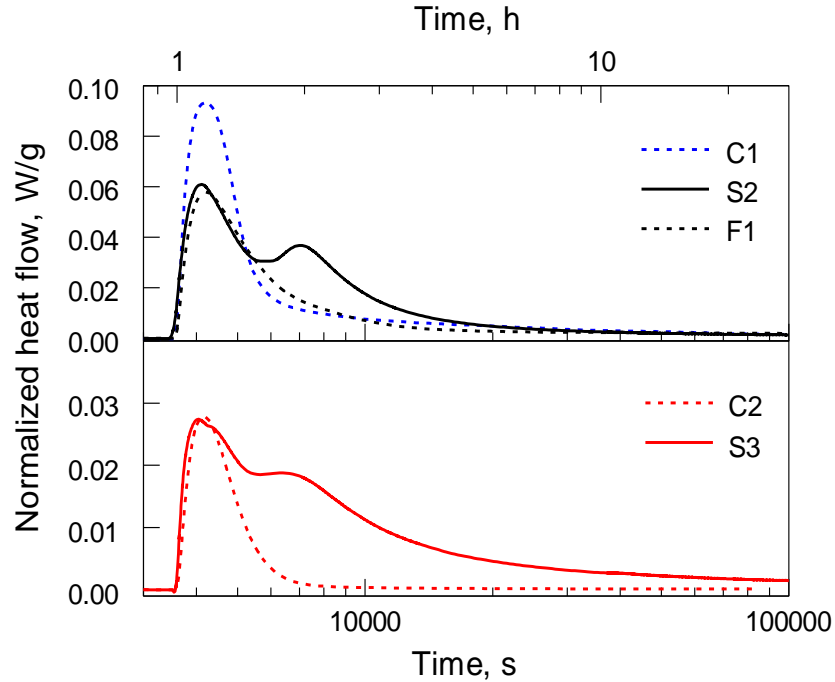


Figure 8.5 Normalized heat flow traces for different boron powder oxidizing in air at 80% relative humidity at 70°C.

8.4.4 Heated Filament Ignition

Ignition was recognized as a brightness increase of the powder relative to the heated Ni-Cr wire. However, particles were not ejected and no standoff flame formed. The finer spheres S2 prepared from C1 ignited at an average temperature of 625 ± 40 °C. Spheres S3, prepared using fresh boron C2 and with sizes close to those of S1, ignited at a higher average temperature of 1070 °C. Commercial boron C1, C2, reference powder F1 and spheres S0 and S1 (larger spheres prepared using aged boron) did not ignite.

8.4.5 Constant Volume Explosion (CVE)

Results from CVE experiments are shown in figure 8.6. Characteristic pressure traces shown for commercial boron C2 and spherical boron S2 were normalized by initial pressure P_o . The pressure traces follow the experimental sequence: a low pressure in the evacuated

vessel is followed by a ramp produced by the air blast introducing the powder in the vessel. That is followed by a delay after which the igniter is initiated. The pressure rises sharply due to the combustion of the thermite in the igniter; following slower pressure rise is caused by combustion of the aerosolized boron.

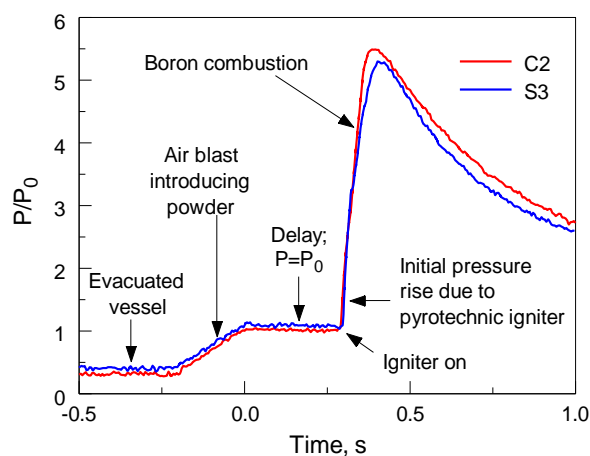


Figure 8.6 Characteristic pressure traces recorded in CVE experiments.

Material recovered after the combustion was examined to estimate combustion completeness. The combustion products were digested in water, assuming boron oxides dissolve and any residue is unreacted boron. Details of the procedure are given in section D.1, Appendix D. The results show no significant difference between combustion products of spherical and irregularly shaped boron particles.

To interpret the CVE results, expected peak pressure were calculated using the NASA CEA code [196]. Further details are given in Appendix D, section D.2. Table 8.2 shows the results of these calculations, compared to the present experimental results. The measured pressures are consistently lower than expected based on the equilibrium calculations. The powders C2 and S3 tested in CVE generate similar pressures with the powder C2 producing a slightly higher rate of pressure rise.

Table 8.2 Maximum Pressure and Pressurization Rate from CVE Experiments

Sample ID	Maximum pressure P_{\max}/P_0	Maximum rate of pressure rise, $(dP/dt)_{\max}$, atm/s
Boron (calculated)	10.13	N/A
C2	5.16 ± 0.37	650 ± 97
S3	4.71 ± 0.65	466 ± 110

8.4.6 Combustion of Boron KNO₃ Blends

Boron samples C2 and S3 without an added oxidizer could not be ignited by a 450 nm laser. However, both powders blended with KNO₃ ignited readily after some delay. Characteristic sequences of high-speed video frames are shown in figure 8.7. Each frame is labeled with the time elapsed after the laser beam was turned on. The first shown frame follows ignition closely; subsequent frames were selected to illustrate the shape of the growing bright plume produced by ejected burning particles. The spherical powders ignited after a shorter delay for the same laser power. It was further observed that the plume was growing faster for the spherical powders, although the size of the plume formed was similar for both types of samples. The total burn time observed in the high-speed videos was longer for the powder C2. These observations are presented in quantitative form in figure. 8.8.

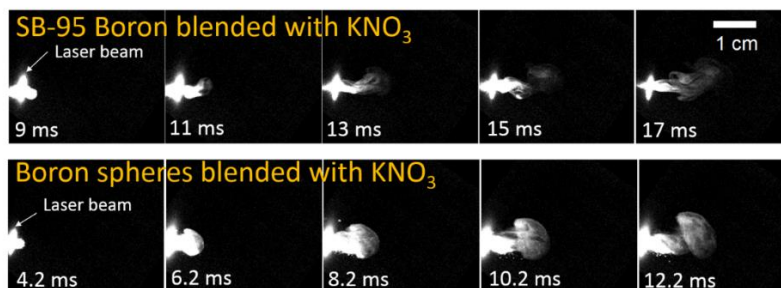


Figure 8.7 Snapshots from high-speed videos capturing B-KNO₃ combustion

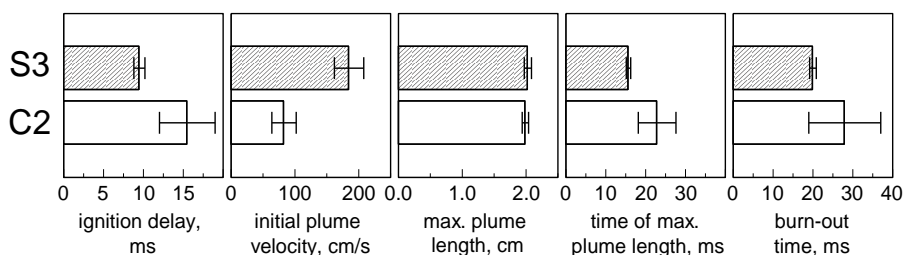


Figure 8.8 Combustion characteristics for boron/KNO₃ blends ignited by a laser beam: Ignition delay, initial plume velocity, maximum plume length, time to reach the maximum plume length, and total burn time.

8.5 Discussion

The effect of boron morphology on its reactivity is most readily evaluated based on the results of thermal analysis. The onset of mass gain observed in the TG curves is a clear indicator of oxidation, and when it occurs at a lower temperature, it is likely that the ignition delay will be reduced. Analysis of mass gain observed at greater temperatures becomes increasingly difficult to interpret. When substantial oxide growth occurs, the morphology of the powder is altered; particles can sinter, blocking part of the surface initially accessible to the gaseous oxidizer. The changes in morphology are particularly significant when substantial amounts of molten B₂O₃ are produced. Liquid oxide can clog the pores in the powder loaded in the TG sample holder and prevent its further oxidation. The processes

associated with powder sintering and redistribution of the molten B_2O_3 are irrelevant for reactions involving combustion of aerosolized boron particles and thus interpretation of TG measurements should focus on low-temperature observations.

In order to locate the onset of oxidation detectable in TG measurements, the data from figure 8.4A were replotted in figure 8.9, where the effect of the initial, low temperature mass loss was removed by subtracting a straight baseline fitted to the temperature range of 150-300 °C. This allows comparison of the initial stages of the oxidation, where the mass gain rises above the noise level of the measurement. A reference level of 0.4 % mass gain (a horizontal line in figure 8.9) was chosen somewhat arbitrarily as a point of comparison. This analysis shows that for all powders oxidation begins at temperatures below the B_2O_3 melting point of 450 °C [197], marked as a vertical line in figure 8.9. For the spherical powders the onset of oxidation occurs as much as 100 K below B_2O_3 melting. No marked change in the oxidation rate noted around the B_2O_3 melting point, suggesting that when the thickness of B_2O_3 layer is small, its melting does not appreciably affect the oxidation. Diffusion of boron and oxygen through the protective layer are, therefore, the rate-limiting processes for this reaction leading to ignition. The aged commercial boron C1 shows the highest oxidation onset, consistent with the presence of a thicker initial surface oxide.

Figure 8.10 shows the oxidation onset temperature vs. the specific surface area for different boron powders. Nitrogen absorption measurements showed that spherical powders had an increased surface area and porosity compared to irregularly shaped boron powders, whether as received or milled. Respectively, spherical boron powders had a lower oxidation onset temperature. Thus, an earlier oxidation of the spherical boron powders is

explained by the increased surface area accessible in such powders for the external gas oxidizer. Consistently with the earlier oxidation onset, the powder with the greatest measured surface area, S2, also had the fastest increase in the oxidation rate, as was seen from DTG curves in figure. 8.4. Conversely, the presence of Fluorel® does not appear affect the oxidation rate appreciably. Supporting further the noted above correlation of early oxidation reactions with reduced ignition delays, in the present experiments the ignition temperatures measured using an electrically heated filament for samples S2 and S3 spheres correlate with (but not equal to) the temperatures at which an increase in DTG was observed for these materials figure 8.4. For all other powders, the increase in DTG occurred at higher temperatures, making it impossible to detect their ignition in the present heated filament experiments, in which the temperature was limited by melting of the filament.

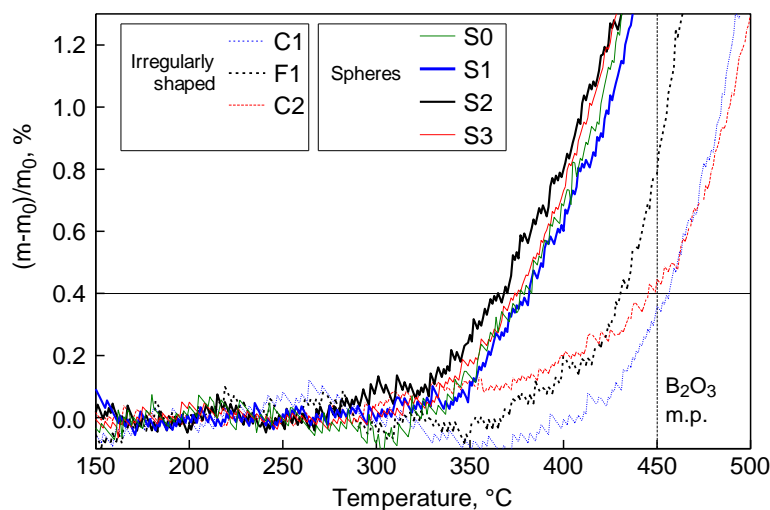


Figure 8.9 Earliest oxidation onset for spherical and irregular boron powders.

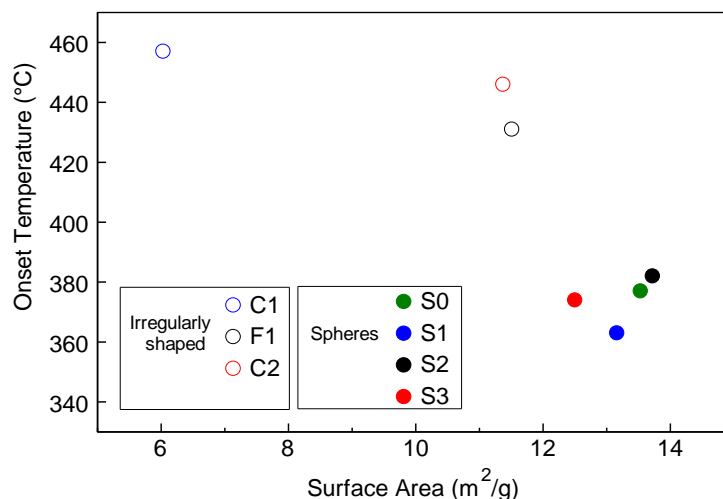


Figure 8.10 Relation between specific surface area and oxidation onset for spherical and reference boron powders.

It is of further interest to attempt interpreting the present TG oxidation curves using a previously developed quantitative oxidation model for boron [198]. It is observed here that the oxidation occurs sooner for spherical powders prepared by milling than for commercial, irregularly shaped boron. The question to be answered is whether milling and forming powder particles with spherical morphology changed the reaction mechanism (affecting the activation energy) or simply changed the surface area at which oxidation occurs. The previously developed oxidation model accounts for the fact that any TG measurement represents the sum of oxidation curves for all particles in the sample. The model deconvolutes the TG measurements by using the known particle size distribution to reconstruct oxidation curves for particles with specific sizes. Different oxidation kinetics are tested against TG curves observed for powders with distinct but overlapping particle size distributions [109, 198, 199]. The kinetics predicting that oxidation of the same size particles present in different samples occurs at the same rate is assumed to be correct. The oxidation model in Ref. [198] considers boron particles as roughly spherical agglomerates that oxidize from the outside inward. The particles are described in terms of their overall

size, the size of the primary particles, and the thickness of an outer layer participating in the oxidation as distinct from a core that is effectively shielded from external gaseous oxidizer. The deconvolution depends on the volume fraction of the particle that oxidizes. This volume fraction, and therefore the thickness of the outer layer is determined from a comparison of separate measurements for powders with distinct but overlapping size distributions. This approach assumes that the temperature-dependent mass $m_i(T)$ for a particle in size bin i and recovered from one size distribution should match that recovered from a different size distribution for the same size bin. In this work, materials S1 and S2 were used as samples with different size distributions (see figure 8.2). To process the experimental data, the assumed thicknesses of the oxidizing outer layer varied and the mismatch between oxidation curves for different size bins was calculated. A global minimum was observed for the layer thickness of 1.6 μm . This is shown in figure D.5 in appendix D.

Following Ref. [198], the growth of the oxide is assumed to occur on the surface of primary particles. After deconvolution, the mass change of a primary particle, Δm_{pp} , is recovered from measurements using the mass m_i of particles in size bin i , the respective initial mass $m_{i,0}$, and the mass of the core that does not oxidize, $m_{i,core}$:

$$\Delta m_{pp} = \frac{m_i - m_{i,0}}{m_{i,0} - m_{i,core}} \quad (8.1)$$

The rate of oxide growth on a primary particle can be described by:

$$\frac{dm_{pp}}{dt} = k \cdot f(m_{pp}) \cdot \exp\left(-\frac{E}{RT}\right) \quad (8.2)$$

Where k is a rate constant, $f(m_{pp})$ describes the dependence of the rate on the oxidation degree, E is the activation energy, and the temperature T is a function of the time t .

With appropriate values for the activation energy and the mass dependent rate coefficient $[k \cdot f(m_{pp})]$ and with the volume fraction of each particle participating in oxidation and represented by the 1.6- μm outer layer determined above, the mass of a particle in size bin i , and, with the measured particle size distribution, the mass of the entire sample can be calculated. Activation energies and mass-dependent rate coefficients are available for boron in previously published work [200]. Based on these assumptions, theoretical oxidation curves for powders S1 and S2 were calculated. For this, following [200], the particle packing density of primary particles in spherical boron was assumed to be 85 %. A match between calculation and observed oxidation curves shown in figure 8.11 could be obtained with a slightly reduced activation energy of 125.8 kJ/mol compared with 148 kJ/mol reported in [200]. Considering the approximate nature of the present analysis and multiple assumptions made to assess the activation energy, it is reasonable to conclude that the oxidation mechanism is not altered; instead, the accelerated reaction is due to the increased surface available to the external oxidizer.

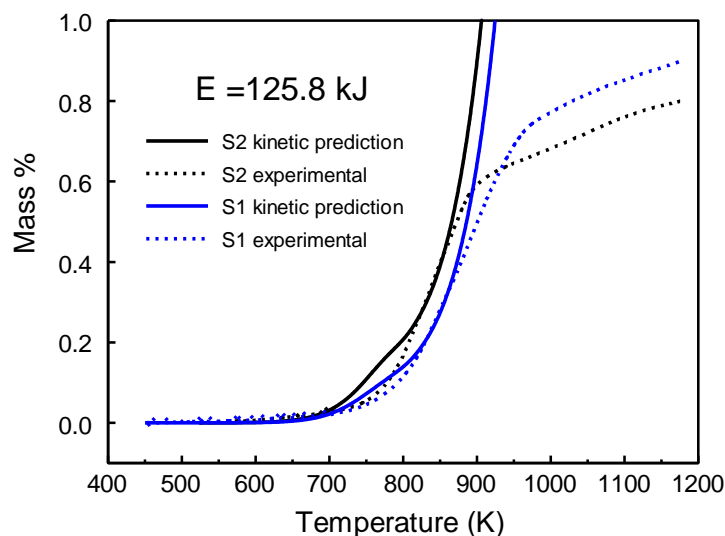


Figure 8.11 Observed (dotted) and calculated (bold) TG oxidation curves for boron powders S1 and S2.

The lack of detectable improvement in combustion of spherical boron powders in CVE experiments vs. commercial boron is initially surprising. However, the processes occurring in CVE are complex and depend, in significant part, on the initial formation of the powder aerosol during the blast of gas introducing the powder in the reaction vessel. A number of effects can occur making it difficult to interpret the measured pressure trace. Spherical powders, which flow better than irregularly shaped commercial boron, can be more readily deposited onto the walls of the chamber instead of staying in aerosol. Also, commercial boron has a much broader particle size distribution, so that ultra-fine particles can remain in aerosol longer than larger spherical particles, which do not include a similar fraction of fines (figures 8.1, 8.2). Thus, a more readily occurring ignition for spherical powder could be offset by the lower concentration of the particles in aerosol, leading summarily to a similar pressure traces as measured for commercial powder. The presence of aerosolized fine particles can also explain a slightly greater rate of pressure rise observed for the commercial powder.

In the laser-ignited combustion experiment using $B \cdot KNO_3$ blends, aerosol formation was no longer a process affecting the powder initiation. In agreement with thermo-analytical and ignition experiments, the S3- $B \cdot KNO_3$ sample showed a shorter and more reproducible ignition delay compared to the blend prepared from (fresh) commercial boron, C2- $B \cdot KNO_3$. In both samples burning particles were observed to travel nearly identical distances, although the spherical S3 reached that distance in about 2/3 of the time of the commercial boron C2. Combined with the higher particle ejection velocities for the spherical powder S3, this suggests higher particle burn rates for the spherical particles prepared in this work. This would be consistent with the overall shorter burnout times observed for S3 as well. One possible explanation can be traced back to the greater specific surface area accessible to the gaseous oxidizer in sample S3 compared to C2. It is likely that KNO_3 decomposes upon heating, generating gaseous oxygen and the sample S3 with a greater surface capable of reacting with that oxygen ignites more vigorously. Possible additional explanations include more uniform mixing between the spherical boron particles and the oxidizer because of the absence of large agglomerates unavoidable in any commercial boron, and in powder C2, in particular. It is also possible that the milling process forming spherical particles disrupted surface B_2O_3 present on unmilled powders, leading in turn to a diminished ignition barrier for the milled spherical particles.

8.6 Conclusion

Milling in mixed solvents substantially improves particle morphology and boron reactivity. The prepared powders have uniform spherical shapes with a narrow size distribution which makes material handling easier. Curing of Fluorel® improves mechanical stability and powders retain their structure. Particles with spherical morphology oxidize faster in thermogravimetric experiments than commercial boron, are able to be ignited on a heated filament, and tentatively have higher burn rates than commercial boron. The present measurements show that the onset of boron oxidation is not affected by melting of the surface B_2O_3 film; instead, it is rate-limited by diffusion of reacting species through the growing oxide layer. The improvements in reactivity of the prepared spherical boron powders are attributed to the increased specific surface area available in such powder to react with external gaseous oxidizer.

CHAPTER 9

FUTURE WORK AND CONCLUSION

Upon introducing PCAs comprising mixed fluids, which is a new approach in the field of mechanochemically prepared energetic and reactive materials, particle features and behaviors can be tuned based on their applications. Thereby, for most of our work in the future, we would like to explore further the mixed PCA systems consisting of two immiscible liquids. However, challenges related to aging and particle handling still remain important and need to be addressed. Hence, our future work aims towards further improvement of the materials upon resolving the existing problems.

We explored different parameters associated with mixed PCA conditions which have not been explored before. For instance, the number of milling balls and their size determine the dimensions of the emulsions, eventually affecting particle size. Several other parameters such as amount of solid, PCA volume, type of milling media, BPR, have been investigated followed by analysis of their effect on ignition and combustion of the produced materials. Introducing mixture of PCAs during mechanical milling is likely to add new dimensions in the synthesis of reactive materials. We assume that this approach can be applied to diverse reactive material systems having different chemistries apart from the ones explored in our study thus far. It will be interesting to apply this method in the mechanical milling of metal fluorides, for example. It is likely that mixture of PCAs will also affect the behavior of different metal-based alloys such as Al-Mg, B-Mg, Ti-Mg, B-Zr, B-Ti, Zr-C, Si-C, and so on.

For future work, a dedicated experiment exploring ballistic interaction of suspended particles and droplets in emulsion can be designed. For example, a microfluidic, counter flow configuration accelerating a power-laden jet into an emulsion might be considered. While not suitable for practical preparation of filled spherical particulates, such an experiment might be helpful in elucidating the processes involved in such an interaction and effects of such parameters as impact energy, dimensions of particles and droplets, and surface energy of the liquid/liquid and liquid/solid interactions occurring in the system. Designing such an experiment in the future is deemed to be both interesting and useful.

There is lack of mechanistic understanding of the interfacial kinetics of the reactive materials triggering ignition and combustion. This work made an effort to perform kinetic analysis of boron oxidation and find the correlation between particle morphology and oxidation of the powders prepared using mixed PCAs. The kinetic modeling approach for boron powders attempted in this work laid the initial groundwork for understanding such kinetics.

In related work, it will be important to understand and quantify the processes leading to aging in the prepared composite materials. It is widely accepted that nanocomposites, owing to their large surface area, are highly reactive compared to their micron size counterparts. However, this also makes them prone to aging upon exposure to air. One possible way to prevent aging of reactive nanocomposite is to use a binder covering fresh reactive surface [110]. This dissertation work touched upon the use of energetic binder to provide mechanical integrity to the powders. However, there is a broad scope for future aging studies involving different binders added to PCAs. For example, the fine particles formed by ACN-assisted milling can be treated with a nitrocellulose-based

binder. Such binders have been reported to be effective in protecting mesoparticles, which are micron-sized aggregated reactive nanoparticulates, generally improving their combustion [26]. Also, the particles can be coated by energetically favorable organometallic compounds or aerosolized using a non-reactive and/or agglomeration prohibiting liquid (may be ACN itself) rather than being used dry.

Certainly, the choice of PCA does not need to be confined to hexane and acetonitrile only. Different immiscible binary systems can be generated based on their chemistry and interaction with the material to be synthesized. Liquids like benzonitrile, xylene, pyridine, cyclohexane and several other polar and nonpolar hydrocarbons can be considered in this regard. The work certainly has the potential to be extended in industries other than energetics. Spherical particulates are highly desired in industries involving pharmaceuticals, catalysts, additive manufacturing, cosmetics, food processing and paint additives. The mixed PCA approach can be introduced to those industries as well and need not be confined to inorganic materials only. Based on our findings, we can affirm that mixtures of different process control agents can be used as an effective tool for the tunability of particle morphology, shape, and size, which eventually affects material handling and reactivity. And the work can be extended to design a new interesting generation of engineered powders.

APPENDIX A

STEM-EELS ANALYSIS OF Al-CuO NANOTHERMITES PRODUCING COPPER NANODOTS AT 650K

Characterization on Al-CuO nanothermite samples quenched at 650K are presented below

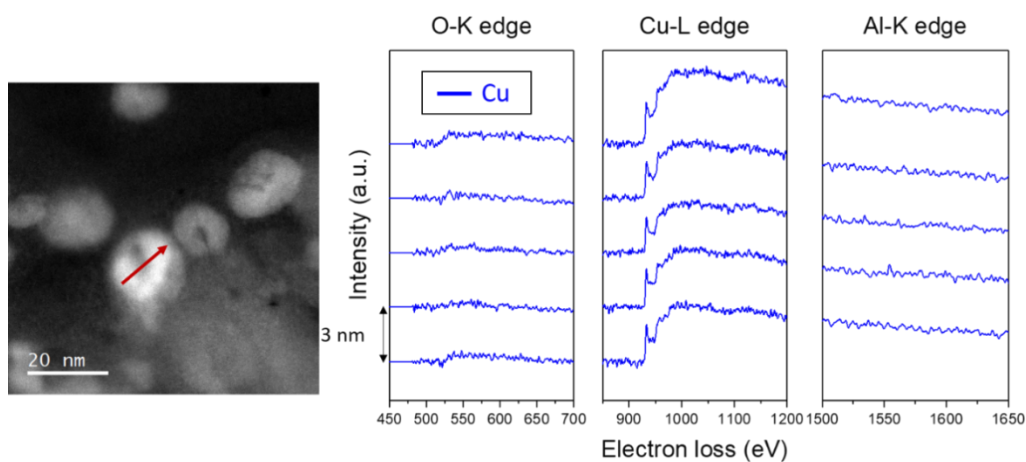


Figure A.1 The Cu-L_{2,3} edge spectra acquired across a dot observed in sample ApC- after quenching at 650K.

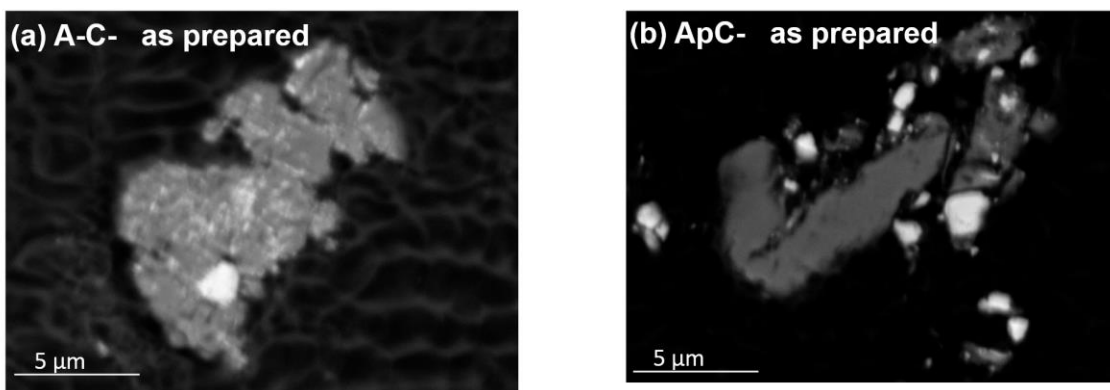


Figure A.2 SEM images of A-C- and ApC- as prepared (samples prepared for microprobe analysis).

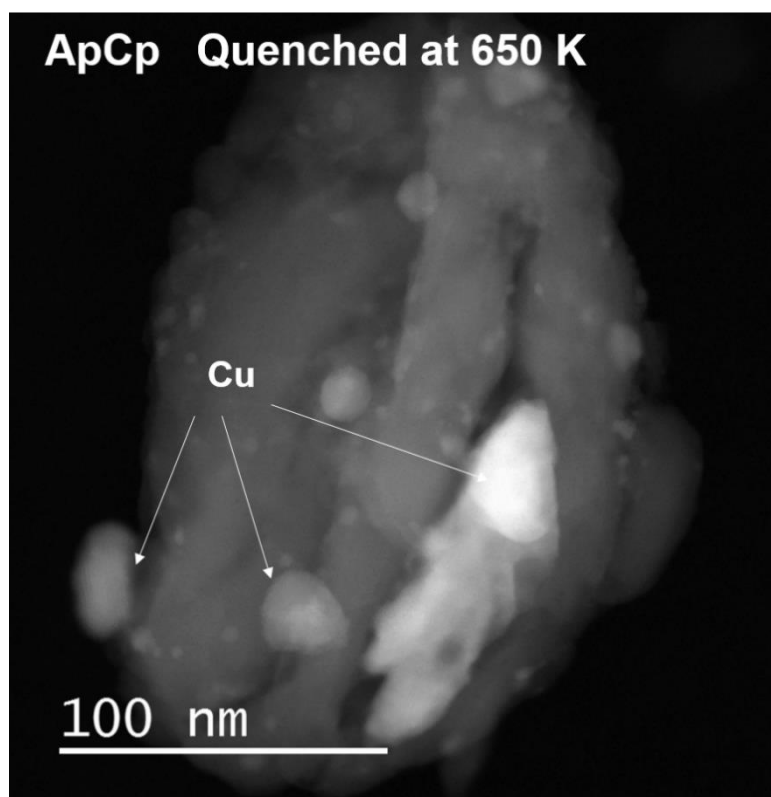


Figure A.3 Cross-sectional STEM-HAADF image of ApCp heated to 650 K.

APPENDIX B

DENSELY FILLED SPHERICAL POWDER PREPARED BY MECHANICAL MILLING

Further characterization of the prepared spherical powders are presented below

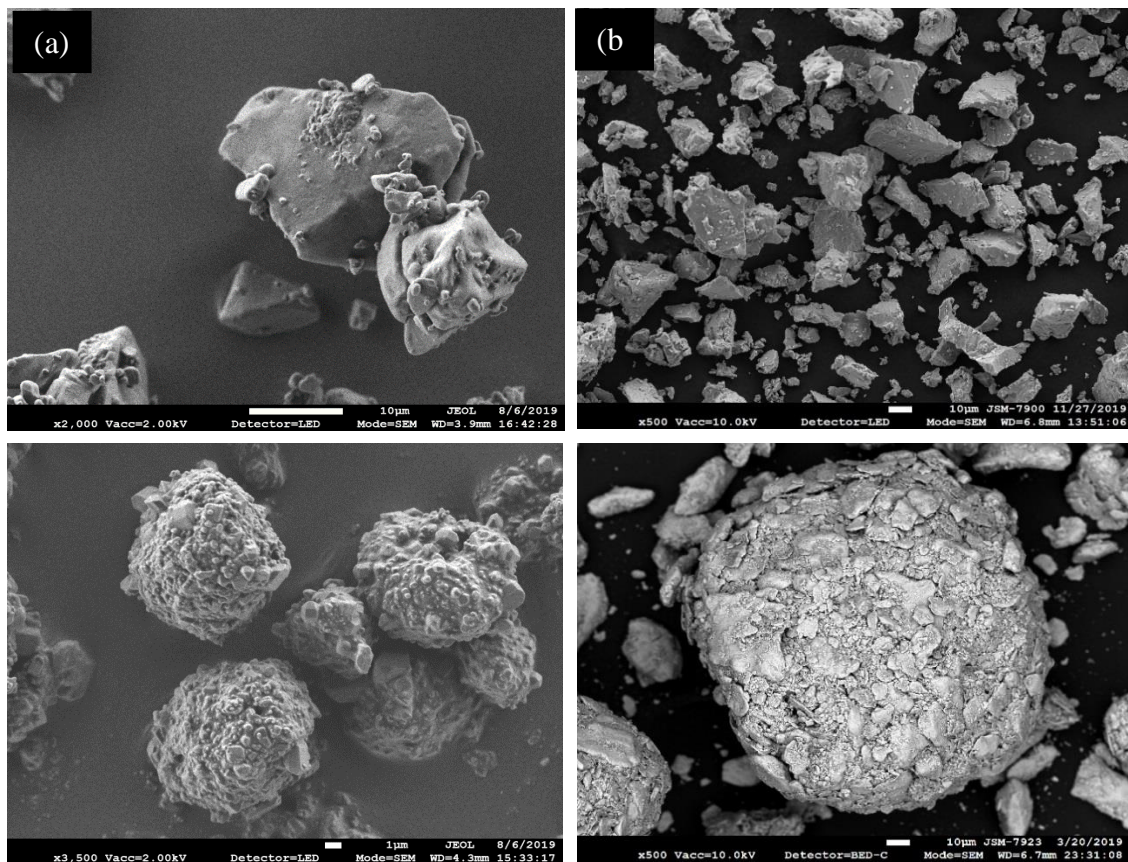


Figure B.1 Electron images of starting materials (top) and resulting microspheres (bottom) of (a) Sucrose, (b) Titanium.

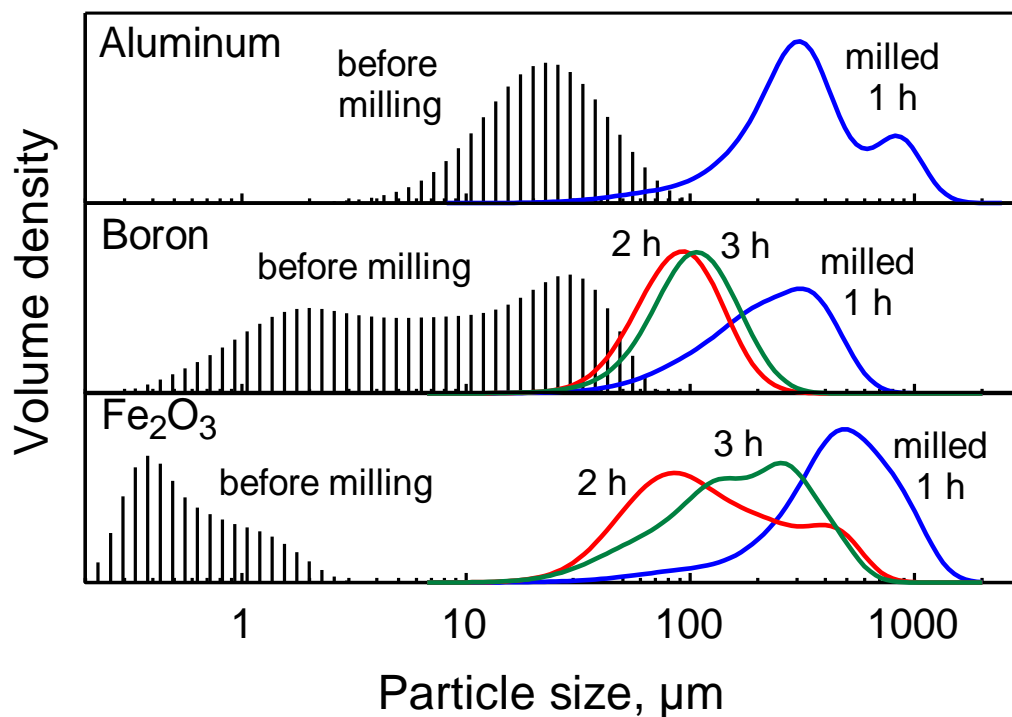


Figure B.2 Selected particle size distributions of materials before milling (vertical bars), and after sphere formation (solid lines). Sizes of spheres formed after different milling times are shown. Initial size distributions were determined by light scattering in a Malvern Mastersizer apparatus, where particles were suspended in ethylene glycol. Particle sizes of spheres were determined from low-magnification optical microscope images by image processing using ImageJ software.

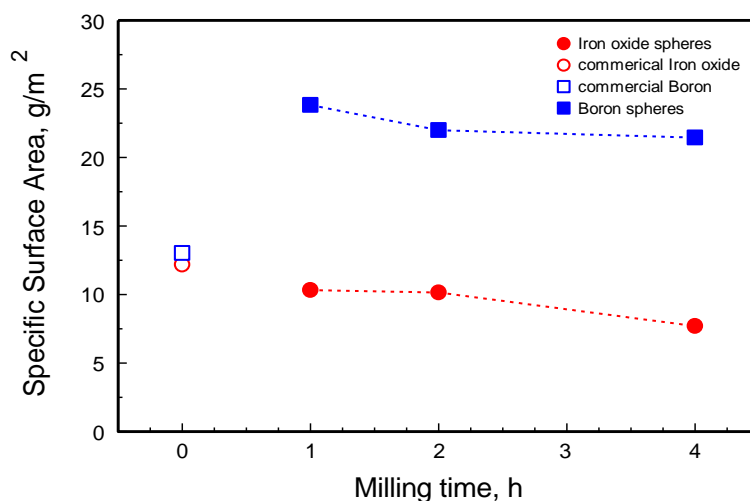


Figure B.3 Specific surface areas (BET method) of iron oxide and boron spheres and their respective starting materials.

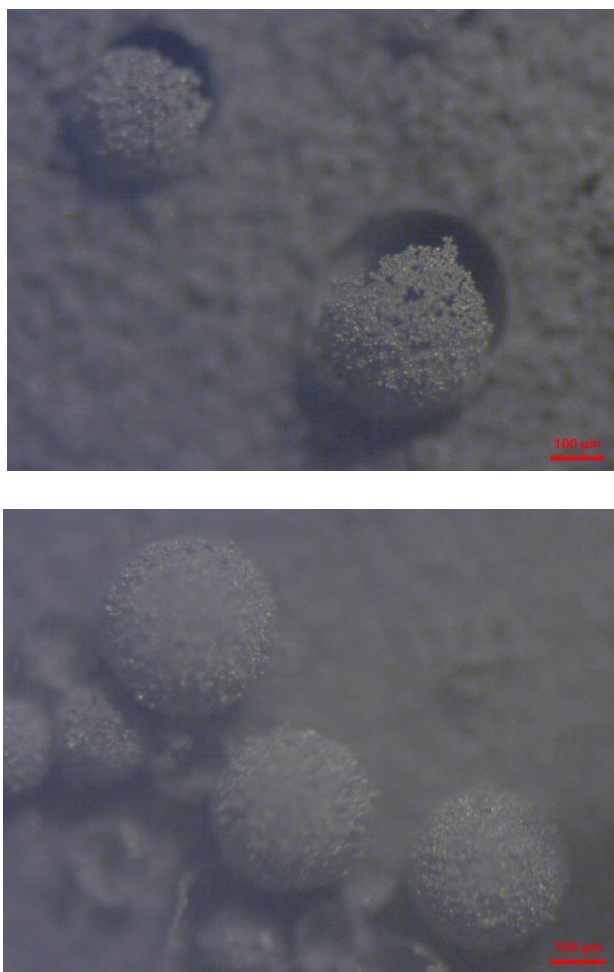


Figure B.4 Optical microscope images of hollow and fragile PR emulsion droplets formed after ultrasonication of 5 μm aluminum particles in a hexane-acetonitrile mixture.

APPENDIX C

SPHERICAL BORON MORPHOLOGY AND SIZE DISTRIBUTION

Additional characterizations on prepared spherical boron are presented below.

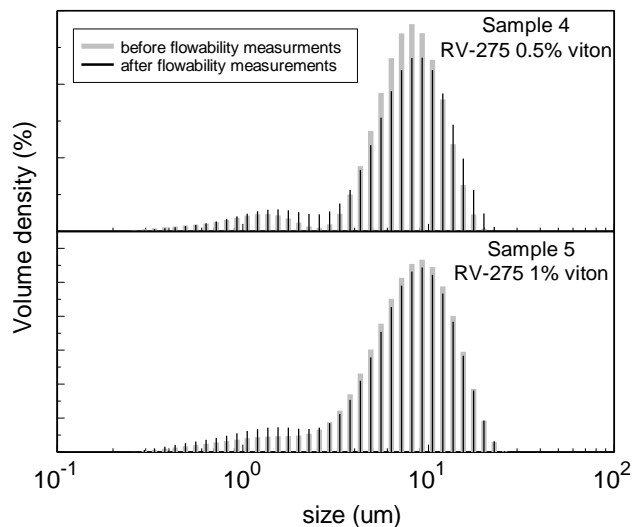


Figure C.1 Particle size distribution of sample 4 and 5 before and after flowability measurements.

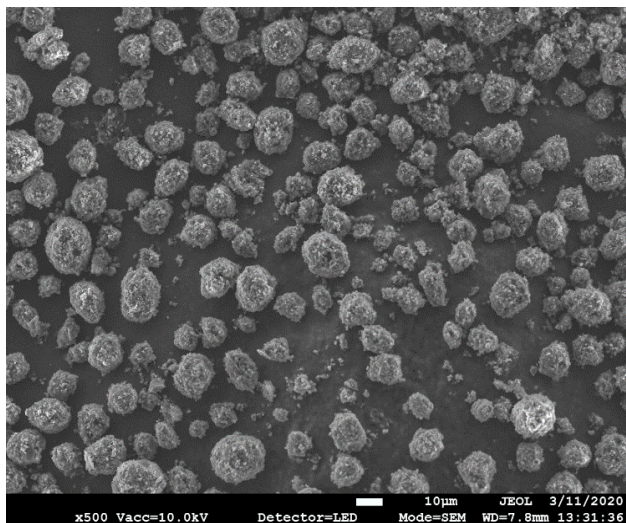


Figure C.2 SEM image of sample 29 collected after passing through 635 mesh (20um) sieve.

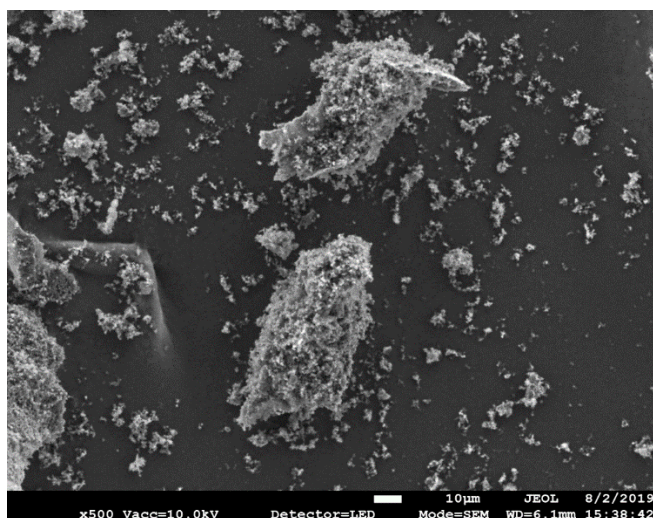


Figure C.3 SEM image of commercial boron (SB-95).

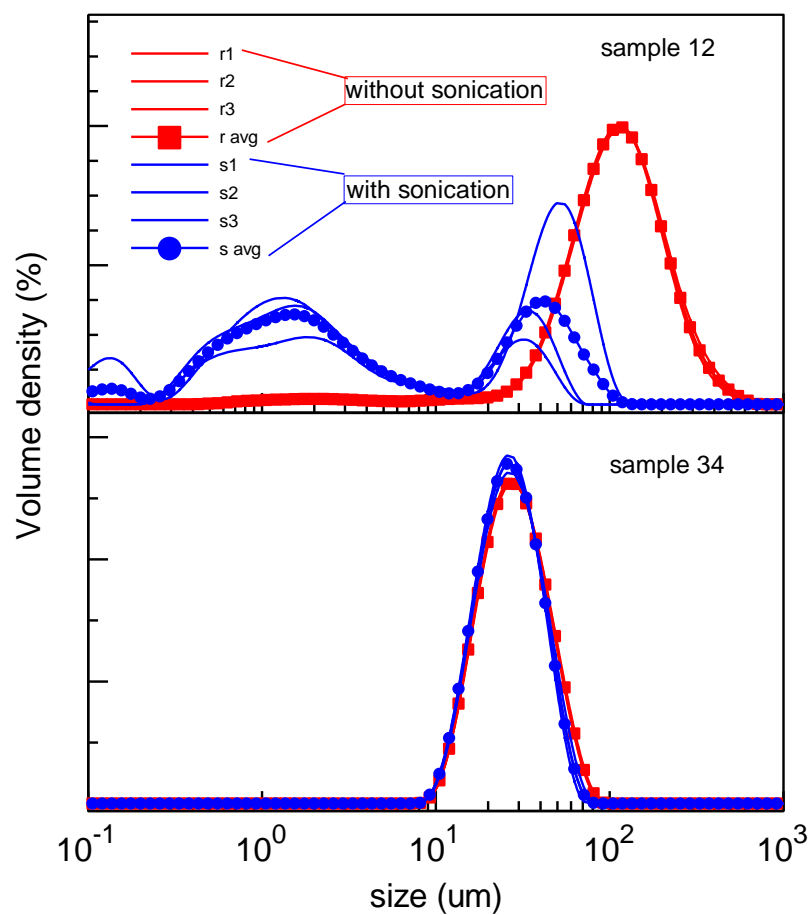


Figure. C.4. Particle size distribution with and without sonication for sample 12 and 34.

APPENDIX D

EFFECT OF SPHERICAL MORPHOLOGY ON BORON COMBUSTION

Combustion diagnostic set-up and additional characterizations are presented below.

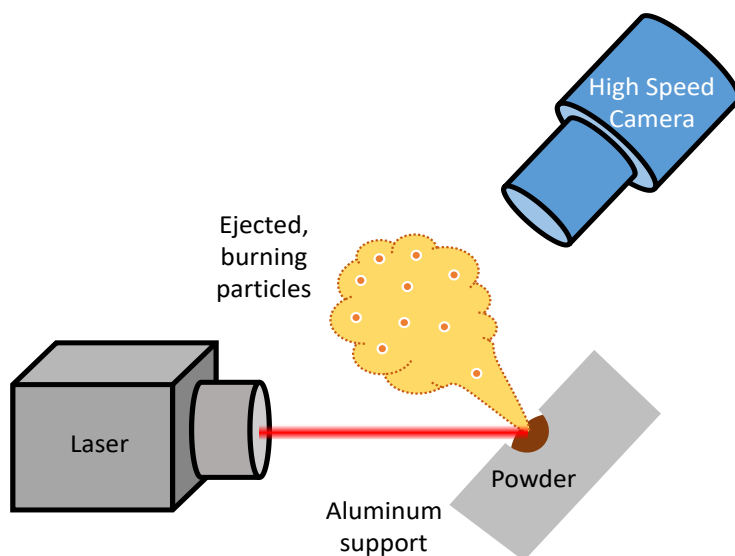


Figure D.1: Schematic diagram of the custom flame diagnostic laser set-up

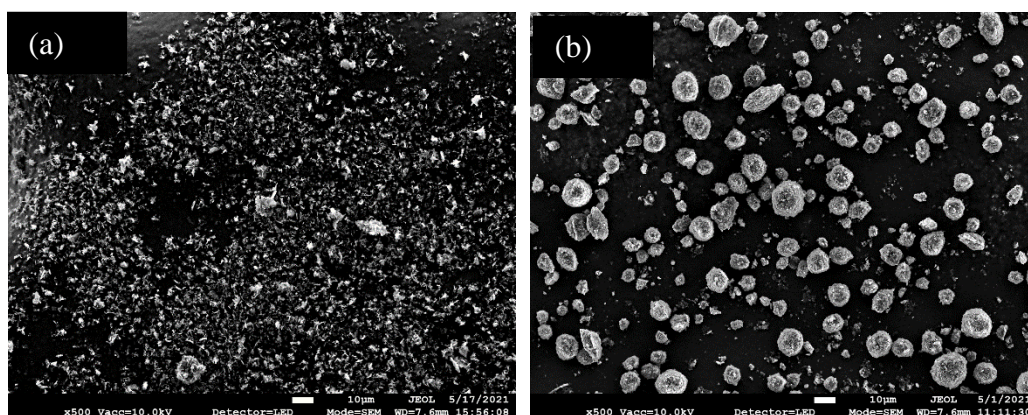


Figure D.2: SEM images of a) Commercial boron C2 and b) spheres S3

D.1 Combustion Product Analysis

The condensed CVE products were collected and analyzed to quantify the portion of boron that remained unreacted for commercial powder C2 and S3 spheres prepared using that powder. A sample of 300 mg of each combustion product was stirred continuously in 250 mL of water for 8 h to dissolve B_2O_3 . The solubility of B_2O_3 is reported to be 2.77 g per 100 mL at room temperature. The product was washed with water to remove B_2O_3 . The dried products were weighed and the amount of unreacted boron was calculated assuming that all material dissolved in water was B_2O_3 . In addition, the NASA CEA Chemical Equilibrium with Applications (CEA) code was run to calculate the maximum pressure expected in present experiments, accounting for both boron and the Al-CuO thermite present in the igniter reacting with air inside the vessel. No substantial differences between characteristics measured with irregularly shaped and spherical boron powders were observed. The mass of boron was varied in the NASA CEA code. A boron mass vs Pmax plot was generated as follows in Figure 6. Once compared with the experimental results, the commercial boron C2 appeared to have a combustion efficiency of 46% while S4 spheres showed 43% combustion efficiency.

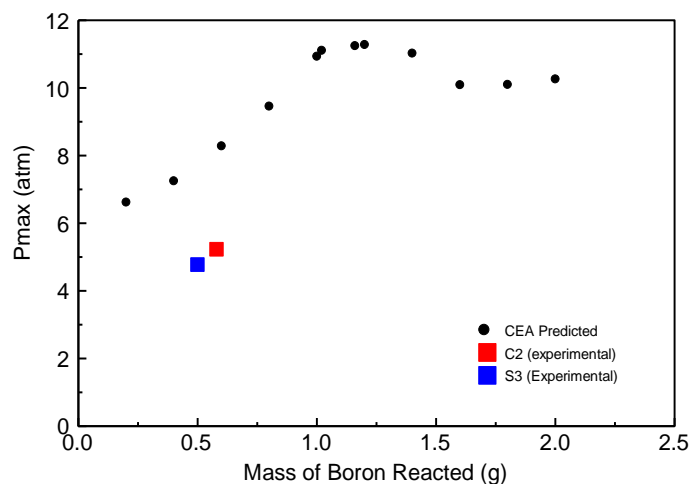


Figure S.3: CEA predicted vs experimental Pmax with mass of reacted boron.

D.2 Reaction Onset Determination

Reaction onset was determined by fitting a baseline for each TG trace as shown in Fig. S5. This baseline was subtracted from the experimentally obtained TG traces and subtracted traces were investigated. Anything below 4% of the maximum signal was considered to be noise.

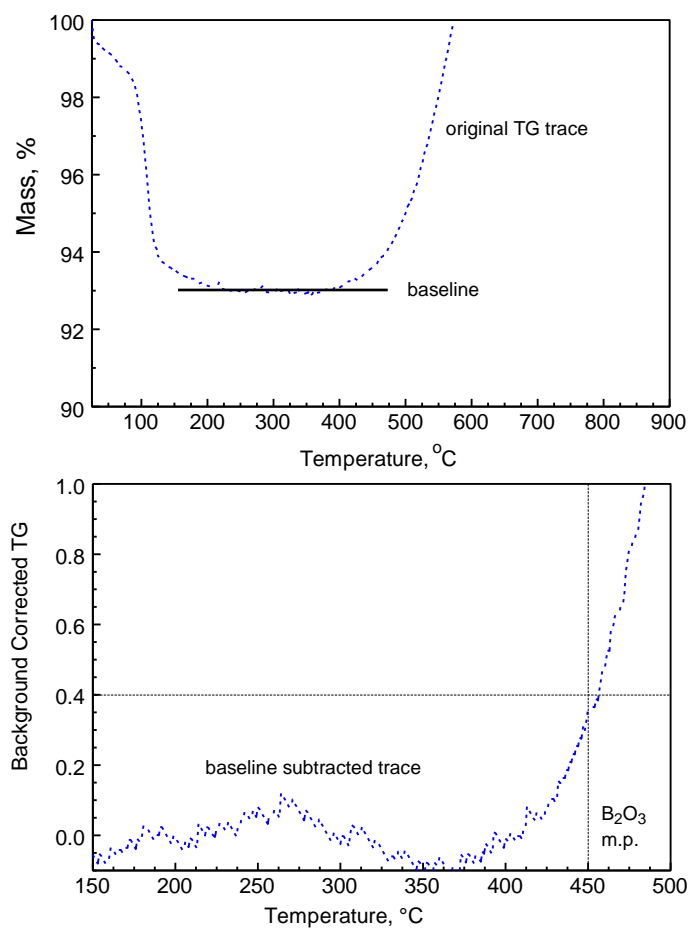


Figure D.4: Onset Processing from TG traces

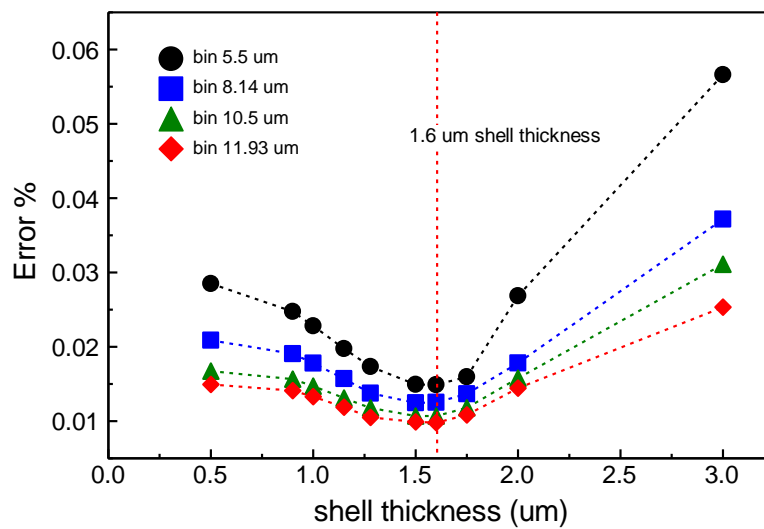


Figure D.5: Error calculation between mass gains for size bins 5.5, 8.14, 10.5 and 11.93 um for samples S1 and S2

REFERENCES

1. Yetter, R.A., G.A. Risha, and S.F. Son, *Metal particle combustion and nanotechnology*. Proceedings of the Combustion Institute, 2009. 32(2): p. 1819-1838.
2. Kuo, K.K, *Potential Usage of Energetic Nano-sized powders for combustion and rocket propulsion*. Materials Research Society Proceedings, 2003. 800: p. AA1.1.
3. Dreizin, E.L, *Metal-based reactive nanomaterials*. Progress in Energy and Combustion Science, 2009. 35(2): p. 141-167.
4. Walter, K.C, D.R. Pesiri, and D.E. Wilson, *Manufacturing and performance of nanometric Al/MoO₃ energetic materials*. Journal of Propulsion and Power, 2007. 23(4): p. 645-650.
5. Osborne, D.T. and M.L. Pantoya, *Effect of Al Particle size on the thermal degradation of Al/Teflon mixtures*. Combustion Science and Technology, 2007. 179(8): p. 1467-1480.
6. Blobaum, K.J, *Al/Ni formation reactions: Characterization of the metastable Al₉Ni₂ phase and analysis of its formation*. Acta Materialia, 2003. 51(13): p. 3871-3884.
7. Sen, S, *Synthesis and characterization of Ti/Al reactive multilayer films with various molar ratios*. Thin Solid Films, 2017. 631: p. 99-105.
8. Coffey, B.A., Schropp Jr., Donald R, Kwiatkowski, Krzysztof Czeslaw, *Solid-state thermite composition based heating device*. 2014, HeatGenie, Inc. (Austin, TX, United States).
9. Lanthony, C, *Elementary Surface Chemistry during CuO/Al Nanolaminate-Thermite Synthesis: Copper and Oxygen Deposition on Aluminum (111) Surfaces*. ACS Applied Materials & Interfaces, 2014. 6(17): p. 15086-15097.
10. Rossi, C, *Nanoenergetic Materials for MEMS: A Review*. Journal of Microelectromechanical Systems, 2007. 16(4): p. 919-931.
11. Kuntz, J.D, *Tantalum–tungsten oxide thermite composites prepared by sol–gel synthesis and spark plasma sintering*. Combustion and Flame, 2010. 157(8): p. 1566-1571.

12. Trunov, M.A, Schoenitz M. and Dreizin E.L, *Oxidation and Melting of Aluminum Nanopowders*. The Journal of Physical Chemistry B, 2006. 110(26): p. 13094-13099.
13. Sundaram, D., V. Yang, and R.A. Yetter, *Metal-based nanoenergetic materials: Synthesis, properties, and applications*. Progress in Energy and Combustion Science, 2017. 61: p. 293-365.
14. Price, E.W., *Effect of multidimensional flamelets in composite propellant combustion*. Journal of Propulsion and Power, 1995. 11(4): p. 717-729.
15. Sundaram, V., K.V. Logan, and R.F. Speyer, *Reaction path in the magnesium thermite reaction to synthesize titanium diboride*. Journal of Materials Research, 1997. 12(10): p. 2657-2664.
16. Kopeliovich, B.L., *Combustion of iron-zirconium thermite in a cylindrical channel of near-critical diameter*. Russian Journal of Physical Chemistry B, 2010. 4(2): p. 242-248.
17. Chintersingh, K.-L., M. Schoenitz, and E.L. Dreizin, *Oxidation kinetics and combustion of boron particles with modified surface*. Combustion and Flame, 2016. 173: p. 288-295.
18. Ulas, A., K.-K. Kuo, and C. Gotzmer, *Ignition and combustion of boron particles in fluorine-containing environments*. Combustion and Flame, 2001. 127(1-2):p. 1935-1957.
19. King, M.K., *Ignition and combustion of boron particles and clouds*. Journal of Spacecraft and Rockets, 1982. 19(4): p. 294-306.
20. Young, G., *Combustion characteristics of boron nanoparticles*. Combustion and Flame, 2009. 156(2): p. 322-333.
21. Nie, H., M. Schoenitz, and E.L. Dreizin, *Oxidation of magnesium: implication for aging and ignition*. The Journal of Physical Chemistry C, 2016. 120(2): p. 974-983.
22. Williams, R.A., J.V. Patel, and E.L. Dreizin, *Ignition of fully dense nanocomposite thermite powders by an electric spark*. Journal of Propulsion and Power, 2014. 30(3): p. 765-774.

23. Blobaum, K.J., *Deposition and characterization of a self-propagating CuOx/Al thermite reaction in a multilayer foil geometry*. Journal of Applied Physics, 2003. 94(5): p. 2915-2922.
24. Subramaniam, S., *Self-assembled ordered energetic composites of CuO nanorods and nanowells and Al nanoparticles with high burn rates*. Materials Research Society Proceedings, 2005. 896: p. 0896-H01-05.
25. Dong, Z., *Combined flame and electrodeposition synthesis of energetic coaxial tungsten-oxide/aluminum nanowire arrays*. Nano Letters, 2013. 13(9): p. 4346-4350.
26. Wang, H., *Assembly and reactive properties of Al/CuO based nanothermite microparticles*. Combustion and Flame, 2014. 161(8): p. 2203-2208.
27. Sanders, V.E., *Reaction propagation of four nanoscale energetic composites (Al/MoO₃, Al/WO₃, Al/CuO, and Bi₂O₃)*. Journal of Propulsion and Power, 2007. 23(4): p. 707-714.
28. Puszynski, J.A., C.J. Bulian, and J.J. Swiatkiewicz, *Processing and ignition characteristics of aluminum-bismuth trioxide nanothermite system*. Journal of Propulsion and Power, 2007. 23(4): p. 698-706.
29. Sullivan, K.T., *Reactive sintering: An important component in the combustion of nanocomposite thermites*. Combustion and Flame, 2012. 159(1): p. 2-15.
30. Monk, I., Schoenitz M. and Dreizin E.L. *Combustion characteristics of stoichiometric Al-CuO nanocomposite thermites prepared by different Methods*. Combustion Science and Technology, 2017. 189(3): p. 555-574.
31. Monk, I., M. Schoenitz, and E.L. Dreizin, *Modes of ignition of powder layers of nanocomposite thermites by electrostatic discharge*. Journal of Energetic Materials, 2017. 35(1): p. 29-43.
32. Cheng, J.L., *Synthesis and characterization of self-assembled nanoenergetic Al-Fe₂O₃ thermite system*. Journal of Physics and Chemistry of Solids, 2010. 71(2): p. 90-94.
33. Tillotson, T.M., *Nanostructured energetic materials using sol-gel methodologies*. Journal of Non-Crystalline Solids, 2001. 285(1): p. 338-345.

34. Alexander S. Tappan, M.F., Mial E. Warren, *Investigations of the small-scale thermal behavior of sol-gel thermites*. 2009: United States. Department of Energy.
35. Kwon, J., *Interfacial chemistry in Al/CuO reactive nanomaterial and its role in exothermic reaction*. ACS Applied Materials & Interfaces, 2013. 5(3): p. 605-613.
36. Abraham, A., M. Schoenitz, and E. Dreizin, *Energy storage materials with oxide-encapsulated inclusions of low melting metal*. Acta Materialia, 2016. 107: p. 254-260.
37. Qin, L., *Enhanced energy performance from core-shell structured Al@Fe₂O₃ nanothermite fabricated by atomic layer deposition*. Royal Society of Chemistry Advances, 2017. 7(12): p. 7188-7197.
38. Schoenitz, M., S.M. Umbrajkar, and E.L. Dreizin, *Kinetic analysis of thermite reactions in Al-MoO₃ nanocomposites*. Journal of Propulsion and Power, 2007. 23(4): p. 683-687.
39. Suryanarayana, C., *Mechanical alloying and milling*. Progress in Materials Science, 2001. 46(1-2): p. 1-184.
40. Umbrajkar, S.M., Schoenitz M. and Dreizin E.L, *Effect of temperature on synthesis and properties of aluminum–magnesium mechanical alloys*. Journal of Alloys and Compounds, 2005. 402(1): p. 70-77.
41. Umbrajkar, S.M., M. Schoenitz, and E.L. Dreizin, *Control of structural refinement and composition in Al-MoO₃ nanocomposites prepared by arrested reactive milling*. Propellants, Explosives, Pyrotechnics, 2006. 31(5): p. 382-389.
42. Santhanam, P.R. and E.L. Dreizin, *Predicting conditions for scaled-up manufacturing of materials prepared by ball milling*. Powder Technology, 2012. 221: p. 403-411.
43. Kinsey, A.H., *Enhanced reaction velocity and diluent homogenization in redox foils using arrested reactive milling thermite powder*. Journal of Materials Science, 2017. 52(18): p. 11077-11090.
44. Bazyn, T., *Combustion measurements of fuel-rich aluminum and molybdenum oxide nano-composite mixtures*. Propellants, Explosives, Pyrotechnics, 2010. 35(2): p. 93-99.

45. Monk I, Schoenitz M. and Dreizin E.L, *Combustion of a rapidly initiated fully dense nanocomposite Al-CuO thermite powder*. Combustion theory and modelling. Combustion Theory and Modelling, 2019. 23(4): p. 651-673
46. Yu, J., *Aluminum Nanoparticle production by acetonitrile-assisted milling: effects of liquid- vs vapor-phase milling and of milling method on particle size and surface chemistry*. The Journal of Physical Chemistry C, 2016. 120(35): p. 19613-19629.
47. L. Shoshin, Y., Schoenitz M. and Dreizin E.L, *Ignition of aluminum-rich Al-Ti mechanical alloys in air*. Vol. 144. 2006. 688-697.
48. Stamatis, D., Dreizin E.L., and Higa K., *Thermal initiation of Al-MoO₃ nanocomposite materials prepared by different methods*. Journal of Propulsion and Power, 2011. 27(5): p. 1079-1087.
49. Monk, I., Schoenitz M. and Dreizin E.L., *The effect of heating rate on combustion of fully dense nanocomposite thermite particles*. Combustion Science and Technology, 2018. 190(2): p. 203-221.
50. McMahon, B.W., *Synthesis of nanoparticles from malleable and ductile metals using powder-free, reactant-assisted mechanical attrition*. ACS Applied Materials & Interfaces, 2014. 6(22): p. 19579-19591.
51. Shaw, L., *Effects of process-control agents on mechanical alloying of nanostructured aluminum alloys*. Metallurgical and Materials Transactions A, 2003. 34(1): p. 159-170.
52. Machio, C., Chikwanda H.K., and Chikosha S., *Effect of process control agent (PCA) on the characteristics of mechanically alloyed Ti-Mg powders*. Journal of the Southern African Institute of Mining and Metallurgy, 2011. 111: p. 149-153.
53. Umbrajkar, S.M., Schoneitz M. and Dreizin E.L., *Exothermic reactions in Al-CuO nanocomposites*. Thermochimica Acta, 2006. 451(1): p. 34-43.
54. Williams, R.A., Schoneitz M. and Dreizin E.L., *On gas release bt thermally-initiated fully-dense 2Al-3CuO nano composite powder*, International Journal of Energetic Materials and Chemical Propulsion 2012. 11(3): p. 275-292.
55. Nguyen, Q., Schoneitz M. and Dreizin E.L. *Nanocomposite thermite powders with improved flowability prepared by mechanical milling*. Powder Technology, 2018. 327: p. 368-380.

56. Williams, R.A., Schoneitz M. and Dreizin E.L., *Validation of the thermal oxidation model for Al/CuO nanocomposite powder*. Combustion Science and Technology, 2014. 186(1): p. 47-67.
57. Badiola, C., *Nanocomposite thermite powders prepared by cryomilling*. Journal of Alloys and Compounds, 2009. 488(1): p. 386-391.
58. Rietveld, H.M., *Rietveld method - a historical perspective*. Australian Journal of Physics, 1988. 41(2): p. 113-116.
59. Degen, T., *The HighScore suite*. Powder Diffraction, 2014. 29(S2): p. S13-S18.
60. Hastings, D.L., Schoneitz M. and Dreizin E.L., *High density reactive composite powders*. Journal of Alloys and Compounds, 2018. 735: p. 1863-1870.
61. Kissinger, H.E., *Reaction kinetics in differential thermal analysis*. Analytical Chemistry, 1957. 29(11): p. 1702-1706.
62. Ermoline, A., D. Stamatis, and Dreizin E.L., *Low-temperature exothermic reactions in fully dense Al-CuO nanocomposite powders*. Thermochimica Acta, 2012. 527: p. 52-58.
63. Olefjord, I. and Nylund A., *Surface analysis of oxidized aluminium. 2. Oxidation of aluminium in dry and humid atmosphere studied by ESCA, SEM, SAM and EDX*. Surface and Interface Analysis, 1994. 21(5): p. 290-297.
64. Chen, C., *Measurement of oxide film growth on Mg and Al surfaces over extended periods using XPS*. Surface Science, 1997. 382(1): p. L652-L657.
65. Sander, J.S. and Studart A.R., *Multiwalled functional colloidosomes made small and in large quantities via bulk emulsification*. Soft Matter, 2014. 10(1): p. 60-68.
66. Folter D, *Particle shape anisotropy in pickering emulsions: cubes and peanuts*. Langmuir, 2014. 30(4): p. 955-964.
67. Yang, Y., *An overview of pickering emulsions: solid-particle materials, classification, morphology, and applications*. Frontiers in Pharmacology, 2017. 8: p. 287-287.
68. Dreizin, E.L., *Metal-Based Reactive Nanomaterials*. Vol. 35. 2009. 141-167.

69. Dreizin, E.L. and M. Schoenitz, *Nano-composite energetic powders prepared by arrested reactive milling*, in *US Patent 7,524,355* 2009.
70. Monk, I., Schoenitz M., and Dreizin E.L., *Combustion of a rapidly initiated fully dense nanocomposite Al–CuO thermite powder*. *Combustion Theory and Modelling*, 2019: p. 1-23.
71. Stamatis, D., A. Ermoline, and Dreizin E.L., *A multi-step reaction model for ignition of fully-dense Al-CuO nanocomposite powders*. *Combustion Theory and Modelling*, 2012. 16(6): p. 1011-1028.
72. Stamatis, D., Schoenitz M., and Dreizin E.L., *Fully dense, aluminum-rich Al-CuO nanocomposite powders for energetic formulations*. *Combustion Science and Technology*, 2009. 181(1): p. 97-116.
73. Umbrajkar, S.M., Schoenitz M., and Dreizin E.L., *Exothermic reactions in Al-CuO nanocomposites*. *Thermochimica Acta*, 2006. 451(1-2): p. 34-43.
74. Williams, R.A., Schoenitz M., and Dreizin E.L., *On gas release by thermally-initiated fully-dense 2Al·3CuO nanocomposite powder*. . *International Journal of Energetic Materials and Chemical Propulsion*, 2012. 11(3): p. 275-292.
75. Mursalat, M., Schoenitz M., and Dreizin E.L., *Composite Al-Ti powders prepared by high-energy milling with different process controls agents*. *Advanced Powder Technology*, 2019: p. 1319-1328.
76. Yu, J., *Aluminum nanoparticle production by acetonitrile-assisted milling: Effects of liquid- vs vapor-phase milling and of milling method on particle size and surface chemistry*. *Journal of Physical Chemistry C*, 2016. 120(35): p. 19613-19629.
77. Schindelin, J., *Fiji: an open-source platform for biological-image analysis*. *Nature Methods*, 2012. 9(7): p. 676-682.
78. Brocher, J., *Qualitative and quantitative evaluation of two new histogram limiting binarization algorithms*. *Int. J. Image Process.*, 2014. 8: p. 30-48.
79. Degen, T., *The high score suite*. *Powder Diffraction*, 2014. 29: p. S13-S18.
80. Okamoto H., Schlesinger M.E., and Mueller E.M, Editors. *Aluminum binary alloy phase diagrams, Alloy Phase Diagrams*, , ASM International. 2016

81. Schoenitz, M. and Dreizin E.L., *Structure and properties of Al-Mg mechanical alloys*. Journal of Materials Research, 2003. 18(8): p. 1827-1836.
82. Mursalat, M., Schoenitz, M. and Dreizin E.L., *Custom particle morphology in energetic nanocomposites prepared by arrested reactive milling in immiscible liquids*. Powder Technology, 2020. 359: p. 238-246.
83. Chase M.W., *NIST-JANAF thermochemical tables, Fourth Edition*. Journal of Physical and Chemical Reference Data, 1998(Monograph 9): p. 1-1951.
84. Puszynski, J.A., Bulian C.J., and Swiatkiewicz J.J., *The effect of nanopowder attributes on reaction mechanism and ignition sensitivity of nanothermites*. in *Materials Research Society Symposium Proceedings*. 2006.
85. Wang, H., *Electrospray formation and combustion characteristics of iodine-containing Al/CuO nanothermite microparticles*. Combustion and Flame, 2015. 162(7): p. 2823-2829.
86. Petrantonio, M., *Multilayered Al/CuO thermite formation by reactive magnetron sputtering: Nano versus micro*. Journal of Applied Physics, 2010. 108(8).
87. Zhou, X., *Influence of Al/CuO reactive multilayer films additives on exploding foil initiator*. Journal of Applied Physics, 2011. 110(9).
88. Blobaum, K.J., *Deposition and characterization of a self-propagating CuOx/Al thermite reaction in a multilayer foil geometry*. Journal of Applied Physics, 2003. 94(5): p. 2915-2922.
89. Blobaum, K.J., *Investigating the reaction path and growth kinetics in CuOx/Al multilayer foils*. Journal of Applied Physics, 2003. 94(5): p. 2923-2929.
90. Yu, C., *Core/shell CuO/Al nanorod thermite film based on electrochemical anodization*. Nanotechnology, 2018. 29(36).
91. Hu, B., *Electrochemical synthesis of Al/CuO thermite films on copper substrates*. Industrial and Engineering Chemistry Research, 2019. 58(17): p. 7131-7138.
92. Wang, Y.T., *Fabrication and characterization of Al–CuO nanocomposites prepared by sol-gel method*. Defence Technology, 2020.
93. Calais, T., *Correlation between DNA self-assembly kinetics, microstructure, and thermal properties of unburnable highly energetic Al-CuO nanocomposites for*

- micropyrotechnic applications*. ACS Applied Nano Materials, 2018. 1(9): p. 4716-4725.
94. Shende, R., *Nanoenergetic composites of CuO nanorods, nanowires, and Al-nanoparticles*. Propellants, Explosives, Pyrotechnics, 2008. 33(2): p. 122-130.
 95. Calais, T *DNA grafting and arrangement on oxide surfaces for self-assembly of Al and CuO nanoparticles*. Langmuir, 2017. 33(43): p. 12193-12203.
 96. Kwon, J., *Interfacial chemistry in Al/CuO reactive nanomaterial and its role in exothermic reaction*. ACS Applied Materials and Interfaces, 2013. 5(3): p. 605-613.
 97. Lanthony, C., *Elementary surface chemistry during CuO/Al nanolaminate-thermite synthesis: Copper and oxygen deposition on aluminum (111) surfaces*. ACS Applied Materials and Interfaces, 2014. 6(17): p. 15086-15087.
 98. Rossi, C., *Engineering of Al/CuO Reactive Multilayer Thin Films for Tunable Initiation and Actuation*. Propellants, Explosives, Pyrotechnics, 2019. 44(1): p. 94-108.
 99. Marín, L., *Performance enhancement via incorporation of ZnO nanolayers in energetic Al/CuO multilayers*. Langmuir, 2017. 33(41): p. 11086-11093.
 100. Julien, B., *Integration of gold nanoparticles to modulate the ignitability of nanothermite films*. ACS Applied Nano Materials, 2020.
 101. Kinsey, A.H., *Gas suppression via copper interlayers in magnetron sputtered Al-Cu₂O multilayers*. ACS Applied Materials and Interfaces, 2017. 9(26): p. 22026-22036.
 102. Schoenitz, M., T. Ward, and Dreizin E.L., *Preparation of energetic metastable nano-composite materials by arrested reactive milling*. Material Research Society Proceedings, 2011. 800: p. AA2.6.
 103. Mursalat, M., Schoenitz, M. and Dreizin E.L., *Effect of premilling Al and CuO in acetonitrile on properties of Al-CuO thermites prepared by arrested reactive milling*. Combustion and Flame, 2020. 214: p. 57-64.
 104. Gates S.. and T. Blanton, *The Powder Diffraction File: a quality materials characterization database*. Powder Diffraction, 2019. 34(4): p. 352-360.

105. Huang, C., Schoenitz, M. and Dreizin E.L., *Displacement of powders from surface by shock and plasma generated by electrostatic discharge*. Journal of Electrostatics, 2019. 100: p. 103353.
106. Huang, C., Schoenitz, M. and Dreizin E.L., *Ignition of zirconium powders placed near an electrostatic discharge*. Combustion and Flame, 2021. 226: p. 1-13.
107. Fonseca P.C. and G.W. Scherer, *An image analysis procedure to quantify the air void system of mortar and concrete*. Materials and Structures, 2015. 48(10): p. 3087-3098.
108. Jiang N., and Spence J.C.H., *Interpretation of oxygen K pre-edge peak in complex oxides*. Ultramicroscopy, 2006. 106(3): p. 215-219.
109. Zhang S.. and Dreizin E.L, *Reaction interface for heterogeneous oxidation of aluminum powders*. Journal of Physical Chemistry C, 2013. 117(27): p. 14025-14031.
110. Smith T., *Solid propellants-elastomeric-binder and mechanical property requirements for solid propellants*. Industrial & Engineering Chemistry, 1960. 52(9): p. 776-780.
111. Price E.W., *Combustion of metallized propellants*. Progress in Astronautics and Aeronautics, ed. K.K.K.a.M. Summerfield. Vol. 90. 1984, New York: AIAA. 479-513.
112. Gany A. and Caveny L.H., *Agglomeration and ignition mechanism of aluminum particles in solid propellants*. Symposium (International) on Combustion, 1979. 17(1): p. 1453-1461.
113. Sambamurthi J.K., Price E.W., and Sigman R.K., *Aluminum agglomeration in solid-propellant combustion*. AIAA Journal, 1984. 22(8): p. 1132-1138.
114. Babuk, V.A. and Vasilyev V.A., *Model of aluminum agglomerate evolution in combustion products of solid rocket propellant*. Journal of Propulsion and Power, 2002. 18(4): p. 814-823.
115. Breiter, A.L., Mal'tsev V.M., and Popov E.I., *Means of modifying metallic fuel in condensed systems*. Combustion, Explosion, and Shock Waves, 1990. 26(1): p. 86-92.

116. Tüzün, F.N., *The effect of aluminum and ammonium perchlorate content on temperature sensitivity, mechanical properties and performance of HTPB propellants*. Transactions of the Japan Society for Aeronautical and Space Sciences, 2007. 50(169): p. 175-180.
117. Shoshin, Y., L, Scheonitz M. Dreizin E.L., *Ignition of aluminum-rich Al–Ti mechanical alloys in air*. Combustion and Flame, 2006. 144: p. 688-697.
118. Scheonitz M. Dreizin E.L., *Structure and properties of Al–Mg mechanical alloys*. Journal of Materials Research, 2003. 18(8): p. 1827-1836.
119. Zenin, A.A., Kuznetsov G.P. and Kolesnikov V.I., *Combustion of aluminum-magnesium alloy particles in micro gravity*. Khim. Fiz., 2011. 30(Copyright (C) 2012 American Chemical Society (ACS). All Rights Reserved.): p. 28-41.
120. Chen R.H., Suryanarayana C., and Chaos M., *Combustion characteristics of mechanically alloyed ultrafine-grained Al-Mg powders*. Adv. Eng. Mater., 2006. 8(Copyright (C) 2012 American Chemical Society (ACS), p. 563-567.
121. Schoenitz, M. and Dreizin E.L., *Structure and properties of Al–Mg mechanical alloys*. Journal of Materials Research, 2011. 18(8): p. 1827-1836.
122. Aly, Y., Schoenitz, M. and Dreizin E.L., *Reactive, Mechanically Alloyed Al-Mg Powders with Customized Particle Sizes and Compositions*. Journal of Propulsion and Power, 2013. 30(1): p. 96-104.
123. Schoenitz M., X. Zhu, and Dreizin E.L., *Mechanical alloys in the Al-rich part of the Al-Ti binary system*. Journal of Metastable and Nanocrystalline Materials, 2004. 20-21: p. 455-461.
124. Santhanam, P.R., Schoenitz, M. and Dreizin E.L., *Characteristics of aluminum combustion obtained from constant-volume explosion experiments*. Combustion Science and Technology, 2010. 182(7): p. 904-921.
125. Schoenitz, M. Dreizin E.L., and Shtessel E., *Constant volume explosions of aerosols of metallic mechanical alloys and powder blends*. Journal of Propulsion and Power, 2003. 19(3): p. 405-412.
126. Zhu X., Schoenitz, M. and Dreizin E.L., *Oxidation processes and phase changes in metastable Al-Ti mechanical alloys*. in *Materials Research Society Symposium - Proceedings*. 2003.

127. Baláž, P., *Hallmarks of mechanochemistry: From nanoparticles to technology*. Chemical Society Reviews, 2013. 42(18): p. 7571-7637.
128. Do, J.L. and T. Friščić, *Mechanochemistry: A force of synthesis*. ACS Central Science, 2017. 3(1): p. 13-19.
129. Howard J.L., Cao Q. and Browne D.L., *Mechanochemistry as an emerging tool for molecular synthesis: What can it offer?* Chemical Science, 2018. 9(12): p. 3080-3094.
130. Tan, D. and Friščić T., *Mechanochemistry for organic chemists: An update*. European Journal of Organic Chemistry, 2018. 2018(1): p. 18-33.
131. Suryanarayana, C., *Mechanical alloying and milling*. Mechanical Alloying and Milling. 2004. 1-472.
132. Fullenwider, B., *Two-stage ball milling of recycled machining chips to create an alternative feedstock powder for metal additive manufacturing*. Powder Technology, 2019. 342: p. 562-571.
133. Zhang, Y.F., *Particle size evolution of V-4Cr-4Ti powders in high energy vibrating and planetary ball milling*. Materials Research Express, 2019. 6(6).
134. Radlinski, A.P., *Application of surface active substances in mechanical alloying*. Materials Science and Engineering A, 1991. 134(C): p. 1346-1349.
135. Nouri, A. and Wen C., *Surfactants in mechanical alloying/milling: A catch-22 situation*. Critical Reviews in Solid State and Materials Sciences, 2014. 39(2): p. 81-108.
136. Anas, N.S., *Influence of process control agents on microstructure and mechanical properties of Al alloy produced by mechanical alloying*. Materials Science and Engineering A, 2019. 751: p. 171-182.
137. Fu, X., *Effect of particle shape and size on flow properties of lactose powders*. Particuology, 2012. 10(2): p. 203-208.
138. Attar, H., *Effect of powder particle shape on the properties of in situ Ti-TiB composite materials produced by selective laser melting*. Journal of Materials Science and Technology, 2015. 31(10): p. 1001-1005.

139. Kaialy, W., *Effect of carrier particle shape on dry powder inhaler performance*. International Journal of Pharmaceutics, 2011. 421(1): p. 12-23.
140. Balázs, N., *The effect of particle shape on the activity of nanocrystalline TiO₂ photocatalysts in phenol decomposition*. Applied Catalysis B: Environmental, 2008. 84(3-4): p. 356-362.
141. Tekce, H.S., Kumlutas D., and Tavman I.H., *Effect of particle shape on thermal conductivity of copper reinforced polymer composites*. Journal of Reinforced Plastics and Composites, 2007. 26(1): p. 113-121.
142. Yekeler M., Ulusoy U., and Hiçyılmaz C., *Effect of particle shape and roughness of talc mineral ground by different mills on the wettability and floatability*. Powder Technology, 2004. 140(1-2): p. 68-78.
143. Jiajun W.. and Xiao-Su Y., *Effects of interfacial thermal barrier resistance and particle shape and size on the thermal conductivity of AlN/PI composites*. Composites Science and Technology, 2004. 64(10-11): p. 1623-1628.
144. Hayashi, Y., *Method and apparatus for production of metal particles for solder paste*. 2017, Tohoku University, Japan; Panasonic Corp. . p. 17pp.
145. Zhu, J. and Li X., *A kind of high-efficiency preparing superfine spherical metal particle method and apparatus for [Machine Translation]*. 2018, Zhangjiagang Cobo Metal Technology Co., Ltd., Peop. Rep. China . p. 7pp.
146. Chevalier Y. and Bolzinger M.A., *Emulsions stabilized with solid nanoparticles: Pickering emulsions*. Colloids and Surfaces A: Physicochemical and Engineering Aspects, 2013. 439: p. 23-34.
147. Dinsmore, A.D., *Colloidosomes: selectively permeable capsules composed of colloidal particles*. Science, 2002. 298(5595): p. 1006-1009.
148. Williams M., *Double emulsions and colloidosomes-in-colloidosomes using silica-based pickering emulsifiers*. Langmuir, 2014. 30(10): p. 2703-2711.
149. Lee D. and Weitz D.A., *Double emulsion-templated nanoparticle colloidosomes with selective permeability*. Advanced Materials, 2008. 20(18): p. 3498-3503.
150. Whitby C.P. and Wanless E.J., *Controlling pickering emulsion destabilisation: A route to fabricating new materials by phase inversion*. Materials, 2016. 9(8).

151. Zhao, L., *A new mechanism of sediment attachment to oil in turbulent flows: projectile particles*. Environmental Science and Technology, 2017. 51(19): p. 11020-11028.
152. Pang, W., *Application of amorphous boron granulated with hydroxyl- terminated polybutadiene in fuel-rich solid propellant*. Propellants, Explosives, Pyrotechnics, 2011. 36(4): p. 360-366.
153. Hu, X.L., *Effect of boron powder and agglomerated boron particles on the rheological property of HTPB*. Gutu Huojian Jishu/Journal of Solid Rocket Technology, 2014. 37(3): p. 369-375.
154. Pivkina, A.N., *Comparative analysis of boron powders obtained by various methods and. Microstructure and Oxidation Parameters during Heating*. Combustion, Explosion and Shock Waves, 2018. 54(4): p. 450-460.
155. Meerov, D., *Boron particles agglomeration and slag formation during combustion of energetic condensed systems*. Physics Procedia, 2015. 72: p. 85-88.
156. Cheng, L., *Preparation of B/Nitrocellulose/Fe particles and their effect on the performance of an ammonium perchlorate propellant*. Combustion and Flame, 2020. 211: p. 456-464.
157. Goodman I.A., and Fenn V.O., *Preparation and properties of concentrated boron-hydrocarbon slurry fuels*. 1954: National Advisory Committee for Aeronautics.
158. Xu, H.X., *Rheological characteristic of agglomerated boron powder with HTPB mixture*. Tuijin Jishu/Journal of Propulsion Technology, 2008. 29(5): p. 631-636.
159. Pang, W.Q., et al., *Intensity of spherical agglomerated boron particles*. Hanneng Cailiao/Chinese Journal of Energetic Materials, 2009. 17(5): p. 510-513.
160. Xu H.X., Zhao F.Q., and Li Y.H., *Effect of neutralised boron powder on rheological characteristic of b/htpb*. Hanneng Cailiao/Chinese Journal of Energetic Materials, 2007. 15(4): p. 341-344.
161. Zhang, H.L., *Preparation of agglomerated boron particles by extrusion-spheronization method*. Huozhayao Xuebao/Chinese Journal of Explosives and Propellants, 2019. 42(5): p. 497-503.
162. Jung, H.J., *Physicochemical properties of ball milled boron particles: Dry vs. wet ball milling process*. Powder Technology, 2015. 269: p. 548-553.

163. Pontes, R., *Boron nanoparticle-rich fuels for gas generators and propellants*. International Journal of Energetic Materials and Chemical Propulsion, 2010. 9: p. 437-446.
164. Hernández T., *Micro and nanoparticles by electrospray: advances and applications in foods*. Journal of Agricultural and Food Chemistry, 2015. 63(19): p. 4699-4707.
165. Mursalat M., Schoenitz M. and Dreizin E.L., *Microspheres with diverse material compositions can be prepared by mechanical milling*. Advanced Engineering Materials, 2019.
166. Lumay, G., *Influence of temperature on the packing dynamics of polymer powders*. Advanced Powder Technology, 2020.
167. Saker, A., *Powders flowability assessment in granular compaction: What about the consistency of Hausner ratio?* Powder Technology, 2019. 354: p. 52-63.
168. Traina, K., *Flow abilities of powders and granular materials evidenced from dynamical tap density measurement*. Powder Technology, 2013. 235: p. 842-852.
169. Lumay, G., *Effect of relative air humidity on the flowability of lactose powders*. Journal of Drug Delivery Science and Technology, 2016. 35: p. 207-212.
170. Rescaglio, A., et al., *Tribo-electrification of pharmaceutical powder blends*. Particulate Science and Technology, 2019. 37(8): p. 1024-1031.
171. Lumay G., *Measuring the flowing properties of powders and grains*. Powder Technology, 2012. 224: p. 19-27.
172. Agresti A., *Foundations of linear and generalized linear models*. Wiley series in probability and statistics. 2016, Hoboken, New Jersey: John Wiley & Sons Inc. 472.
173. Leys, C., *Detecting outliers: Do not use standard deviation around the mean, use absolute deviation around the median*. Journal of Experimental Social Psychology, 2013. 49(4): p. 764-766.
174. *NIST/SEMATECH e-Handbook of Statistical Methods*. 2012; Available from:
175. Heintzenberg J., *Properties of the log-normal particle size distribution*. Aerosol Science and Technology, 1994. 21(1): p. 46-48.

176. Gany, A., *Thermodynamic limitation on boron energy realization in ramjet propulsion*. Acta Astronautica, 2014. 98(1): p. 128-132.
177. Young, G., *Combustion of PTFE-boron compositions for propulsion applications*. International Journal of Energetic Materials and Chemical Propulsion, 2012. 11(5): p. 451-471.
178. Gany, A. and Timnat Y.M., *Advantages and drawbacks of boron-fueled propulsion*. Acta Astronautica, 1993. 29(3): p. 181-187.
179. Ulas, A., Risha G.A., and Kuo K.K., *An investigation of the performance of a boron/potassium-nitrate based pyrotechnic igniter*. Propellants, Explosives, Pyrotechnics, 2006. 31(4): p. 311-317.
180. Huang S., *Experimental effective metal oxides to enhance boron combustion*. Combustion and Flame, 2019. 205: p. 278-285.
181. Burke, A.R., et al., *Ignition mechanism of the titanium–boron pyrotechnic mixture*. Surface and Interface Analysis, 1988. 11(6-7): p. 353-358.
182. Eslami A., Hosseini S.G., and Pourmortazavi S.M., *Thermoanalytical investigation on some boron-fuelled binary pyrotechnic systems*. Fuel, 2008. 87(15-16): p. 3339-3343.
183. Rashkovskiy S.A., *Formation of solid residues in combustion of boron-containing solid propellants*. Acta Astronautica, 2019. 158: p. 277-285.
184. Martinez- J., Franco P., and Ramirez F.F.J., *Rheological characterization of energetic materials by rotational testing techniques*. in ASME 2014 12th Biennial Conference on Engineering Systems Design and Analysis, ESDA 2014. 2014.
185. Pang, W.Q., *Surface and interfacial properties of fuel rich propellant with agglomerated boron particles*. Gutu Huojian Jishu/Journal of Solid Rocket Technology, 2013. 36(4): p. 521-525.
186. Hu, X.L., *Influence of acidic impurities on rheological properties of boron/agglomerated boron and HTPB slurry*. 2013. p. 898-904.
187. Shyu, I.M. and Liu T.K., *Combustion characteristics of GAP-coated boron particles and the fuel-rich solid propellant*. Combustion and Flame, 1995. 100(4): p. 634-644.

188. Gao, D.L., *Effect of coating and agglomerating on combustion of boron*. Hanneng Cailiao/Chinese Journal of Energetic Materials, 2007. 15(4): p. 378-381.
189. Mursalat, M., Schoenitz M. and Dreizin E.L., *Spherical boron powders prepared by mechanical milling in immiscible liquids*. Powder Technology, 2021. 388: p. 41-50.
190. Wang, H., *Comparison study of the ignition and combustion characteristics of directly-written Al/PVDF, Al/Viton and Al/THV composites*. Combustion and Flame, 2019. 201: p. 181-186.
191. Verma, P., *Effect of different binders on mechanical and ballistic properties of boron -viton based fuel rich propellant*. AIP Conference Proceedings, 2013. 1536: p. 1248-1249.
192. Hastings, D., Schoenitz M., and E.L. Dreizin, *Highly reactive spheroidal milled aluminum*. Materialia, 2020: p. 100959.
193. Mursalat, M., Schoenitz M., and Dreizin E.L., *Composite Al-Ti powders prepared by high-energy milling with different process controls agents*. 2019.
194. Eapen, B.Z., *Combustion of aerosolized spherical aluminum powders and flakes in air*. Combustion Science and Technology, 2004. 176(7): p. 1055-1069.
195. Aly, Y. and Dreizin E.L., *Ignition and combustion of Al-Mg alloy powders prepared by different techniques*. Combustion and Flame, 2015. 162(4): p. 1440-1447.
196. Gordon, S. and McBride B., *Computer program for calculation of complex chemical equilibrium compositions and applications*. 1996, NASA Reference Publication 1311.
197. Chase, M.W., *NIST-JANAF Thermochemical Tables, Fourth Edition*. J. Phys. Chem. Ref. Data, 2001: p. 1-1951.
198. Sun, Y., Chintersingh K.L., Schoenitz M. and Dreizin E.L., *Reactive Shell Model for Boron Oxidation*. Journal of Physical Chemistry C, 2019. 123(18): p. 11807-11813.
199. Nie, H., *Reaction interface between aluminum and water*. International Journal of Hydrogen Energy, 2013. 38(26): p. 11222-11232.

200. Chintersingh, K.L., Schoenitz M. and Dreizin E.L, *Heterogeneous reaction kinetics for oxidation and combustion of boron*. Thermochemica Acta, 2019. 682.